IMAGE-GUIDED INTERVENTIONS USING CONE-BEAM CT: IMPROVING IMAGE QUALITY WITH MOTION COMPENSATION AND TASK-BASED MODELING

by
Sarah Janet Capostagno

A dissertation submitted to Johns Hopkins University in conformity with the requirements for the degree of Doctor of Philosophy

Baltimore, Maryland
May 2020

Abstract

Cone-beam CT (CBCT) is an increasingly important modality for intraoperative 3D imaging in interventional radiology (IR). However, CBCT exhibits several factors that diminish image quality — notably, the major challenges of patient motion and detectability of low-contrast structures — which motivate the work undertaken in this thesis.

A 3D–2D registration method is presented to compensate for rigid patient motion. The method is fiducial-free, works naturally within standard clinical workflow, and is applicable to image-guided interventions in locally rigid anatomy, such as the head and pelvis. A second method is presented to address the challenge of deformable motion, presenting a 3D autofocus concept that is purely image-based and does not require additional fiducials, tracking hardware, or prior images. The proposed method is intended to improve interventional CBCT in scenarios where patient motion may not be sufficiently managed by immobilization and breath-hold, such as the prostate, liver, and lungs.

Furthermore, the work aims to improve the detectability of low-contrast structures by computing source–detector trajectories that are optimal to a particular imaging task. The approach is applicable to CBCT systems with the capability for general source–detector positioning, as with a robotic C-arm. A "task-driven" analytical framework is introduced, various objective functions and optimization methods are described, and the method is investigated via simulation and phantom experiments and translated to task-driven source–detector trajectories on a clinical robotic C-arm to demonstrate the potential for improved image quality in intraoperative CBCT.

Overall, the work demonstrates how novel optimization-based imaging techniques can address major challenges to CBCT image quality.

Readers

Jeffrey H. Siewerdsen, Ph.D. (advisor)
John C. Malone Professor, Department of Biomedical Engineering
Johns Hopkins University

Jerry L. Prince, Ph.D.
William B. Kouwenhoven Professor, Department of Electrical and Computer Engineering
Johns Hopkins University

Alejandro Sisniega Crespo, Ph.D.
Research Associate, Department of Biomedical Engineering
Johns Hopkins University

J. Webster Stayman, Ph.D.
Associate Professor, Department of Biomedical Engineering
Johns Hopkins University

Clifford R. Weiss, M.D.
Associate Professor, Russell H. Morgan Department of Radiology
Johns Hopkins University

Acknowledgements

First and foremost I must thank my advisor Dr. Jeffrey H. Siewerdsen for his exceptional guidance in helping me perform the work in this thesis and to become a better scientist. He has been tireless in his support of my efforts and passing on his vast amount of knowledge. He has been an enormous influence on where I am headed professionally, and I look forward to many more years benefiting from his guidance and knowledge.

I would also like to thank my family, to whom this thesis is dedicated. Dan for being my never ending support and for going on this exciting and difficult journey with me, Joe for being the best role model a little sister could ask for and blazing a path that I have simply followed, and Mom and Dad for their never-ending support and encouraging me to dream big.

I must thank my wonderful mentors and lab mates in the I-STAR Lab — Alex, Web, Jen, Hao, Qian, Michael, Ali, Tharindu, Grace, Adam, Ja, Joseph, Matt, Amir, Sophia, Nicole, Niral, Pengwei, Esme, Runze, Rohan, and Prasad. Alex in particular has been exceptional in helping me see this work through and I want to thank him for his patience and kindness.

I have also had several clinical mentors whose influence has helped me make the decision to attend medical school. They include Dr. Clifford R. Weiss in interventional radiology, Dr. William “Stan” Anderson in neurosurgery, and Drs. John Carey and Francis “Pete” Creighton in otolaryngology. I am unable to thank them enough for their willingness to let me observe their practice, answer my many questions, and their guidance on incorporating a PhD with a career in medicine.

I would also like to mention the heroic graduate students who laid the groundwork of "task-based" image quality assessment and optimization over the last 20 years. That started with Samuel Richard (who used it to optimize DE imaging protocols), followed by Daniel Tward (who used it to analyze CBCT image quality), then Prakhar Prakash (who designed a whole extremities CBCT scanner with it), then Grace Gang (who used it to analyze CBCT and tomosynthesis, and extended it to MBIR), then Jennifer Xu (who extended it to photon counting detectors and used it to optimize the design of a CBCT head scanner), then Qian Cao (who used it to revisit the question of optimal detector design), and then Hao Dang (who used it to optimize MBIR reconstruction parameters). It will not end there, but every one of those students put a brick in the foundation upon which the work in this thesis was built.

As the story goes, "Once upon a time (circa 1996), there was a grad student who looked at his models for NEQ and DQE and said, 'hey — I could weight the DQE by some spatial-frequency function, integrate, and tell you how well the system performs at that.' Then ICRU-54 came out and said what that spatial-frequency function should look like based on SDT. Et voila." But I am told that I do not need to mention that guy in the litany of grad students.

Dedication:
For Dan, Joe, Mom, and Dad.

Table of Contents

List of Tables

List of Figures

Chapter 1: Introduction

1.1. Image-Guided Interventions

Image-guided interventions (IGI) are medical procedures that use images of the patient to help the physician precisely visualize and target anatomical structures in a minimally invasive manner. Conventionally, images obtained prior to the procedure and spatially registered to the patient at the time of intervention form the basis of surgical "navigation." However, images acquired *during* the procedure (i.e., intraoperative images) provide numerous benefits — most notably, visualization of anatomy, implanted devices, and other therapeutic agents introduced at the time of intervention. The last several decades have seen great advances in intraoperative imaging techniques and computing power, offering to improve the accuracy and outcomes of current procedures and enabling new procedures altogether (Cleary and Peters 2010).

IGI has its main applications in interventional radiology (IR, including abdominal, cardiovascular, and neurovascular interventions), image-guided radiation therapy (IGRT, including external beam radiation therapy and brachytherapy), and surgery (including neurosurgery, orthopedic surgery, and otolaryngology – head and neck surgery). The main applications discussed in the context of this thesis include neuro-IR and abdominal IR. Both subspecialties use intraoperative imaging to assist in delivering treatment endovascularly. Such treatments include embolization of vascular anomalies, tumors, and feeder vessels, performing biopsies, and various methods of tissue ablation (Cleary and Peters 2010).

A wide range of imaging modalities and techniques are used for IGI, and combinations of one or more are often used throughout a case to provide image guidance. Prior to the procedure, a pre-operative image (or images) are obtained typically using either a diagnostic multi-detector CT (MDCT) system and / or magnetic resonance (MR) imaging, depending on the anatomical structures of interest. The pre-operative image is used for planning purposes and can be referenced throughout the case. At the start of the case, ultrasound imaging may be utilized to visualize vessels and blood flow to introduce a catheter into the vascular system (either arterial or venous, depending on the approach). With vascular access achieved, fluoroscopy may be acquired to visualize the catheter as it is advanced to the treatment site. Once at the treatment site, 3D cone-beam CT (CBCT) may be acquired to better visualize the target lesion and / or local vasculature and to ensure that the catheter is in the correct location. 2D fluoroscopy and 3D CBCT may continue to be acquired throughout the treatment phase of the case for additional guidance and quality assurance. Following the procedure, diagnostic quality MDCT and / or MR images may be used again to assess the outcome.

Figure 1.1 shows several examples of images acquired during an abdominal IGI to treat hepatocellular carcinoma. Figure 1.1a shows a 2D fluoroscopy image acquired to help the clinician guide the catheter to the hepatic vasculature. The catheter can be seen in the superior-inferior (SI) direction parallel to the spine, and the hepatic vasculature is filled with iodine contrast making it radiopaque. Figure 1.1b shows a 3D rendering of the patient anatomy after contrast injection. This type of rendering is created from a 3D CBCT image and can provide the clinician more complete understanding of complicated 3D structures. Figures 1.1c and 1.1d show axial slices of two CBCT images acquired during the case. The

first (Figure 1.1c) was acquired when the iodine contrast was in the arterial system of the patient. The arteries are bright in the image, allowing the clinician to visualize a "roadmap" that will allow the catheter to traverse to the treatment area through the arterial system. The second image (Figure 1.1d) was acquired after the contrast had perfused into the tumor. The tumor is bright in the image, allowing the clinician to visualize the treatment area.

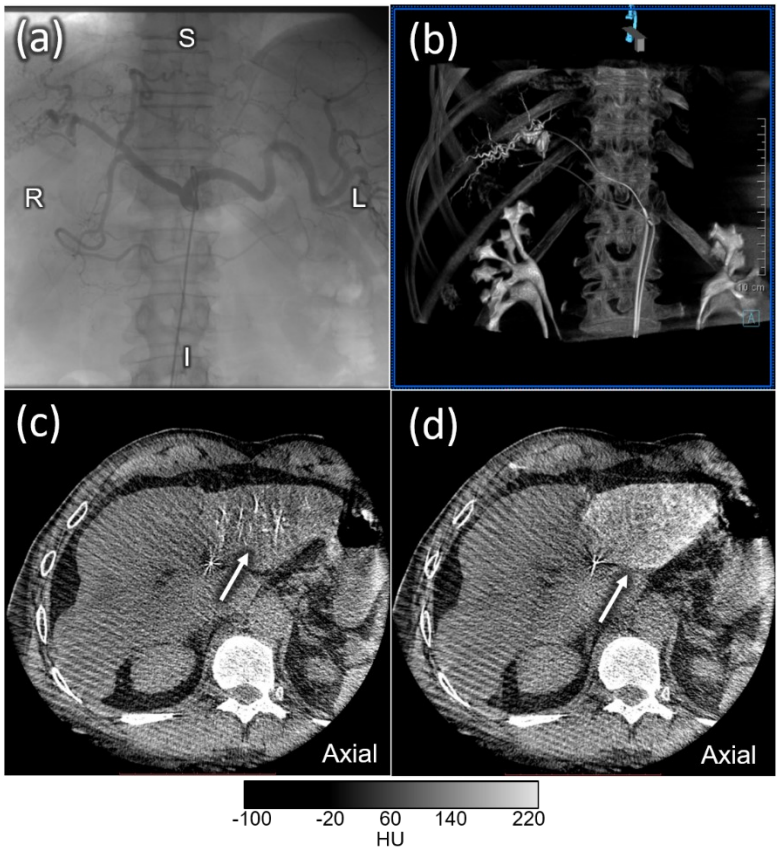

Figure 1.1. Example images used for an abdominal IGI. (a) A fluoroscopy image showing the catheter, spine, and contrast-enhanced hepatic vasculature. (b) A 3D rendering of the CBCT image acquired during the intervention, showing the high-contrast structures (spine, ribs, contrast-filled kidneys and hepatic vasculature, catheter). (c) A 3D CBCT image acquired when contrast is entering the arterial vasculature (indicated by the white arrow). (d) A 3D CBCT image acquired after contrast has perfused throughout the hepatic tumor (indicated by the white arrow).

The following sections of this chapter focus on the use of CBCT imaging during IGI. Section 1.2 provides details on CBCT imaging systems used in the clinical setting and

an overview of CBCT system geometry. Section 1.3 discusses CBCT image reconstruction using both analytic and iterative methods, and Section 1.4 addresses basic principles of image registration, including 3D–3D and 3D–2D image registration. Section 1.5 discusses several image quality challenges in CBCT to provide a basis for the novel methods presented in the following chapters of this thesis. Finally, Section 1.6 presents the outline of the thesis and the overarching thesis statement.

1.2. Cone-Beam CT Systems

1.2.1. Clinical Systems

A wide variety of CBCT systems have been developed in recent years, with increased utilization in IGRT (Jaffray et al 2002), image-guided surgery (Siewerdsen et al 2005), and IR (Fahrig et al 2006). Several clinical CBCT systems are shown in Figure 1.2. Figure 1.2a shows a mobile C-arm system (Cios Spin 3D, Siemens Healthineers, Forchheim Germany) that supports use between operating rooms in image-guided surgery. The open gantry can be brought to the operating table and rotated around the patient with minimal disruption to the operating setup. Figure 1.2b shows a mobile O-arm system (O-arm, Medtronic, Dublin Ireland). The O-arm system has similar surgical applications to the mobile C-arm system in Figure 1.2a, with the exception that it has a breakable, closed-ring gantry to house the x-ray source and detector (cf., an open gantry).

Figure 1.2c shows a fixed-room biplane system (Artis Zee Biplane, Siemens Healthineers, Forchheim Germany) used for procedures in IR. The fixed-room setup allows higher power to be delivered to the x-ray tube and includes dedicated room features (e.g., large television screens to display images and a motorized patient table integrated with the

imaging system). The biplane aspect indicates that there are two orthogonal x-ray sources and detectors. As such, 2D projections can be acquired from orthogonal views to provide 3D localization. Fixed-room systems are ideal for IR procedures, in which the imaging system is used throughout the case and relied on heavily for guidance and verification during the intervention. Figure 1.2d shows a fixed-room robotic C-arm system (Artis Zeego, Siemens Healthineers, Forchheim Germany) with similar interventional applications to the biplane system. However, the robotic C-arm has additional degrees of freedom (DoF) of movement around the patient and table and can move to pre-programmed positions desired by the clinician.

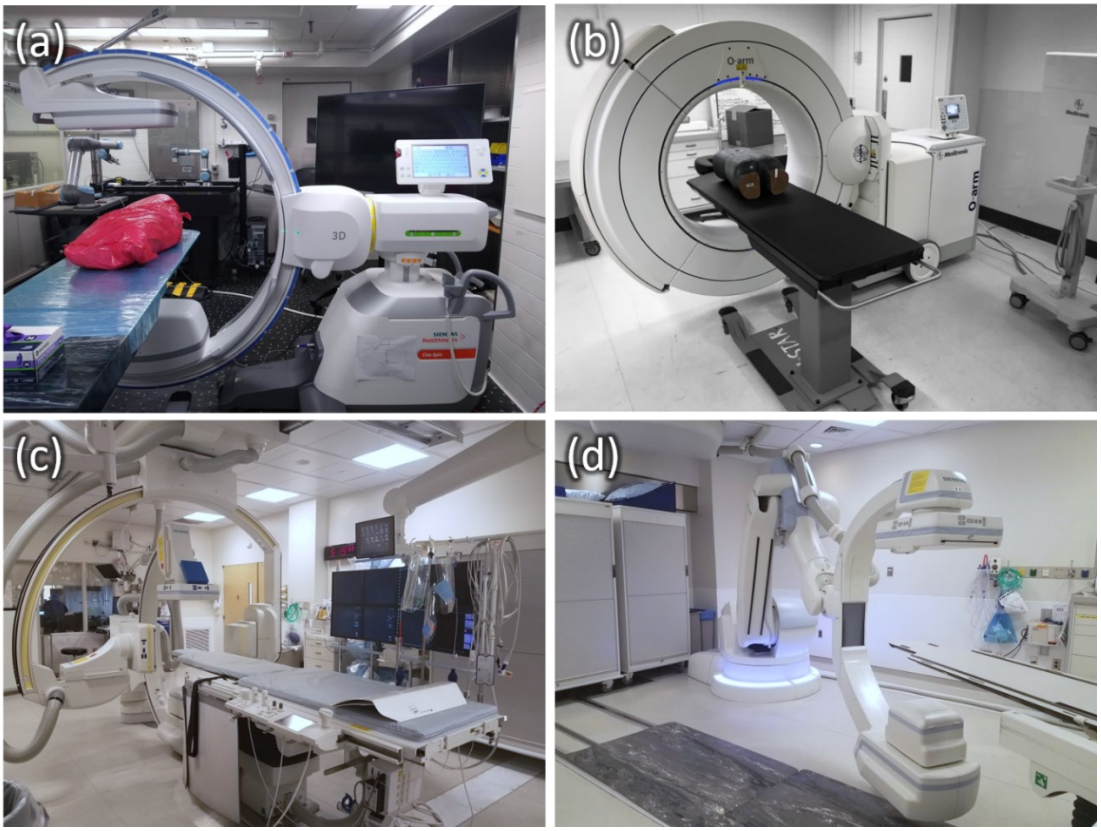

Figure 1.2. Examples of clinical CBCT systems. (a) Mobile C-arm system for image-guided surgery (Siemens Healthineers). (b) Mobile O-arm system for image-guided surgery (Medtronic, photo courtesy of Dr. A. Uneri, Johns Hopkins University). (c) Fixed-room biplane system for IR (Siemens Healthineers). (d) Fixed-room robotic C-arm system for IR (Siemens Healthineers).

Additional clinical systems beyond those shown in Figure 1.2 include variations of fixed-room systems used in IR with C-arms mounted to the floor, wall, or ceiling, CBCT systems in which the x-ray source and detector are mounted to the rotating gantry of a linear accelerator for IGRT (Jaffray et al 2002), and a wide variety of dedicated CBCT systems, including dental / maxillofacial imaging (Miracle and Mukherji 2009), extremity imaging (Carrino et al 2014), breast imaging (Boone et al 2001), and head imaging (Xu et al 2016).

1.2.2. System Geometry

All of the CBCT systems discussed in Section 1.2.1 are composed of an x-ray source, a divergent beam of x-rays passing through the object / patient, and a flat-panel detector (FPD). The position and orientation of these three components represents the system geometry. The x-ray source and FPD typically move in a circle about the patient to acquire the set of 2D projections that are reconstructed into a 3D image. CBCT systems differ from diagnostic MDCT systems in that the longitudinal coverage of the x-ray beam is extended and only a single rotation of the source and FPD is needed to reconstruct a volumetric field of view (FOV). Due to mechanical differences in such open geometries, CBCT systems also tend to be much slower in acquiring an image than MDCT acquisitions (~5–60 s vs 0.2 s / rotation).

3D image reconstruction requires accurate specification of the system geometry and errors in geometric calibration result in artifacts, distortion, and other undesirable image features (Li et al 1994, Jaffray et al 2002). System geometry for each projection in a CBCT scan can be divided into intrinsic and extrinsic parameters. Intrinsic parameters define the x-ray source position relative to the FPD and can be parameterized by 3 DoF. Most CBCT

systems have fixed intrinsic geometry, including dental, extremity, and head CBCT scanners, and some mobile C-arms. Conversely, some systems have adjustable intrinsic geometry, such as robotic C-arm systems. Extrinsic parameters relate the patient pose to the detector coordinate frame and are represented by a 6 DoF translation and rotation.

The projection geometry for a single view is illustrated in Figure 1.3. The origin of the world coordinate frame is located at the lower left corner of the detector with the *x* and *y* axes parallel to the detector edge and the *z* axis formed by their cross product. The patient coordinate frame is located at the center of the CBCT volume. Its position and orientation with respect the world coordinate frame (extrinsic parameters) are represented as a 6-element vector of translations and rotations ($t_x, t_y, t_z, \theta_x, \theta_y, \theta_z$). The projection geometry is parameterized by the source position (s_x, s_y, s_z) with respect to the detector coordinates (intrinsic parameters), where s_z represents the length of the perpendicular line from the source to the detector (source-to-detector distance, SDD) and (s_x, s_y) represents the detector piercing point.

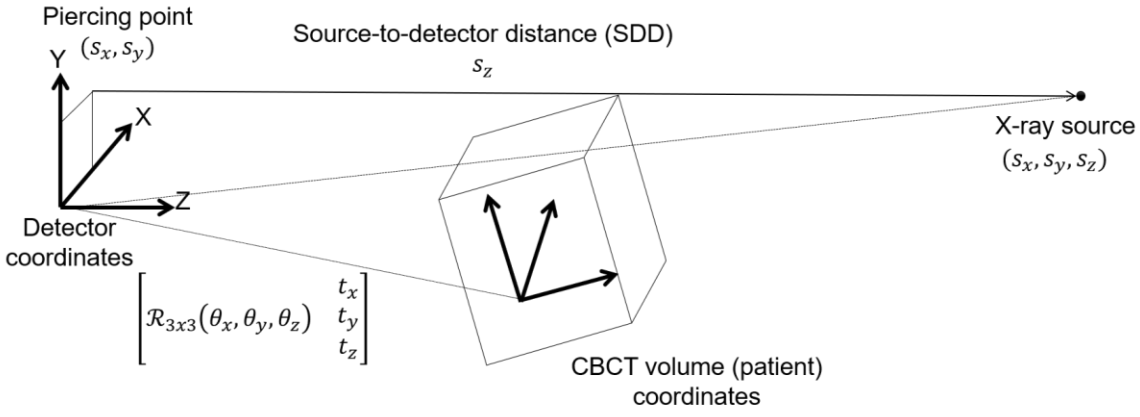

Figure 1.3. Projection geometry and parameters associated with the x-ray source, CBCT volume, and detector coordinate frames.

These nine parameters come together to form a projection matrix (PM), which relates a 3D location in the image volume $(x, y, z)^T$ to a 2D location in the projection $(u, v)^T$ according to:

$$\begin{pmatrix} u \\ v \end{pmatrix} \sim \text{PM} \begin{pmatrix} x \\ y \\ z \\ 1 \end{pmatrix} = \begin{pmatrix} s_z & 0 & s_x & 0 \\ 0 & s_z & s_y & 0 \\ 0 & 0 & 1 & 0 \end{pmatrix} \begin{pmatrix} \mathcal{R}_{3x3}(\theta_x, \theta_y, \theta_z) & \begin{matrix} t_x - s_x \\ t_y - s_y \\ t_z - s_z \end{matrix} \\ 0 \quad 0 \quad 0 & 1 \end{pmatrix} \begin{pmatrix} x \\ y \\ z \\ 1 \end{pmatrix} \tag{1.1}$$

The system geometry can be broadly defined by the SDD, corresponding to s_z, and the source-to-axis distance (SAD), corresponding to $(s_z - t_z)$, with the geometric magnification of the system given by:

$$\text{Mag} = \frac{\text{SDD}}{\text{SAD}} \tag{1.2}$$

1.3. Image Reconstruction

1.3.1. Filtered Backprojection

CT reconstruction computes a 3D image from a series of 2D projections acquired from many angles around the object / patient using the defined system geometry. One of the most widely used reconstruction algorithms for CT is filtered backprojection (FBP). FBP is an analytic method that relates weighted, ramp-filtered projection data to the attenuation coefficient of the original object. FBP for a 2D object with 1D projections may be defined as

$$f(x, y) = \int_0^{\pi} \left[\int_{-\infty}^{\infty} P(\rho, \theta) |\rho| e^{2\pi j \rho u} \, \mathrm{d}\rho \right]_{u = x \cos\theta + y \sin\theta} \mathrm{d}\theta \tag{1.3}$$

where $f(x, y)$ represents the object (spatial distribution of attenuation coefficient), and $P(\rho, \theta)$ is the Fourier transform of the projection at angle θ. The inner integral is the

inverse Fourier transform of $P(\rho, \theta)$ multiplied with a frequency-domain ramp filter, $|\rho|$. Therefore, the reconstructed image $f(x, y)$ at location (x, y) is the summation of all filtered projection samples that pass through that point. With this definition of the reconstruction process, it is a requirement for FBP that the source–detector geometry follow a circular orbit.

Equation (1.3) describes the underlying essence of FBP in terms of the Fourier slice theorem for a 2D image with 1D projections (Hsieh 2003). A practical algorithm for 3D FBP developed by Feldkamp et al (1984) extended this 2D slice reconstruction algorithm to three dimensions using additional weighting factors to account for the cone-beam geometry of the system. The resulting Feldkamp-Davis-Kress (FDK) algorithm is the basis for many of the CBCT reconstructions used throughout this thesis.

A practical, voxel-driven method for backprojection for 3D image reconstruction is illustrated in Figure 1.4. Each 3D location $(x, y, z)^T$ in the reconstructed image volume is related to a 2D location $(u, v)^T$ in the projection data via the PM defined by Equation (1.1). Since the resulting location $(u, v)^T$ will likely not fall at the center of a pixel in the discretized filtered projections, 2D bilinear interpolation is performed to determine the value that is assigned to the voxel.

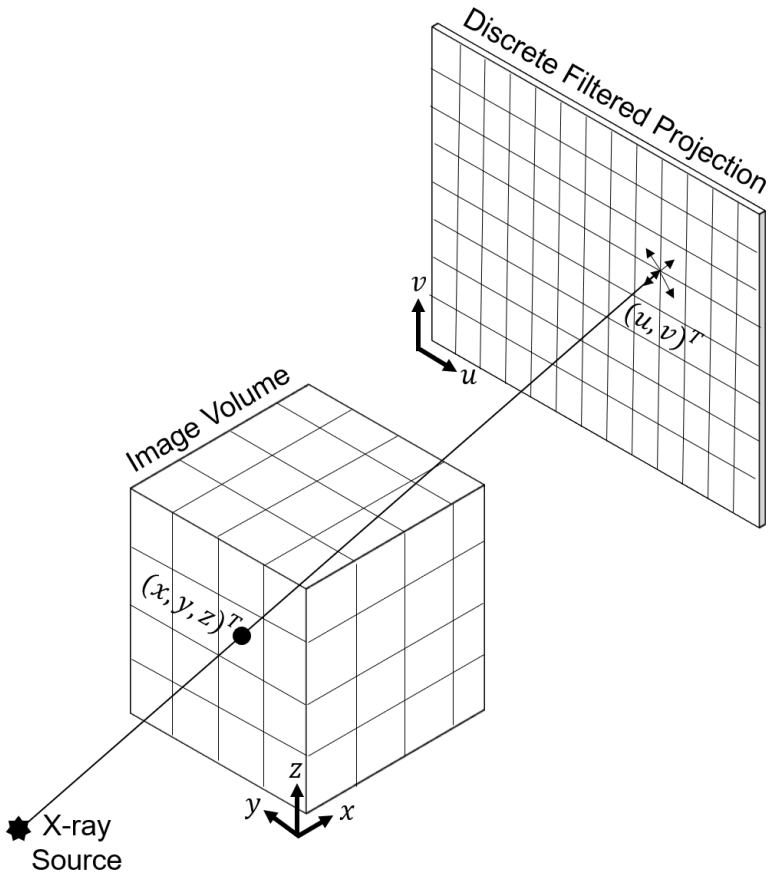

Figure 1.4. Depiction of voxel-driven backprojection used in CBCT reconstruction by FBP. The 3D location $(x, y, z)^T$ in the image volume is related to the 2D location $(u, v)^T$ in the filtered projection image using the system geometry. 2D interpolation is used in the discrete projection to determine the value assigned to the voxel.

1.3.2. Model-Based Iterative Reconstruction

An alternative class of 3D image reconstruction techniques is often referred to as optimization-based, or more commonly, model-based iterative reconstruction (MBIR), whereby the image is estimated through successive iterations that maximize an objective function. MBIR methods have become attractive in part because of their ability to incorporate prior knowledge in the reconstruction process through statistical modeling and their ability to reconstruct images from non-circular orbits. For example, anatomical images can be reasonably expected to be piece-wise constant, and such desirable image

properties (i.e., sharp edges) can be included in the reconstruction process. Enforcement of such properties makes MBIR methods particularly attractive when reconstructing low-contrast image features from noisy (i.e., low dose) projection data. Figure 1.5a shows the reconstruction of a low-dose image using FBP as described in Section 1.3.1, whereas Figure 1.5b shows the same data reconstructed using an MBIR method. The noise in the soft-tissue regions is markedly decreased for the MBIR method, allowing improved visualization of soft-tissue structures.

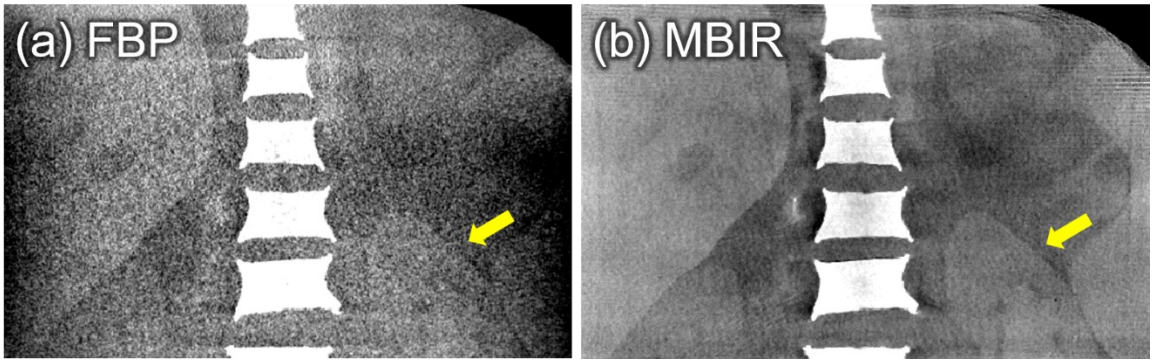

Figure 1.5. Reconstruction of a low-dose image using (a) FBP and (b) MBIR methods. The MBIR method results in markedly decreased noise in the reconstructed image and better visualization of the low-contrast soft-tissue structures (yellow arrows).

MBIR starts with an initial guess of the attenuation values within the reconstruction and successively refines these values using an optimization algorithm. In general, the objective function for optimization can be written as

$$\widehat{\boldsymbol{\mu}} = \arg\min_{\boldsymbol{\mu}} \|\boldsymbol{y}, \mathbf{A}\boldsymbol{\mu}\| \tag{1.4}$$

where $\boldsymbol{y}$ represents the projection measurements, $\boldsymbol{\mu}$ represents the current image estimate, and $\mathbf{A}$ represents a mathematical forward model that relates the 3D image voxel values to 2D pixel values and can be arbitrarily complex with the inclusion of various aspects of x-ray imaging physics such as quantum noise, x-ray scatter, and polyenergetic effects. To minimize the objective in Equation (1.4), with each iteration, the true projection

measurements are compared to the forward-projected values from the current image estimate, and the optimization algorithm updates the image estimate to minimize the difference.

The specific form of MBIR used throughout this thesis is penalized-likelihood (PL) estimation. The PL objective includes a log-likelihood term that incorporates a Poisson model of image statistics (quantum noise) and a regularization term to enforce particular properties in the image:

$$\widehat{\boldsymbol{\mu}} = \arg\max_{\boldsymbol{\mu}} L(\boldsymbol{y};\boldsymbol{\mu}) - \beta R(\boldsymbol{\mu}) \tag{1.5}$$

In Equation (1.5), the regularization term $R(\boldsymbol{\mu})$ is subtracted from the log-likelihood term $L(\boldsymbol{y};\boldsymbol{\mu})$ with the parameter β controlling the balance between the terms. The regularization term commonly takes the form:

$$R(\boldsymbol{\mu}) = \sum_{v} \sum_{j \in N_j} \Psi\left(\mu_v - \mu_j\right) \tag{1.6}$$

where the difference of voxels in a defined neighborhood penalizes according to the potential function Ψ. A common choice is a quadratic penalty related to the squared difference between voxels:

$$\Psi\left(\mu_v - \mu_j\right) = \frac{\left(\mu_v - \mu_j\right)^2}{2} \tag{1.7}$$

where $(\mu_v - \mu_j)$ denotes a difference between neighboring voxels in the 3D image reconstruction (described in greater detail in Chapter 2). Alternatively, a Huber penalty may be used, providing regularization that is quadratic for small differences (smoothing noise) and linear for large differences (enforcing sharp edges):

$$\Psi(\mu_v - \mu_j) = \begin{cases} \dfrac{(\mu_v - \mu_j)^2}{2\delta} & \text{for } |\mu_v - \mu_j| < \delta \\ \left|(\mu_v - \mu_j) - \dfrac{\delta}{2}\operatorname{sgn}(\mu_v - \mu_j)\right|, & \text{otherwise.} \end{cases} \tag{1.8}$$

where $\operatorname{sgn}(\cdot)$ is the sign function and δ is an adjustable parameter below which the penalty is quadratic and above which it is linear.

1.4. Image Registration

1.4.1. 3D–3D Registration

Registering medical images is a challenging task, subject to a broad spectrum of ongoing research. For IGI, it is especially useful in localizing information that is defined in a previous image (e.g., the pre-operative image) relative to an image acquired during the procedure. Image registration is the process of aligning two images (of the same underlying object — e.g., the patient) in a common coordinate system such that shared image features are spatially coincident. One image is designated as the "fixed" image and the other as the "moving" image. With these designations, the moving image is transformed into the coordinate system of the fixed image such that the structures within the images align as well as possible. Image registration involves application of a transformation (e.g., rigid or deformable) to the moving image, a similarity objective (e.g., cross-correlation of the images), and an optimization algorithm (e.g., gradient descent).

The basic process of 3D–3D image registration is illustrated in Figure 1.6a. The fixed image is held static, while a transformation (either deformable or rigid) is applied to the moving image to maximize a similarity objective computed between the fixed image and the transformed moving image. The optimization algorithm works to maximize the

similarity objective by updating the transformation parameters such that the similarity calculated at the next iteration is increased. With the similarity objective maximized, the resulting transformation is applied to the moving image to generate the final registered image and to resolve information defined in the previous image within the context of the current image.

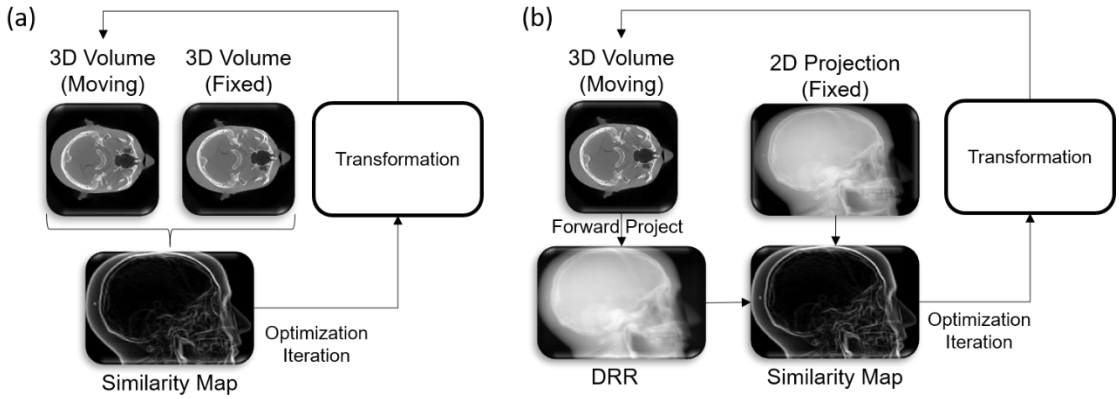

Figure 1.6. Illustrative flowcharts for image registration. (a) 3D–3D image registration. (b) 3D–2D image registration.

1.4.2. 3D–2D Registration

Registering a 3D image to a 2D image is often helpful in IGI that uses 2D fluoroscopy. For example, it may be desirable to register a prior 3D MDCT or CBCT image to 2D fluoroscopic images acquired at various times during the case. 3D–2D image registration is similar to 3D–3D image registration in that it relies on a transformation applied to the moving image, a similarity objective, and an optimization algorithm. However, the similarity between the 3D image (e.g., CBCT) and the 2D image (e.g., fluoroscopy) involves an additional step that transforms the 3D image to 2D.

The basic process of 3D–2D registration is illustrated in Figure 1.6b. Typically the 3D image is designated the moving image, and the fixed 2D projection image is held static. The transformation (e.g., a 6 DOF rigid translation and rotation) is applied to the 3D image,

and the transformed volume is forward-projected (according to the system geometry) to generate a 2D digitally reconstructed radiograph (DRR). Similarity is calculated between the fixed 2D projection and the 2D DRR, and the optimization algorithm seeks to maximize the similarity by updating the transformation with each iteration.

1.5. Challenges to Image Quality in Cone-Beam CT

CBCT involves a number of factors that diminish image quality compared to MDCT that are the subject of a wide range of ongoing research. Image quality degradation (image artifacts) in CBCT can arise from many components of the imaging system and image reconstruction pipeline, including detector defects, image lag, lateral truncation of the object, sparse sampling, the cone-beam null space, geometric error, high scatter-to-primary ratio, and patient motion.

The sources of image degradation listed above are distinct from MDCT, and many methods have been developed to address them. Two major challenges that underlie the bulk of this thesis relate to the challenges presented by patient motion and to the detectability of fine or low-contrast structures. The first stems from involuntary motion during relatively slow (~5–60 s) CBCT scans, and the latter from numerous factors of the CBCT imaging chain (e.g., blur and noise).

Figure 1.7 illustrates a number of such image quality challenges in a CBCT image. During the intraoperative CBCT scan, the patient was overly-sedated and unable to comply with breath-hold techniques. As a result, significant motion artifacts are seen throughout the image as indicated by cyan arrows. Motion artifacts manifest as streaks, blur, and distortion within the image. Streaks are particularly evident about the small contrast-

enhanced vessels throughout the image as well as the ribs at the anterior of the patient. The deformable nature of the motion is evident in that the anterior is more severely affected by such artifacts (motion of the abdominal surface during respiration), whereas the posterior is relatively unaffected (patient laying prone on the operating table). Artifacts from x-ray scatter and beam-hardening are evident as dark shading indicated by yellow arrows between highly attenuating bone structures.

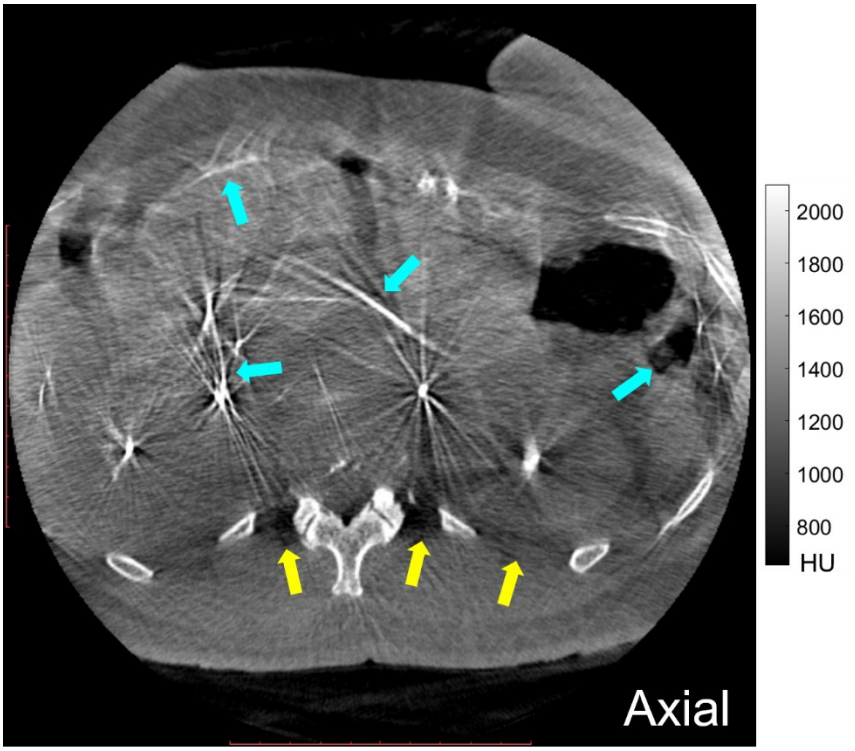

Figure 1.7. An intraoperative CBCT image demonstrating the effects of patient motion and x-ray scatter on image quality. The cyan arrows indicate locations where motion artifacts are obvious, typified by blurring and streaks about structures of interest, and the yellow arrows indicate locations where artifact from x-ray scatter is obvious, typified by loss of contrast and reduced attenuation value (shading).

1.6. Outline of the Thesis

Thesis Statement: Image quality in CBCT for IGI can be improved through patient motion compensation and task-based design of CBCT imaging protocols. Motion compensation methods presented in this thesis focus on both rigid and deformable motion, and methods to design a task-based imaging protocol focus on the source–detector trajectory.

In Chapter 2 we present a method to compensate for rigid patient motion that can occur during the long scan times associated with CBCT (~5–60 s) with applications in neuro-IR. Motion compensation is achieved through image registration of the 2D projections images to a prior, motion-free 3D image. The method is applied to both the simulated motion of a phantom and real patient motion in clinical datasets. The results demonstrate the potential to recover image quality nearly identical to that of a motion-free reference image while compensating for large motion magnitude. Research in Chapter 2 was presented at the following scientific conference:

> Ouadah, S.,† Jacobson, M., Stayman, J. W., Ehtiati, T., and Siewerdsen, J. H. (2016). Correction of patient motion in C-arm cone-beam CT using 3D–2D registration. *AAPM 58th Annual Meeting & Exhibition*, Washington, D.C., July 31–August 4, 2016, Oral presentation.

and published in the following peer-review journal and conference proceeding:

> Ouadah, S.,† Jacobson, M., Stayman, J. W., Ehtiati, T., Weiss, C., and Siewerdsen, J. H. (2017). Correction of patient motion in cone-beam CT using 3D–2D registration. *Physics in Medicine & Biology*, 62(23), 8813–8831.
>
> Ouadah, S.,† Jacobson, M., Stayman, J. W., Ehtiati, T., and Siewerdsen, J. H. (2016). Correction of patient motion in C-arm cone-beam CT using 3D–2D registration. *Medical Physics*, 43(6Part38), 3792–3793.

†S. Capostango, née S. Ouadah – here and throughout this thesis.

In Chapter 3 we extend motion compensation to the more difficult problem of deformable motion that occurs in the soft-tissue of the abdomen. Deformable motion compensation is performed by estimating rigid motion for multiple small regions throughout the image. Motion is estimated through use of an autofocus objective with regularization to maximize sharpness of image gradients while enforcing constraints on the smoothness of the motion in both time and space. The subsequent interpolation of a 4D deformation field captures the deformable nature of the motion. This method is shown to be successful in cadavers undergoing complex, deformable motion throughout the abdomen. Research in Chapter 3 was presented at the following scientific conferences:

> Capostagno, S., Sisniega, A., Stayman, J. W., Ehtiati, T., Weiss, C. R., and Siewerdsen, J. H. (2020). Image-based deformable motion compensation in cone-beam CT: translation to clinical studies in interventional body radiology. *SPIE Medical Imaging 2020*, Houston, TX, February 15–20, 2020, Oral presentation.
>
> Capostagno, S., Sisniega, A., Ehtiati, T., Stayman, J. W., Weiss, C. R., and Siewerdsen, J. H. (2019). Correction of organ motion in cone-beam CT-guided transarterial chemoembolization. *SIR 2019 Annual Scientific Meeting*, Austin, TX, March 23–28, 2019, ePoster presentation.
>
> Capostagno, S., Sisniega, A., Ehtiati, T., Stayman, J. W., Weiss, C. R., and Siewerdsen, J. H. (2019). Deformable motion correction for interventional cone-beam CT. *APS March Meeting 2019*, Boston, MA, March 4–8, 2019, Oral presentation.
>
> Sisniega, A., Capostagno, S., Zbijewski, W., Weiss, C. R., and Siewerdsen, J. H. (2019). Image-based deformable motion compensation for interventional cone-beam CT. *SPIE Medical Imaging 2019*, San Diego, CA, February 16–21, 2019, Oral presentation.

and published in the following peer-review journal and conference proceedings:

> Capostagno, S., Sisniega, A., Stayman, J. W., Ehtiati, T., Weiss, C. R., and Siewerdsen, J. H. (2020). Image-based deformable motion compensation for interventional cone-beam CT. *Physics in Medicine & Biology*, under review.
>
> Capostagno, S., Sisniega, A., Stayman, J. W., Ehtiati, T., Weiss, C. R., and Siewerdsen, J. H. (2020). Image-based deformable motion compensation in cone-beam CT: translation to clinical studies in interventional body radiology. *Medical*

Imaging 2020: Image-Guided Procedures, Robotic Interventions, and Modeling, 11315, 113150B.

Capostagno, S., Sisniega, A., Ehtiati, T., Stayman, J., Weiss, C., and Siewerdsen, J. (2019). Correction of organ motion in cone-beam CT-guided transarterial chemoembolization. *Journal of Vascular and Interventional Radiology*, 30(3), S215.

Capostagno, S., Sisniega, A., Ehtiati, T., Stayman, J., Weiss, C., and Siewerdsen, J. (2019). Deformable motion correction for interventional cone-beam CT. *Bulletin of the American Physical Society*, 64(2), L30.00003.

Sisniega, A., Capostagno, S., Zbijewski, W., Weiss, C. R., Ehtiati, T., and Siewerdsen, J. H. (2019). Image-based deformable motion compensation for interventional cone-beam CT. *Medical Imaging 2019: Physics of Medical Imaging*, 10948, 109481O.

In Chapter 4 we present the theory of task-based design of source–detector trajectories for CBCT. Task-based imaging can be considered analogous to personalized (precision) medicine in the sense that imaging parameters are tailored to the specific patient and procedure. The task is modeled mathematically in terms of its location, contrast, and spatial frequencies of interest, and the optimization aims to maximize the "detectability index" associated with the imaging task by changing the sampling pattern — i.e., the source–detector trajectory. Research in Chapter 4 was published in the following peer-review journal:

Stayman, J. W.,* Capostagno, S.,* Gang, G. J., and Siewerdsen, J. H. (2019). Task-driven source–detector trajectories in cone-beam computed tomography: I. Theory and methods. *Journal of Medical Imaging*, 6(2), 025002.

In Chapter 5 we present a geometric calibration method that uses a 3D–2D image registration technique like that of Chapter 2. Since task-driven source–detector trajectories deviate from a standard circular orbit, a method for geometric calibration of such orbits is necessary to reconstruct task-driven images. When compared to standard calibration

*J. W. Stayman and S. Capostagno contributed equally to this work.

techniques for a circular orbit, the so called "self-calibration" method performed as well as or better than the standard methods. Research in Chapter 5 was presented at the following scientific conferences:

> Ouadah, S.,† Stayman, J. W., Gang, G., Jacobson, M., Ehtiati, T., and Siewerdsen, J. H. (2015). Self-calibration of cone-beam CT geometry using 3D–2D image registration. *5th Annual Hopkins Imaging Conference*, Baltimore, MD, October 26, 2015, Poster presentation.
>
> Ouadah, S.,† Stayman, J. W., Gang, G., Uneri, A., Ehtiati, T., and Siewerdsen, J. H. (2015). Self-calibration of cone-beam CT geometry using 3D–2D image registration: development and application to task-based imaging with a robotic C-arm. *SPIE Medical Imaging 2015*, Orlando, FL, February 21–26, 2015, Oral presentation.

and published in the following peer-review journal and conference proceeding:

> Ouadah, S.,† Stayman, J. W., Gang, G. J., Ehtiati, T., and Siewerdsen, J. H. (2016). Self-calibration of cone-beam CT geometry using 3D–2D image registration. *Physics in Medicine & Biology*, 61(7), 2613–2632.
>
> Ouadah, S.,† Stayman, J. W., Gang, G., Uneri, A., Ehtiati, T., and Siewerdsen, J. H. (2015). Self-calibration of cone-beam CT geometry using 3D–2D image registration: development and application to task-based imaging with a robotic C-arm. *Medical Imaging 2015: Image-Guided Procedures, Robotic Interventions, and Modeling,* 9415, 94151D.

In Chapter 6 we apply the methodology detailed in Chapter 4 to scenarios emulating imaging tasks in neuro-IR. The task-driven imaging framework is used to optimize the CBCT source–detector trajectory by maximizing a detectability index. The approach was applied to simulated cases of endovascular embolization of an aneurysm and arteriovenous malformation (AVM) and was translated to real data first using a CBCT test bench followed by implementation on an interventional robotic C-arm. The improvements in detectability and the demonstration of the task-driven workflow using a real interventional imaging system show the potential of the task-driven imaging framework to improve

imaging performance on motorized, multi-axis C-arms in neuro-IR. Research in Chapter 6 was presented at the following scientific conference:

> Ouadah, S.,† Jacobson, M., Stayman, J. W., Ehtiati, T., Weiss, C., and Siewerdsen, J. H. (2017). Task-driven orbit design and implementation on a robotic C-arm system for cone-beam CT. *SPIE Medical Imaging 2017*, Orlando, FL, February 11–16, 2017, Oral presentation.

and published in the following conference proceeding and peer-review journal:

> Capostagno, S.,* Stayman, J. W.,* Jacobson, M. W., Ehtiati, T., Weiss, C. R., and Siewerdsen, J. H. (2019). Task-driven source–detector trajectories in cone-beam computed tomography: II. Application to neuroradiology. *Journal of Medical Imaging*, 6(2), 025004.
>
> Ouadah, S.,† Jacobson, M., Stayman, J. W., Ehtiati, T., Weiss, C., and Siewerdsen, J. H. (2017). Task-driven orbit design and implementation on a robotic C-arm system for cone-beam CT. *Medical Imaging 2017: Physics of Medical Imaging*, 10132, 101320H.

In the final chapter of the thesis, the key findings from each chapter are reviewed, and the underlying theme of optimization-based imaging intrinsic to each of the methods is reflected upon within a larger context and potential future work. We discuss the clinical utility of each method, including how such methods may be incorporated into clinical workflow to improve intraoperative CBCT image quality. This final discussion aims to bridge the translational gap between research and clinical application with the hope of seeing such advanced imaging techniques brought to the benefit of patient safety and outcomes for procedures in IGI.

Chapter 2: Rigid Motion Compensation for Interventional Cone-Beam CT Using 3D–2D Registration

2.1. Introduction

CBCT for IGI involves relatively long scan times (~5–60 s) and can be subject to artifacts from patient motion. A similar challenge exists in CBCT for IGRT where acquisition times may be even longer (~30–120 s, Jaffray et al 2002). Patient motion can arise from respiration, the cardiac cycle, gas moving in the intestines, or involuntary muscle motion or twitches; motion artifacts are evident as blurring, streaks, and / or distortion of the reconstructed image. Such motion, even at the millimeter scale, can confound accurate localization of anatomical structures, which is critical for IGI. For example, in studying motion of the head in 20 patients undergoing CT without rigid fixation, Wagner et al (2003) found that all 20 patients exhibited detectable motion, with four patients showing perceptible motion artifacts in the reconstructed image. Li et al (2010a) similarly concluded in a study of 19 volunteers that all subjects displayed head motion while undergoing CT scans without rigid fixation, and further estimated that the head motion of patients without rigid fixation will not be smaller than 0.35 mm, which cannot be neglected in high-resolution CBCT imaging.

A variety of methods for motion compensation in CBCT have been proposed. Many of these methods were developed in the context of 4D imaging. For example, several motion compensation methods have employed gating for cyclical motion (either prospective or retrospective), most notably for periodic motion of the lungs and heart in

thoracic imaging (Rit et al 2009, Rohkohl et al 2013, Müller et al 2014). These methods typically use a general or patient-specific motion model to divide projection data into various phases, with the quality of the resulting images dependent on the accuracy of the model and the number and distribution of projection views in each phase bin. Other 4D imaging techniques employ deformable image registration to solve for the motion vector field (MVF) on a voxel-wise basis (Isola et al 2010, Tang et al 2012, Brehm et al 2013).

For static 3D imaging — e.g., imaging of the head — involuntary motion rarely follows a pre-defined model, and the 4D motion "model" is usually of secondary or no interest compared to clear visualization and static localization of the anatomy. Methods to minimize motion during the scan include instructions to the patient (e.g., breath-hold) and / or physical immobilization (e.g., frames and / or straps), but may be impractical or insufficient in many interventional imaging scenarios.

A number of approaches have been described to compensate for motion in 3D image reconstruction using fiducial markers. Tracking systems can be used to optically track the positions of fiducial markers placed on the patient (Dinelle et al 2006); however, tracker-based motion measurement introduces additional hardware, may face difficulty with line-of-sight occlusion by the imaging gantry or interventional devices, and the geometric accuracy may not be sufficient to correct for sub-millimeter errors (i.e., at the level of the voxel size in 3D image reconstruction). The tracked motion measurements must also be accurately synchronized with projection data acquisition, and proper calibration is needed to convert tracker coordinates to image coordinates (Nazarparvar et al 2012).

Recognizing such drawbacks to motion estimation from externally tracked fiducials, various methods have been proposed to track radiopaque fiducial markers within

the projection data. Jacobson and Stayman (2008) simultaneously estimated marker positions and their corresponding orientation using 6 DoF for each projection, allowing the marker configuration to adjust for different patients. Marchant et al (2011) tracked the 3D locations of fiducial markers placed on a patient and warped the 2D projection images to match the 2D locations of their forward-projected 3D locations. Choi et al (2013) extended this idea by comparing simple projection shifting with projection warping using methods that prevent unrealistic warping due to noise in the marker locations. Choi et al (2013) also studied a 3D rigid body warping method and found it to outperform both 2D methods. Overall, such *image* fiducial methods (including fiducials placed internal to the patient) appear advantageous to externally tracked fiducials, but they still require placement of fiducials that can interrupt clinical workflow and may not accurately represent the internal motion of the patient — i.e., the fiducials give a fairly sparse representation of motion and convey only the motion of structures to which the fiducials are attached.

Other work seeks to correct patient motion by maximizing (or minimizing) various characteristics of the resulting 3D image reconstruction (e.g., image sharpness). Yu and Wang (2007) estimated patient motion by minimizing an objective function based on data redundancy in the sinogram. Similarly, Wicklein et al (2013) minimized an entropy criterion to optimize the underlying geometric parameters of the imaging system, thereby adjusting for system misalignments as well as patient motion. Sisniega et al (2017) combined a gradient objective and an entropy term with a penalty that encourages smooth motion for high-resolution extremity imaging. Such methods can accommodate complex source–detector trajectories, as they only rely on the reconstructed image and have shown promising results for improving image quality.

Other methods employ a motion-free prior image to correct for motion in a subsequent scan. For example, Berger et al (2016) used 3D–2D registration to estimate the motion of individual bones in the weight-bearing knee, showing that registration based on image similarity (specifically, gradient correlation (GC) and normalized gradient information (NGI)) outperformed motion compensation using fiducial markers. Chen et al (2008) used prior image constrained compressed sensing (PICCS) to reconstruct images from highly undersampled projection data sets, providing a method to reconstruct dynamic data without motion or undersampling artifacts.

In this chapter we report the development and characterization of a fiducial-free method for motion compensation in interventional CBCT. The focus of clinical application is 3D imaging of the head, as in otolaryngology – head and neck surgery, intracranial neurosurgery, or neuro-IR, where involuntary patient motion can give rise to severe artifacts. The method registers all projection views to a previously acquired, motion-free 3D image, providing the information necessary to reconstruct a motion-compensated image using MBIR. Using this framework, the method aims to correct large-scale or small-scale rigid motion that occurs during a scan and restore image quality to that of the motion-free image.

The similarity objective is based on GO, which is robust against mismatch in image content between the prior 3D image and the current acquisition (demonstrated by De Silva et al 2016). This is an important characteristic when the prior image is acquired at the beginning of the case, and the current image is acquired with a variety of devices and instrumentation in the FOV (e.g., retractors, catheters, stents, coils, clips, staples, and / or implants) that may otherwise confound the registration. A fast scan (5 s, 200° orbit) is

employed for the prior image, providing a 3D CBCT image that is less susceptible to motion (assumed nominally motion-free). The fast, low-dose scan exhibits lower image quality (higher quantum noise and view sampling effects) compared to a longer, higher-dose scan and requires a registration method that is robust against such image quality degradation.

Finally, the applicability of the algorithm is demonstrated in patient data exhibiting strong, realistic motion in which factors such as complexity of the motion pattern and mismatch between a prior image and the projection data present a challenge to the registration. By treating the motion of the C-arm gantry and the motion of the patient simultaneously in 3D–2D registration, the method corrects for both the motion of the patient and potential errors in the system geometric calibration.

The work appearing in this chapter was reported in the following conference proceeding and journal paper: (S. Ouadah et al, *Med. Phys.* 46(38), 2016) and (S. Ouadah et al, *Phys. Med. Biol.* 62(23), 2017).

2.2. Motion Compensation Framework

2.2.1. Overview

The motion compensation method is illustrated in Figure 2.1 (with associated parameters summarized in Table 2.1) assuming a previously acquired, motion-free 3D image denoted $\boldsymbol{\mu}_{\mathbf{prior}}$ and a current CBCT scan that contains patient motion with projection data denoted $\boldsymbol{y}$. The algorithm performs a 3D–2D image registration for each projection in the current scan (alternatively, a subset of projections could be used — subject to smoothing or regularization — to reduce computational burden and improve runtime).

Each 2D projection is registered to a forward-projection of the previously acquired image (the DRR, denoted $\boldsymbol{y}_{\mathbf{prior}}$). The nominal PM for system geometric calibration (Navab et al 1998, Cho et al 2005, Ouadah et al 2016) is used to initialize the first registration and the result of previous registrations is used to initialize subsequent registrations. The PM used to initialize each registration is denoted $\mathbf{PM}_{\mathbf{init}}^{\boldsymbol{k}}$**.** The 6 or 9 DoF transformation that optimizes each registration yields a new PM (denoted $\mathbf{PM}_{\mathbf{MC}}^{\boldsymbol{k}}$) that encodes the motion of the object at the k^{th} projection view ($k = 1, \ldots, N_{\text{proj}}$). This process is performed for each projection in the uncompensated CBCT acquisition (typically N_{proj} ~ 200–500 projections), and a motion-compensated 3D image is reconstructed according to the system geometry defined by $\mathbf{PM}_{\mathbf{MC}}$. Using this method, the rigid motion of the object is defined within $\mathbf{PM}_{\mathbf{MC}}$, which combines both the source and detector motion with that of the object (patient). For cases in which the patient motion is small (or more specifically, in which $\mathbf{PM}_{\mathbf{MC}}$ describes an approximately circular system geometry), conventional 3D FBP using the FDK algorithm (Feldkamp et al 1984) is applicable as a reasonable approximation. However, stronger motion amplitude, as investigated below, results in an effective system geometry that is markedly non-circular and violates basic assumptions in conventional FDK. This invites the application of more general MBIR methods that are free from strong assumptions on system geometry. In the work reported below, we use PL estimation to reconstruct the motion-compensated CBCT image.

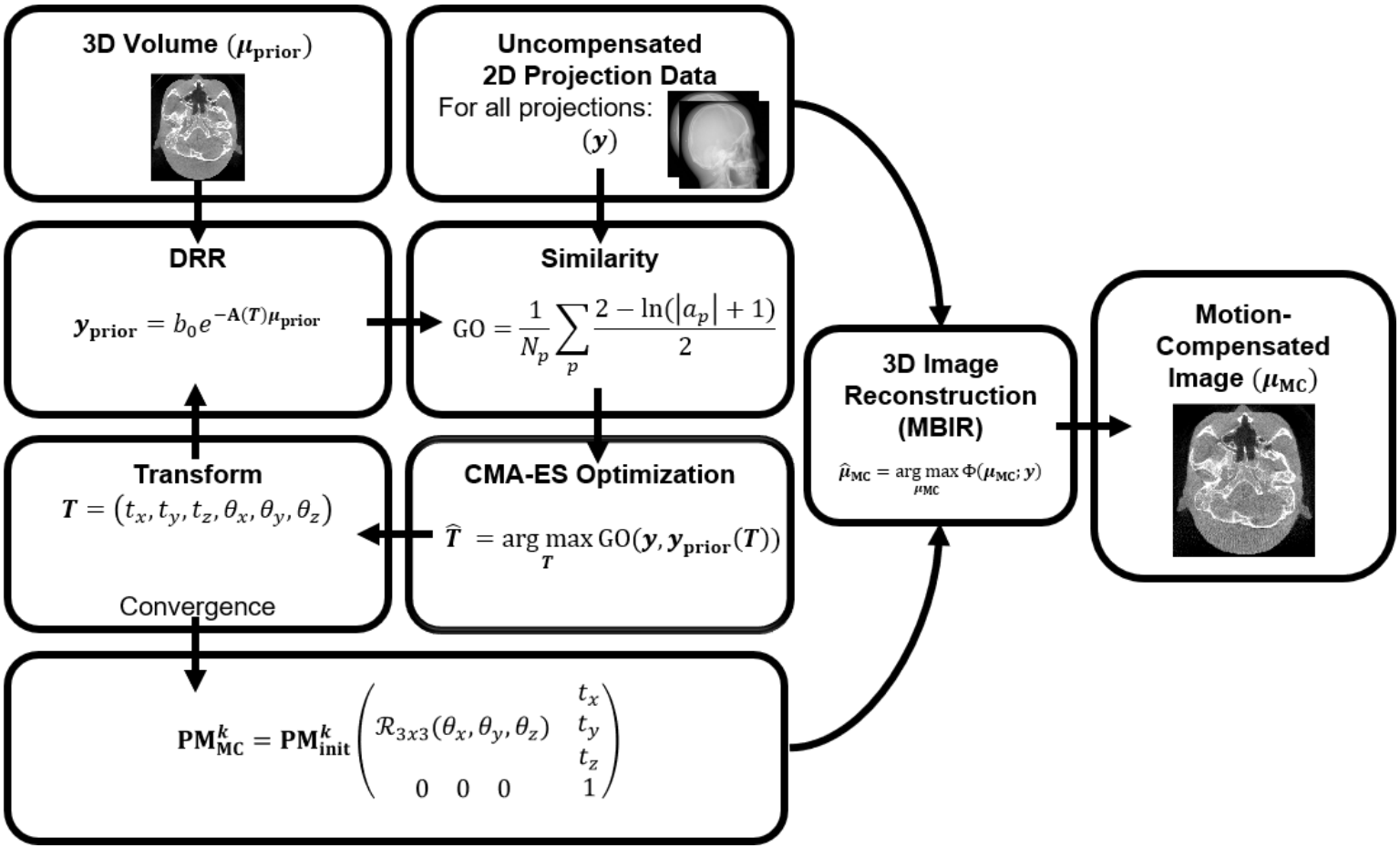

Figure 2.1. Overview of the motion compensation method. Each 2D projection ($\boldsymbol{y}$) in the CBCT scan is registered to a DRR ($\boldsymbol{y}_{\mathbf{prior}}$) of a previously acquired 3D volume ($\boldsymbol{\mu}_{\mathbf{prior}}$) to determine a rigid transformation ($\boldsymbol{T}$). The transform is encoded in $\mathbf{PM}_{\mathbf{MC}}$ (6 DoF transform shown), combining the motion of the source, detector, and object (patient) within the description of system geometry for reconstruction of the motion-compensated image ($\boldsymbol{\mu}_{\mathbf{MC}}$).

Table 2.1. Notation for the rigid motion compensation method.

Property	Symbol
3D–2D registration	
2D projections	$\boldsymbol{y}$
Projection view	$k = 1, \ldots, N_{\text{proj}}$
Prior 3D volume	$\boldsymbol{\mu}_{\mathbf{prior}}$
Digitally reconstructed radiograph (DRR)	$\boldsymbol{y}_{\mathbf{prior}}$
Forward-projection operator	$\mathbf{A}$
Bare-beam x-ray fluence	b_0
Estimated 6 or 9 DoF motion	$\boldsymbol{T}$
Source translation	$\boldsymbol{s}$
Object (patient) translation	$\boldsymbol{t}$
Object (patient) rotation	$\boldsymbol{\theta}$
3D rotation matrix	$\mathcal{R}_{3x3}$
Initial projection matrix (PM)	$\mathbf{PM}_{\mathbf{init}}$
Motion-compensated PMs	$\mathbf{PM}_{\mathbf{MC}}$
Similarity objective	
Gradient orientation	$\text{GO}(\boldsymbol{y}, \boldsymbol{y}_{\mathbf{prior}})$
Gradient information	$\text{GI}(\boldsymbol{y}, \boldsymbol{y}_{\mathbf{prior}})$
Gradient correlation	$\text{GC}(\boldsymbol{y}, \boldsymbol{y}_{\mathbf{prior}})$
Pixels in projection data	$p = 1, \ldots, N_p$
Gradient operator	∇
Gradient magnitude thresholds	t_1, t_2
Angle between gradient vectors	θ_p
Penalized-likelihood reconstruction	
Motion-compensated volume	$\boldsymbol{\mu}_{\mathbf{MC}}$
Log-likelihood	$L(\boldsymbol{\mu}_{\mathbf{MC}}; \boldsymbol{y})$
Regularization strength	β
Roughness penalty	$R(\boldsymbol{\mu}_{\mathbf{MC}})$
Voxels in volume reconstruction	$v = 1, \ldots, N_v$
Experimental variables	
Rotation amplitude	A_ϕ
Rotation period	P_ϕ
Translation amplitude	A_z
Rotation phase	φ_ϕ
Scan time	T_{scan}
Performance evaluation	
Motion-free reference image	$\boldsymbol{\mu}_{\mathbf{ref}}$
Structural similarity	$\text{SSIM}(\boldsymbol{\mu}_{\mathbf{MC}}, \boldsymbol{\mu}_{\mathbf{ref}})$
Average attenuation	$\bar{\mu}$
Image variance	σ^2

2.2.2. Initialization

Registration of the first projection image is initialized with a PM taken from the system geometric calibration. The second projection is initialized with the PM resulting from the first registration ($\mathbf{PM}^{\mathbf{2}}_{\mathbf{init}} \leftarrow \mathbf{PM}^{\mathbf{1}}_{\mathbf{MC}}$). For the third and subsequent projections (through the $N_{\mathrm{proj}}{}^{\mathrm{th}}$ projection), $\mathbf{PM}^{\boldsymbol{k}}_{\mathbf{init}}$ is generated by bilinear extrapolation of the extrinsic parameters of the previous two projection matrices to predict the pose of the current projection. Alternative constraints on realistic motion of the C-arm could be implemented, including those that do not depend on sequential registration of projections to better parallelize the 3D–2D registration process described below.

2.2.3. 3D–2D Registration

The motion compensation method has at its "inner loop" a 3D–2D registration method based on work by Penney et al (1998) and Pluim et al (2000), and later expanded to include alternative similarity objectives and optimizers as in Otake et al (2013), Uneri et al (2013), and De Silva et al (2016). The method involves a moving 3D volume ($\boldsymbol{\mu}_{\mathbf{prior}}$) registered to a fixed 2D projection ($\boldsymbol{y}$) by means of its DRR (denoted $\boldsymbol{y}_{\mathbf{prior}}$). For this work we used the gradient orientation (GO) similarity objective as in De Silva et al (2016), defined as:

$$\mathrm{GO} = \frac{1}{N_{\mathrm{p}}} \sum_{p} \frac{2 - \ln\left(\left|a_p\right| + 1\right)}{2} \tag{2.1}$$

where $a_p = \cos^{-1}(\cos\theta_p)$ and $p \in \{|\nabla \mathbf{y}(p)| > t_1 \cap \left|\nabla \boldsymbol{y}_{\mathbf{prior}}(p)\right| > t_2\}$. The GO similarity objective describes how well image gradient vectors align, with θ_p indicating the angle between gradient vectors. To exclude small gradients associated with image noise,

the summation in Equation (2.1) includes only gradient magnitude values exceeding thresholds t_1 and t_2, defined as the median gradient magnitude in $\boldsymbol{y}$ and $\boldsymbol{y}_{\mathbf{prior}}$, respectively, and is normalized by the number of overlapping pixels, N_{p}. As shown by De Silva et al (2016), GO is robust against mismatch in image content (e.g., soft-tissue deformation and / or instrumentation present in $\boldsymbol{y}$ but not $\boldsymbol{y}_{\mathbf{prior}}$), since it relies on the orientation of gradients, rather than their magnitude.

The similarity objective was iteratively optimized using the covariance matrix adaptation-evolution strategy (CMA-ES, Hansen 2006) to solve for the 6 or 9 DoF transform:

$$\widehat{\boldsymbol{T}} = \arg\max_{\boldsymbol{T}} \mathrm{GO}\left(\boldsymbol{y}, \boldsymbol{y}_{\mathbf{prior}}(\boldsymbol{T})\right) \tag{2.2}$$

where $\boldsymbol{T} = (\boldsymbol{t}, \boldsymbol{\theta})$ for 6 DoF and $\boldsymbol{T} = (\boldsymbol{s}, \boldsymbol{t}, \boldsymbol{\theta})$ for 9 DoF. The vector $\boldsymbol{t} = [t_x, t_y, t_z]^T$ represents a 3D translation of the object (patient) with respect to the detector in mm,$\boldsymbol{\theta} = [\theta_x, \theta_y, \theta_z]^T$ represents a 3D rotation of the object (patient) with respect to the detector in degrees, and $\boldsymbol{s} = [s_x, s_y, s_z]^T$ represents a 3D translation of the source with respect to the detector in mm. CMA-ES is a non-linear, non-convex evolutionary optimizer that adjusts the covariance matrix of a population (set to $\lambda_{\mathrm{CMAES}} = 200$, consistent with previous studies (Ouadah et al 2016)) with each iteration. The optimization was taken to be complete (converged) when the change in each parameter in $\boldsymbol{T}$ between iterations was < 0.1 mm or degrees, corresponding to sub-voxel changes in the placement of backprojected rays.

A linear forward-projector (i.e., the adjoint of a standard voxel-driven backprojector) was used to compute $\boldsymbol{y}_{\mathbf{prior}}$, where $\boldsymbol{y}_{\mathbf{prior}} = b_0 e^{-\mathbf{A}(\boldsymbol{T})\boldsymbol{\mu}_{\mathbf{prior}}}$, with matrix $\mathbf{A}$ being a linear projection operator and b_0 indicating the bare-beam image signal. A linear

projector was chosen for speed, although other forms are available, such as Siddon's method (Siddon 1985, as used in Otake et al 2013) or a simplified separable footprints projector as shown in Wang et al (2014). The final PM for the motion-compensated geometry was computed as:

$$\mathbf{PM}_{\mathbf{MC}}^{\boldsymbol{k}} = \mathbf{PM}_{\mathbf{init}}^{\boldsymbol{k}} \begin{pmatrix} \mathcal{R}_{3x3}(\theta_x, \theta_y, \theta_z) & \begin{matrix} t_x \\ t_y \\ t_z \end{matrix} \\ \begin{matrix} 0 & 0 & 0 \end{matrix} & 1 \end{pmatrix} \tag{2.3}$$

for 6 DoF and

$$\mathbf{PM}_{\mathbf{MC}}^{\boldsymbol{k}} = \begin{pmatrix} s_z & 0 & s_{,x} & 0 \\ 0 & s_z & s_y & 0 \\ 0 & 0 & 1 & 0 \end{pmatrix} \begin{pmatrix} \mathcal{R}_{3x3}(\theta_x, \theta_y, \theta_z) & \begin{matrix} t_x - s_x \\ t_y - s_y \\ t_z - s_z \end{matrix} \\ \begin{matrix} 0 & 0 & 0 \end{matrix} & 1 \end{pmatrix} \tag{2.4}$$

for 9 DoF. The formulation of the final PM for 9 DoF does not rely on $\mathbf{PM}_{\mathbf{init}}^{\boldsymbol{k}}$ as in the 6 DoF case; rather, it is constructed using intrinsic and extrinsic parameters de novo for each projection.

2.3. Experimental Methods

2.3.1. Imaging Systems

Phantom experiments (described in Section 2.3.2) used a robotic C-arm (Artis Zeego, Siemens Healthineers, Forchheim Germany), shown in Figure 2.2a. Three scan protocols were used, each based on standard head scan protocols available on the system (all 102 kV with a 200° circular orbit): (Scan Protocol A) N_{proj} = 496 projections acquired in 20 s (with reference point air kerma 37 mGy as reported by the system); (Scan Protocol B) N_{proj} = 248 projections acquired in 10 s (19 mGy); and (Scan Protocol C) N_{proj} = 133 projections acquired in 5 s (10 mGy).

The motion compensation method was applied in clinical studies (described in Section 2.3.5) using a prototype CBCT head scanner (Xu et al 2016) to image patients with suspected intracranial hemorrhage (ICH). The fairly long (30 s) scan time combined with the sometimes unstable condition of critically ill patients (prone to involuntary movement) made the system susceptible to patient motion. Scan protocols involved N_{proj} = 450 projections acquired in a 360° rotation at 100 kV, 216 mAs (23 mGy). Each patient received an MDCT scan prior to the CBCT scan using a standard, non-contrast-enhanced head scan protocol (120 kV, 274 mAs, 44.4 mGy) and reconstructed with 0.44 × 0.44 × 0.5 mm^3 voxels and a H20s soft-tissue kernel (Somatom Definition AS, Siemens Healthineers, Forchheim Germany). The MDCT scan was taken as the 3D prior image for 3D–2D registration with the CBCT projection data.

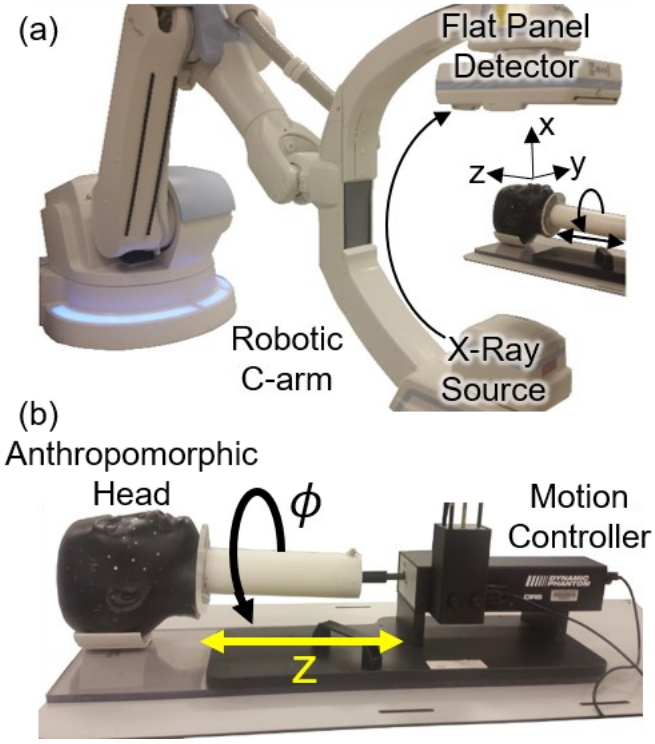

Figure 2.2. Experimental setup. (a) Robotic C-arm system. (b) Custom motion phantom consisting of an anthropomorphic head attached to a motion controller showing direction of motion in ϕ and z.

2.3.2. Phantom Experiments

A custom motion phantom was built by attaching an anthropomorphic head phantom to a motion controller (Figure 2.2b). The head phantom consisted of a human skull encased in tissue-equivalent plastic (RANDO, The Phantom Laboratory, Greenwich NY) with a 0.13 mm diameter tungsten wire placed in the trachea for spatial resolution assessment. The CIRS Dynamic Thorax Phantom (Model 008A) and software (CIRS, Norfolk VA) were used for computer-controlled motion of the head phantom during the scan.

The motion phantom provided 2 DoF under computer control: longitudinal rotation in the ϕ direction (approximately about the z axis of the object and opposite to the C-arm gantry rotation) following a sigmoidal profile; and periodic SI translation along the z axis following a sinusoidal profile that persisted for the duration of the scan. The amplitude (A_ϕ, units of degrees) and duration (P_ϕ, units of seconds) of rotational motion and the amplitude (A_z, units of mm) of translational motion were variable. For experiments containing periodic translational motion, the period was held constant at 4 s, comparable to the respiratory cycle. The phase of rotational motion during the scan (φ_ϕ, units of degrees) was adjusted so that the midpoint of the motion profile occurred near the beginning (50°), middle (100°), or end (150°) of the 200° scan. The motion profiles transferred to the anthropomorphic head were not precisely reproducible, owing to friction between the phantom and its support base and instability or backlash in the attachment piece, so the requested motion profiles were not taken as "truth." However, this was not a factor in experiments described below since the performance of the motion compensation

method was assessed with respect to the quality of the resulting 3D image reconstruction and not in comparison to the motion profiles.

The performance of the 6 DoF motion compensation method was tested for motion profiles defined by the amplitude of longitudinal rotation (A_ϕ), the duration of longitudinal rotation (P_ϕ), the angular phase of the motion relative to the scan (φ_ϕ), the amplitude of SI translation (A_z), and the scan time (T_{scan}), as defined by protocols A, B, and C described in Section 2.3.1. For each experiment, the values of each variable are shown in Table 2.1, and the corresponding motion profiles are shown in Figure 2.3.

Table 2.2. Experimental variables. Corresponding motion profiles are shown in Figure 2.3.

Exp	A_ϕ (°)	P_ϕ (s)	φ_ϕ (°)	A_z (mm)	T_{scan} (s)
1	{5, 10, 15}	6	100	0	20
2	10	{2, 6, 10}	100	0	20
3	10	2	{50, 100, 150}	0	20
4	5	6	100	{2.5, 5, 7.5}	20
5	5	2	100	5	{20, 10, 5}

One motion-free scan was acquired for each of the three scanning protocols as a basis of comparison and taken as the "true" reference image without motion artifact. The motion-free image from Protocol C was used as the 3D volume input ($\boldsymbol{\mu}_{\text{prior}}$) to the motion compensation algorithm for all experiments. Using the fast scan image from Protocol C as the motion-free prior corresponds to a clinical scenario in which a fast (T_{scan} = 5 s) CBCT is acquired at the beginning of a case and is subsequently used as the 3D input for slower scans (higher quality, but susceptible to motion) taken later in the procedure. This also stresses the algorithm in that the 3D input image from Protocol C is of fairly low quality, containing a high degree of noise due to low dose and angular sampling artifacts due to the low angular sampling of N_{proj} = 133 projections over 200°.

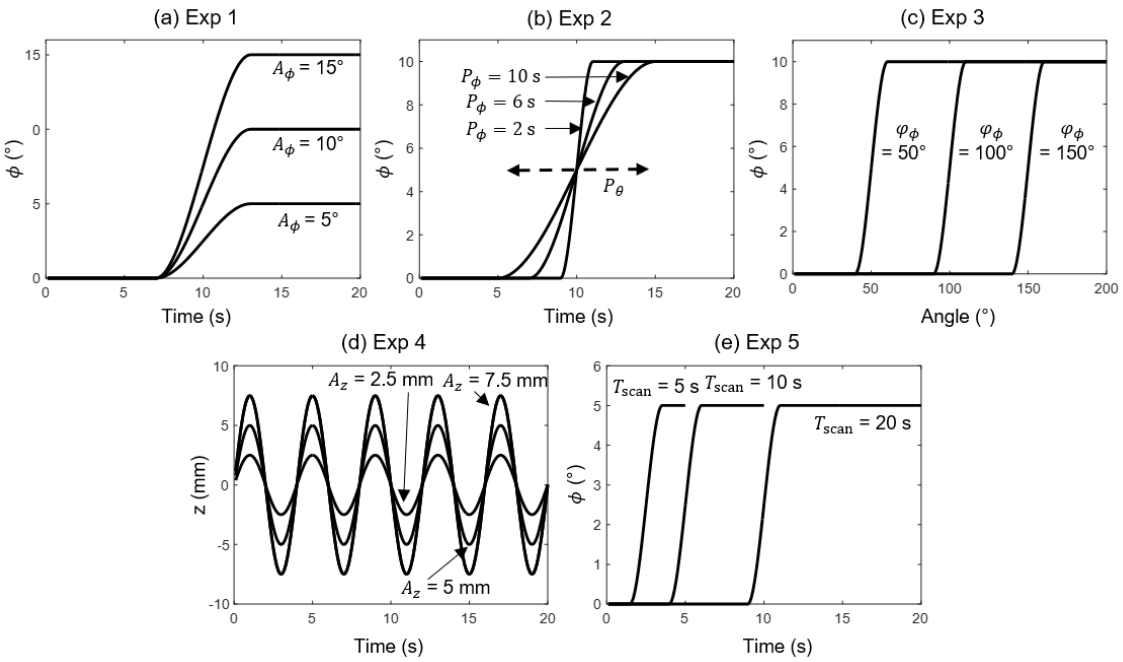

Figure 2.3. Motion profiles for each experiment. (a) Experiment 1 involved three amplitudes of rotational motion. (b) Experiment 2 involved three durations of rotational motion. (c) Experiment 3 involved three phases (relative to the scan orbit) at which motion occurred. (d) Experiment 4 involved three amplitudes of periodic longitudinal translation. (e) Experiment 5 involved three scan durations according to the three scan protocols.

2.3.3. Image Reconstruction

Projection data were read from the robotic C-arm system in Digital Imaging and Communications in Medicine (DICOM) format at isotropic pixel size of 0.308 mm. Since automatic exposure control (AEC, in which the mAs varies from view to view according to the minimum detected signal in the previous view) was implemented on this system, a frame-to-frame intensity correction was performed by dividing each frame by the mAs for each projection as recorded in the DICOM header. A simple scatter correction was performed by subtracting a fraction of the minimum pixel value for each frame. A fraction equal to 0.97 was found to minimize cupping artifact and was used throughout phantom experiments shown below.

The FDK algorithm was used to reconstruct uncompensated images to illustrate the magnitude of motion artifacts without compensation. A 512 × 512 × 512 voxel grid size was used with 0.75 mm isotropic voxel size, apodization filter cutoff at 50% of the Nyquist frequency, and 200 mm lateral extrapolation to reduce truncation effects. An MBIR method based on PL estimation was used to reconstruct images using $\mathbf{PM_{MC}}$. The method is irrespective of the non-circular geometry implicit in $\mathbf{PM_{MC}}$ and formulates the reconstructed image ($\boldsymbol{\mu}_{\mathbf{MC}}$) by maximizing an objective function comprising the log-likelihood of the projection data $L(\boldsymbol{\mu}_{\mathbf{MC}}; \boldsymbol{y})$ and a regularization term with roughness penalty $R(\boldsymbol{\mu}_{\mathbf{MC}})$ and penalty strength β:

$$\widehat{\boldsymbol{\mu}}_{\mathbf{MC}} = \arg\max_{\boldsymbol{\mu}_{\mathbf{MC}}} L(\boldsymbol{\mu}_{\mathbf{MC}}; \boldsymbol{y}) - \beta R(\boldsymbol{\mu}_{\mathbf{MC}}) \tag{2.5}$$

The log-likelihood is:

$$L(\boldsymbol{\mu}_{\mathbf{MC}}; \boldsymbol{y}) \cong -\sum_i [b_0 \exp(-\mathbf{A}\boldsymbol{\mu}_{\mathbf{MC}})]_i + y_i [\mathbf{A}\boldsymbol{\mu}_{\mathbf{MC}}]_i \tag{2.6}$$

and relates the consistency of $\boldsymbol{\mu}_{\mathbf{MC}}$ with the projection measurements $\boldsymbol{y}$ through the forward-projection operator $\mathbf{A}$. For simplicity, a quadratic penalty was used:

$$R(\boldsymbol{\mu}_{\mathbf{MC}}) = \sum_v \sum_{j \in N_j} \frac{(\mu_v - \mu_j)^2}{2} \tag{2.7}$$

with v indexing all voxels, and j indexing the 6 nearest-neighbor voxels around voxel v in 3D (Wang et al 2014). For phantom experiments, the penalty strength β was set to a low value of 1×10^2 relative to a bare-beam b_0 value of 1×10^5 photons per pixel. The relatively low penalty strength decreased the strength of regularization (smoothing) in the reconstruction, which in turn emphasized high-spatial resolution characteristics of the reconstructed images. The MBIR was initialized using an FDK image reconstructed using

the motion-compensated projection matrices. A 512 × 512 × 512 voxel grid was used with 0.75 mm isotropic voxel size, and the optimization used 50 iterations with 10 subsets each. Linear forward-projectors and backprojectors implemented on a graphics processing unit (GPU) were used for both FDK and PL reconstructions.

2.3.4. Figures of Merit

Image reconstructions were qualitatively and quantitatively assessed to evaluate performance of the motion compensation method. Qualitative assessment of motion artifacts included visualization of high-contrast bone details in regions of the temporal bone and sinuses. Quantitative assessment involved analysis of structural similarity (SSIM) measured between the motion-compensated images ($\boldsymbol{\mu}_{\mathbf{MC}}$) and the corresponding motion-free reference images ($\boldsymbol{\mu}_{\mathbf{ref}}$) as in Wang et al (2004):

$$\mathrm{SSIM}(\boldsymbol{\mu}_{\mathbf{MC}}, \boldsymbol{\mu}_{\mathbf{ref}}) = \frac{(2\bar{\mu}_{\mathrm{MC}}\bar{\mu}_{\mathrm{ref}})(2\sigma_{\mathrm{MC-ref}})}{(\bar{\mu}_{\mathrm{MC}}^2 + \bar{\mu}_{\mathrm{ref}}^2)(\sigma_{\mathrm{MC}}^2 + \sigma_{\mathrm{ref}}^2)} \tag{2.8}$$

where $\bar{\mu}_{\mathrm{MC}}$ and $\bar{\mu}_{\mathrm{ref}}$ are the mean value of images $\boldsymbol{\mu}_{\mathbf{MC}}$ and $\boldsymbol{\mu}_{\mathbf{ref}}$, respectively, σ_{MC}^2 and σ_{ref}^2 are the variance of $\boldsymbol{\mu}_{\mathbf{MC}}$ and $\boldsymbol{\mu}_{\mathbf{ref}}$, respectively, and $\sigma_{\mathrm{MC-ref}}$ is the cross-covariance of $\boldsymbol{\mu}_{\mathbf{MC}}$ and $\boldsymbol{\mu}_{\mathbf{ref}}$. The SSIM was measured over 100 corresponding axial slices about the central axial slice. Only voxels falling within the head (i.e., excluding air; voxel value > 0.01 mm^{-1}) were used for calculating SSIM. In addition, the full-width at half-maximum (FWHM) of the point spread function (PSF) formed by the tungsten wire placed in the trachea of the head phantom was measured over 10 axial slices in the motion-compensated images and compared to that of the motion-free reference images (using PL reconstruction). To calculate FWHM, images were reconstructed at finer voxel size ($0.1 \times 0.1 \times 0.5$ mm^3) to oversample the image within limitations of GPU memory. Line

profiles through the center of the wire were sampled radially over 360°. A Gaussian distribution was fit to each line profile, and the FWHM was averaged over all line profiles and slices. The uncompensated images were not suitable to analysis of FWHM, because the wire PSF was too severely degraded by motion artifact.

2.3.5. Clinical Data

The method was further tested in clinical data for patients with known or suspected ICH under an Institutional Review Board (IRB)-approved study. Two cases were selected that exhibited strong patient motion artifacts and presented several challenges beyond the phantom studies. First, of course, was that motion patterns were unknown, uncontrolled, and realistic — with one of the cases exhibiting up to ~50 mm motion (noncompliant or involuntary raising of the head during the CBCT scan). Overall motion of the head, jaw, and neck was complex and non-rigid. The CBCT scan data were also collimated to ~12 cm FOV along the SI axis to limit patient dose, with the reduced FOV presenting an additional challenge to 3D–2D registration. Registration parameters were as described in Section 2.3.1, and pose was estimated using both 6 and 9 DoF motion models for each projection in the CBCT scan. 3D images were reconstructed with and without motion compensation using 250 projections covering a 200^{o} arc (half-scan) centered on the occurrence of motion. The quadratic PL algorithm was used with 200 iterations and 10 subsets to reach convergence ($0.44 \times 0.44 \times 0.44$ mm^3 voxels).

To further evaluate the performance of the GO objective under such challenging conditions, the motion compensation algorithm was repeated for Patient #2 (who demonstrated large motion with limited FOV and, therefore, a more difficult registration) using GC and GI as a similarity objective, leaving other parameters unchanged. Images

were reconstructed with the resulting $\mathbf{PM_{MC}}$ using the PL algorithm and compared with the motion-compensated image obtained using the GO similarity objective.

2.4. Results

2.4.1. Phantom Images

Images of the anthropomorphic head phantom with and without motion compensation are shown in Figure 2.4. All motion profiles described in Section 2.3.2 resulted in strong motion artifacts, and none of the uncompensated images would be clinically acceptable. The motion-compensated images are shown in the right column of Figure 2.4 for the most severe motion profile. Motion-compensated images for less severe motion profiles (not shown in Figure 2.4) were qualitatively indistinguishable from the worst case (right column) and are quantified below. The motion-compensated images appear to be free from motion artifact and are qualitatively indistinguishable from the motion-free image for even the most extreme cases (A_ϕ = 15°, P_ϕ = 10 s, φ_ϕ = 150°, A_z = 7.5 mm, and T_{scan} = 5 s).

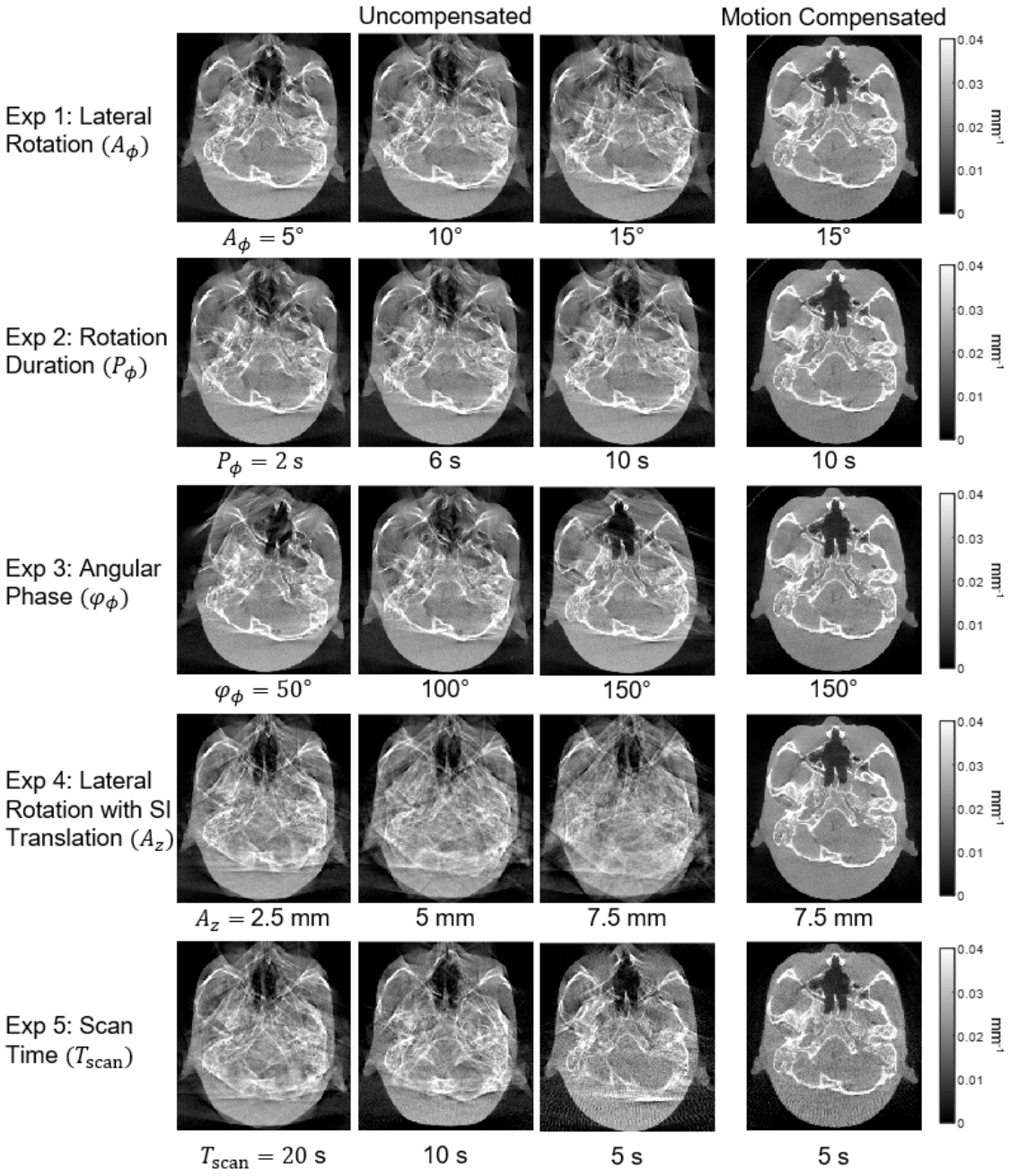

Figure 2.4. Axial slices from the uncompensated reconstructions (left three columns) for five experiments exhibiting various motion profiles in A_ϕ, P_ϕ, φ_ϕ, A_z, and T_{scan}. The right column shows the same axial slice reconstructed using the motion compensation method for the worst-case motion pattern (corresponding to the 3rd column from the left).

Considering the results in Figure 2.4 more closely, it can be noted that different types of motion artifacts resulted from the various motion profiles imparted in the five experiments. In Experiment 1, the severity of motion artifact increases with the magnitude of A_ϕ as expected. As evident in Experiment 2, P_ϕ has a less obvious effect, but it appears that a shorter rotation period (i.e., faster speed of rotation, as in a sudden twitch of the head) results in more severe artifact than a slower rotation (as in a slow drift of head angulation). The effect of $\varphi_\phi$with respect to the scan orbit is shown in Experiment 3 to affect the appearance of motion artifact, and one may distinguish to some extent the pose of the source and detector during object motion based on the directionality of the motion artifacts. Moreover, motion at the midpoint of the scan results in the strongest artifacts, associated with sampling over a short scan (i.e., there is less data redundancy at the mid-point of a short scan to lessen the conspicuity of the motion artifact). In Experiment 4 in-plane features become nearly indistinguishable due to out-of-plane motion contamination that worsens with increasing A_z, as expected. The severity of motion artifact in Experiment 5 appears to be greatest for the longest scan time, which corresponds to the scan with the highest frequency of projection sampling during the period of motion.

2.4.2. Structural Similarity

Measurements of SSIM for uncompensated and motion-compensated images are shown in Figure 2.5. In each case, SSIM was restored to > 0.995 following motion compensation, a statistically significant difference (increase) compared to the uncorrected image ($p < 0.001$) in each case. For the uncompensated images, many of the trends in SSIM match the qualitative observations of artifact magnitude discussed in Section 2.4.1. For

example, SSIM decreases with increasing A_ϕ, decreases with increasing A_z, and increases with P_ϕ. For Experiment 4, SSIM for the uncompensated images appears better (perhaps surprisingly, given the strong artifacts exhibited in Figure 2.4) than in other experiments, indicating that SSIM as a figure of merit is more sensitive to strong gradients about high-contrast bones and the skin line than it is to an overall loss of resolution. The SSIM measured for Experiment 3 shows a somewhat unexpected trend increasing with φ_ϕ, compared to visual impression of images in Figure 2.4 suggesting worst performance for motion centered about φ_ϕ = 100°. The SSIM measurements for Experiment 5 also show a somewhat unexpected trend in that the 20 s scan time might be expected to exhibit the worst SSIM, rather than the 5 s scan. However, these trends have more to do with limitations in SSIM as a metric of visual image quality than the performance of the motion compensation method. In each case, the compensation method restored SSIM to a level that was equivalent to (or at least statistically indistinguishable from) the motion-free case.

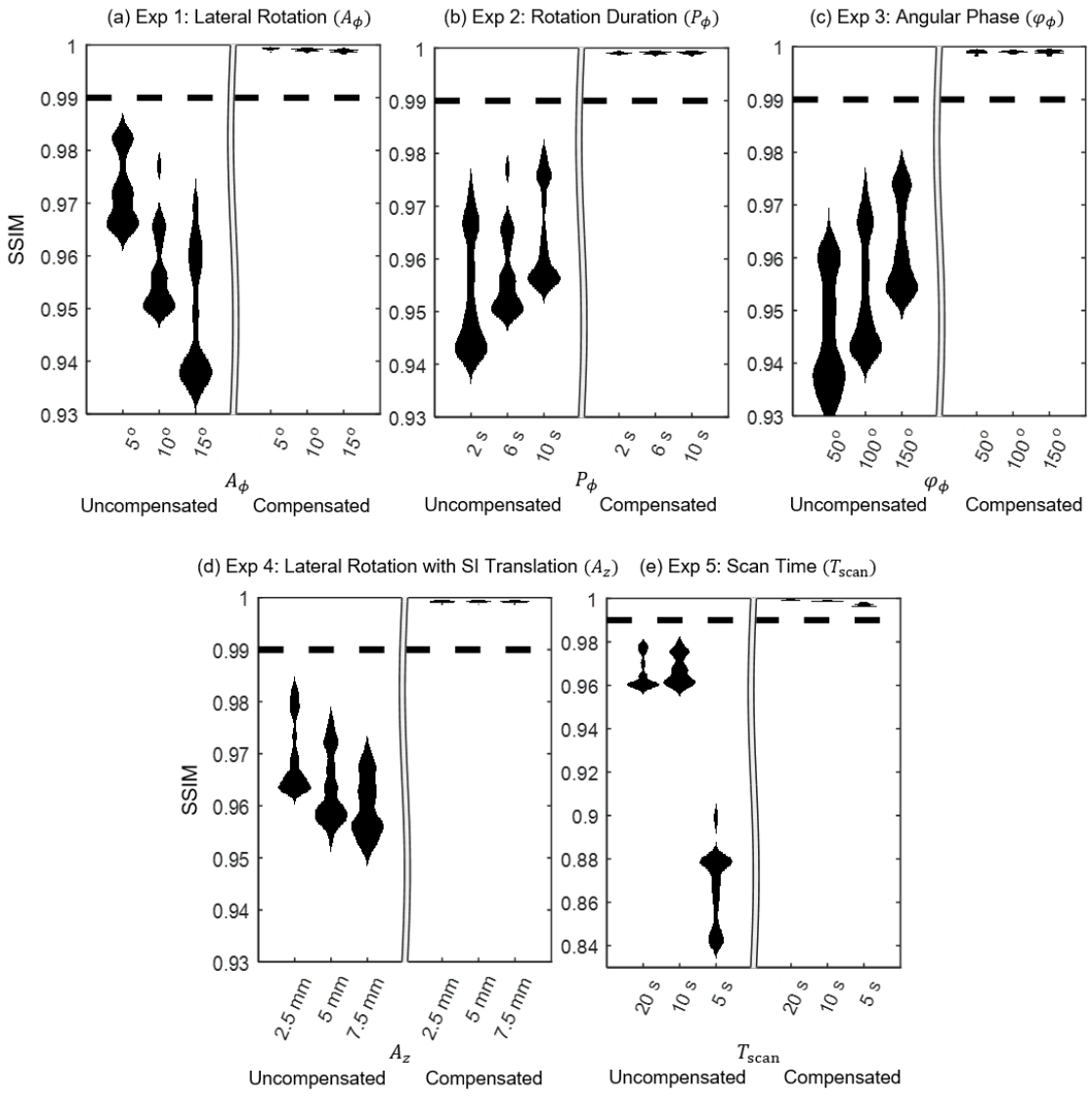

Figure 2.5. SSIM (measured across 100 axial slices) for each of the five motion experiments. The SSIM for the uncompensated images is shown on the left of each plot, and the SSIM for the motion-compensated images is shown on right (> 0.995 for all cases).

2.4.3. FWHM of the PSF

Figure 2.6 shows the FWHM of the wire PSF following motion compensation. The mean FWHM measured for the motion-free reference image was (0.94 ± 0.01 mm). By comparison, the FWHM for the various cases of object motion was ~0.94 mm, indicating that the motion compensation algorithm was able to recover spatial resolution to

approximately the same level as the motion-free case. Without motion compensation, the PSF images (not shown) were entirely confounded by artifact and did not permit FWHM analysis.

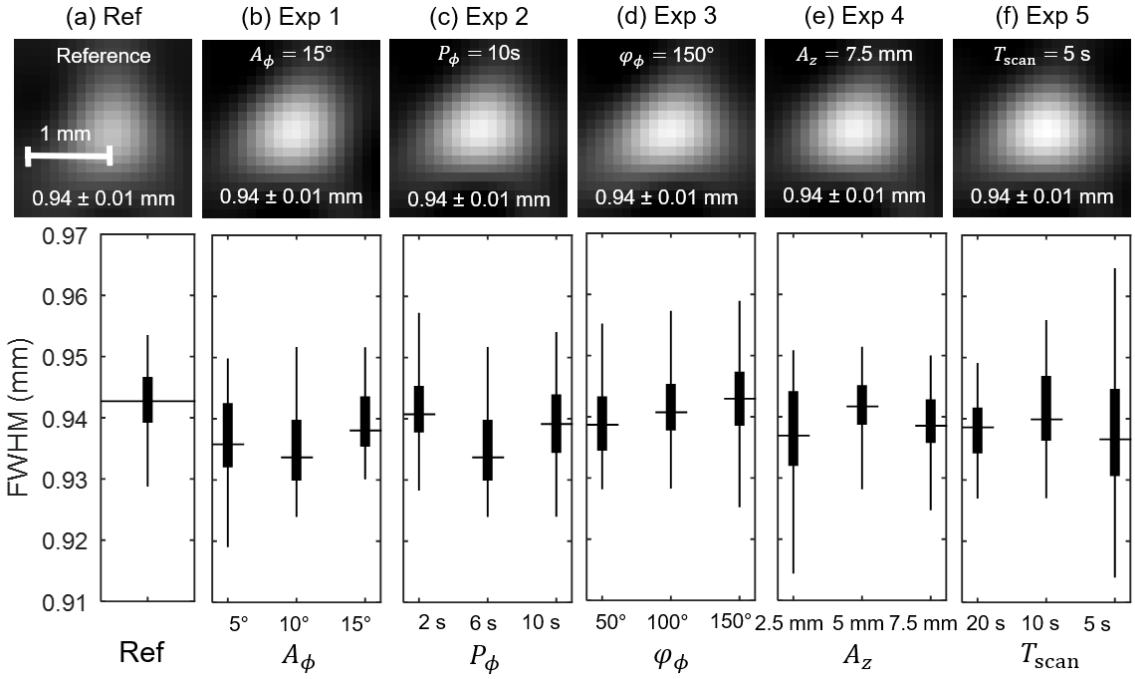

Figure 2.6. FWHM of the PSF of a thin (0.13 mm) tungsten wire placed in the head phantom. The FWHM for the motion-compensated images is shown for each of the five motion studies, compared to the motion-free (reference) image. Each plot indicates the full range (whiskers), interquartile range (box), and median (horizontal line) FWHM analyzed in 10 axial slices.

2.4.4. Application to Clinical Data

Application of the motion compensation algorithm to clinical data is illustrated in Figures 2.7 and 2.8. Patient motion artifacts are evident in the uncompensated images as distortion (streaks, blur, and doubling), particularly in relation to high-contrast structures. The motion compensation method is seen to significantly improve image quality for both cases. For such complex motion, the 9 DoF model outperformed the 6 DoF (not shown for brevity) due to the ability to solve for both the source and object positions simultaneously,

resulting in greater accuracy in translation and rotation parameters. This is similar to results found in previous studies comparing 3D–2D registration using 6 DoF with 9 DoF (e.g., Otake *et* al 2015). For Patient #1, the motion profile resulting from the registration suggested ~10 mm motion at approximately the midpoint of the scan due to involuntary tremor. The most noticeable improvement is increased delineation of the anterior skull base (Figure 2.7e) and hard palate (Figure 2.7f). Patient #2 exhibited even stronger motion artifacts (Figure 2.8a) that render the uncorrected image largely unusable. In this case, the registration suggested ~50 mm motion during the latter half of the scan, during which the patient lifted his / her head from the support. The motion compensation algorithm resolved most of the motion artifacts from the image (Figure 2.8d) with strongly improved visualization of a metal mesh placed within a craniotomy (Figure 2.8e) and an intraventricular shunt within the cranium (Figure 2.8f). Residual artifacts (e.g., at the posterior skin line) may be due to motion / truncation at the edge of the FOV and possibly to non-rigidity of superficial soft tissues and / or patient support.

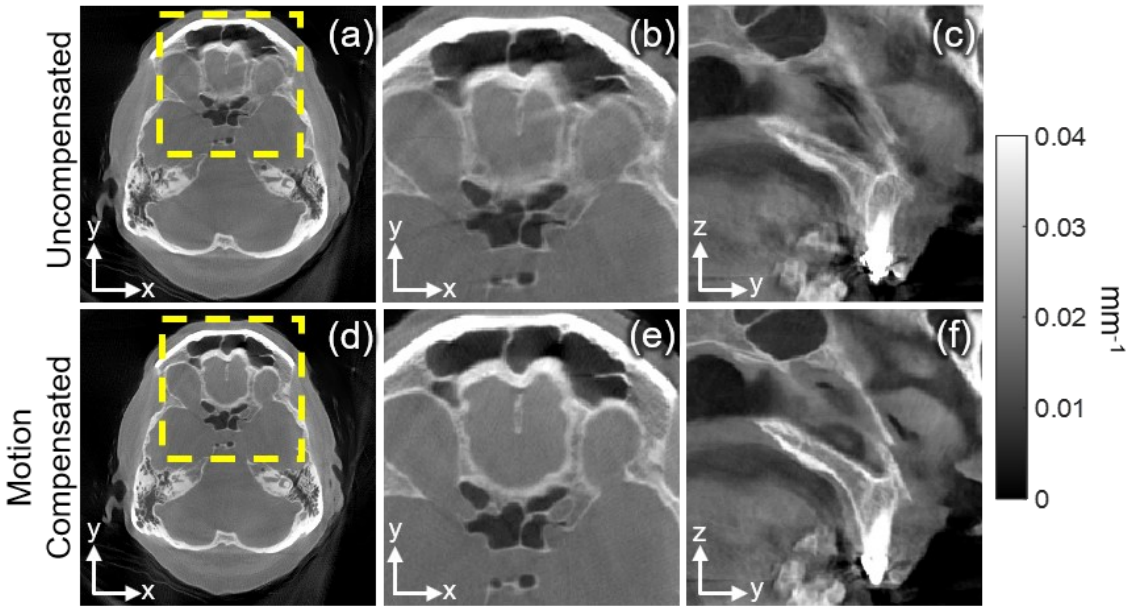

Figure 2.7. Motion compensation applied to clinical data exhibiting moderate motion artifacts (Patient #1). (a–c) Uncompensated and (d–f) compensated CBCT images. Images in (b) and (e) show a magnified axial view of the anterior skull base marked by the dashed box in (a) and (d). Images in (c) and (f) show a magnified sagittal view of the hard palate.

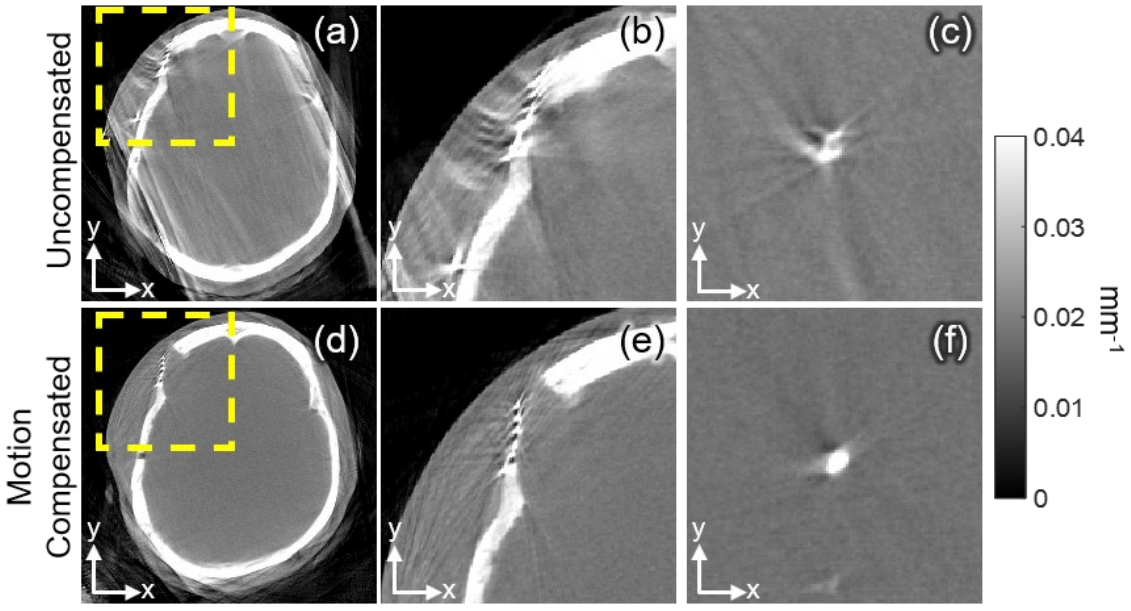

Figure 2.8. Motion compensation applied to clinical data exhibiting severe motion artifacts (Patient #2). (a–c) Uncompensated and (d–f) compensated CBCT images. Images in (b) and (e) show a magnified axial view in the region of a craniotomy and implanted mesh marked by the dashed box in (a) and (d). Images in (c) and (f) show a magnified axial view in the region of an intraventricular shunt.

The results of the clinical study demonstrate the robustness of the algorithm under realistic conditions, including challenges of complex motion and mismatch between MDCT and CBCT images. Both cases exhibited a mismatch in FOV between MDCT and CBCT — with CBCT exhibiting less coverage in the SI direction due to patient positioning and / or narrow collimation — such that the shoulders, neck, and jaw (including dental implants) appear in the DRRs but not in the CBCT projections. The additional gradients can confound the registration by driving the solution to false local maxima associated with high contrast features.

Such sensitivity was especially evident for the GI and GC similarity objectives, which rely on gradient magnitude. As shown in Figure 2.9 for Patient #2, the GI objective (Figure 2.9a) failed to give reliable registration for such strong and complex motion. The GC objective (Figure 2.9b) performed better but was subject to spurious registration failure (false maxima) for numerous views, and the resulting reconstructions demonstrated correspondingly severe artifacts. The GO objective (Figure 2.9c), on the other hand, better incorporated the broad distribution of strong and subtle gradients across the image. These results are consistent with previous studies (De Silva et al 2016) in which GO demonstrated superior robustness to image mismatch compared to GI, GC, and other similarity objectives under conditions of challenging registration.

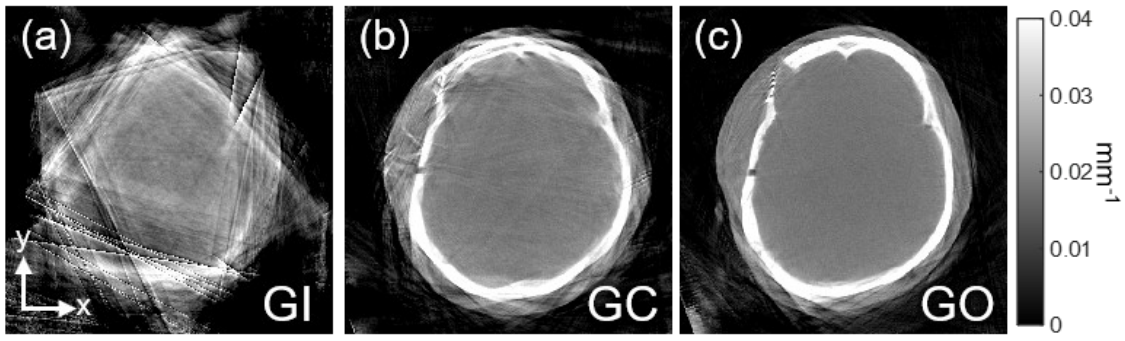

Figure 2.9. Comparison of (a) GI, (b) GC, and (c) GO similarity objectives in motion compensation applied to clinical data exhibiting strong motion (Patient #2). The GI and GC objectives were subject to false local maxima arising from high-contrast features, whereas GO was more robust and better incorporated the full distribution of strong and subtle gradients in the registration process.

2.5. Discussion and Conclusions

The motion compensation method presents a promising framework for the mitigation of large-amplitude motion artifacts in CBCT images acquired during IGI, specifically for non-periodic, involuntary motion (e.g., the head) that can be assumed to be locally rigid and well described by 6 or 9 DoF. The method yields a fiducial-free approach that has been shown to be robust against misregistration in the presence of image mismatch between the prior and current scan (e.g., introduction of surgical instruments, collimation, and / or additional anatomy) by virtue of the GO similarity objective. The resulting transform incorporates the intrinsic and extrinsic parameters of the system geometry with patient motion and can therefore be used in combination with systems that have a non-reproducible orbit and / or vibration in the rotation of the gantry.

The method demonstrated compensation of images with image quality that was quantitatively and qualitatively indistinguishable from the motion-free CBCT image. The registration method underlying the compensation technique is also highly parallelizable in

that multiple projections can be registered simultaneously. The current work initialized each pose with bilinear extrapolation of the two preceding poses, which is not parallelizable but provides a good estimate and fast convergence. Alternatively, one may envision a fully parallelized implementation without such initialization. In such an implementation (depending on the form and search range of the optimizer), the time required for each pose estimate would likely increase due to coarser initialization; however, the total time for registration of all projections would likely decrease and be more compatible with clinical workflow than the current sequential implementation. The method could in principle be run with every scan to remove image artifact stemming from both geometric errors and patient motion; alternatively, the method could run on-demand in cases where motion artifacts appear to confound the imaging task.

The method is well suited to IGI in which a prior 3D image is available (e.g., MDCT acquired for diagnosis and / or planning, or a CBCT scan acquired at the beginning of the case for surgical navigation). Similarly, in IGRT, treatment planning normally involves an MDCT acquired with the patient in the treatment position, and many therapies involve repeat CBCT on successive treatment fractions. In such scenarios, the prior MDCT or CBCT may be suitable as input to the 3D–2D registration underlying the motion compensation method.

Note that the motion-compensated CBCT image is reconstructed in the coordinates of the input 3D image, since the 3D–2D registration algorithm takes the origin of the transformation to be the center of the prior 3D image. This may be beneficial for purposes of image guidance, since the motion compensation yields an image that is automatically registered to the prior 3D image, which is often the pertinent coordinate system for the

surgical navigation system, surgical robot, or linear accelerator. Put another way, the motion compensation method described here can be alternatively viewed as a means of automatically registering a CBCT image to a prior MDCT (or CBCT) via 3D–2D registration.

The phantom study used a fast, low-dose, short scan CBCT as the motion-free prior, and results were unchanged (i.e., not improved) when using a high-quality MDCT as the prior image, indicating the robustness of the registration framework to image quality (quantum noise) in the 3D image. Additionally, the clinical cases demonstrated realistic situations of moderate to severe motion, as well as mismatch between a prior MDCT image and the projection data, indicating the robustness of the registration framework using the GO objective.

The primary objective of this study was to assess the feasibility of motion compensation in conjunction with geometric calibration in cases of strong, involuntary, non-periodic motion, and therefore the run-time of the algorithm was not fully optimized. The framework was implemented in Matlab (The MathWorks, Inc., Natick MA) and the average registration time per projection was 9 s, with total runtime scaling according to the number of projections in the uncompensated dataset. Although the method in its current form registers projections sequentially, a parallel registration scheme (all projections registered simultaneously) could certainly be implemented and decrease total runtime for practical clinical implementation.

One limitation to the motion compensation algorithm is that the accuracy of the registration and subsequent artifact correction is somewhat dependent on the quality of the 3D volume and the 2D images. The method appears to be robust against quantum noise,

evidenced by performance achieved using the lowest-dose CBCT image as the input 3D image for phantom studies. Although the algorithm is robust to many types of artifact present in either of the images (e.g., cone-beam artifacts, scatter, truncation, and / or angular sampling), anatomical gradients must be sufficiently distinct for their orientation to be matched between DRRs and projection views. Another limitation is the assumption of local rigid motion, which may be applicable for the skull, pelvis, and extremities, but limits the algorithm in application to scenarios such as the abdomen and thorax. However, even in cases of non-rigid deformation of soft tissue, the method may still be applicable to local regions of interest (ROIs) where motion can be approximated as rigid.

Overall, the motion compensation method produced CBCT images of the same quality as motion-free images, demonstrating robustness in cases of strong non-periodic motion of the object (patient) using either a low-dose, fast, short-scan prior CBCT image or high quality MDCT.

Chapter 3: Deformable Motion Compensation for Interventional Cone-Beam CT Using Autofocus

3.1. Introduction

In addition to the neurological procedures discussed in the previous chapter, CBCT is increasingly prevalent in minimally invasive IGI in the abdomen as a means of 3D image guidance and quality assurance. Transarterial chemoembolization (TACE) is an established technique that leverages CBCT guidance, treating hepatocellular carcinoma by delivery of chemotherapeutic / embolic agents to the tumor via the hepatic artery (Tacher et al 2015). Identification of the tumor and surrounding vascular structures — small feeder vessels in particular — is crucial to selective embolization that delivers the embolic agent as close as possible to the tumor to concentrate the chemotherapeutic effect while sparing adjacent healthy tissue. Selective embolization, with or without combined injection of cytotoxic drugs, can also be extended to the treatment of benign prostate hyperplasia (McWilliams et al 2014), renal carcinoma (Hall et al 2000), neuroendocrine tumors (Gupta et al 2005), uterine fibroids (Goodwin et al 1997), aneurysms (Brilstra et al 1999), and AVM (Miracle and Mukherji 2009). CBCT guidance offers better identification of small tumors and feeder vessels than conventional 2D fluoroscopic techniques and enables super-selective embolization with substantial benefit to treatment outcomes (Kakeda et al 2007).

However, as discussed in Chapter 2, CBCT for IGI involves moderately long scan time (~5–60 s), making it susceptible to patient motion. For awake interventional procedures such as TACE, patients can have difficulty with breath-hold and remaining still,

and even with ideal compliance, CBCT can be confounded by involuntary organ motion from peristalsis or gas movement in the abdomen. Consequently, motion artifacts evident as streaks, blurring, and loss of soft-tissue edges often diminish CBCT image quality. For example, in CBCT-guided TACE, up to 25% of images demonstrated moderate to severe motion artifacts (Lee et al 2014).

Chapter 2 discussed in detail the current methods for motion compensation in CBCT and showed a method for compensation of rigid-body motion (e.g., the cranium) based on a prior 3D image and 3D–2D image registration. In this chapter, we focus on challenges of deformable motion (as in soft tissues of the abdomen) and develop a compensation method that operates without a prior 3D image and instead enforces image sharpness criteria in the image reconstruction in a manner analogous to "autofocus" (Bueno-Ibarra et al 2005, Kyriakou et al 2008, Kingston et al 2011, Wicklein et al 2012, Sisniega et al 2017, Sisniega et al 2019b). Previously reported autofocus methods for CBCT are promising but are largely constrained to rigid motion applied to the entire CBCT volume. This work, first reported by Sisniega et al (2019a) and Capostagno et al (2020), develops a *deformable* motion compensation method that leverages the autofocus concept to compute a 4D spatiotemporal MVF for soft-tissue CBCT in the abdomen.

As detailed below, MVFs are estimated by interpolating M locally rigid motion trajectories across N temporal nodes and are incorporated in a modified 3D FBP approach. Because the method is entirely image-based, it does not require additional input beyond the raw projection data — for example, the method operates without respiratory or cardiac gating or external monitoring of the patient. The studies reported below describe the development of the method in simulation studies that test the robustness of algorithm

parameters over a wide range of operating conditions and translate the method to cadaver studies involving realistic, complex motion as precursors to translation to the interventional setting.

The work appearing in this chapter was reported in the following conference proceeding: (A. Sisniega et al, *Proc. SPIE Medical Imaging,* 10948, 2019), (S. Capostagno et al, *APS March Meeting*, 64(2), 2019), (S. Capostagno et al, *J. Vasc. Int. Rad.,* 30(3), 2019), and (S. Capostagno et al, *Proc. SPIE Medical Imaging,* 11315, 2020).

3.2. Motion Compensation Framework

3.2.1. Overview

The motion compensation algorithm is built on the premise that a complex deformable motion field can be formed as a composition of locally rigid motion trajectories sparsely sampled across the volumetric FOV. The algorithm is illustrated in Figure 3.1, with parameters summarized in Table 3.1. The process begins by selecting a set of M ROIs throughout the uncompensated volume $\boldsymbol{\mu}$. Each ROI is presumed to undergo locally rigid motion described by 6 DoF (3 translations and 3 rotations) defined relative to the center of each ROI. This is a fair assumption in that the motion is expected to be spatially smooth, making it quasi-rigid for reasonably small ROIs (e.g., ~50 × 50 × 50 mm^3 as described below). The motion trajectory for each ROI ($\boldsymbol{T_m}$), therefore consists of a sequence of 6 DoF transformations — one transformation for each projection view ($k = 1, \dots, N_{\text{proj}}$), with projection views corresponding to scan time ($t \in [0\ T_{\text{scan}}]$). The vector $\boldsymbol{T}$ contains all $\boldsymbol{T_m}$ ($m = 1, \dots, M$) trajectories.

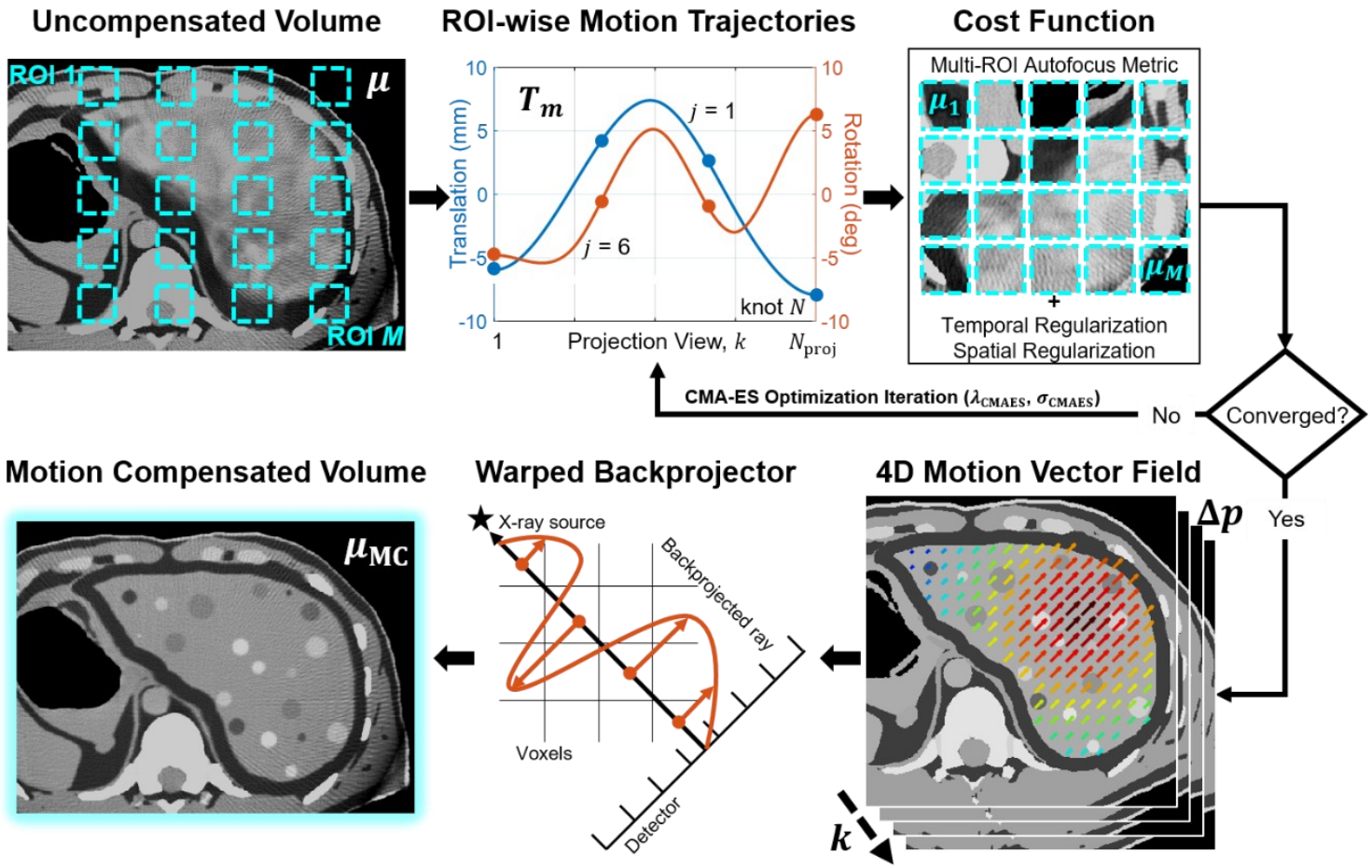

Figure 3.1. Overview of the motion estimation and compensation algorithm. A set of M ROIs is selected in the uncompensated volume $\boldsymbol{\mu}$ to compute a cost function consisting of an autofocus objective and spatiotemporal regularization penalties. Locally rigid motion trajectories $\boldsymbol{T_m}$ are computed using CMA-ES optimization and, once converged, used to interpolate a 4D deformable MVF $\boldsymbol{\Delta p}$. The motion-compensated volume $\boldsymbol{\mu_{\text{MC}}}$ is reconstructed using a variation of the FDK algorithm featuring a warped backprojector.

Table 3.1. Notation for the deformable motion compensation method.

Property	Symbol
Motion estimation	
Uncompensated image	$\boldsymbol{\mu}$
Region of interest (ROI)	$m = 1, \dots, M$
Degree of freedom (DoF)	$j = 1, \dots, 6$
Projection view	$k = 1, \dots, N_{\text{proj}}$
Gantry angle	$\theta \in [0\ \Theta_{\text{scan}}]$
Scan time	$t \in [0\ T_{\text{scan}}]$
Spatial location	$\boldsymbol{x}$
Estimated motion trajectory	$\boldsymbol{T}$
Motion trajectory for ROI *m*	$\boldsymbol{T_m}(k, j)$
Motion vector field	$\Delta\boldsymbol{p}(k, \boldsymbol{x})$
Motion magnitude	$\lvert\Delta\boldsymbol{p}\rvert$
Temporal motion model	
Cubic b-spline kernel	B
B-spline knot	$n = 1, \dots, N$
B-spline kernel coefficient	c_{nj}
Autofocus objective	
Motion-compensated reconstruction for ROI *m*	$\boldsymbol{\mu_m}$
Autofocus objective (see Table 2)	$S(\boldsymbol{\mu_m})$
Voxel in reconstructed image	$v = 1, \dots, N_v$
Directional gradient operator	$\nabla_x, \nabla_y, \nabla_z$
Normalized intensity histogram	h
Histogram bin	$l = 1, \dots, L$
Spatiotemporal regularization	
Temporal regularization parameter	β_t
Spatial regularization parameter	$\beta_{\boldsymbol{x}}$
Temporal regularization penalty	$R_t(\boldsymbol{T_m})$
Spatial regularization penalty	$R_{\boldsymbol{x}}(\boldsymbol{T_m})$
Reference point location	$\boldsymbol{p}$
Reference point	$p = 1, \dots, P$
CMA-ES optimization	
Population size	λ_{CMAES}
Search range	σ_{CMAES}
Performance evaluation	
Motion-free reference image	$\boldsymbol{\mu}_{\mathbf{ref}}$
Motion-compensated image	$\boldsymbol{\mu}_{\mathbf{MC}}$
Structural similarity	$\text{SSIM}(\boldsymbol{\mu}_{\mathbf{ref}}, \boldsymbol{\mu}_{\mathbf{MC}})$
SSIM regularization constant	c_1, c_2
Average attenuation	$\bar{\mu}$
Image variance	σ^2

The algorithm estimates $\widehat{\boldsymbol{T}}$ by minimizing the cost function in Equation (3.1) consisting of: (1) an autofocus objective that is applied to each ROI to provide a measure of image sharpness; (2) a temporal regularization term that encourages smooth motion trajectories in time t, alternatively, projection view k or gantry angle θ; and (3) a spatial regularization term that encourages smooth changes in motion over the spatial extent of the image volume:

$$\widehat{\boldsymbol{T}} = \arg\min_{\boldsymbol{T}} \sum_{m=1}^{M} S(\boldsymbol{\mu_m}) + \beta_t R_t(\boldsymbol{T_m}) + \beta_{\mathbf{x}} R_{\mathbf{x}}(\boldsymbol{T_m}) \tag{3.1}$$

In Equation (3.1), m enumerates the ROIs ($m = 1, \dots, M$), S is the autofocus objective (detailed in Section 3.2.4), $\boldsymbol{T_m}$ is the sequence of 6 DoF local transforms for ROI m (detailed in Section 3.2.2), $\boldsymbol{\mu_m}$ is the motion-compensated reconstruction of ROI m, β_t and $\beta_{\boldsymbol{x}}$ are scalars controlling the strength of temporal and spatial regularization, respectively, and R_t and $R_{\boldsymbol{x}}$ are temporal and spatial regularization penalties, respectively (detailed in Section 3.2.5). The motion-compensated reconstruction for each ROI ($\boldsymbol{\mu_m}$) is obtained using the FDK algorithm (Feldkamp et al 1984) with $\boldsymbol{T_m}$ applied during backprojection by adjusting the position of the reconstructed ROI according to the 6 DoF motion estimate at each projection view k.

Minimization of Equation (3.1) yields a set of transforms $\widehat{\boldsymbol{T}}$ that are spatially interpolated to form a 4D MVF described by displacements $\Delta\boldsymbol{p}$ at each voxel such that motion at the center of each ROI is described by the 6 DoF motion estimate, and motion throughout the local and surrounding regions is estimated by interpolation between each ROI. The interpolated MVF $\Delta\boldsymbol{p}$ is incorporated into the final image reconstruction using a

variation of FDK with a warped backprojector, forming the motion-compensated image $\boldsymbol{\mu}_{\mathbf{MC}}$ (detailed in Section 3.2.6).

3.2.2. B-Spline Representation of 6 DoF Motion

To reduce the dimensionality of motion estimation, each DoF in $\boldsymbol{T}_{\boldsymbol{m}}$ is modeled as a cubic b-spline with N knots that are nominally placed at equally distributed timepoints (i.e., projection view angles) of the scan:

$$\boldsymbol{T}_{\boldsymbol{m}}(k, j) = \sum_{n=0}^{N} c_{nj} B(k - k_n) \tag{3.2}$$

where k represents projection views ($k = 1, \dots, N_{\text{proj}}$), j enumerates the DoF ($j = 1, \dots, 6$), n enumerates the b-spline knots ($n = 0, \dots, N$), c_{nj} are constants estimated using Equation (3.1), and B is a cubic b-spline kernel. The number of estimated motion parameters is thereby reduced from (N_{proj} projections × 6 DoF × M ROIs) with $N_{\text{proj}} \sim 1{\times}10^2$ to (N knots × 6 DoF × M ROIs) with $N \sim 1{\times}10^1$. A b-spline representation assumes a temporally smooth motion trajectory, which is consistent with the use of temporal regularization in the cost function. Additionally, the average transformation across all N_{proj} projections is subtracted from each $\boldsymbol{T}_{\boldsymbol{m}}$ to ensure that the resulting transformations do not significantly displace the reconstructed ROIs from their original position and orientation.

3.2.3. Optimization of Motion Parameters

The non-convex optimization in Equation (3.1) challenges conventional gradient-based methods. The CMA-ES algorithm (Hansen 2006) was shown in previous work to perform well in similar non-convex optimization for 3D–2D image registration (Otake et

al 2012, Ouadah et al 2016), CBCT source–detector orbit optimization (Stayman et al 2019, Capostagno et al 2019), and, of particular interest for this work, autofocus motion compensation in CBCT for estimation of rigid motion trajectories (Sisniega et al 2017). As described in Chapter 2, the CMA-ES algorithm iteratively generates a set of λ_{CMAES} candidate solutions sampled from a normal distribution. Initially, the optimization parameters are taken as independent random variables with zero mean and standard deviation σ_{CMAES}. During CMA-ES iterations, the mean and covariance matrix of the joint probability distribution of the motion parameters evolve to solutions that minimize the cost function. In the experiments outlined below, a convergence criterion was defined such that the estimated parameters changed from iteration to the next by $< 1\times10^{-2}$ mm (translation) and $< 1\times10^{-3}$ degrees (rotation).

3.2.4. Autofocus Objectives for Soft-Tissue CBCT

Sisniega et al (2017) previously evaluated autofocus objectives suitable to rigid motion compensation for high-contrast (bone) imaging. With those findings as a starting point, autofocus objectives suitable for motion estimation in low-contrast (soft-tissue) CBCT were investigated including gradient variance, gradient norm, entropy, and gradient entropy as summarized in Table 3.2.

Table 3.2. Autofocus objectives evaluated for motion compensation in soft-tissue CBCT.

Objective	Formula	Equation	Reference
Gradient Variance	$S(\boldsymbol{\mu_m}) = -\sum_{v=1}^{N_v}\left(\sqrt{\nabla_x(\mu_{mv})^2 + \nabla_y(\mu_{mv})^2 + \nabla_z(\mu_{mv})^2} - \frac{1}{N_v}\sum_{v=1}^{N_v}\left(\sqrt{\nabla_x(\mu_{mv})^2 + \nabla_y(\mu_{mv})^2 + \nabla_z(\mu_{mv})^2}\right)\right)^2$	(3.3a)	Bueno-Ibarra et al (2005)
Gradient Norm	$S(\boldsymbol{\mu_m}) = -\sum_{v=1}^{N_v}\nabla_x(\mu_{mv})^2 + \nabla_y(\mu_{mv})^2 + \nabla_z(\mu_{mv})^2$	(3.3b)	Kingston et al (2011)
Entropy	$S(\boldsymbol{\mu_m}) = -\sum_{l=1}^{L} h_l(\boldsymbol{\mu_m}) \cdot \log h_l(\boldsymbol{\mu_m})$	(3.3c)	Wicklein et al (2012)
Gradient Entropy	$S(\boldsymbol{\mu_m}) = -\sum_{l=1}^{L} h_l\left(\sqrt{\nabla_x(\boldsymbol{\mu_m})^2 + \nabla_y(\boldsymbol{\mu_m})^2 + \nabla_z(\boldsymbol{\mu_m})^2}\right) \cdot \log h_l\left(\sqrt{\nabla_x(\boldsymbol{\mu_m})^2 + \nabla_y(\boldsymbol{\mu_m})^2 + \nabla_z(\boldsymbol{\mu_m})^2}\right)$	(3.3d)	McGee et al (2000)

3.2.5. Spatiotemporal Regularization

Two regularization terms are explicit in Equation (3.1): (1) a temporal regularization term to discourage abrupt motion; and (2) a spatial regularization term to encourage similar motion for ROIs that are close together. The temporal regularization penalizes the squared 2-norm of the displacement of a set of reference points associated with each ROI computed between projection views:

$$R_t(\boldsymbol{T}_m) = \sum_{p=1}^{P} \sum_{k=2}^{N_{\text{proj}}} \left\| \boldsymbol{p}_{p,k} - \boldsymbol{p}_{p,k-1} \right\|_2^2 \tag{3.4}$$

where p enumerates the reference points ($p = 1, \ldots, P$), k enumerates projection views, and $\boldsymbol{p}_{p,k}$ indicates the spatial coordinates of the p^{th} reference point at the timepoint corresponding to the k^{th} projection view. This temporal regularization penalty is similar to that in Sisniega et al (2017); however, in this work, a set of $P = 2$ reference points per ROI was selected, with one point corresponding to a vertex of the ROI and the second corresponding to the center of the ROI.

The spatial regularization penalizes the magnitude of the difference between motion trajectories normalized by the Euclidean distance between ROIs:

$$R_{\mathbf{x}}(\boldsymbol{T}_m) = \sum_{i \neq m} \frac{\| \Delta \boldsymbol{p}_i(\boldsymbol{T}_i) - \Delta \boldsymbol{p}_m(\boldsymbol{T}_m) \|}{\| \boldsymbol{p}_i - \boldsymbol{p}_m \|_2} \tag{3.5}$$

where $\boldsymbol{p}$ contains the spatial coordinates of a reference point (chosen here to be the center of the ROI), and $\Delta \boldsymbol{p}_m$ is the displacement of the reference point over scan time t according to the motion trajectory $\boldsymbol{T}_m$.

3.2.6. FBP Reconstruction Using a 4D MVF and Warped Backprojector

The motion estimates for each ROI are interpolated via thin plate spline to obtain $\Delta\boldsymbol{p}$:

$$\Delta\boldsymbol{p}(k,\boldsymbol{x}) = \sum_{m=1}^{M+8} \boldsymbol{c_m}(k) B(\boldsymbol{x} - \boldsymbol{x_m}) \tag{3.6}$$

where $\boldsymbol{c_m}$ are spline coefficients that give the displacement of a reference point associated with each ROI (chosen to be the center of the ROI) as estimated by the motion compensation algorithm, m enumerates ROIs, k enumerates projection views, $\boldsymbol{x}$ represents 3D spatial coordinates, and B is a cubic b-spline kernel. Eight additional reference points were included at the eight corners of a volume expanded from the size of the reconstructed volume $\boldsymbol{\mu_{MC}}$ by 10 cm to provide boundary conditions with zero motion, ensuring that $\Delta\boldsymbol{p}(k)$ smoothly decreases at the edges of $\boldsymbol{\mu_{MC}}$. Spatial interpolation is repeated for all N_{proj} projection views using the temporally interpolated motion profiles (Section 3.2.2 and Equation (3.2)) to generate $\Delta\boldsymbol{p}$.

The motion-compensated volume ($\boldsymbol{\mu_{MC}}$) is formed by 3D FBP incorporating $\Delta\boldsymbol{p}$ for each projection view ("warped backprojection"). Each view is backprojected using the nominal system geometry and weighting factors according to the FDK algorithm, and $\Delta\boldsymbol{p}(k)$ is applied to resample the position of the voxels according to the motion estimate at time t corresponding to projection view k.

By virtue of the 4D motion estimate, the reconstruction $\boldsymbol{\mu_{MC}}$ can be formed at any (or all) time points by shifting $\Delta\boldsymbol{p}$ to a specific projection view k. As noted below, the mid-point of the scan ($k = N_{\text{proj}}/2$) is nominally selected for reconstruction of $\boldsymbol{\mu_{MC}}$.

3.3. Experimental Methods

A systematic progression of experiments outlined below investigated the parameter settings and performance of the deformable motion compensation algorithm. The first experiment focused on selection of the autofocus objective for use in Equation (3.1) suitable to soft-tissue CBCT using a digital phantom (Table 3.2). The second used a simulated CBCT dataset to test the performance of deformable motion compensation in realistic anatomy, specifically investigating the effect of regularization strength as a function of the amplitude of deformable motion. The third experiment involved a CBCT-capable mobile C-arm and cadavers subjected to simple or complex motion during the scan to investigate performance with realistic anatomy and other image quality considerations (e.g., truncation, scatter, and geometric calibration).

3.3.1. Determination of an Autofocus Objective for Soft-Tissue CBCT

The first experiment determined which of the autofocus objectives in Table 3.2 is best suited to soft-tissue motion compensation. A digital phantom was used to generate motion-contaminated CBCT volumes consisting of spheres placed in a cylinder (240 mm diameter × 350 mm height) with attenuation approximately equal to that of liver (50 HU). Five hundred 12 mm diameter spheres (–50 to 150 HU) were added to the cylinder at random, non-overlapping locations.

A sinusoidal motion trajectory with variable magnitude $|\boldsymbol{\Delta p}|$ ranging from 4 mm to 20 mm in 4 mm increments was applied to the phantom with equal motion magnitude allocated to the three cardinal directions. For each projection view k, the phantom was shifted according to the motion trajectory and then projected using a linear forward-

projector on GPU to generate CBCT projections. N_{proj} = 360 projections were computed over total scan angle θ_{scan} = 360°, with the simulated CBCT geometry matching that of a clinical robotic C-arm system (Artis Zeego, Siemens Healthineers, Forchheim Germany, SAD = 800 mm, SDD = 1200 mm).

Each autofocus objective in Table 3.2 was investigated as a basis for motion estimation with the number of bins set to L = 256 for calculation of the normalized intensity histogram h in entropy (Equation (3.3c)) and gradient entropy (Equation (3.3d)). A single ROI (M = 1) of 50 × 50 × 50 voxels with size 1.0 × 1.0 × 1.0 mm^3 was placed at the center of the phantom. CMA-ES optimization used λ_{CMAES} = 20 candidate solutions and σ_{CMAES} = 0.5 mm for translations and 0.05° for rotations. To provide equivalent temporal regularization strength when using different autofocus objectives in Equation (3.1) and to ensure that the estimated motion was primarily dependent on the objective (as opposed to strength of regularization), the nominal value of β_t was set to 0.001 × the value of each objective calculated in the motion-free image (units mm^{-2}). Reconstruction of the motion-compensated volume ($\boldsymbol{\mu}_{\mathbf{MC}}$) used a grid of 512 × 512 × 512 voxels of size 0.5 × 0.5 × 0.5mm^3.

The performance of motion compensation was evaluated using SSIM (Wang et al 2004) to compare $\boldsymbol{\mu}_{\mathbf{MC}}$ with the motion-free reference image ($\boldsymbol{\mu}_{\mathbf{ref}}$), similar to analysis in Chapter 2:

$$\mathrm{SSIM}(\boldsymbol{\mu}_{\mathbf{ref}}, \boldsymbol{\mu}_{\mathbf{MC}}) = \frac{(2\bar{\mu}_{\mathrm{ref}}\bar{\mu}_{\mathrm{MC}} + c_1)(2\sigma_{\mathrm{ref-MC}} + c_2)}{(\bar{\mu}_{\mathrm{ref}}^2 + \bar{\mu}_{\mathrm{MC}}^2 + c_1)(\sigma_{\mathrm{ref}}^2 + \sigma_{\mathrm{MC}}^2 + c_2)} \tag{3.7}$$

where $\bar{\mu}_{\mathrm{ref}}$ is the average attenuation of $\boldsymbol{\mu}_{\mathbf{ref}}$ with variance σ_{ref}^2, $\bar{\mu}_{\mathrm{MC}}$ is the average attenuation of $\boldsymbol{\mu}_{\mathbf{MC}}$ with variance σ_{MC}^2, and $\sigma_{\mathrm{ref-MC}}$ is the cross-covariance between the two

images. The regularization terms c_1 and c_2 were assigned values of 5×10^{-3} mm^{-2} and 1×10^{-2} mm^{-2}, respectively.

3.3.2. Selection of Spatiotemporal Regularization Parameters

The second experiment investigated the sensitivity of the motion compensation algorithm to the temporal and spatial regularization parameters (β_t and $\beta_{\boldsymbol{x}}$), seeking stable settings that can be applied over a broad range of potential motion magnitudes $|\boldsymbol{\Delta p}|$. Figure 3.2 illustrates the phantom and motion trajectories investigated in this study. An MDCT dataset from The Cancer Imaging Archive (TCIA) was used as a digital phantom and $N_{\text{proj}} = 248$ projections were computed over $\theta_{\text{scan}} = 195°$, with CBCT geometry as described in Section 3.3.1. Motion was modeled as a sequence of 3D MVFs with the motion at each voxel implementing one cycle of a cosine wave over the simulated scan time t (alternatively, projection views k or scan angles θ), as in Figure 3.2c. The applied motion magnitude $|\boldsymbol{\Delta p}|$ was maximized near the anterior skin line and decreased to $|\boldsymbol{\Delta p}| = 0$ mm at the posterior skin line (Figure 3.2a–b). Variable maximum motion magnitude $|\boldsymbol{\Delta p}|_{\text{max}}$ ranged from 10 mm to 25 mm in 5 mm increments. The motion trajectory allocated 70% of the motion along the anterior-posterior (AP) direction (y axis, Figures 3.2a, c) and 30% along the SI direction (z axis, Figures 3.2b, c).

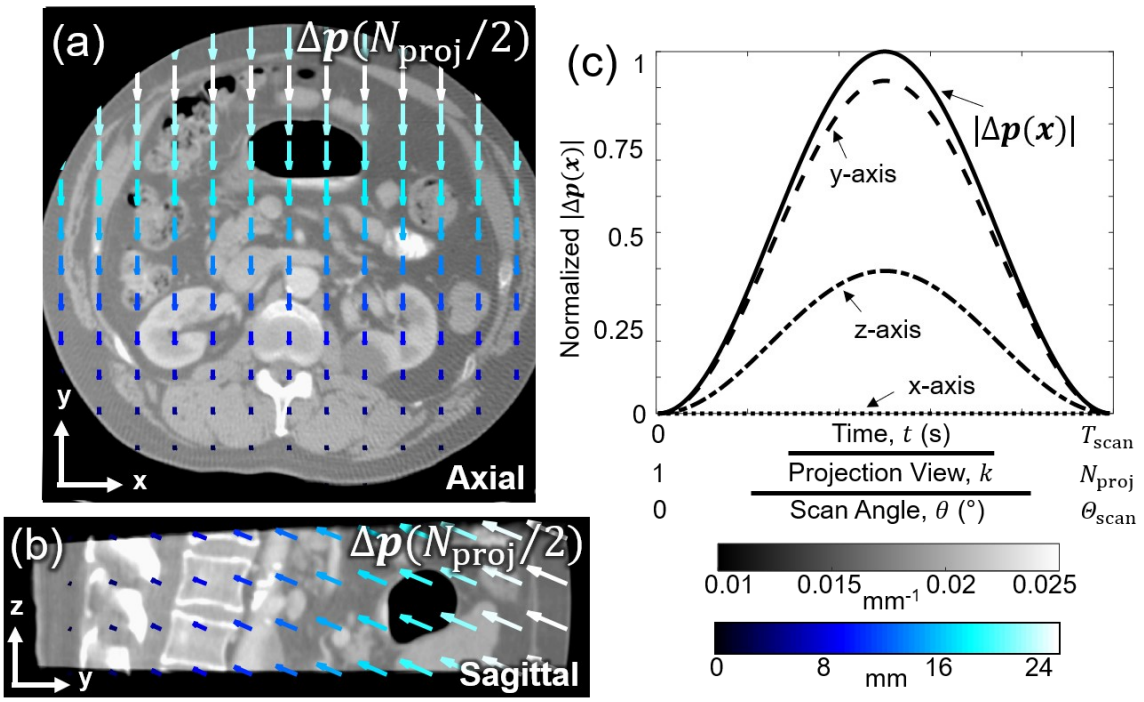

Figure 3.2. Deformable motion applied to an image from the TCIA dataset. (a) An axial plane of the applied 3D MVF ($\Delta\boldsymbol{p}(k)$) at the timepoint corresponding to $k = N_{\text{proj}}/2$, with maximum motion magnitude $|\boldsymbol{\Delta p}|_{\text{max}}$ = 25 mm. (b) A sagittal plane of $\Delta\boldsymbol{p}(N_{\text{proj}}/2)$. (c) Sinusoidal profile of the applied motion at a single location ($\Delta\boldsymbol{p}(\boldsymbol{x})$) over the scan time t, alternatively, projection views k or scan angles θ. The relative motion magnitude applied along the x, y, and z axes is indicated in (c) and reflected in the length and color of the arrows in (a–b).

For motion estimation, M = 27 ROIs of 50 × 50 × 20 voxels with size 1.0 × 1.0 ×1.0 mm^3 were placed in a grid throughout the volume. The parameter β_t was assigned values {0.1, 0.5, 1, 5, 10} mm^{-2}, and $\beta_{\boldsymbol{x}}$ was assigned values {0.01, 0.05, 0.1, 0.5,1}. The b-spline representation of each DoF used N = 4 knots resulting in a total of 648 motion parameters to be estimated (N = 4 knots × j= 6 DoF × M = 27 ROIs). CMA-ES optimization used $\lambda_{\text{CMAES}} = 50$ and $\sigma_{\text{CMAES}} = 2.0$ mm in translations (and 0.2° in rotations). Image reconstruction of $\boldsymbol{\mu}_{\text{MC}}$ used a grid of 650 × 650 × 200 voxels with size 0.5 × 0.5 × 0.5 mm^3.

The motion-compensated image $\boldsymbol{\mu_{MC}}$ was evaluated for each $(\beta_t, \beta_x; |\boldsymbol{\Delta p}|_{\max})$ combination in terms of SSIM using the same regularization constants c_1 and c_2 as in Section 3.3.1. The SSIM was calculated for 248 instances of the motion-compensated volume $\boldsymbol{\mu_{MC}}$ by shifting the estimated MVF $\boldsymbol{\Delta p}$ to the timepoint corresponding to each of the N_{proj} = 248 projection views. Similarly, 248 instances of a reference volume $\boldsymbol{\mu_{ref}}$ were reconstructed using the applied MVFs. For each reconstruction instance, a rigid registration was performed between $\boldsymbol{\mu_{MC}}$ and $\boldsymbol{\mu_{ref}}$ to align image structures, and SSIM was calculated at the central axial slice, excluding the skin line and surrounding air regions. The SSIM values for the uncompensated images $\boldsymbol{\mu}$ were also calculated as a basis of comparison.

3.3.3. Performance Evaluation with Complex Anatomical Motion

The third experiment advanced the method to realistic imaging scenarios with additional challenges such as scatter, truncation, and geometric calibration. Two cadaver specimens (one male with BMI > 25 and one female with BMI < 25) were imaged on a mobile C-arm system (Cios Spin 3D, Siemens Healthineers, Forchheim Germany, Figure 3.3), and applied simple and complex motion during the CBCT scan. Simple motion was achieved by translating the bed superiorly (along the *z* axis at approximately 1 mm per second during the middle third of the scan), and complex motion involved flexing the pelvic and lower abdominal regions anteriorly through a range of approximately 20 mm. Each scan acquired N_{proj} = 400 projections over θ_{scan} = 195° with T_{scan} = 60 s at 111 kV totaling 153 mAs. A motion-free scan for each cadaver was obtained using the same parameters.

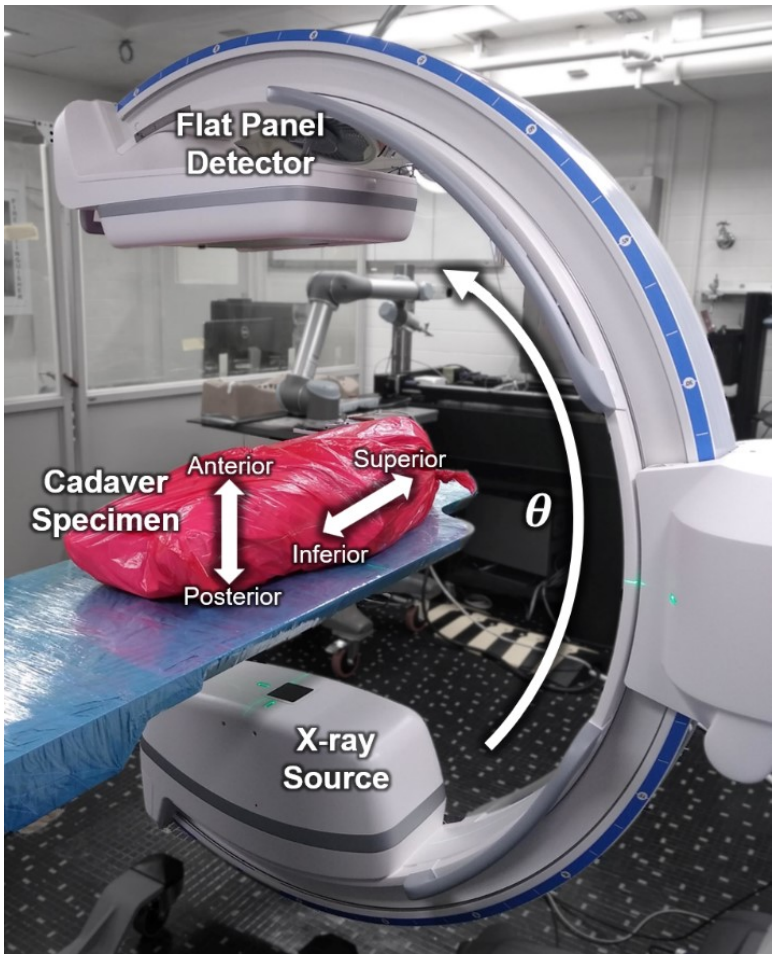

Figure 3.3. Cadaver setup with a mobile C-arm. Two motion profiles were applied during scanning: (1) simple motion in which the cadaver was translated in the SI direction; and (2) complex motion in which the pelvis and abdomen were flexed anteriorly and superiorly by means of an inflatable air bladder placed under the pelvis.

Motion estimation used $M = 27$ ROIs ($40 \times 40 \times 40$ voxels with size $1.0 \times 1.0 \times 1.0$ mm^3) placed in a grid throughout the volume, b-splines used $N = 4$ knots, and CMA-ES optimization used $\lambda_{\text{CMAES}} = 50$ and $\sigma_{\text{CMAES}} = 2.0$ mm (and 0.2°). The regularization constants (β_t and β_x) were selected according to the results of Section 3.3.2. Reconstruction of $\boldsymbol{\mu}_{\mathbf{MC}}$ used a grid of $512 \times 512 \times 512$ voxels with size $0.313 \times 0.313 \times 0.313$ mm^3.

To evaluate image quality, three ROIs ($100 \times 100 \times 100$ voxels with size $0.313 \times 0.313 \times 0.313$ mm^3) containing anatomical features of interest were identified in both $\boldsymbol{\mu}$ and $\boldsymbol{\mu}_{\mathbf{MC}}$, and each ROI was rigidly registered to corresponding structures in $\boldsymbol{\mu}_{\mathbf{ref}}$ The SSIM was calculated for each ROI, with the c_2 regularization term increased to 1×10^{-1} mm^{-2} to reduce the influence of image noise. The root-mean-square error (RMSE) between registered ROIs was also computed.

As a final demonstration of performance in complex anatomical motion, an exemplary result from initial translation of the method to clinical studies is shown.

3.4. Results

3.4.1. Determination of an Autofocus Objective for Soft-Tissue CBCT

Figure 3.4 shows motion compensation for the digital cylindrical phantom with applied motion magnitude $|\boldsymbol{\Delta p}|$ = {4, 8, 12, 16, 20} mm. Figure 3.4a shows the uncompensated volume $\boldsymbol{\mu}$, the motion-free reference volume $\boldsymbol{\mu}_{\mathbf{ref}}$, and the motion-compensated volume $\boldsymbol{\mu}_{\mathbf{MC}}$ using gradient variance, gradient norm, entropy, and gradient entropy (Equations (3.3a–d), respectively) as the autofocus objective in Equation (3.1) for $|\boldsymbol{\Delta p}|$ = 8 mm. Gradient variance produced images with distorted features, while entropy and gradient norm produced images with residual blur. Gradient entropy performed best overall by reducing blur without distorting the spherical features.

Figure 3.4b shows SSIM over the full range of $|\boldsymbol{\Delta p}|$ investigated, with gradient entropy producing the highest SSIM values overall. For gradient norm, entropy, and gradient variance the SSIM is seen to increase with motion magnitude, indicating that the nominal temporal regularization strength had a more pronounced positive effect on the cost

function in the presence of larger motion. This was not seen for gradient entropy, indicating that the objective is more robust in the presence of weak regularization. Based on this result, gradient entropy was used as the autofocus objective in the following experiments.

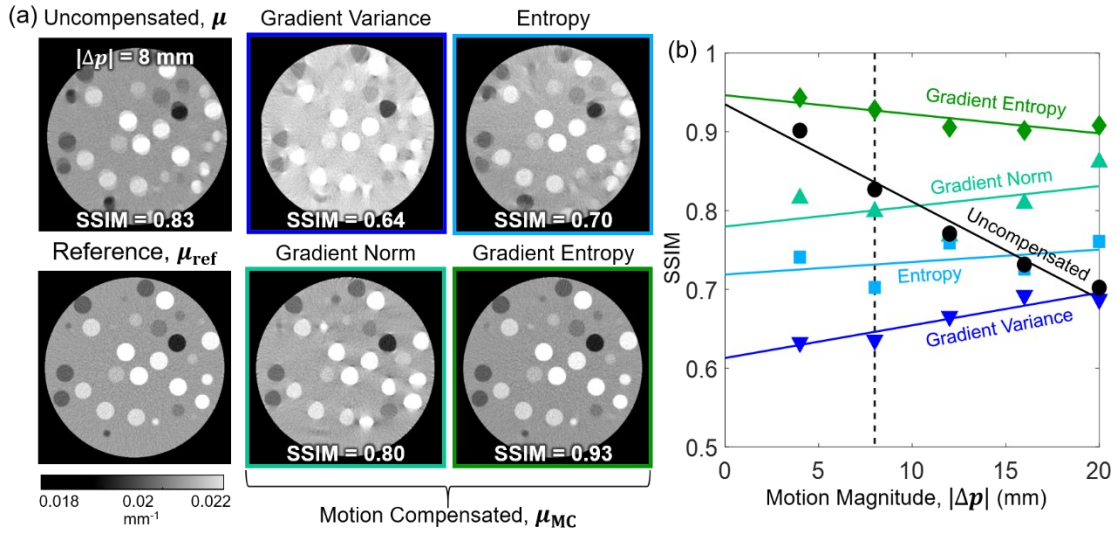

Figure 3.4. Motion compensation with four choices of autofocus objective. Images in (a) show the uncompensated volume $\boldsymbol{\mu}$ of the digital phantom with motion magnitude $|\boldsymbol{\Delta p}|$ = 8 mm and the motion-free reference volume $\boldsymbol{\mu}_{\mathbf{ref}}$. Motion-compensated volumes $\boldsymbol{\mu}_{\mathbf{MC}}$ are shown using the autofocus objectives listed in Table 3.2. (b) SSIM for the resulting $\boldsymbol{\mu}_{\mathbf{MC}}$ compared to $\boldsymbol{\mu}_{\mathbf{ref}}$ measured as a function of $|\boldsymbol{\Delta p}|$ for each autofocus objective.

3.4.2. Selection of Spatiotemporal Regularization Parameters

Figure 3.5 shows SSIM for motion compensation applied to cases of simulated motion in the TCIA dataset. The SSIM values were calculated for each maximum motion magnitude $|\boldsymbol{\Delta p}|_{\max}$ over the specified range of β_t and $\beta_{\boldsymbol{x}}$. For $|\boldsymbol{\Delta p}|_{\max}$ = 10 mm (Figure 3.5a), the maximum SSIM value was 0.88, occurring at (β_t = 5 mm^{-2}, $\beta_{\boldsymbol{x}}$ = 0.1). For $|\boldsymbol{\Delta p}|_{\max}$ = 15 mm (Figure 3.5b), the maximum SSIM value was 0.82, occurring at (β_t = 5 mm^{-2}, $\beta_{\boldsymbol{x}}$ = 0.1). For $|\boldsymbol{\Delta p}|_{\max}$ = 20 mm (Figure 3.5c), the maximum SSIM value was 0.79 occurring at (β_t = 1 mm^{-2}, $\beta_{\boldsymbol{x}}$ = 0.1), and for $|\boldsymbol{\Delta p}|_{\max}$ = 25 mm (Figure 3.5d), the maximum SSIM value was 0.74 occurring at (β_t = 0.5 mm^{-2}, $\beta_{\boldsymbol{x}}$ = 0.1). These results indicate that β_t is sensitive to $|\boldsymbol{\Delta p}|$ in that the optimal value of β_t decreases from 5 to

0.5 mm^{-2} as $|\boldsymbol{\Delta p}|_{\max}$ increases from 10 to 25 mm. In contrast, $\beta_{\boldsymbol{x}}$ does not appear sensitive to $|\boldsymbol{\Delta p}|$ and maintains a constant optimal value (0.1) for all $|\boldsymbol{\Delta p}|_{\max}$ for the smooth spatial distribution of motion amplitude in this experiment. Based on this result and considering a typical range of anatomical motion (~20 mm), β_t = 1 mm^{-2} and $\beta_{\boldsymbol{x}}$ = 0.1 were selected for motion estimation in the following experiment.

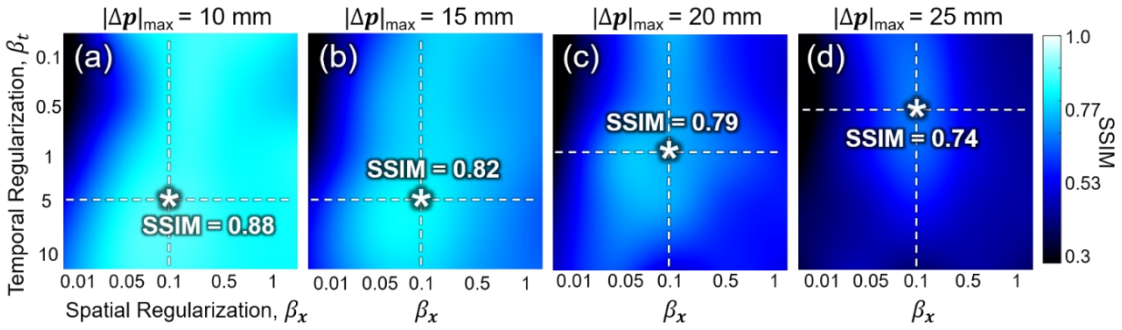

Figure 3.5. Selection of spatiotemporal regularization. SSIM values were evaluated over a range of maximum motion magnitude ($|\boldsymbol{\Delta p}|_{\max}$ = {10, 15, 20, 25} mm), showing optimal temporal regularization (i.e., maximum SSIM marked by the *) to range from β_t = 0.5 to 5 mm^{-2}, whereas optimal spatial regularization was relatively constant at $\beta_{\boldsymbol{x}}$ = 0.1.

Figure 3.6 shows the improvement in SSIM of the motion-compensated volume $\boldsymbol{\mu}_{\mathbf{MC}}$ compared to the uncompensated volume $\boldsymbol{\mu}$ for the optimal (β_t, $\beta_{\boldsymbol{x}}$) pairs determined in Figure 3.5. The vertical bars for $\boldsymbol{\mu}_{\mathbf{MC}}$ indicate the range of SSIM calculated over 248 reconstruction instances — i.e., reconstructed at various points in time t, or alternatively, projection views k over the course of the scan. Deformable motion compensation is seen to increase the maximum SSIM value (from its uncorrected value in $\boldsymbol{\mu}$) by 42%, 64%, 78%, and 92% for $|\boldsymbol{\Delta p}|_{\max}$ = {10, 15, 20, 25} mm, respectively.

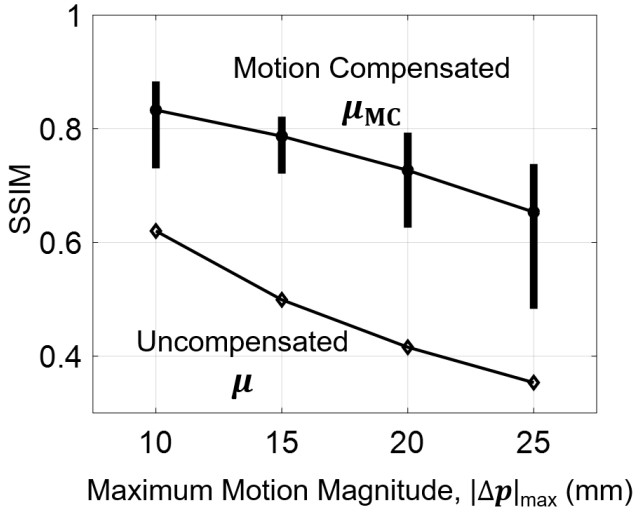

Figure 3.6. Measurements of SSIM for the motion-compensated volume $\boldsymbol{\mu}_{\mathbf{MC}}$ compared to the uncompensated volume $\boldsymbol{\mu}$ as a function of the maximum motion magnitude $|\boldsymbol{\Delta p}|_{max}$. The range bars show SSIM calculated over 248 instances of $\boldsymbol{\mu}_{\mathbf{MC}}$ (i.e., at the 248 time-points corresponding to each projection view).

The resulting images for $|\boldsymbol{\Delta p}|_{max} = 25$ mm are shown in Figure 3.7. The uncompensated volume ($\boldsymbol{\mu}$) is shown in the left-most column, the motion-compensated volume ($\boldsymbol{\mu}_{\mathbf{MC}}$, with optimal ($\beta_t$, β_x) from Figure 3.5) is shown in the middle column, and the motion-free reference volume ($\boldsymbol{\mu}_{\mathbf{ref}}$) is shown in the right-most column. Axial slices (Figure 3.7a–c), demonstrate the ability to compensate for large deformations in soft-tissue near the anterior skin line while maintaining structures that are relatively stable at the posterior skin line. This exemplifies the need for a *deformable* motion model to achieve compensation throughout the entire volume. Sagittal slices (Figure 3.7d–f) demonstrate that the 3D aspect of the motion was successfully compensated.

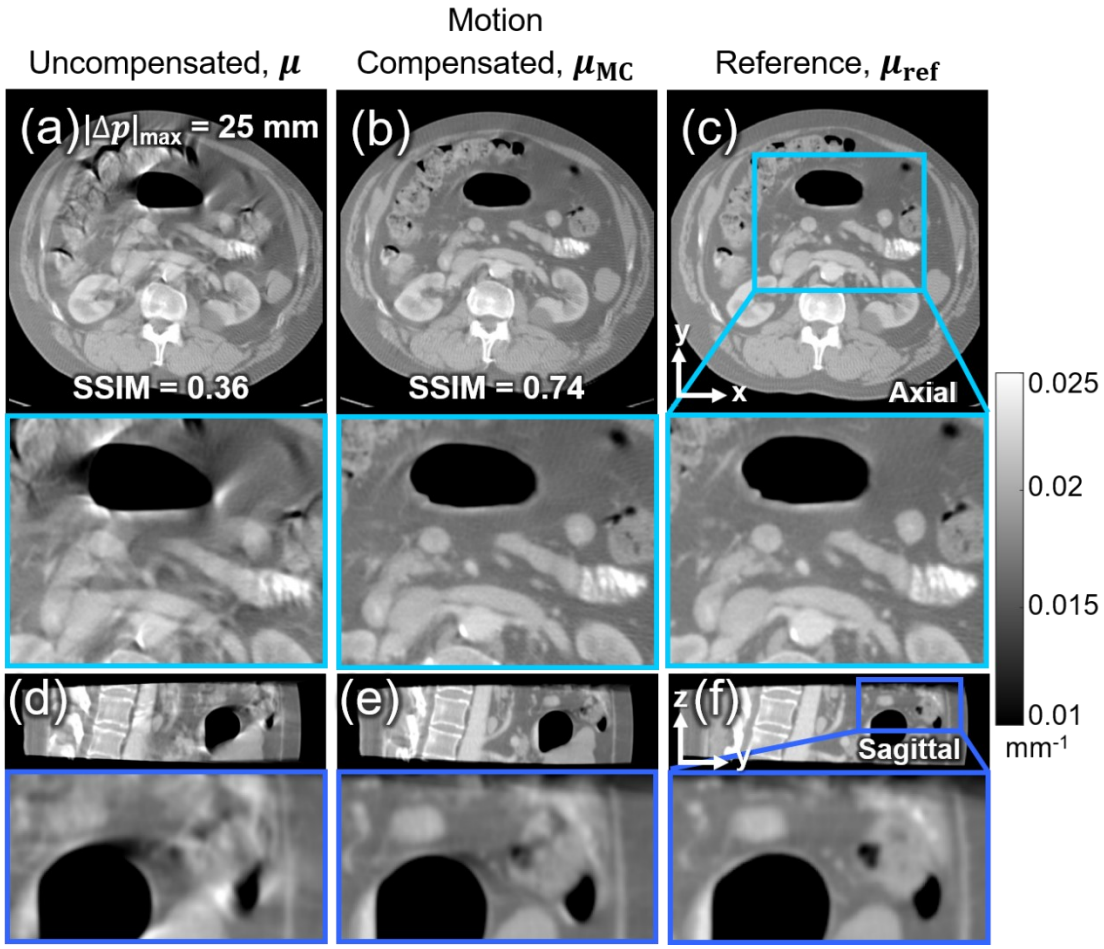

Figure 3.7. Motion compensation for simulated deformable motion in CT of the abdomen from the TCIA dataset: uncompensated ($\boldsymbol{\mu}$), motion-compensated ($\boldsymbol{\mu_{MC}}$), and motion-free reference ($\boldsymbol{\mu_{ref}}$) for maximum motion magnitude of $|\boldsymbol{\Delta p}|_{max}$ = 25 mm. (a–c) Soft-tissue details in the central axial slice (3 mm thickness). (d–f) Soft-tissue details in the central sagittal slice (3 mm thickness).

3.4.3. Performance Evaluation with Complex Anatomical Motion

Figure 3.8 shows images resulting from motion compensation applied to images of the cadaver undergoing a relatively simple motion profile (translation roughly along its SI axis). The sagittal slice in Figure 3.8a shows the uncompensated volume ($\boldsymbol{\mu}$, sagittal plane) with blurring artifacts obscuring much of the soft-tissue anatomy and streak artifacts around high-contrast structures. Motion compensation (Figure 3.8b) brings these features into focus, including the vertebrae, calcifications in the aorta, the soft-tissue boundary of

the liver, and a cardiac stent (shown in the zoomed inset and indicated by the arrow in Figure 3.8b).

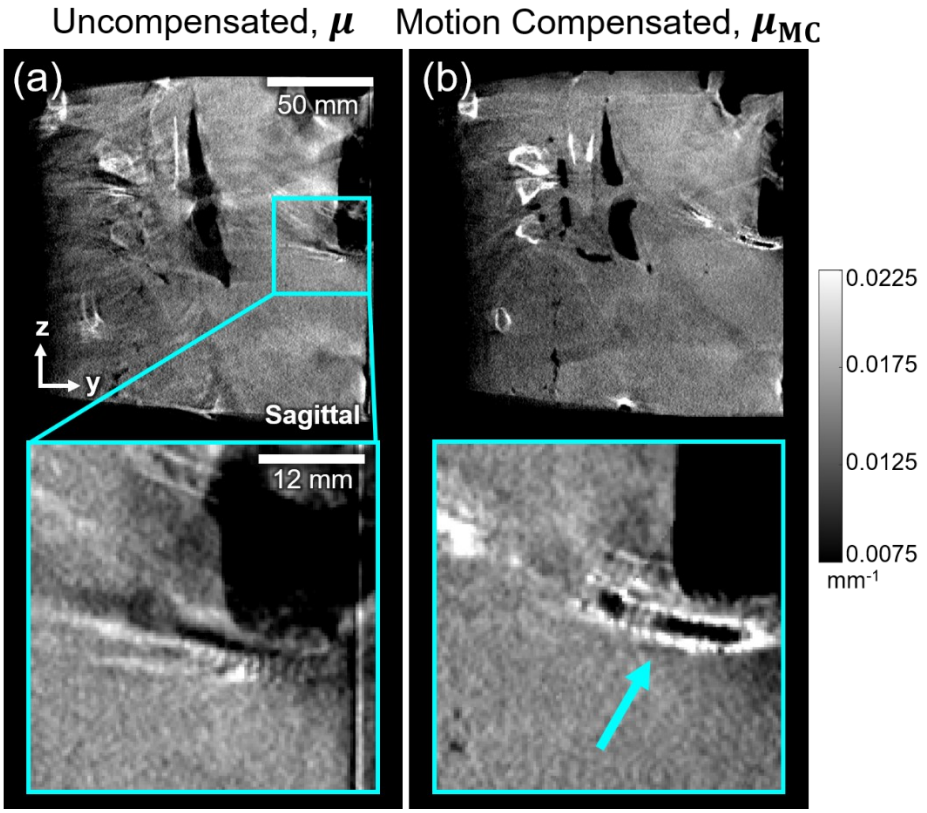

Figure 3.8. Motion compensation in cadaver (simple motion). (a) Uncompensated ($\boldsymbol{\mu}$) and (b) motion-compensated ($\boldsymbol{\mu_{MC}}$). Sagittal slices are shown (top row) with a zoomed-in view (bottom row) in the region of a cardiac stent.

The performance of motion compensation is further illustrated in Figure 3.9, showing local SSIM and RMSE for the cadaver undergoing simple motion. Structures of interest include a transverse process in the coronal plane (Figure 3.9a) and aortic calcifications in the axial (Figure 3.9b) and sagittal (Figure 3.9c) planes. The SSIM values improved with motion compensation from (a) 0.68 to 0.87 (28%), (b) 0.73 to 0.85 (16%), and (c) 0.75 to 0.87 (16%), respectively. The improvement is further quantified by the reduction in RMSE from (a) 0.10 to 0.05 mm^{-1} (50%), (b) 0.09 to 0.06 mm^{-1} (33%), and (c) 0.11 to 0.06 mm^{-1} (45%).

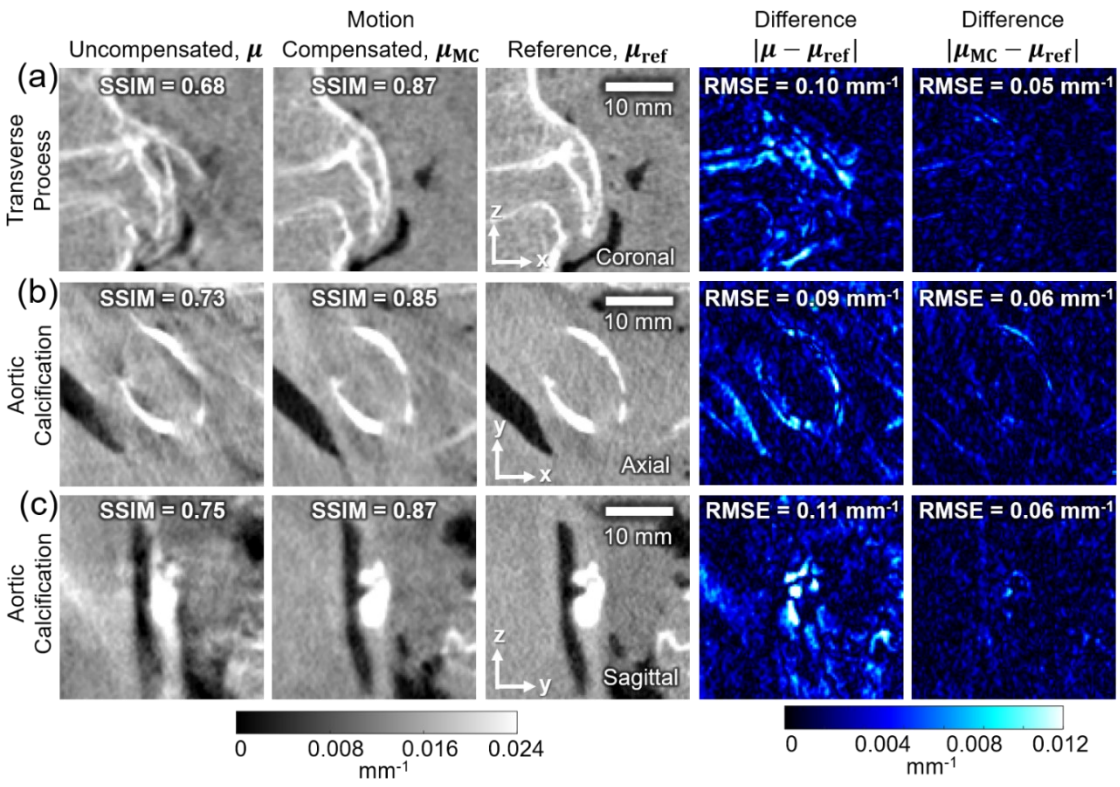

Figure 3.9. Visualization of structures of interest along with quantitative analysis (local SSIM and RMSE) in motion-compensated reconstructions. (a) Vertebral transverse process (coronal image). (b) Aortic calcification (axial plane). (c) Aortic calcification (sagittal plane). Columns from left to right show ROIs for $\boldsymbol{\mu}$, $\boldsymbol{\mu_{MC}}$, and $\boldsymbol{\mu_{ref}}$ and the difference $|\boldsymbol{\mu} - \boldsymbol{\mu_{ref}}|$ and $|\boldsymbol{\mu_{MC}} - \boldsymbol{\mu_{ref}}|$.

Similar results were observed for the cadaver undergoing complex motion (Figure 3.10). Figure 3.10a shows the uncompensated volume ($\boldsymbol{\mu}$, sagittal plane) with blurring and distortion of the vertebral bodies, aorta, and major vessels within the liver. Motion compensation recovered features throughout the volume, as seen in Figure 3.10b. The zoomed-in regions in the bottom row of Figure 3.10 show the improvement in image quality around a compression fracture in a thoracic vertebrae and nearby aortic calcifications (indicated by arrows).

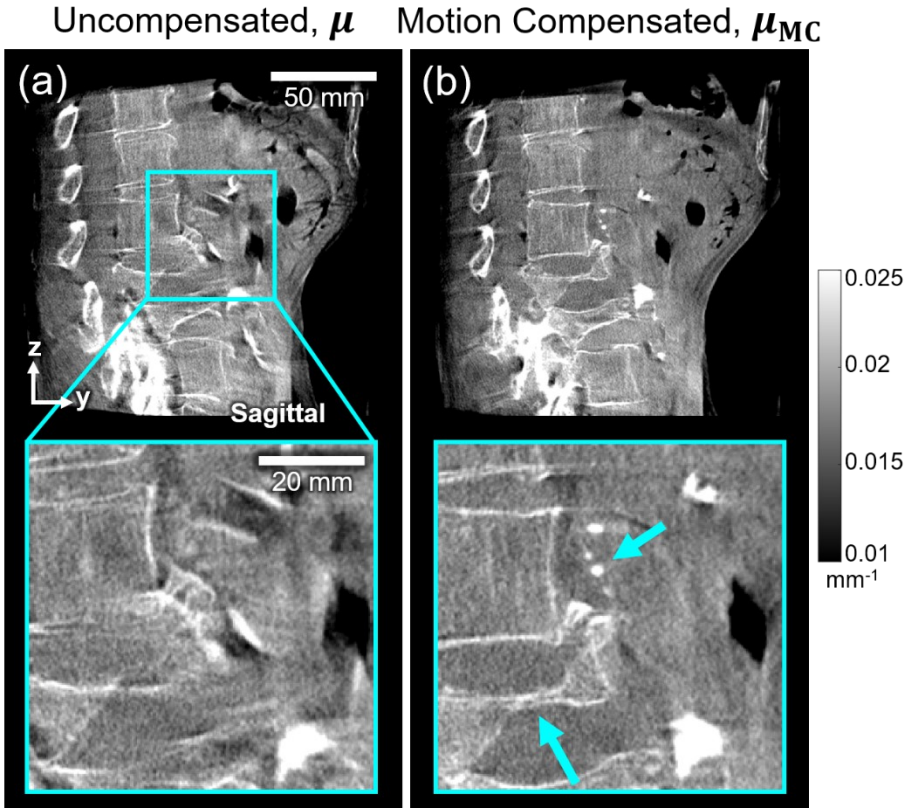

Figure 3.10. Motion compensation in cadaver (complex motion). (a) Uncompensated ($\boldsymbol{\mu}$) and (b) motion-compensated ($\boldsymbol{\mu_{MC}}$) shown as sagittal slices with a zoomed-in region showing a vertebral compression fracture and aortic calcification indicated by arrows in (b).

Figure 3.11 shows local SSIM and RMSE for the cadaver undergoing complex motion. Anatomical structures of interest include a gallstone (coronal plane, Figure 3.11a) and aortic calcifications (axial plane in Figure 3.11b and sagittal plane in Figure 3.11c). Deformable motion compensation increased local SSIM from (a) 0.68 to 0.80 (18%), (b) 0.65 to 0.76 (17%), and (c) 0.60 to 0.77 (28%). The corresponding reduction in RMSE was from (a) 0.13 to 0.08 mm^{-1} (38%), (b) 0.14 to 0.11 mm^{-1} (21%), and (c) 0.11 to 0.07 mm^{-1} (36%).

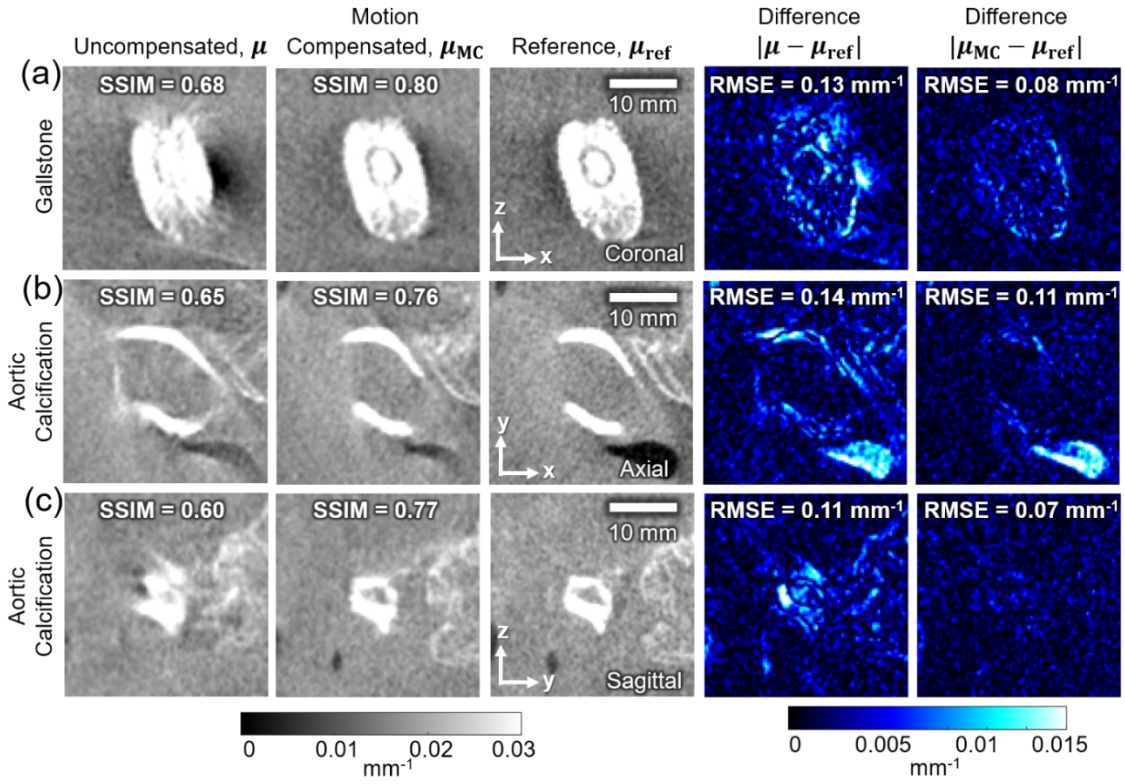

Figure 3.11. Visualization of structures of interest along with quantitative analysis (local SSIM and RMSE) in motion-compensated reconstructions of the cadaver undergoing complex deformation. Local SSIM and difference images (with RMSE) are shown for structures of interest: (a) gallstone (coronal plane), (b) aortic calcification (axial plane), and (c) aortic calcification (sagittal plane). Columns from left to right show ROIs for $\boldsymbol{\mu}$, $\boldsymbol{\mu_{MC}}$, and $\boldsymbol{\mu_{ref}}$ and the difference $|\boldsymbol{\mu} - \boldsymbol{\mu_{ref}}|$ and $|\boldsymbol{\mu_{MC}} - \boldsymbol{\mu_{ref}}|$.

Initial translation of the method to clinical studies is illustrated in Figure 3.12. In this case, visualization of the catheter and hepatic vessels is confounded by involuntary motion artifacts arising from inconsistent breath-hold during the scan. The complex deformable nature of the motion is evident in that the anterior aspect of the image exhibits much more severe artifacts than the posterior, which is relatively stable, as the patient laid prone on the operating table. The motion-compensated result shows substantial improvement in visualization of features in the region of interest, illustrated further by

zoomed-in views. Residual artifact (streaks) is attributable to unresolved motion and beam-hardening effects.

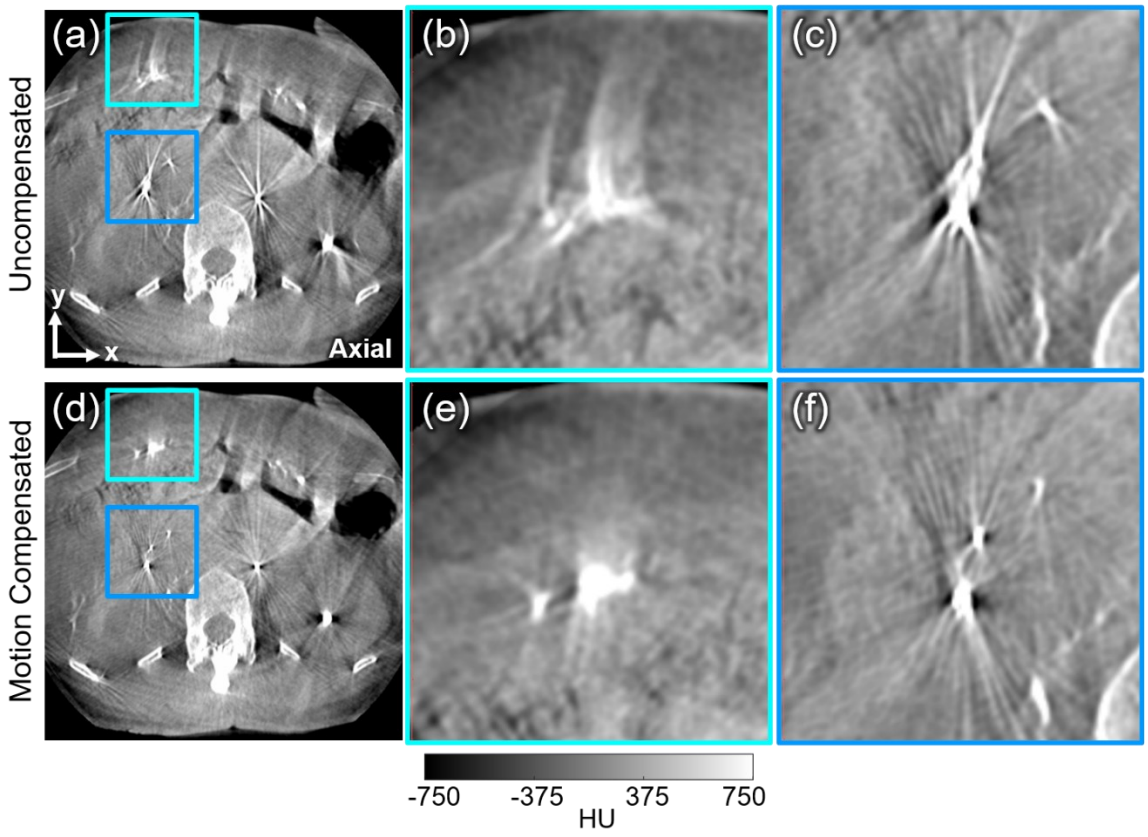

Figure 3.12. Initial demonstration of deformable motion compensation results in clinical data. (a) Axial slice of the uncompensated image. (b–c) Zoomed regions corresponding to the cyan and blue boxes in (a), respectively, showing a reduction of blurring and streaks about contrast-enhanced arteries due to motion. (d–f) The same image after deformable motion compensation.

3.5. Discussion and Conclusions

A deformable, image-based motion compensation method was developed to improve image quality in CBCT of soft-tissue anatomy, as in abdominal IGI. In this chapter, we investigated the performance of various autofocus objectives suitable to soft-tissue structures, determined the selection of spatiotemporal regularization parameters, and

assessed the performance of the algorithm in the presence of realistic anatomy undergoing simple and complex motion of various magnitudes.

Among the autofocus objectives investigated (gradient variance, gradient norm, entropy, and gradient entropy), gradient entropy was shown to be best suited to soft-tissue CBCT. Previously, Sisniega et al (2017) evaluated entropy, negative variance, total variation, gradient norm, and gradient variance as autofocus objectives for high-contrast CBCT of musculoskeletal extremities, finding gradient variance to be best suited to that application. Negative variance and total variation were found to be highly unstable for this application and were therefore excluded from the study. The results of Sisniega et al (2017) served as a starting point for selection of a suitable soft-tissue autofocus objective, and the current finding (best performance with gradient entropy) is attributed to differences in subject contrast and spatial-frequency content (viz., soft-tissue structures forming the focus of this work).

The experiments also guided selection of algorithm parameters and identification of stable settings — most notably, the spatiotemporal regularization strength (β_t and β_x). For the smooth deformation fields applied, the studies showed the ideal temporal regularization strength (β_t) to be dependent on the magnitude of motion (varying by a factor of 10 for motion magnitudes ranging from 10 to 25 mm), whereas the ideal spatial regularization strength (β_x) is relatively insensitive (constant at 0.1 over the range of motion investigated). These findings informed the parameter selection for subsequent studies, choosing β_t = 1 mm^{-2} as a value roughly correspondent with the anticipated motion magnitude (and fixing β_x = 0.1). Note also that (due to the summations in Equations (3.1)

and (3.5)) these parameters scale with the number of ROIs (held fixed at $M = 27$ for these studies).

While these settings of spatiotemporal regularization strength were well justified for the experiments herein, one can imagine scenarios for which the parameter settings may require adjustment — for example, a motion pattern featuring abrupt change ("jerk") or sliding motion between soft-tissue interfaces. There may also be realistic motion scenarios not well described by a low-order spline (e.g., spasm, tremor, dyskinesia) for which an increase in the number of spline knots or a different basis function all together may be needed to represent the motion accurately. Furthermore, the performance of motion estimation may benefit from allowing the regularization strength to vary either in time or space. Such considerations are the subject of ongoing and future work, including strategies to estimate the motion magnitude directly from the scan data and / or uncompensated reconstruction to set parameters accordingly. Such methods for estimation of the motion magnitude could also be extended to parameters of the CMA-ES algorithm (e.g., σ_{CMAES}), allowing regions with large estimated deformation to be solved via larger search space. Conversely, regions with small estimated deformations would undergo motion compensation with larger values of temporal / spatial regularization and a smaller search space. A refined variation could also apply directional weights in the spatial regularization, discouraging similarity between regions close in space but with largely different motion amplitude / direction.

In the current work, we developed and tested the feasibility of deformable motion compensation, but computational speed was far from optimal. Runtime depended on numerous factors, including the magnitude of deformation and number of parameters. For

example, the case of complex motion in the cadaver required ~7 hours to reach the solution shown in Figures 3.10 and 3.11. Further parallelization could be implemented in calculation of the cost function (in parallel for each ROI) and in the CMA-ES sampling process. The use of a morphological pyramid may also improve convergence time. Initially, a small number of ROIs with coarse voxel size and a large value of σ_{CMAES} could be used to estimate large components of the motion. Finer scale motion components would be estimated by progressively increasing the number of ROIs while simultaneously decreasing the voxel size and value of σ_{CMAES}. Additionally, improved initialization of the motion estimate (currently initialized as zero motion) would speed optimization by requiring fewer iterations of the CMA-ES algorithm. An initialization method is currently being developed to estimate the magnitude and spatial distribution of deformation (Sisniega et al 2020). As noted above, such estimation could be used not only for selection of spatiotemporal regularization and optimization parameters, but also to appropriately tune the number of b-spline knots and add directional information to discourage exploration of unlikely directions of motion (e.g., reducing σ_{CMAES} in the lateral direction if motion is along the AP direction) to provide more rapid convergence.

It can also be recognized that there may be cases in which a fully deformable compensation method is not necessary to produce a clinically acceptable image. For example, the simple motion case (simple translation of the cadaver) could potentially have been solved by a single 3D motion trajectory applied to the entire image, similar to the method presented by Sisniega et al (2017). In this special case, one may reasonably expect performance comparable to that shown above with deformable motion compensation.

Rigid motion compensation may be sufficient for scenarios in which only a small, targeted ROI is needed for IGI. However, it should be recognized that complex motion in regions outside the ROI may confound the result. Confounding effects from regions with motion trajectories deviating from that of the target ROI are particularly conspicuous in scenarios combining motion compensation with MBIR methods. For example, Sisniega et al (2018) and Wu et al (2020) showed that treating motion separately between interior and exterior ROIs benefited image quality in CBCT of the head, where the motion of the head (interior) was distinct from that of the head support (exterior). Appreciable image quality improvement with minimal increase in computational burden was achieved through a combination of two motion fields (interior and exterior) and a multi-resolution penalized weighted least-squares (PWLS) reconstruction method featuring a reconstruction voxel grid with coarse voxels in the exterior region and fine voxels in the interior ROI. Similar techniques could be envisioned in abdominal CBCT implementing rigid motion compensation inside a small ROI and coarse sampling (in time and space) of the deformable motion field outside that region, in combination with multi-resolution MBIR. These issues deserve further investigation in future work and would also benefit from methods to estimate / initialize motion profiles from the uncorrected image.

In summary, the experiments presented above advanced an algorithm for compensation of deformable soft-tissue motion in CBCT from initial digital simulations to semi-realistic conditions using a mobile C-arm, including factors of complex anatomy, scatter, truncation, and geometric calibration. Following motion compensation, the SSIM and RMSE in images of the cadaver improved by up to ~30% and ~50%, respectively, with clear improvement in visualization of numerous structures of interest. Translation to

clinical studies is the subject of ongoing work to demonstrate utility in real clinical scenarios.

Chapter 4: Task-Driven Source–Detector Trajectories for Interventional Cone-Beam CT

4.1. Introduction

CBCT is prevalent in a growing scope of medical interventions to provide intraoperative imaging for improved localization and assessment of treatment delivery (Siewerdsen et al 2005, Daly et al 2006, Hirota et al 2006, Orth et al 2008, Hohenforst-Schmidt et al 2014). As introduced in Chapter 1, interventional CBCT imaging systems include a variety of mobile or fixed-room C-arms capable of radiography / fluoroscopy in addition to 3D CBCT. Such systems are commonly motorized for computer-controlled motion of the x-ray source and detector about several axes — for example, floor-mounted and ceiling-mounted C-arms as well as robotic C-arms (Binder et al 2005) with multiple DoF. In addition to C-arm systems, some CBCT mammography (Shah et al 2018) and body imaging systems (Fieselmann et al 2016, Zhao et al 2019) are also capable of complex source–detector trajectories.

The additional flexibility provided by these systems permits more general orbits beyond the traditional circular and helical source–detector trajectories that have been the norm for CT for decades. To date, these flexible orbits have mainly been used to address FOV and sampling issues in interventional CBCT. For example, non-circular trajectories have been used to provide extended axial (Yu et al 2016) and elliptical (Herbst et al 2015) FOV and improve 3D sampling and data completeness (Tuy 1983, Zeng and Gullberg

1992, Noo et al 1998, Tang and Ning 2001) to avoid cone-beam artifacts that arise from traditional circular cone-beam orbits.

Tilted circular orbits are commonly used for their ability to positively impact image quality. For example, tilting the CT gantry relative to the patient's longitudinal axis is used to improve image quality adjacent to the skull base (Menzel et al 2000), reduce eye lens dose (Nikupaavo et al 2015), improve localization in CT-guided biopsies (Hussain 1996, Yamagami et al 2004), and reduce metal artifacts associated with prostheses (Lewis et al 2010). These examples suggest that modifications of the orbit beyond simple tilts may also provide clinical advantages. However, selection of an *optimal* trajectory presents many challenges. For example, the simple tilt examples above depend on the patient anatomy and / or the interventional procedure — e.g., aligning the gantry along the canthomeatal line or the axis of the biopsy needle. Thus, the "optimal" trajectory is both patient-dependent and task-dependent. Moreover, data acquired from non-circular trajectories can be difficult to reconstruct, since the sampling conditions for traditional FBP methods no longer apply.

There is a growing trend in the use of task-based measures in performance assessment (Siewerdsen and Antonuk 1998, Park et al 2010, Reiser and Nishikawa 2010). Such measures have also been used in *prospective task-driven* optimization of system design (Siewerdsen and Jaffray 2000, Prakash et al 2011, Xu et al 2016, Cao et al 2018), regularization in MBIR (Dang et al 2015), and CT data acquisition parameters like dual-energy imaging (Richard and Siewerdsen 2008), tube current modulation (Gang et al 2017a), and fluence-field modulation (Gang et al 2017b). Thus, it is expected that task-

based performance models similarly provide a basis for optimizing the source–detector orbit in CBCT.

Interventional CBCT presents an ideal opportunity to customize orbits to the patient and imaging task for a number of reasons: (1) previous imaging studies are usually available, giving a detailed representation of the patient-specific anatomy; (2) additional information regarding the surgical plan, the location and type of implants or tools, and particular anatomical targets is known prior to the intervention; and (3) the imaging task in interventional procedures tends is relatively well-defined (compared to diagnostic imaging), including the volume of interest and specific image features that need to be identified or localized.

In this chapter, we present a mathematical framework that leverages a model of signal and noise performance in CBCT along with prior knowledge of patient anatomy to predict imaging task performance for different source–detector trajectories. The predictor is integrated into an optimization framework that seeks the source–detector trajectory that maximizes performance. This "task-driven" imaging framework builds upon previous work by Stayman and Siewerdsen (2013), Stayman et al (2015), and Ouadah et al (2017). This chapter details the analytical and algorithmic basis of the framework as well as optimization for multiple tasks that vary in location and / or spatial-frequency content. Subsequent chapters address practical issues of implementation and application of the task-driven imaging approach.

The work appearing in this chapter was reported in the following journal paper: (J. W. Stayman* and S. Capostagno* et al, *J. Med. Imag.,* 6(2), 2019).

*J. W. Stayman and S. Capostagno contributed equally to this work.

4.2. Task-Driven Trajectory Framework

4.2.1. Overview and Proposed Imaging Workflow

CBCT image quality can be highly dependent on patient size, anatomical site, and the presence of interventional hardware in the FOV. Even within a scan for a single patient, the data fidelity can vary widely with orders of magnitude differences in the noise for different measurements. The "task-driven" approach introduces a new imaging workflow in which CBCT scans are defined by the particular patient anatomy, selecting projections that maximize data fidelity for a specific imaging task. In general, some knowledge of patient anatomy is required for prospective trajectory design. Such information is often available in IGI but is typically not used directly by the imaging device.

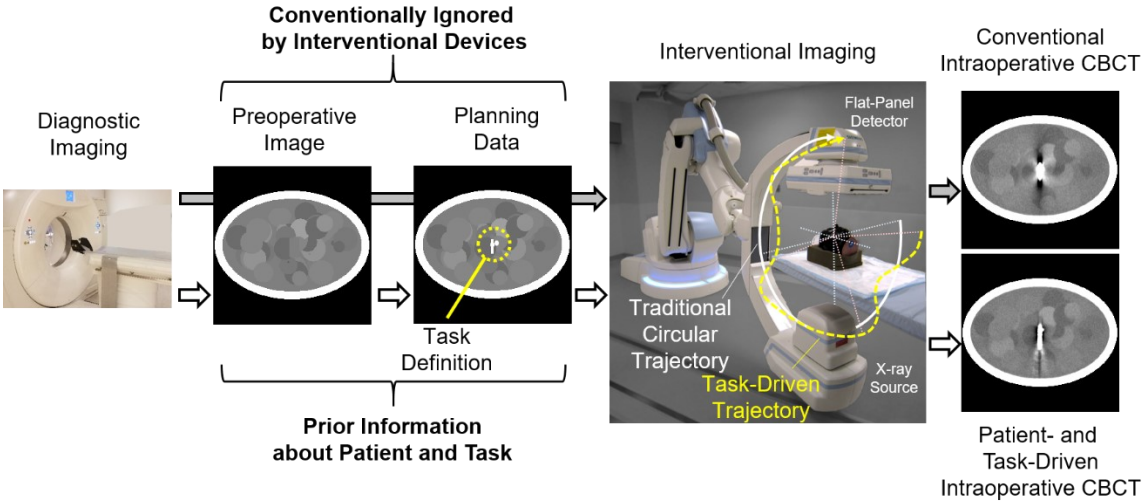

Figure 4.1. Illustration of prospective task-driven imaging using a robotic C-arm. Preoperative data from a diagnostic MDCT scan may be used for both preoperative planning (e.g., defining the interventional approach) as well as prospective design of the intraoperative scan. That is, an initial MDCT may be used to define the location of interest and the anatomical model used in predicting data characteristics like noise in projection data. The proposed task-driven workflow (white arrows) integrates knowledge that is conventionally ignored (gray arrows) directly into acquisition design with the goal of optimized performance.

Figure 4.1 illustrates a proposed imaging workflow that leverages preoperative imaging and planning data and contrasts the proposed methodology with a conventional workflow. Conventionally, a patient's diagnosis is obtained via MDCT (or other modality) to define and plan the interventional approach. In many procedures involving implantation of exogenous devices, the interventional plan includes specification of the hardware required for the procedure (e.g., device size, location for deployment, and model number). Unfortunately, intraoperative image quality is often challenged by the surgical tools and implants delivered during the procedure — often metallic and / or high density — and image quality tends to suffer most in the vicinity of the implant (which is often the ROI where complications are most likely to occur). In a conventional workflow, the imaging system ignores the wealth of knowledge about the patient anatomy, planned hardware delivery, and specifics of the imaging task. In contrast, the task-driven imaging workflow leverages this information to improve performance for pertinent imaging tasks associated with the intervention.

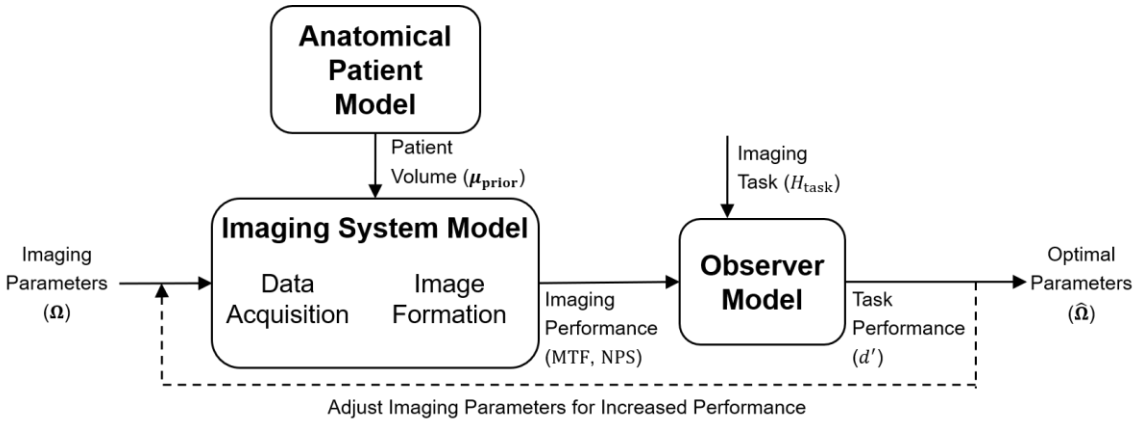

Figure 4.2. Illustration of the task-driven imaging framework.

An overview of the task-driven optimization is illustrated in Figure 4.2, and parameters are summarized in Table 4.1. The approach combines an anatomical model of the patient (as well as planning information), which is important for predicting the fidelity of the projection data, with an imaging system model, which accounts for the entire imaging chain and any parameters to be optimized (e.g., source–detector trajectory). Patient and system models incorporate prediction of imaging performance, including local spatial resolution and noise in the reconstructed image volume. Such measures of imaging performance may then be used to compute task performance using an observer model. With the ability to model the end-to-end system from data collection to observer performance, various parameters may be tuned in an iterative process to find the optimal source–detector trajectory that maximizes imaging performance. The modeling and predictive framework in Figure 4.2 are detailed in the following sections.

Table 4.1. Notation for task-driven source–detector trajectories.

Property	Symbol
Detectability	
Imaging parameters	$\boldsymbol{\Omega}$
Spatial frequencies	$\boldsymbol{f}$
Location of interest	v
Region of interest (ROI)	$\boldsymbol{v}_{\mathbf{ROI}}$
Detectability index	$d'(\boldsymbol{\Omega}; v)$
Modulation transfer function	$\mathrm{MTF}(\boldsymbol{f}, \boldsymbol{\Omega}; v)$
Noise power spectrum	$\mathrm{NPS}(\boldsymbol{f}, \boldsymbol{\Omega}; v)$
Task definition	$H_{\mathrm{task}}(\boldsymbol{f}; v)$
System model	
Projection measurements	$\boldsymbol{y}$
Measurement gain	b_0
Projection operator	$\mathbf{A}$
Image volume	$\boldsymbol{\mu}$
Log-likelihood	$L(\boldsymbol{\mu}; \boldsymbol{y})$
Roughness penalty	$R(\boldsymbol{\mu})$
Regularization strength parameter	β
Performance prediction	
Local impulse response	$\boldsymbol{l}_v$
Local covariance	$\boldsymbol{c}_v$
Unit vector for location v	$\boldsymbol{e}_v$
Diagonal matrix operator	$D\{\cdot\}$
Fourier transform operator	$F\{\cdot\}$
Fourier transform of projection-backprojection operation	$\boldsymbol{L}_v$
Statistical weighting	$\boldsymbol{w}$
Prior patient image	$\boldsymbol{\mu}_{\mathbf{prior}}$
Source–detector trajectory	
Rotation angle	θ
Tilt angle	ϕ

4.2.2. Task-Based Performance Prediction and Optimization

Various mathematical observer models have been used for performance prediction. Gang et al (2011) previously demonstrated basic agreement between human observer performance and a non-prewhitening observer model over a broad range of imaging conditions, therefore this model has been elected to evaluate imaging tasks in this work. Alternative objectives could be considered in future work — e.g., a prewhitening observer model to examine fundamental signal and noise content or a channelized Hoteling observer model to potentially capture aspects more closely related to a human observer. An objective based on large-area transfer characteristics (e.g., contrast-to-noise ratio) captures only the low-frequency performance and would likely miss aspects related to spatial resolution and frequency response. The non-prewhitening model chosen here derives detectability in terms of the local spatial resolution and noise properties of the reconstructed image as well as a task function that specifies the spatial frequencies of interest. The detectability index for the non-prewhitening observer model is written as:

$$d'(\boldsymbol{\Omega}; v) = \left[\frac{\left[\iiint \left(\mathrm{MTF}(\boldsymbol{f}, \boldsymbol{\Omega}; v) \cdot H_{\mathrm{task}}(\boldsymbol{f}; v) \right)^2 df_x df_y df_z \right]^2}{\iiint \mathrm{NPS}(\boldsymbol{f}, \boldsymbol{\Omega}; v) \cdot \left(\mathrm{MTF}(\boldsymbol{f}, \boldsymbol{\Omega}; v) \cdot H_{\mathrm{task}}(\boldsymbol{f}; v) \right)^2 df_x df_y df_z} \right]^{1/2} \tag{4.1}$$

where $\mathrm{MTF}(\boldsymbol{f}, \boldsymbol{\Omega}; v)$ denotes the local modulation transfer function, $\mathrm{NPS}(\boldsymbol{f}, \boldsymbol{\Omega}; v)$ is the local noise-power spectrum, and $H_{\mathrm{task}}(\boldsymbol{f}; v)$ is the task function describing the location of interest (v) and the spatial frequencies of interest ($\boldsymbol{f}$, formed by the difference of Fourier transforms between two stimuli in a binary hypothesis test, such as signal-present vs. signal-absent, or discrimination between two stimuli). The parameter v indicates the locality of the various measures, centered at voxel v within the reconstructed image. The

various quantities associated with image acquisition and / or reconstruction technique are denoted generally as $\boldsymbol{\Omega}$, which in this work refers to the source–detector trajectory.

The detectability index provides an objective for the design of an optimal source–detector orbit. The most straightforward objective that seeks to optimize detectability index for a *single location* in the imaging volume is written as:

$$\widehat{\boldsymbol{\Omega}} = \underset{\boldsymbol{\Omega}\in\boldsymbol{\Omega}_{\mathbf{feasible}}}{\arg\max}\, d'(\boldsymbol{\Omega}; v) \tag{4.2}$$

where the parameter set $\widehat{\boldsymbol{\Omega}}$ that yields the maximum detectability index constrained by the physical or practical limitations ($\boldsymbol{\Omega} \in \boldsymbol{\Omega}_{\mathbf{feasible}}$) is desired. Constraints on the acquisition parameters permit specification of maximum tilt angles achievable by the system as well as limits to avoid collision of the gantry with the patient, table, or other structures.

While optimization with respect to a single location and task may be appropriate for some scenarios, a single-location objective does not consider performance at any other location in the image, leading to solutions that may be highly optimized to a single point and sacrifice image quality everywhere else in the image. As such, *multi-location objectives* are also considered. There are many possible choices for a multi-location objective; however, the principal concern is how to weight the relative importance of performance at different locations in the FOV. Three choices are explored in this work:

1. *Maximum mean detectability* (*maxi-mean*) — in which the average detectability index over an ensemble of locations within a specified ROI, $\boldsymbol{v}_{\mathbf{ROI}}$, is computed and maximized. Mathematically, this objective is written:

$$\widehat{\boldsymbol{\Omega}} = \underset{\boldsymbol{\Omega}\in\boldsymbol{\Omega}_{\mathbf{feasible}}}{\arg\max}\, \underset{v\in\boldsymbol{v}_{\mathbf{ROI}}}{\mathrm{mean}}\{d'(\boldsymbol{\Omega}; v)\} \tag{4.3}$$

The maxi-mean objective treats all performance gains equally throughout the ROI, including potential solutions where detectability is decreased in one region for a larger gain in another region.

2. *Maximum median detectability* (*maxi-median*) — in which the median detectability index over the regional ensemble is maximized. Mathematically:

$$\widehat{\boldsymbol{\Omega}} = \underset{\boldsymbol{\Omega}\in\boldsymbol{\Omega}_{\mathbf{feasible}}}{\arg\max} \underset{v\in\boldsymbol{v}_{\mathbf{ROI}}}{\text{median}}\{d'(\boldsymbol{\Omega}; v)\} \tag{4.4}$$

The maxi-median objective is like the maxi-mean objective, except that it permits larger outliers. For example, overall detectability can be increased at the cost of a significant decrease at a few locations.

3. *Maximum minimum detectability* (*maxi-min*) — in which one seeks to achieve the highest minimum detectability over an ensemble of locations. Mathematically:

$$\widehat{\boldsymbol{\Omega}} = \underset{\boldsymbol{\Omega}\in\boldsymbol{\Omega}_{\mathbf{feasible}}}{\arg\max} \underset{v\in\boldsymbol{v}_{\mathbf{ROI}}}{\text{minimum}}\{d'(\boldsymbol{\Omega}; v)\} \tag{4.5}$$

The maxi-min objective indicates that the location of minimum performance drives the design, and that imaging performance cannot be sacrificed in one location (in the designated ROI) for an improvement in another location.

Both the single-location and multi-location objectives are investigated below. We used the CMA-ES algorithm (Hansen 2006) to estimate the solution to the objective functions. As described previously, in CMA-ES, a population sample size of λ_{CMAES} is randomly drawn according to a multivariate normal distribution at each iteration. The best solutions in the population are used to estimate the local covariance matrix of the objective function in an adaptive manner. The mean, covariance matrix, step size, and evolutionary paths are updated to generate the next population with the goal of maximizing the number of successful samples in each successive population. Updates are repeated until

convergence, defined as the iteration beyond which changes in function evaluation are negligible. A stochastic algorithm is attractive since only function evaluations are required and populations of solutions are used, helping to find global optima in nonlinear and nonconvex objectives. Another attractive feature of CMA-ES is its improved robustness with increased function evaluations (e.g., increasing λ_{CMAES}), which can be tuned to help avoid local optima.

4.2.3. Imaging System and Reconstruction Model

Imaging properties (viz., local spatial resolution and noise) must be predicted to use the performance objectives defined in the previous section. Such predictions are made through an imaging system model that includes both imaging physics and acquisition parameters as well as the reconstruction process. Starting with data acquisition, the following forward model for a CBCT system was adopted, for which mean measurements are modeled as:

$$\bar{y}_i = b_0 \exp\left(-[\mathbf{A}(\boldsymbol{\Omega})\boldsymbol{\mu}]_i\right) \tag{4.6}$$

where the subscript i denotes values associated with the i^{th} measurement in vector $\boldsymbol{y}$, b_0 denotes a measurement gain (e.g., unattenuated x-ray fluence and detector sensitivity), $\boldsymbol{\mu}$ is a vector of attenuation values specifying the image volume, and $\mathbf{A}$ represents the projection operation for a particular trajectory, parameterized by the vector $\boldsymbol{\Omega}$. The specific parameterization of $\boldsymbol{\Omega}$ is discussed below.

Traditional analytic reconstruction methods are challenged by orbits that deviate from standard designs (e.g., circular and helical). However, MBIR methods are straightforward to apply to unusual and even incomplete data orbits — providing the "best" possible estimates given the data that was collected. Thus, a statistically motivated MBIR

method was adopted for this work. Presuming a Poisson noise model for the measurements, the following PL estimator may be written:

$$\widehat{\boldsymbol{\mu}} = \arg\max_{\boldsymbol{\mu}} L(\boldsymbol{\mu}; \boldsymbol{y}) - R(\boldsymbol{\mu}) \tag{4.7}$$

where $L(\boldsymbol{\mu}; \boldsymbol{y}) = \sum_{i=1}^{N} y_i \log(b_0 \exp(-[\mathbf{A}(\boldsymbol{\Omega})\boldsymbol{\mu}]_i)) - b_0 \exp(-[\mathbf{A}(\boldsymbol{\Omega})\boldsymbol{\mu}]_i)$ and denotes the log-likelihood function, which is a function of the pre-log transformed measurements, $\boldsymbol{y}$, and $R(\boldsymbol{\mu}) = \beta \boldsymbol{\mu}^T \mathbf{R} \boldsymbol{\mu}$, representing a roughness penalty used to control noise in the reconstruction with a strength parameter β. We used a quadratic penalty that is specified by the matrix $\mathbf{R}$, a constant matrix that defines how voxels are combined and penalized such that $R(\boldsymbol{\mu}) = \frac{1}{2} \sum_j \sum_k w_{j,k} (\mu_j - \mu_k)^2$, where $w_{j,k} = 1$ for the 6 nearest neighbors in 3D space and 0 otherwise. While there are many more sophisticated regularization schemes, this particular choice of roughness penalty is well-suited to previously developed imaging performance predictors (Fessler and Rogers 1996).

Another advantage of the PL framework is that arbitrary source–detector trajectories may be reconstructed without modification of the underlying algorithm used to solve Equation (4.2). In contrast, many direct reconstruction approaches will not implicitly handle noncircular or non-helical trajectories without substantial modification or re-derivation of the algorithm. In this work, we solved Equation (4.7) iteratively using the ordered subsets, separable quadratic surrogate approach discussed in Erdogan and Fessler (1999). At each iteration, all voxels were updated simultaneously, requiring one forward-projection and one backprojection to compute the likelihood gradient. The penalty gradient and curvature were computed directly from the image. In experiments described below, the PL estimator was run to convergence using a specific number of iterations and a zero image was used for initialization.

4.2.4. Parameterization of the Source–Detector Trajectory

As described above, the system geometry associated with the source–detector trajectory is parameterized by the vector $\boldsymbol{\Omega}$. Parameterization of the trajectory can take many possible forms that depend on the capabilities of the imaging system. Two parameterizations of the orbit are considered in this work, concentrating on orbits that sample a sphere around a common center of rotation whose x-ray source positions are specified by the coordinate pair (θ, ϕ) with rotation angle θ and tilt angle ϕ. Other geometric parameters, such as SDD and translations remained fixed in the current studies. The experiments described below used orbits that are continuous functions of the rotation angle θ such that the gantry tilt ϕ is defined by the rotation angle.

A simple parameterization of the source–detector trajectory involves *periodic basis functions* using constant, sine, and cosine terms such that:

$$\phi(\theta) = \sum_{i=1}^{K} \Omega_i b_i(\theta) \tag{4.8}$$

with $b_1(\theta) = 1, b_2(\theta) = \sin\theta, b_3(\theta) = \cos\theta, b_4(\theta) = \sin 2\theta$, ..., as shown in Figure 5.3. Both short scans and full 360° orbits may be defined using this scheme with, for example, uniform sampling of the rotation angle θ. Periodic basis functions provide a low-dimensional space to perform the orbital optimization. Because there are practical limitations of the orbit (e.g., collision with the table or patient), hard constraints are applied on the orbit by limiting the maximum tilt angle.

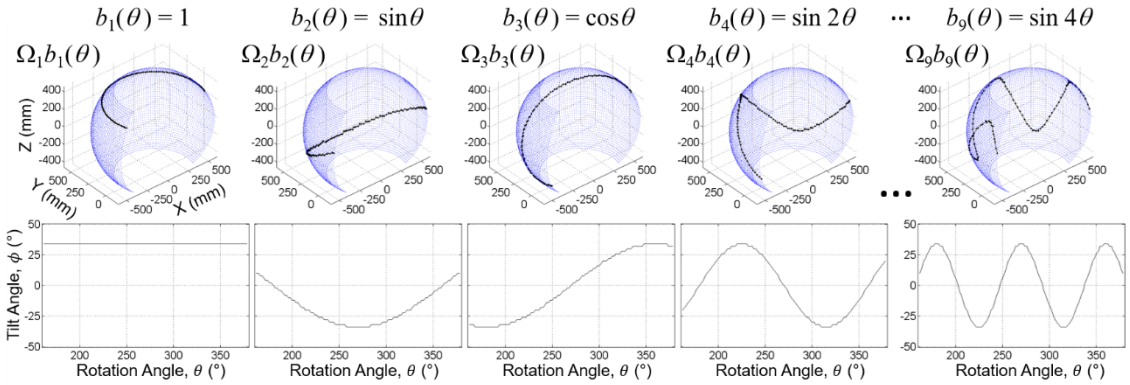

Figure 4.3. Illustration of a short scan orbit parameterized by constant, sine, and cosine basis functions.

A second parameterization of the source–detector trajectory uses *b-spline basis functions*, where the individual parameters Ω_i define a limited set of knot locations. Each knot is fixed to a single rotation angle with equal spacing throughout the orbit and allowed to vary in tilt angle. Using b-spline basis functions may more easily admit non-periodic designs while maintaining relatively low dimensionality. The orbit may be similarly constrained to those feasible with a given C-arm gantry and to avoid table collision. Using either the periodic or b-spline basis functions as presented here not only reduces the dimensionality of the parameterization but also imposes the additional constraint that the trajectory be smoothly changing, which is beneficial for practical implementation of a task-driven orbit from a mechanical point of view.

4.2.5. Imaging Performance Prediction and Anatomical Modeling

For prospective design of source–detector trajectories, the imaging performance must be estimated for various orbits. While exhaustive simulation of projection data, reconstruction, and assessment is possible, it is more practical to estimate the imaging properties of the reconstruction directly. Previous work derived closed-form

approximations for local spatial resolution (Fessler and Rogers 1996) and noise (Fessler 1996) in PL reconstructions of the type in Equation (4.7). Specifically, the local impulse response, $\boldsymbol{l_v}$, and local covariance, $\boldsymbol{c_v}$, may be approximated as:

$$\boldsymbol{l_v} \approx [\mathbf{A}(\boldsymbol{\Omega})^{\mathrm{T}}\mathrm{D}\{\overline{\boldsymbol{y}}\}\mathbf{A}(\boldsymbol{\Omega}) + \beta\mathbf{R}]^{-1}\mathbf{A}(\boldsymbol{\Omega})^{\mathrm{T}}\mathrm{D}\{\overline{\boldsymbol{y}}\}\mathbf{A}(\boldsymbol{\Omega})\boldsymbol{e_v} \tag{4.9}$$

$$\boldsymbol{c_v} \approx [\mathbf{A}(\boldsymbol{\Omega})^{\mathrm{T}}\mathrm{D}\{\overline{\boldsymbol{y}}\}\mathbf{A}(\boldsymbol{\Omega}) + \beta\mathbf{R}]^{-1}[\mathbf{A}(\boldsymbol{\Omega})^{\mathrm{T}}\mathrm{D}\{\overline{\boldsymbol{y}}\}\mathbf{A}(\boldsymbol{\Omega})][\mathbf{A}(\boldsymbol{\Omega})^{\mathrm{T}}\mathrm{D}\{\overline{\boldsymbol{y}}\}\mathbf{A}(\boldsymbol{\Omega}) + \beta\mathbf{R}]^{-1}\boldsymbol{e_v} \tag{4.10}$$

where $\boldsymbol{e_v}$ denotes the v^{th} unit vector (all zeros except for the v^{th} location, which is unity), and $\mathrm{D}\{\cdot\}$ denotes the operator that places its vector argument on the diagonal of a matrix. Note that Equations (4.9) and (4.10) capture the various dependencies of the reconstructed image on system geometry ($\mathbf{A}(\boldsymbol{\Omega})$), regularization ($\beta\mathbf{R}$), location ($v$), and the patient anatomy via projections ($\boldsymbol{y}$) of the attenuation distribution ($\boldsymbol{\mu}_{\mathbf{prior}}$) via Equation (4.6). Recent work (Wang et al 2017) extended these predictors to non-ideal detectors and validated predictions in flat-panel CBCT reconstructions.

Using Equations (4.9) and (4.10), local noise and resolution properties may be predicted prospectively given knowledge of $\boldsymbol{\mu}_{\mathbf{prior}}$ and a system model through which $\boldsymbol{y}$ may be simulated. As discussed previously, preoperative MDCT (or CBCT acquired earlier in the procedure) can provide an anatomical model for prediction, recognizing that the model may be mismatched to the intraoperative data for a number of reasons. First is registration of the previous image to the current measurements. For many anatomical sites (e.g., intracranial), a rigid registration may be sufficient, allowing the designed trajectory to be transformed into the intraoperative patient coordinates using, for example, 3D–2D registration as in Uneri et al (2013). In this chapter, we presume that an accurate registration is achieved and focus on the subsequent improvements in imaging performance gained from a task-driven design of the orbit.

Other mismatches in patient anatomy include the delivery of hardware and changes in anatomy that might be found in the intraoperative data. Again, the workflow presented in Figure 4.1 offers a means to model implanted hardware. Since the preoperative scan is often used for planning — e.g., to determine the size and location of an implant — it is relatively straightforward to include these attenuation changes in a modified anatomical model. Modeling of significant attenuation changes like metal implants is important since such changes have a significant impact on the statistics of the data (i.e., the diagonal weighting $\mathrm{D}\{\bar{\boldsymbol{y}}\}$ in the predictors). In contrast, soft-tissue differences like hemorrhage (an important complication one would like to detect) have a relatively small effect on noise in the projection data, suggesting that those more subtle changes do not need to be modeled explicitly for the proposed trajectory design. In this work, only changes associated with highly attenuating implants were modeled and not the soft-tissue changes that the radiologist seeks to detect.

4.2.6. Approximate Predictors and Practical Implementation

While the predictors in Equations (4.9) and (4.10) describe the basic imaging performance metrics required for evaluation of detectability index, they contain large matrix inversions that challenge efficient computation of the local spatial resolution and noise for such a large optimization space. Previous work used local Fourier approximation (Qi and Leahy 1999, Stayman and Fessler 2000) to yield approximate forms for the local $\mathrm{MTF}(\boldsymbol{f}, \boldsymbol{\Omega}; v)$ and local $\mathrm{NPS}(\boldsymbol{f}, \boldsymbol{\Omega}; v)$ as:

$$\mathrm{MTF}(\boldsymbol{f}, \boldsymbol{\Omega}; v) = \mathrm{F}\{\boldsymbol{l}_v\} \approx \frac{\mathrm{F}\{\mathbf{A}(\boldsymbol{\Omega})^{\mathrm{T}}\mathrm{D}\{\bar{\boldsymbol{y}}\}\mathbf{A}(\boldsymbol{\Omega})\boldsymbol{e}_v\}}{\mathrm{F}\{\mathbf{A}(\boldsymbol{\Omega})^{\mathrm{T}}\mathrm{D}\{\bar{\boldsymbol{y}}\}\mathbf{A}(\boldsymbol{\Omega})\boldsymbol{e}_v + \beta\mathbf{R}\boldsymbol{e}_v\}} \tag{4.11}$$

$$\mathrm{NPS}(\boldsymbol{f},\boldsymbol{\Omega};v)=\mathrm{F}\{\boldsymbol{c_v}\}\approx\frac{\mathrm{F}\{\mathbf{A}(\boldsymbol{\Omega})^{\mathrm{T}}\mathrm{D}\{\overline{\boldsymbol{y}}\}\mathbf{A}(\boldsymbol{\Omega})\boldsymbol{e_v}\}}{|\mathrm{F}\{\mathbf{A}(\boldsymbol{\Omega})^{\mathrm{T}}\mathrm{D}\{\overline{\boldsymbol{y}}\}\mathbf{A}(\boldsymbol{\Omega})\boldsymbol{e_v}+\beta\mathbf{R}\boldsymbol{e_v}\}|^2} \tag{4.12}$$

where $\mathrm{F}\{\cdot\}$ denotes the 3D discrete Fourier transform and the division is element-by-element. While Equations (4.11) and (4.12) eliminate the computationally expensive matrix inverse, they still require repeated computations involving projection, backprojection, and Fourier transforms. Following Stayman and Fessler (2004), several observations permit additional speedups for practical implementation. In particular, one may compute the regularization term once for a shift-invariant penalty, and only local volumes within an $N\times N\times N$ ROI of the voxel v are required. Repeated calculation of the Fourier transform of the weighted projection-backprojection ($\mathrm{F}\{\mathbf{A}(\boldsymbol{\Omega})^{\mathrm{T}}\mathrm{D}\{\overline{\boldsymbol{y}}\}\mathbf{A}(\boldsymbol{\Omega})\boldsymbol{e_v}\}$) represents a significant computational burden in direct computations of Equations (4.11) and (4.12). However, efficient calculation is possible by leveraging the fact that the projection-backprojection term is linear in the diagonal weighting. Specifically, it may be written

$$\mathrm{F}\{\mathbf{A}(\boldsymbol{\Omega})^{\mathrm{T}}\mathrm{D}\{\boldsymbol{w}\}\mathbf{A}(\boldsymbol{\Omega})\boldsymbol{e_v}\}=\boldsymbol{L_v}\boldsymbol{w} \tag{4.13}$$

which means that a linear operator, $\boldsymbol{L_v}$, may be precomputed and stored for fast application. Additionally, noting that the projection of a single point $\mathbf{A}(\boldsymbol{\Omega})\boldsymbol{e_v}$ is sparse with nonzero values located at about one point per projection view, one may precompute a much smaller $\boldsymbol{L_v}$ that is only $N^3\times N_{\mathrm{views}}$ for each location v. One may form $\boldsymbol{L_v}$ by substituting $\boldsymbol{w}=\boldsymbol{e_k}$ for $k=1,\dots,N_{\mathrm{views}}$ to build up $\boldsymbol{L_v}$ column by column. Thus, as long as the number of potential view angles is sufficiently small (e.g., one needs to store N_{views} Fourier volumes of $N\times N\times N$), this *precomputation approach* becomes tractable without additional modification.

For a large number of projection views, memory limitations may challenge the precomputation approach. In the spirit of Schmitt and Fessler (2015) and Schmitt et al (2017), one can also recognize that $\boldsymbol{L}_v$ may be replaced with an analytic form. That is, each column of $\boldsymbol{L}_v$ is the Fourier transform of the backprojection of a single projection view consisting of a single point projection. The backprojection of a point is a line in 3D space through the original location v connecting both the source and detector. The Fourier transform of this line is a Fourier plane centered at the origin at the same angle as the line. However, for a discrete system model with finite-sized detector elements and voxels, the Fourier plane will not be infinitely thin. While Schmitt derived closed-form analytic expressions that specify the form and profile through this plane, this work uses a plane whose profile is Gaussian with a width specified by fitting an empirical calculation of the Fourier-domain projection-backprojection, resulting in a very fast analytic form for $\boldsymbol{L}_v$ that may be computed given the location v and the coordinates of the x-ray source. This *on-the-fly computation approach* is another efficient alternative to calculation of Equations (4.11) and (4.12). The difference between the precomputation and on-the-fly approaches is largely computational (without significant difference in noise and resolution estimates) and represents a classic computing trade-off between storage and speed. Since both approaches are potentially useful, both are presented in studies below.

4.3. Experimental Methods

Three experiments were conducted to investigate various aspects of the proposed task-driven trajectory design process, summarized in Figure 4.4. Each experiment is detailed in the following subsections.

Two simulation configurations were used in these studies. Studies that investigated basic trajectory design behavior used a *compact geometry* to better illustrate dependencies on location and task, specifically: SDD = 700 mm and SAD = 350 mm. A flat-panel detector with 560 × 1000 pixels at 1 mm pitch was simulated. A second system geometry emulated a *C-arm geometry* with SDD = 1200 mm, SAD = 800 mm, and a 960 × 1240 pixel detector at 0.308 mm pitch.

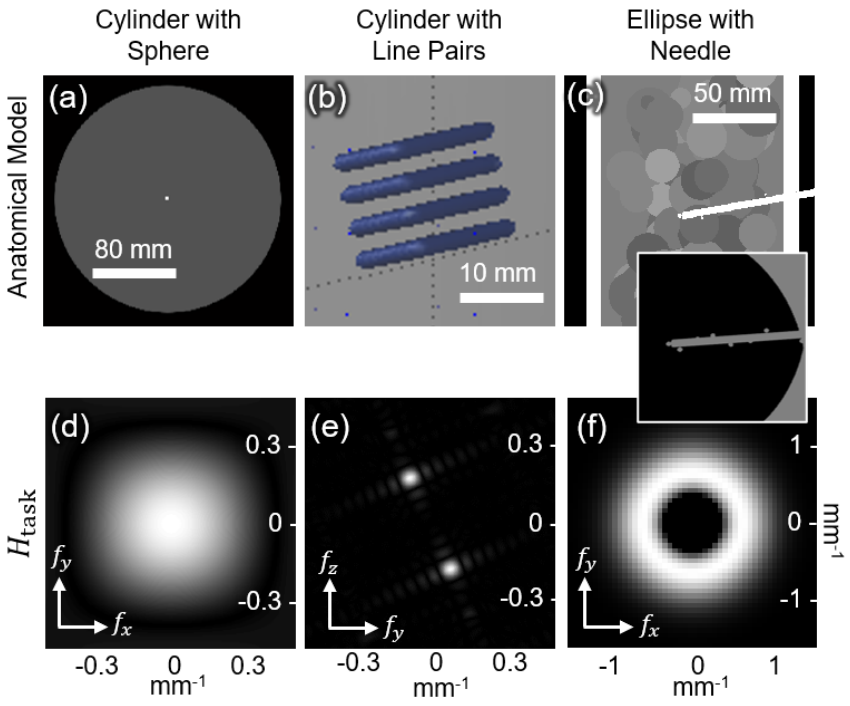

Figure 4.4. Summary of the three simple scenarios studied. Cases are distinguished by the stimulus and anatomical model (a–c) and the frequency-domain task function (d–f). Different task functions were explored, including Gaussian detection, line pair discrimination, and mid-frequency discrimination.

4.3.1. Location Dependence: A Sphere in a Cylinder

The first experiment used a simple object to illustrate location dependence. Specifically, a 20 cm diameter cylinder was simulated with 1 mm voxels and attenuation coefficient $\mu = 0.05$ mm^{-1} (Figure 4.4a). A relatively high attenuation was used to exaggerate location-dependent effects. Two 3 mm spheres with 0.03 mm^{-1} contrast relative to background were added to the cylinder centered in the axial plane at both the central slice and 15 cm below the central slice. This experiment used the compact geometry, and bare-beam fluence was set to 1×10^5 photons per pixel.

Trajectory design was conducted using the single-location objective in Equation (4.2) using nine periodic basis functions given by Equation (4.8), constrained to tilts in the range $\phi = -50°$ to 50°, and with rotation angles $\theta = 1°$ to 360° with 1° increments. The task function in the objective corresponded to the 3 mm spherical stimulus (Figure 4.4d) and optimization was performed for each stimulus location individually. For computation of detectability, the on-the-fly method was applied with statistical weights ($\boldsymbol{w}$, calculated as described in Section 4.2.6) sampled over 110 equally spaced rotation angles and 51 equally spaced tilt angles. To estimate the solution to Equation (4.2), the CMA-ES optimization was applied using $\lambda_{\mathrm{CMAES}} = 40$ without restarts due to the simplicity of the search space.

PL reconstruction using the optimized trajectory found for each sphere location (central slice and 15 cm below the central slice) was performed using dynamically relaxed ordered subsets with the number of subsets changing every five iterations through the sequence {54, 24, 12, 6, 4, 2, 1} for a total of 50 iterations. This schedule was chosen to accelerate convergence of the simple object. Quadratic regularization with a regularization

strength of $\beta = 1\times10^6$ was applied using 1 mm isotropic voxels on a 240 × 240 × 500 grid. Regularization strength was empirically selected based on visual assessment of noise and resolution in the images.

4.3.2. Task Dependence: Line Pairs in a Cylinder

The second experiment used the same 20 cm cylinder as the first experiment — in this case involving a line-pair stimulus placed in the center of the central slice. Specifically, the line pairs were a 20 × 20 × 20 mm^3 cube with 2 lp / mm and a contrast of 0.015 mm^{-1} relative to background. The cube was rotated 20° around the *x* axis to angulate the features relative to the coordinate axes (Figure 4.4b).

Trajectory design was performed using the single-location objective, nine periodic bases, and the same angular sampling, constraints, geometry, and bare-beam fluence as in the first experiment. Two task functions were examined: (1) the 3 mm sphere detection task from the first experiment; and (2) a line pair discrimination task. The discrimination task was defined as the difference between the true rotated line pair stimulus and a stimulus consisting of an identically rotated solid cube of the same dimensions and attenuation — i.e., a binary hypothesis of line pairs "present" or "absent" (Figure 4.4e). As in the first experiment, on-the-fly detectability computations were adopted, and the same CMA-ES parameters used. PL ordered-subset reconstructions were computed as in the first experiment, using the {54, 24, 12, 6, 4, 2, 1} schedule, 50 iterations to reach convergence, $\beta = 1\times10^6$, and 1 mm isotropic voxels on a 240 × 240 × 500 grid.

4.3.3. Multiple Locations: Elliptical Cylinder with a Needle

The third experiment examined task-driven imaging in a situation for which the precise task location is unknown. Several potential task locations were chosen, and a single trajectory was solved that maximized a multi-location objective. A digital elliptical cylinder phantom was modeled with major and minor axis diameters of 25 and 17.5 cm, respectively, and height 25 cm. The elliptical cylinder had a 12 mm outer shell with $\mu = 0.04$ mm^{-1} and the core was filled with low contrast spheres of diameter 80 mm and $\mu \in [0.0175\ 0.0225]$ mm^{-1}. A high contrast cylinder ($\mu = 0.2$ mm^{-1}) with diameter 5 mm and length 75 mm was added at a 10° angle in the central coronal plane to simulate a needle entering the body (shown in Figure 4.4c). Nine 8 mm spheres with 0.08 mm^{-1} contrast were added along the length and tip of the cylinder and all nine locations were used for multi-location optimization. The C-arm geometry was used with bare-beam fluence lowered to 1×10^4 photons per pixel to mimic scanning at lower dosage.

Trajectory design was first performed for each task location using the single-location objective in Equation (4.2), followed by the three multi-location objectives in Equations (4.3), (4.4), and (4.5). B-spline basis functions were used with eight equally spaced knots, and the trajectories were constrained to tilt angles in the range $\phi = -30°$ to 30° and rotation angles $\theta = 1°$ to 360°. The task function at all nine locations consisted of mid-frequency content (Figure 4.4f) corresponding to the discrimination of a single object from two separate objects (needle and sphere) as described in the ICRU Report 54 (Sharp et al 1996). The precomputation approach was used with $\boldsymbol{w}$ sampled over 72 equally spaced rotation angles and 13 equally spaced tilt angles to compute detectability. The CMA-ES optimization algorithm was used to estimate $\widehat{\boldsymbol{\Omega}}$ using $\lambda_{\mathrm{CMAES}} = 200$ with six

restarts and random initialization to ensure that the optimal detectability values were achieved due to the more complicated search space compared to the previous two experiments.

Quadratic PL reconstructions for the nominal circular orbit, nine independent single-location optimizations, and three variations of multi-location optimization were performed using 10 ordered subsets over 200 iterations. The total number of iterations was increased and number of subsets decreased from previous experiments to achieve stability in convergence of the structurally more complex object. Regularization strength β was set to $1\times10^{5.5}$ to decrease noise in the highly attenuating object, and 0.5 mm isotropic voxels were used in a $512\times\ 512 \times 512$ grid.

To illustrate the convergence of the CMA-ES algorithm, the optimization for a single sphere was computed as described above, using a circular orbit for initialization as opposed to random initialization. Detectability index and the associated reconstructed image were compared for the initial circular orbit, an intermediate (suboptimal) orbit, and the resulting optimal orbit.

4.4. Results

4.4.1. Location Dependence: A Sphere in a Cylinder

Results from the first experiment are summarized in Figure 4.5. Task-driven source trajectories are shown for the cylindrical object and two optimizations: maximum detectability of the spherical stimulus at Location #1 (Figure 4.5b) and Location #2 (Figure 4.5c). Source orbits are shown for each case in magenta as well as a sampled sphere of all possible source locations (blue dots). Note that the designed orbits suggest that a

simple equatorial source trajectory around each stimulus is optimal for detection of that stimulus. Reconstructions using the two orbits confirms that conspicuity of each sphere is maximized for such an equatorial orbit, with reduced detectability for the stimulus in the location that was not optimized. That is, the stimulus at Location #2 is more difficult to detect when using the orbit designed to maximize detectability at Location #1, and vice versa.

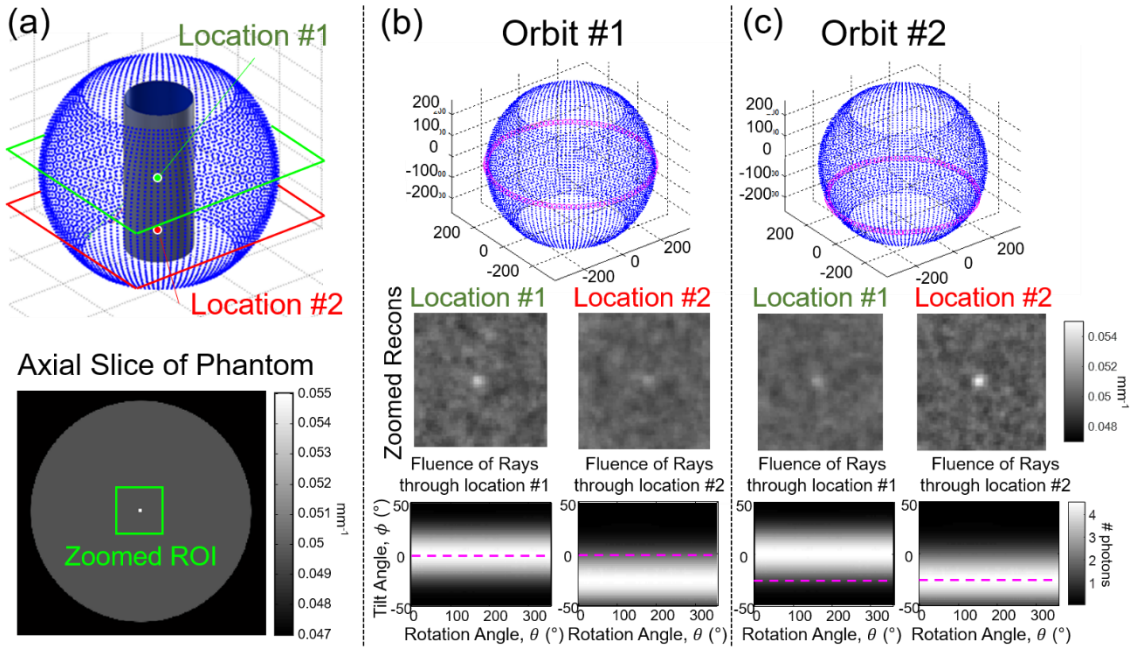

Figure 4.5. Location-dependence of task-driven orbits. (a) Spherical stimuli were placed at the center (Location #1) and 15 cm below (Location #2) in a cylindrical object. (b) Task-driven trajectory design for the sphere detection task at Location #1. (c) Task-driven design for the same task at Location #2. Sample reconstructions and the fluence through each location for all potential views (analogous to the statistical weighting) are shown. Optimal orbits are identified in magenta.

The simple, idealized simulation presented here offers basic intuition to the optimization by considering the fluence through each stimulus location for all potential views. Fluence is equal to the statistical weighting ($\boldsymbol{w}$ in Equation (4.13)) and it is seen that the orbit (dashed magenta line) in each case maximizes fluence through the target location,

thereby maximizing data fidelity by selecting projection views with the shortest path length through the object. This result illustrates the importance of location in task-driven designs and shows that using a single-location objective can maximize task performance at a given location but may do so at the cost of decreased performance at other locations.

4.4.2. Task Dependence: Line Pairs in a Cylinder

The results for a task with strong directional dependence (a line-pair stimulus within a cylinder) are summarized in Figure 4.6. Single-location task-driven designs were performed for two tasks: the sphere detection task from Section 4.3.1 (Figure 4.6b) and a discrimination task corresponding to the frequency content and angulation of the line-pair stimulus (Figure 4.6c). For the task function corresponding to the line-pair stimulus, the task-driven orbit (Orbit A) is tilted to match the angulation of the line-pair stimulus. Example reconstructions illustrate that the task-driven design outperforms the nominal orbit (Orbit S), showing increased noise between the line pairs for the trajectory optimized for the spherical task (Figure 4.6b) and improved discrimination of line pairs for the orbit optimized according to the line-pair task (Figure 4.6c).

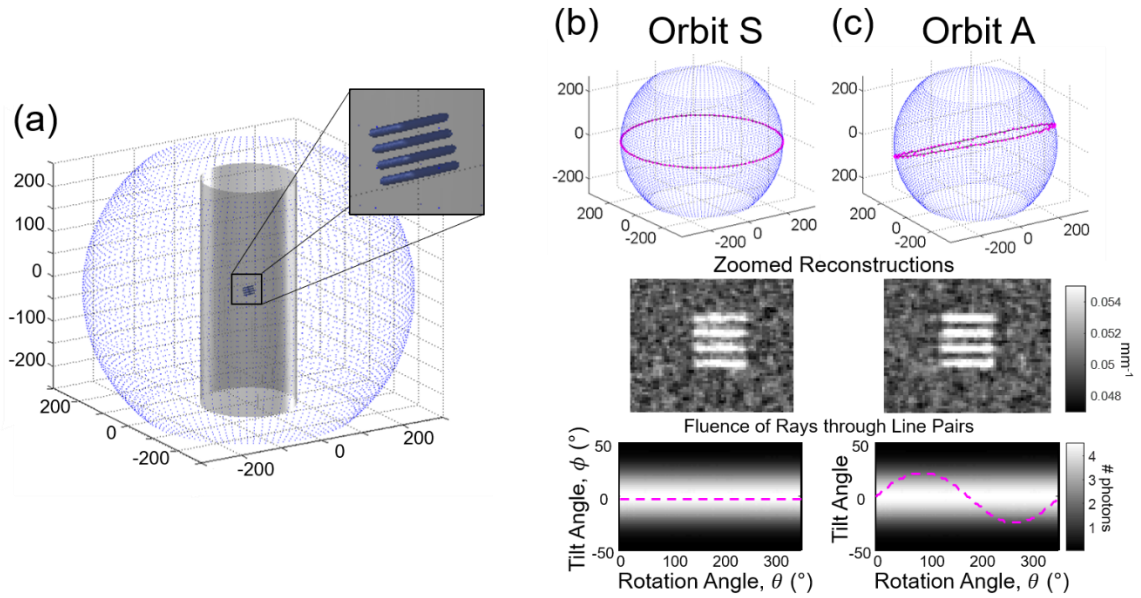

Figure 4.6. Task-dependence of task-driven orbits. (a) Line pair stimuli are placed at the center of a cylindrical object. (b) Task-driven trajectory design for the sphere detection task (Orbit S, not optimal for this object). (c) Task-driven design for an angulated line-pair discrimination task (Orbit A). Sample reconstructions and the fluence through each location for all potential views are shown. Orbits are identified in magenta.

4.4.3. Multiple Locations: Elliptical Cylinder with a Needle

Figure 4.7 summarizes the task-driven trajectories resulting from optimization with respect to a single-location objective (in which d' is optimized for each location independently), and for the three variations of a multi-location objective (maxi-mean, maxi-median, and maxi-min shown in Equations (4.3)–(4.5), in which d' is optimized over all locations simultaneously). The fluence through the stimulus location for all potential views is shown for each of the nine task locations with the optimal orbits shown in magenta. The orbits resulting from a single-location objective are shown in the left-most column, and the single orbit resulting from a multi-location objective is shown in the three right columns for the maxi-mean, maxi-median, and maxi-min objectives for all nine locations.

The single-location objective shows a different orbit for each location, which can be considered the best possible trajectory for each location. Note that at some of the locations the tilt angle differs for the starting and ending views (i.e., Locations #4, #5, and #7). The 2-dimensional b-spline basis function representing the source trajectory was not constrained to be equal at the start and end vertices, allowing a discontinuity. For these three cases, an orbit with a discontinuity produced a higher d' value at the task location. It may be theorized that allowing discontinuities at any point in the orbit (not only at start and end vertices) might increase d'*;* however, doing so loses the advantage of a low-dimensional parametrization and increases the difficulty of implementation on a robotic C-arm.

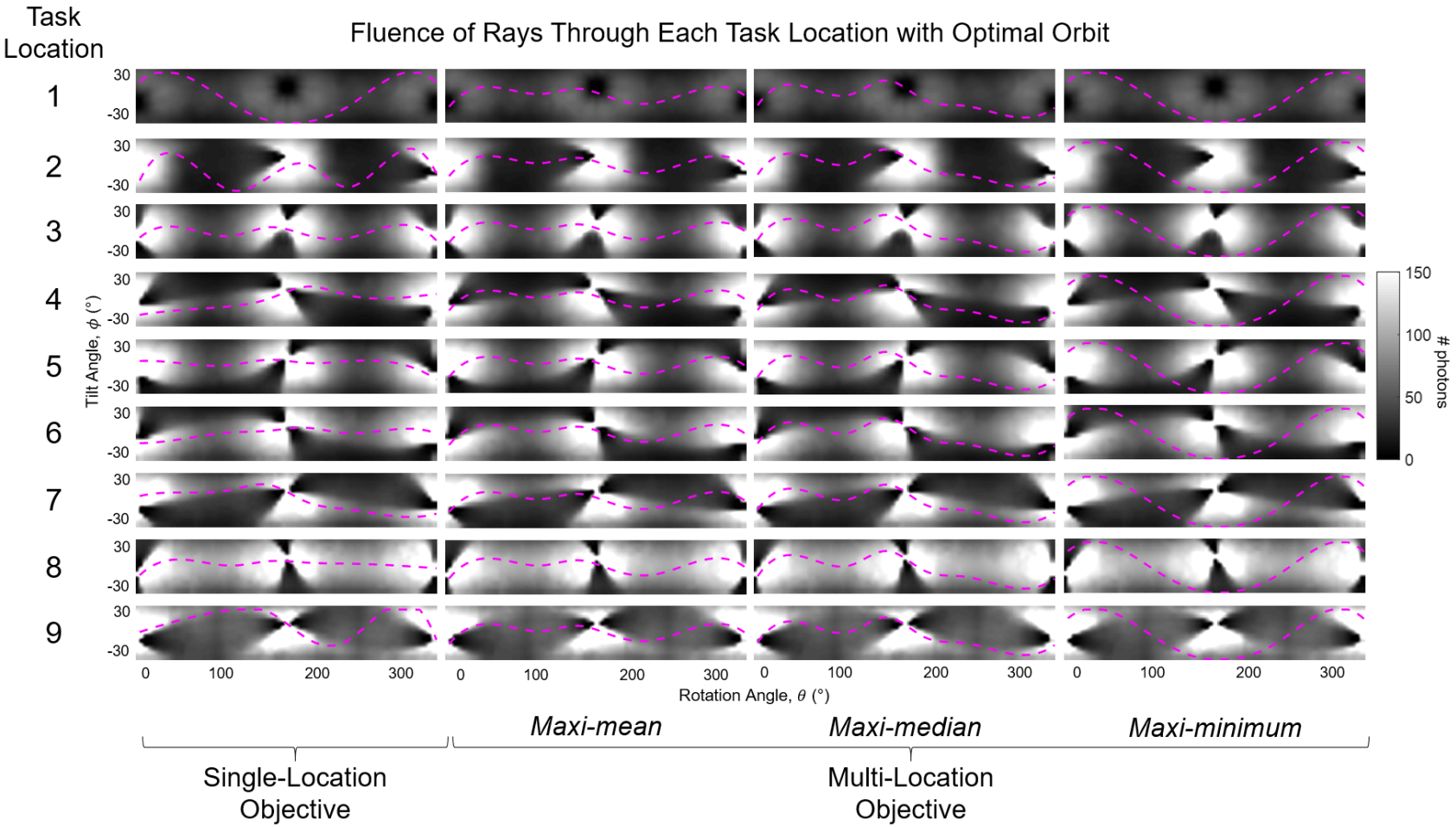

Figure 4.7. Comparison of multi-location and single-location objectives. The task-driven trajectory resulting for each case is shown overlaid on the statistical weights for all source locations at each task location (#1-9). Using a single-location objective shows the ideal task-driven trajectory for each location.

When comparing the three multi-location objectives (in which a single trajectory is generated for all stimulus locations), each objective function yielded a different result, as expected. The trajectory generated for the maxi-median objective was dictated by the median d' value, which in this case corresponded to Location #3 for the optimal trajectory. The range of d' values after optimization are shown in Figure 4.8a. Note that the orbit is not the same as that for Location #3 achieved when using a single-location objective. Further changes to the orbit would cause all d' values to shift, which would generate a new median value that does not maximize the objective function. The maxi-min objective was similarly driven by a single location; Location #1. Location #1 was at the tip of the needle and was subsequently obscured by the angulated needle to some extent at all possible views. Its location resulted in the lowest fluence compared to all other locations for all possible views. Since the d' value at Location #1 was significantly smaller than values at Locations #2-9 due to the lower fluence, it remained the minimum d' value for all trajectories examined during optimization, resulting in an equivalent optimization as when using a single-location objective at Location #1. In contrast, all locations jointly drove the orbit for the maxi-mean objective, and no single location skewed the result.

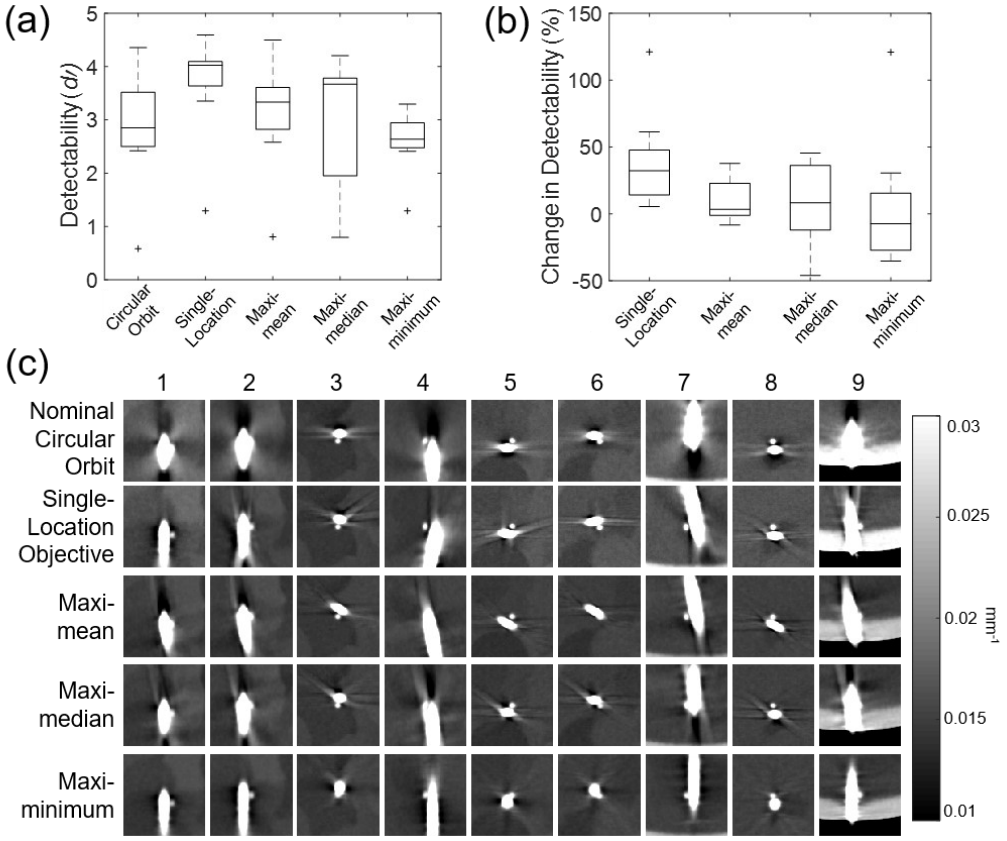

Figure 4.8. Optimization for multiple task locations. (a) Boxplots showing detectability index for the nine locations for a circular orbit, a single-location objective, maxi-mean, maxi-median, and maxi-min objective functions. On each box, the central line indicates the median, and the bottom and top edges of the box indicate the 25th and 75th percentiles, respectively. The whiskers indicate the range of the data excluding outliers, which are indicated with the '+' symbol. (b) Boxplots showing the percent change in detectability from a nominal circular orbit after optimization at all nine locations for the single-location objective function and the three multi-location objective functions. (c) The resulting image for each orbit in a region around each stimulus location, demonstrating improved visualization of small spheres placed adjacent to a high contrast cylindrical 'needle.' Corresponding images from a nominal circular orbit are shown for comparison in the top row.

Figure 4.8a shows detectability index for the nine task locations corresponding to a circular trajectory, using a single-location objective, and using the three multi-location objective functions. The single-location objective is seen to provide the highest d' value and represents the upper limit on improvement in d'. The respective advantage of each multi-location objective function is evident with maxi-mean having the highest mean d'

value at 3.1, maxi-median having the highest median d' value at 3.7, and maxi-min having the highest minimum d' value at 1.3. Figure 4.8b shows the percent increase (or decrease) in d' compared to the location-matched d' value for a circular orbit. For a single-location objective, all d' values increase, ranging from 5.5% at Location #8 to 121.1% at Location #1. In contrast, for all three multi-location objectives there are locations that exhibit a decrease in detectability. For maxi-mean, the change in d' ranges from -8.4% at Location #4 to +37.7% at Location #1. For maxi-median, the range is from -46.1% at Location #4 to +45.4% at Location #9. For maxi-min, the range is from -35.4% at Location #3 to +120.9% at Location #1.

The reconstructed image in the region around each stimulus is shown for each orbit in Figure 4.8c, as well as for a nominal circular orbit for comparison (top row). Either the axial, coronal, or sagittal plane was chosen at each location for visual representation of improvements, although the reconstructed plane could be arbitrary. Improvements are particularly apparent for Locations #2, #7, and #9.

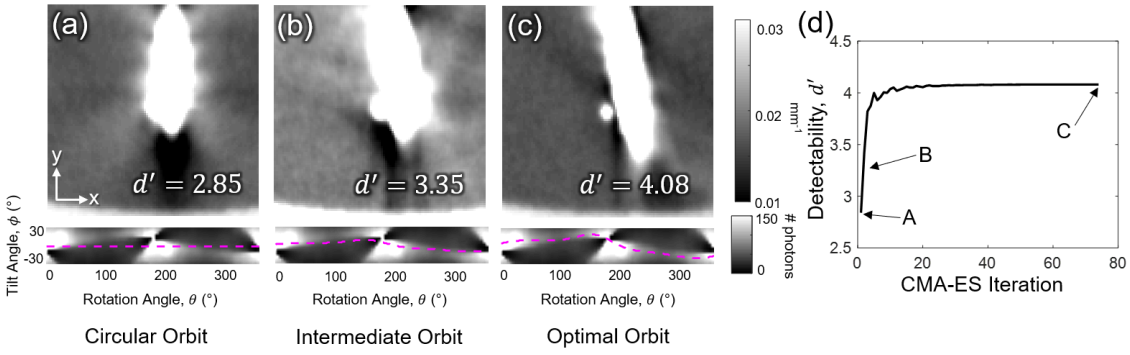

Figure 4.9. Convergence of the optimal orbit at Location #7. (a) Image reconstructed from a circular orbit (inset below the image, plotted in magenta overlaid on a map of statistical weights). (b) Image reconstructed from a suboptimal orbit representing an intermediate solution between a circular orbit and the optimal orbit. (c) Image reconstructed from the optimal orbit for this task and object model. (d) Convergence of the CMA-ES optimization showing detectability (d') vs iteration. The d' value for the orbits shown in (a–c) are indicated on the plot.

Figure 4.9 demonstrates convergence of the CMA-ES algorithm for the single-location objective performed for the task defined at Location #7. Images reconstructed for a circular orbit, suboptimal intermediate orbit, and optimal task-driven orbit are shown in Figure 4.9a–c. The d' value for each was 2.85, 3.35, and 4.08, respectively. Visualization of the spherical stimulus alongside the highly attenuating needle is progressively improved as the algorithm converges on the optimal orbit, consistent with the increase in d'. A plot of detectability index vs. iteration is shown in Figure 4.9d, showing fairly smooth convergence for the CMA-ES optimizer when initialized with the circular orbit. The d' values corresponding to the three orbits (A-B-C) in Figure 4.9a–c are indicated on the plot.

4.5. Discussion and Conclusions

This chapter presented a framework for task-driven trajectory design for advanced CBCT imaging systems that leverages knowledge of both the patient anatomy and imaging task and exercises the motion capabilities of motorized, multi-axis CBCT systems to maximize imaging performance. The task-driven approach provides a strategy to overcome traditional imaging limitations via orbital flexibility — e.g., challenges associated with highly attenuating anatomy or implants that can be mitigated through intelligent data collection, selecting the best projection views to accomplish a particular task.

The importance of both the location and spatial-frequency dependence of the imaging task were investigated. Each of these elements can contribute significantly to which projection views carry the greatest information for a specific task. In general, the task-based approach balances the data fidelity of a view (i.e., noise) with the signal content (frequency response) that each view provides toward the imaging task. Because trajectory

design for a single stimulus location in the image volume can optimize performance at that location to the detriment of performance elsewhere, several multi-location design objectives were examined to obtain optimal performance over ROIs.

The proposed framework is general with respect to various options for parameterization of the source–detector trajectory, including constraints based on system geometry, DoF, and collision avoidance — permitting application to robotic C-arms and other CBCT systems with additional flexibility to gantry tilt and other geometric parameters. This includes short-scan geometries which are popular in CBCT imaging. A short-scan can be optimized similarly to the full scans described above with additional parameters such as start and end rotation angles included in the optimization to seek the views that are best for the object and task. Moreover, it is straightforward to further generalize these methods with additional geometric DoF (e.g., axial translation, variation in SDD), acquisition parameters (e.g., tube current modulation, Gang et al 2017a and fluence-field modulation, Gang et al 2017b), and reconstruction parameters (e.g., regularization strength β, Dang et al 2015). Such factors certainly carry interdependency in a full multi-variate optimization over all parameters — well beyond the scope of the current work, which focuses specifically on optimization of the source–detector orbit (holding other parameters fixed).

It can be noted that Fourier approximation of both MTF$(\boldsymbol{f}, \boldsymbol{\Omega}; v)$ and NPS$(\boldsymbol{f}, \boldsymbol{\Omega}; v)$ is one potential source of error in orbital design. Specifically, this presumes the term $\mathbf{A}^{\mathrm{T}}\mathrm{D}\{\mathbf{w}\}\mathbf{A}\boldsymbol{e}_{\boldsymbol{v}}$ is shift-invariant within an ROI. For heterogeneous objects, the diagonal weighting is variable with location. However, it can be noted that the data-dependence of this term falls between projection and backprojection operations, which have the effect of

strong smoothing even for very nonuniform weights. The impact of this smoothing is that the Fourier approximation tends to hold well even for highly nonuniform objects; however, there is the potential for breakdown of the approximation when shift-variance is pushed to the same scale as the spatial resolution of the system.

Consideration should also be given to challenges of accurate CBCT image reconstruction. Physical factors not accounted in the current analysis include x-ray scatter, beam hardening, image lag, detector glare, and patient motion, which may produce artifacts that confound visualization of the task. Recent work investigated the optimization of orbits based on scatter and scatter-to-primary ratio for imaging the weight-bearing spine using a robotic CBCT system, indicating that these effects are small and can be included in the overall optimization (Zhao et al 2019). Effects that occur from the sampling pattern itself, such as streakiness and cone-beam artifacts, are included in the model of MTF($\boldsymbol{f}, \boldsymbol{\Omega}; v$) and are therefore represented in the task-driven image in such a way as to improve the detectability of the task (although they may not be eliminated from the image).

Accurate geometric calibration of non-circular orbits is also required for accurate image reconstruction. The motion of the C-arm gantry as it moves through complex task-driven orbits may result in gantry wobble. The next chapter addresses this point using a "self-calibration" approach that solves the geometric calibration from the same projection data as acquired in the CBCT scan (Ouadah et al 2016).

Because the design objectives are generally non-convex and require many predictions of image quality, different strategies for efficient evaluation and solution of the design objective were presented. Image quality predictors in the current work focused on

quadratically penalized MBIR; however, future work aims to extend this methodology to non-quadratic regularization (Schmitt et al 2017, Zhang et al 2018, Gang et al 2019).

Task-driven trajectory design has the potential for application in a number of imaging scenarios. This chapter focused on theoretical underpinnings of the framework and illustrated the method in a series of experiments ranging from simple to complex. Although the phantoms used in these scenarios had somewhat uniform backgrounds, the method is designed to incorporate complex anatomic variations in the optimization via the patient model. In fact, the complexity of the model drives the selection of optimal trajectory. This is demonstrated in Chapter 6 in application to imaging scenarios in neuro-interventional radiology with complex surrounding anatomy. It is expected that the methodology also has potentially broad application in other interventional imaging scenarios (e.g., orthopedic procedures). The theoretical foundations detailed above suggest a new paradigm for interventional imaging wherein preoperative information is included explicitly within a rigorous definition of the imaging task to prospectively drive customized data acquisition that maximizes performance. The framework is an important first step in realizing advanced CBCT capabilities and more fully leveraging the wealth of information available in interventional imaging scenarios.

Chapter 5: Self-Calibration of Cone-Beam CT Geometry Using 3D–2D Registration

5.1. Introduction

To reconstruct a 3D CBCT image from 2D projections of an object, the geometric parameters relating the position of the x-ray source relative to the detector must be known accurately for each projection. The parameters characterizing this geometric relationship constitute a geometric calibration of the imaging system, and errors in calibration give rise to image artifacts such as blur, distortion, and streaks. Systems for CBCT in IGI tend to include open gantries with fairly adaptable source–detector orbits (cf., closed ring gantries in MDCT) and are often mobile and mechanically less rigid. While there are several means by which nominal circular orbits can be reliably calibrated for such systems (Navab et al 1998, Noo et al 2000, Cho et al 2005, Li et al 2010b), it may be impractical to calibrate all anticipated orbits, and non-circular orbits may defy conventional calibration approaches. Moreover, geometric errors can arise from out-of-date calibration in which system geometry changes over time (Daly et al 2008) or from irreproducibility in the orbit — for example, vibration during C-arm motion (Dennerlein and Jerebko 2012). Some scenarios may also concern imaging configurations for which the geometry is simply unknown.

As discussed in Chapter 4, robotic C-arms are capable of orbits that can intentionally depart from a circular orbit. Such capability provides acquisition modes that increase FOV (Herbst et al 2015) and / or improve image quality (e.g., reduction of cone-beam artifacts as in Noo et al (1998), Pack et al (2004), and Pearson et al (2010)).

Additionally, task-driven image acquisition approaches (Chapters 4 and 6) customize the source–detector orbit based on the individual patient anatomy and imaging task. Such approaches raise a challenge for geometric calibration due to the patient-specific nature of the orbit and the inability to anticipate all possible trajectories that the system might undertake.

The geometry of a point x-ray source and a flat, rigid detector can be defined by 9 DoF that describe the source and detector position for each projection view, forming a PM that maps the 3D image reconstruction voxels to the 2D projection image pixels (Rougée et al 1993). Various methods have been proposed to measure the geometric parameters associated with these DoF, largely separated into two categories: offline and online calibration. Offline methods perform a *pre*-calibration of the system (before the CBCT scan is acquired) using various phantoms typically consisting of a known arrangement of radiopaque markers. Using the measured locations of the markers within the projection images and a knowledge of the marker configuration, a geometric calibration of the imaging system can be obtained (Navab et al 1998, Noo et al 2000, Von Smekal et al 2004, Cho et al 2005, Yang et al 2006, Mennessier et al 2009, Li et al 2010b, Chetley Ford et al 2011, Li et al 2011, Hu et al 2011). CBCT reconstruction proceeds under the assumption that the system geometry is precisely reproduced in subsequent scans, and such methods are common for most CBCT imaging systems. However, these calibrations can become out-of-date ("aging" of the calibration as the system undergoes gradual mechanical change) and do not account for irreproducibility in the orbit. For CBCT systems in clinical use (e.g., IR (Fahrig et al 2006), IGRT (Jaffray et al 2002), and surgery (Zhang et al 2009)), a fairly high degree of geometric reproducibility is required (and commonly achieved), and offline

geometric *pre*-calibration is the norm, with periodic quality assurance by updating calibrations as required through repeat calibration.

Online calibration methods, on the other hand, compute the system geometry from the scan projection data directly by exploiting knowledge of the object being imaged. Some online methods take advantage of data redundancy in 2D projection images (Panetta et al 2008, Patel et al 2009, Meng et al 2013) while others operate by enforcing desired characteristics within the 3D image reconstruction by iterative optimization — such as image entropy minimization or sharpness maximization (Kyriakou et al 2008, Vidal-Migallón et al 2008, Kingston et al 2011). Such methods have demonstrated the ability to solve the source–detector geometry accurately for uncalibrated systems, and there is ongoing research concerning performance of various objective functions (e.g., entropy, sharpness, and combinations thereof). Such iterative algorithms can involve fairly long computation time for 3D image reconstruction that may not be compatible with clinical workflow (e.g., in IGI).

The work described below is motivated by the potential for "task-driven" imaging as described in Chapter 4 and reports an online geometric calibration method that is suitable to non-circular, task-driven orbits based on the 3D–2D registration method presented in Chapter 2. The 2D projection data are registered to a previously acquired 3D image of the subject, providing a "self-calibration" of the system. The 3D–2D registration process solves for the affine transformation representing the system geometry for each projection. The registration is rigid but incorporates a similarity objective that has been previously shown to be fairly robust against realistic deformation (Otake et al 2013) and includes means for masking of deformed regions. Like 3D–2D registration for motion compensation

(Chapter 2), potential applications of the self-calibration approach include cranial neurosurgery, neurovascular interventions, and orthopaedic trauma surgery, where rigid bone structures driving the registration are consistent with the rigid transformation model. The method allows calibration of arbitrary source–detector orbits, since it assumes a fairly general 9 DoF system geometry (alternatively a 6 DoF approximation with fixed SDD, as investigated below), and it accommodates irreproducibility in the scan orbit, since it derives the system geometry from the projection data for each acquisition. The self-calibration algorithm does not require the use of fiducial markers, and by using dense image-based measurements for registration (cf., a sparse array of fiducials) has potentially higher accuracy. The method is also less computationally intense in comparison to iterative image reconstruction methods.

In the sections below, we detail the proposed method for self-calibration, assess registration performance, and evaluate the resulting CBCT image quality in comparison to conventional offline reference calibration. The method was tested on an experimental CBCT bench using a simple cylindrical phantom and an anthropomorphic head phantom. The algorithm was also applied to data acquired using a robotic C-arm to validate performance on a clinically realistic system. Finally, application of the method to non-circular orbits was tested on the CBCT test bench, described in Section 5.3.2.4 below. Clinical applications of the method are discussed, including the capability to improve reconstruction accuracy for presumably well-calibrated systems, provide a sentinel alert on degradation of geometric calibration, and enable geometric calibration for non-circular orbits and task-driven imaging scenarios.

The work appearing in this chapter was reported in the following conference proceeding and journal paper: (S. Ouadah et al, *Proc. SPIE Medical Imaging,* 9415, 2015) and (S. Ouadah et al, *Phys. Med. Biol.* 61(7), 2016).

5.2. Self-Calibration Framework

5.2.1. Overview

In IGI, a high-quality MDCT image of the patient is commonly acquired prior to the procedure for diagnostic or planning purposes. Furthermore, during IGI, a series of CBCT images may be acquired — one at the beginning of the case, followed by CBCT acquisitions at particular milestones during, or at the conclusion of, the procedure. In these scenarios, the patient-specific 3D image can be registered to the 2D projection data acquired in subsequent CBCT acquisitions. Similar scenarios have been described for prior-image-based 3D image reconstruction to improve image quality and / or reduce radiation dose (Chen et al 2008, Stayman et al 2013, Dang et al 2014). For 3D–2D registration, a PM characterizing the system geometry is required for forward-projection of the 3D volume ($\boldsymbol{\mu}_{\mathbf{prior}}$) to create a 2D DRR ($\boldsymbol{y}_{\mathbf{prior}}$) to be registered to a 2D projection ($\boldsymbol{y}$). The PM can be decomposed in terms of the 9 DoF describing the source position ($\boldsymbol{s}$) and object / patient position ($\boldsymbol{t}$) and rotation ($\boldsymbol{\theta}$), where $\boldsymbol{s} = [s_x, s_y, s_z]^{\mathrm{T}}, \boldsymbol{t} = [t_x, t_y, t_z]^{\mathrm{T}}$ and $\boldsymbol{\theta} = [\theta_x, \theta_y, \theta_z]^{\mathrm{T}}$ as shown in Figure 5.1a. A simplifying assumption is that the source position, $\boldsymbol{s}$, is fixed with respect to the detector, reducing the system geometry to 6 DoF. It is possible to determine the system geometry for each projection by solving for these 6 or 9 DoF using 3D–2D registration. Repeating the registration for all projections ($k =$

$1, \ldots, N_{\text{proj}}$) yields a geometric calibration of the system that can be used for 3D image reconstruction. Figure 5.2 provides a flowchart for the self-calibration method: for each projection, the registration is initialized, registered via 3D–2D registration, and verified for accuracy. Once a system geometry is found for all projections, a 3D volume is reconstructed — for example, by FBP for simple circular orbits or by MBIR for non-circular trajectories. Table 5.1 summarizes the parameters used for the self-calibration method.

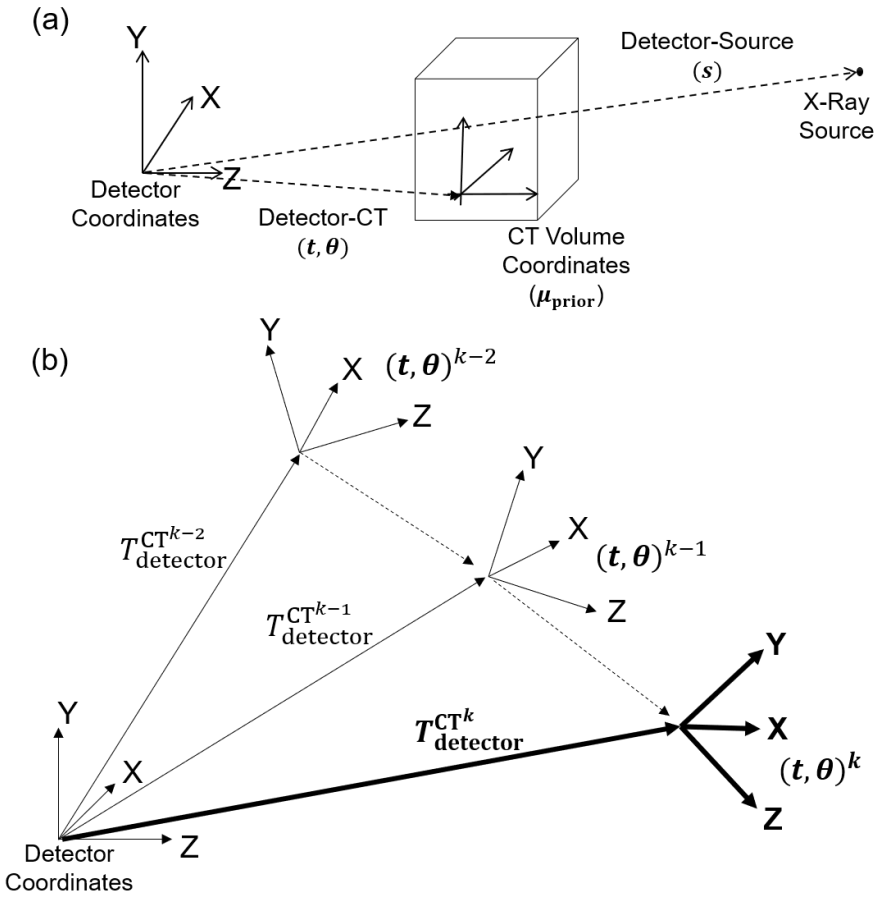

Figure 5.1. CBCT system geometry and coordinate frames. (a) The position of the prior MDCT volume relative to the detector coordinate system is described by 6 DoF in translation ($\boldsymbol{t}$) and rotation ($\boldsymbol{\theta}$). The source position relative to the detector is positioned by 3 DoF in translation ($\boldsymbol{s}$). (b) Initialization of the k^{th} registration (for views $k = 1, \ldots, N_{\text{proj}}$) by linear extrapolation of the previous $(k-1)$ and $(k-2)$ registrations.

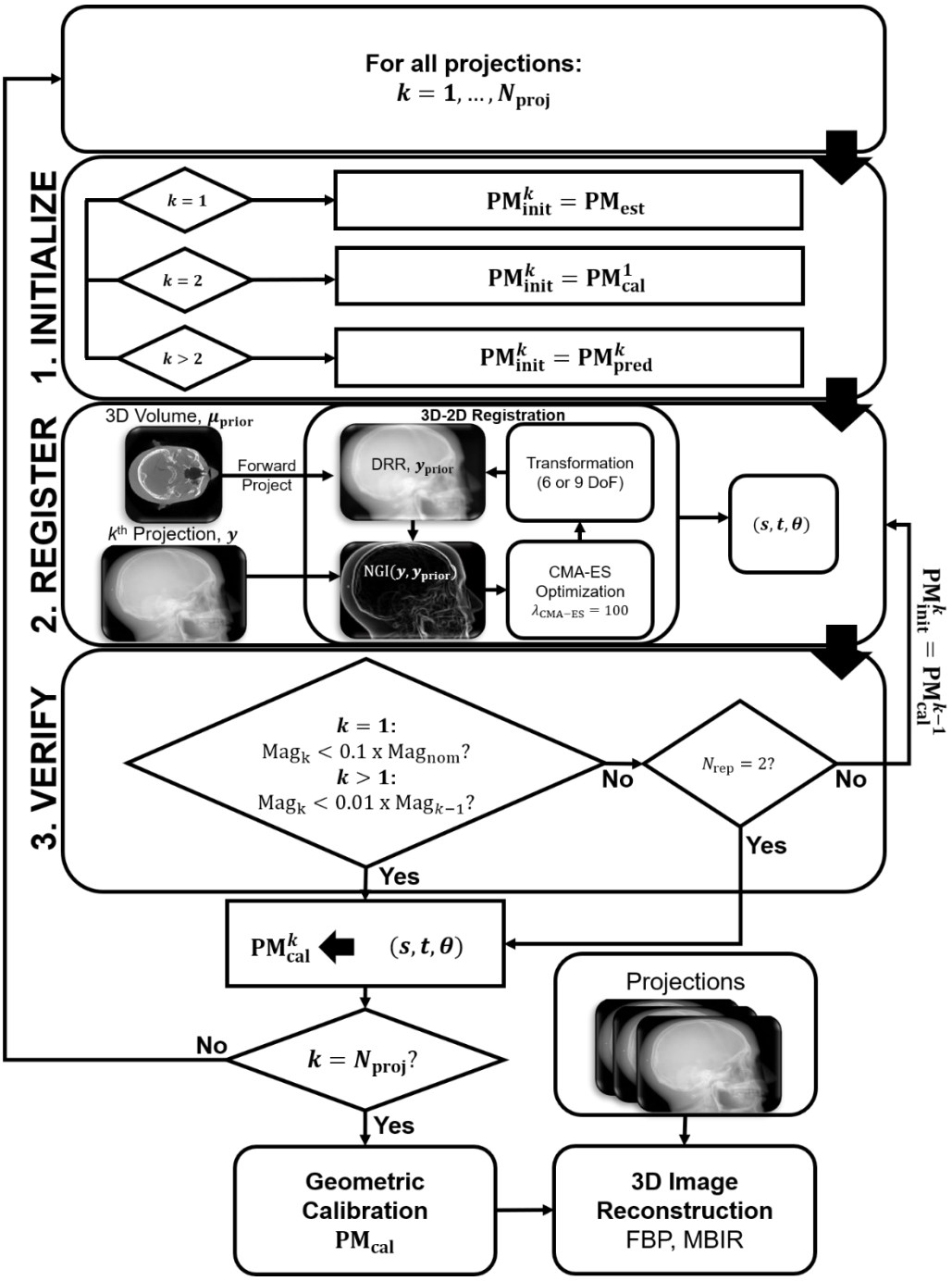

Figure 5.2. Flowchart for the self-calibration process. The system geometry for each 2D projection in a CBCT acquisition is determined by registering each projection to a previously acquired 3D image using a robust 3D–2D registration algorithm. The k^{th} registration is initialized by a simple predictor based on previous registrations. Outliers are detected in results that violate constraints on the smoothness of the orbit or other known characteristics of system geometry (e.g., abrupt change or spurious values of magnification). Registration of all projection views provides the geometric calibration required for 3D image reconstruction.

Table 5.1. Notation for the self-calibration method.

Property	Symbol
3D–2D registration	
2D projections	$\boldsymbol{y}$
Projection view	$k = 1, \ldots, N_{\mathrm{proj}}$
Prior 3D volume	$\boldsymbol{\mu}_{\mathbf{prior}}$
Digitally reconstructed radiograph (DRR)	$\boldsymbol{y}_{\mathbf{prior}}$
Estimated 6 or 9 DoF motion	$\boldsymbol{T}$
Source translation	$\boldsymbol{s}$
Object (patient) translation	$\boldsymbol{t}$
Object (patient) rotation	$\boldsymbol{\theta}$
Normalized gradient information	$\mathrm{NGI}(\boldsymbol{y}, \boldsymbol{y}_{\mathbf{prior}})$
Nominal system magnification	$\mathrm{Mag}_{\mathrm{nom}}$
Number of repeated registrations	N_{rep}
Projection matrices (PM)	
Initial PM	$\mathbf{PM}_{\mathbf{init}}$
Estimated PM	$\mathbf{PM}_{\mathbf{est}}$
Predicted PM	$\mathbf{PM}_{\mathbf{pred}}$
Calibrated PM	$\mathbf{PM}_{\mathbf{cal}}$
3D rotation matrix	$\mathcal{R}_{3x3}$

5.2.2. Initialization

A PM is required to initialize the registration of each projection, $\mathbf{PM}_{\mathbf{init}}$. A coarse estimation of the PM based on nominal parameters of the system geometry is used for initialization of the first ($k = 1$) projection. Specifically, s_z and t_z are initialized according to the SDD and (SDD-SAD), respectively. The orientation of the $k = 1$ projection with respect to the patient (e.g., PA, AP, LLAT, or RLAT) could be simply obtained from information available in the DICOM data on patient and image orientation. As a brute force check on the initial $k = 1$ orientation, the initial rotational values in $\boldsymbol{\theta}$ were changed by increments of 90° about the 3 cardinal axes to account for all possible orientations, registered each of the 24 permutations (called $\mathbf{PM}_{\mathbf{est}}$ in Figure 5.2) and selected whichever result yielded maximum similarity as $\mathbf{PM}_{\mathbf{cal}}^{\mathbf{1}}$. The second ($k = 2$) view was initialized

simply using $\mathbf{PM}_{\mathbf{cal}}^{\mathbf{1}}$ from registration of the first projection. For projections $k = 1, \ldots, N_{\text{proj}}$, the registration was initialized as illustrated in Figure 5.1b using a predicted PM, $\mathbf{PM}_{\mathbf{pred}}$, computed using the geometries of the previous two views.

5.2.3. Predicting the Next View ($k > 2$)

To initialize views $k = 3, \ldots, N_{\text{proj}}$, as illustrated in Figure 5.1b, a prediction estimates the position of the detector as it moves around the object and is used to compose $\mathbf{PM}_{\mathbf{pred}}^{\boldsymbol{k}}$. The prediction is a linear extrapolation in the 6 DoF describing the CT volume position and rotation, $(\boldsymbol{t}, \boldsymbol{\theta})$. The three DoF describing the source position $(\boldsymbol{s})$ are not extrapolated as it is not expected that the source should move significantly with respect to the detector. The prediction is formed based on the geometries of the previous two views by solving the transformation from $(\boldsymbol{t}, \boldsymbol{\theta})^{k-2}$ to $(\boldsymbol{t}, \boldsymbol{\theta})^{k-1}$, where k is the current view:

$$\boldsymbol{T}_{\mathbf{CT}^{k-2}}^{\mathbf{CT}^{k-1}} = \boldsymbol{T}_{\mathbf{detector}}^{\mathbf{CT}^{k-1}} \left(\boldsymbol{T}_{\mathbf{detector}}^{\mathbf{CT}^{k-2}} \right)^{-1} \tag{5.1}$$

The transform $\boldsymbol{T}_{\mathbf{detector}}^{\mathbf{CT}^{k}}$ indicates the homogeneous transformation from 3D detector coordinates to 3D MDCT coordinates for the k^{th} view, and the transform $\boldsymbol{T}_{\mathbf{CT}^{k-2}}^{\mathbf{CT}^{k-1}}$ indicates the homogeneous transformation from 3D MDCT coordinates for the $(k-2)$ view to the $(k-1)$ view. The transformation is then applied to $(\boldsymbol{t}, \boldsymbol{\theta})^{k-1}$ to obtain a prediction for $(\boldsymbol{t}, \boldsymbol{\theta})^{k}$:

$$\boldsymbol{T}_{\mathbf{detector}}^{\mathbf{CT}^{k}} = \boldsymbol{T}_{\mathbf{CT}^{k-2}}^{\mathbf{CT}^{k-1}} \left(\boldsymbol{T}_{\mathbf{detector}}^{\mathbf{CT}^{k-1}} \right) \tag{5.2}$$

which is then taken as initialization for registering the k^{th} view.

5.2.4. 3D–2D Registration

The 3D–2D registration method central to the self-calibration method is based on the work of Otake et al (2012, 2013), which incorporates NGI as a robust similarity objective within the CMA-ES optimizer (Hansen 2006). NGI was chosen for this work (cf., GO explored in Chapter 2) due to its speed, since it avoids the median operation implicit in Equation (2.1). A linear forward-projector implemented on GPU computes the DRR for a particular system pose. Similarity (NGI) is computed between the MDCT ($\boldsymbol{\mu}_{\mathbf{prior}}$, by way of its DRR, $\boldsymbol{y}_{\mathbf{prior}}$, taken as the moving image) and the 2D projection ($\boldsymbol{y}$, taken as the fixed image) as:

$$\mathrm{NGI}\left(\boldsymbol{y}, \boldsymbol{y}_{\mathbf{prior}}\right) = \frac{\mathrm{GI}\left(\boldsymbol{y}_{\mathbf{prior}}, \boldsymbol{y}\right)}{\mathrm{GI}(\boldsymbol{y}, \boldsymbol{y})} \tag{5.3}$$

where

$$\mathrm{GI}(p_1, p_2) = \sum_{i,j} m(i,j) w(i,j) \min(|\nabla p_1(i,j)|, |\nabla p_2(i,j)|) \tag{5.4}$$

$$\boldsymbol{\nabla p}(\boldsymbol{i},\boldsymbol{j}) \triangleq \left(\frac{d}{di}p(i,j).\frac{d}{dj}p(i,j)\right) \tag{5.5}$$

and

$$w(i,j) = \frac{1}{2}\left(\frac{\nabla p_1(i,j) \cdot \nabla p_2(i,j)}{|\nabla p_1(i,j)| \cdot |\nabla p_2(i,j)|} + 1\right) \tag{5.6}$$

Previous work (e.g., Otake et al 2013) showed NGI to exhibit robustness against content mismatch arising from non-rigid anatomical deformation or the presence of surgical tools introduced in the radiograph.

The CMA-ES optimizer was used to solve for the transformation that maximizes NGI:

$$\widehat{\boldsymbol{T}} = \arg\max_{\boldsymbol{T}} \mathrm{NGI}\left(\boldsymbol{y}, \boldsymbol{y}_{\mathbf{prior}}(\boldsymbol{T})\right) \tag{5.7}$$

Parameter selection in the CMA-ES optimization followed that of Otake et al (2012), with downsampling of both $\boldsymbol{y}_{\mathbf{prior}}$ and $\boldsymbol{y}$ by a factor of 3 and λ_{CMAES} set to 100. The stopping criterion was set to changes in translation or rotation of less than 0.1 mm or 0.1° respectively.

From the resulting geometry estimate of the source and detector, the calibrated PM is formed as:

$$\mathbf{PM}_{\mathbf{cal}}^{\boldsymbol{k}} \coloneqq \begin{pmatrix} s_z & 0 & s_x & 0 \\ 0 & s_z & s_y & 0 \\ 0 & 0 & 1 & 0 \end{pmatrix} \begin{pmatrix} \mathcal{R}_{3x3}(\theta_x, \theta_y, \theta_z) & \begin{matrix} t_x - s_x \\ t_y - s_y \\ t_z - s_z \end{matrix} \\ 0 \quad 0 \quad 0 & 1 \end{pmatrix} \tag{5.8}$$

where $\mathcal{R}_{3x3}$ represents a 3D rotation matrix with center of rotation at the origin of the coordinate system of $\boldsymbol{\mu}_{\mathbf{prior}}$. Whereas previous work solved such a registration for one view (Otake et al 2012, 2013) or a small number of views (Uneri et al 2013), the self-calibration method generates a PM for all projections acquired in a CBCT scan.

5.2.5. Outlier Detection

It is possible to identify outliers in pose estimation by detecting spurious values of the system parameters (or combinations of system parameters) resulting from image registration. System magnification was selected as a simple measure for outlier detection, because the ratio allows fluctuations in scale that do not affect the forward-projection or backprojection of rays in 3D image reconstruction, but traps errors that would distort the PM. Each registration result is checked as a possible outlier. For the $k = 1$ projection, the

resulting magnification must be within 10% of that calculated from the known, nominal system magnification ($\mathrm{Mag}_{\mathrm{nom}}$, computed from the SAD ($s_z - t_z$) and SDD (s_z) provided for initialization of the first view). If the magnification is not within this range, then the algorithm is reinitialized. For the $k = 2$ projection, the magnification must be within 1% of the magnification associated with the $k = 1$ projection for the algorithm to continue. If the magnification does not fall within this range, then registration for the $k = 2$ projection is restarted using the same initialization method as the $k = 1$ projection as detailed in Section 5.2.2. For all subsequent ($k > 2$) projections, the magnification must be within 1% of the magnification associated with the previous projection (Mag_{k-1}), and for any view implying magnification outside of this range, the registration is restarted using $\mathbf{PM}_{\mathbf{cal}}^{\boldsymbol{k-1}}$ to initialize (instead of $\mathbf{PM}_{\mathbf{pred}}^{\boldsymbol{k}}$). After this second repetition of the registration ($N_{\mathrm{rep}} = 2$), the result is accepted as the correct geometry, and the self-calibration algorithm continues to the next projection. (In the current study, as detailed below, there were few, if any, outliers for the fairly smooth orbits considered.) If the registration result is not an outlier, the geometry estimate is used to compose $\mathbf{PM}_{\mathbf{cal}}^{\boldsymbol{k}}$.

The outlier detection method was tested by running the self-calibration algorithm on CBCT data acquired in a circular orbit with $N_{\mathrm{proj}} = 360$ projections and a magnification of 1.5 using the experimental bench described below. The predicted pose for each view was purposely perturbed with Gaussian noise with standard deviation σ = 20 mm for translations and 20° for rotations to stress the registration.

5.3. Experimental Methods

5.3.1. Imaging Systems and Phantoms

The proposed methodology was tested using the CBCT imaging bench and clinical robotic C-arm (Artis Zeego, Siemens Healthineers, Forchheim Germany) shown in Figure 5.3a and 5.3b, respectively. The bench includes an x-ray tube (RAD13, Dunlee, Aurora IL), flat-panel detector (PaxScan 4030CB, Varian, Palo Alto CA), and computer-controlled motion system (Compumotor 6k8, Parker Hannifin, Rohnert Park CA) for acquisition of CBCT data in a variety of system configurations. For all studies involving the experimental bench, t_z and s_z were fixed to the nominal values of the robotic C-arm (40 and 120 cm, respectively). Other aspects of the bench are described in previous work (Zhao et al 2014), and the nominal scan technique involved N_{proj} = 360 projections over 360° at 70 kV and 227 mAs. For the robotic C-arm system, t_z and s_z were nominally fixed to 40 and 120 cm respectively, and acquisitions obtained N_{proj} = 496 projections over 200° at 87.2 kV and 229 mAs. The nominal geometric calibration for the bench system was formed using the method of Cho et al (2005) using a cylindrical phantom containing two circles of steel ball bearings (BBs) from which the full 9 DoF geometry of the source and detector can be determined for each projection in a CBCT scan. Alternatively, the nominal calibration for the robotic C-arm was obtained using the standard clinical calibration tool — a cylindrical phantom with a spiral BB pattern derived from the method of Navab et al (1998). In each case, the nominal geometric calibration is referred to below as the "reference calibration."

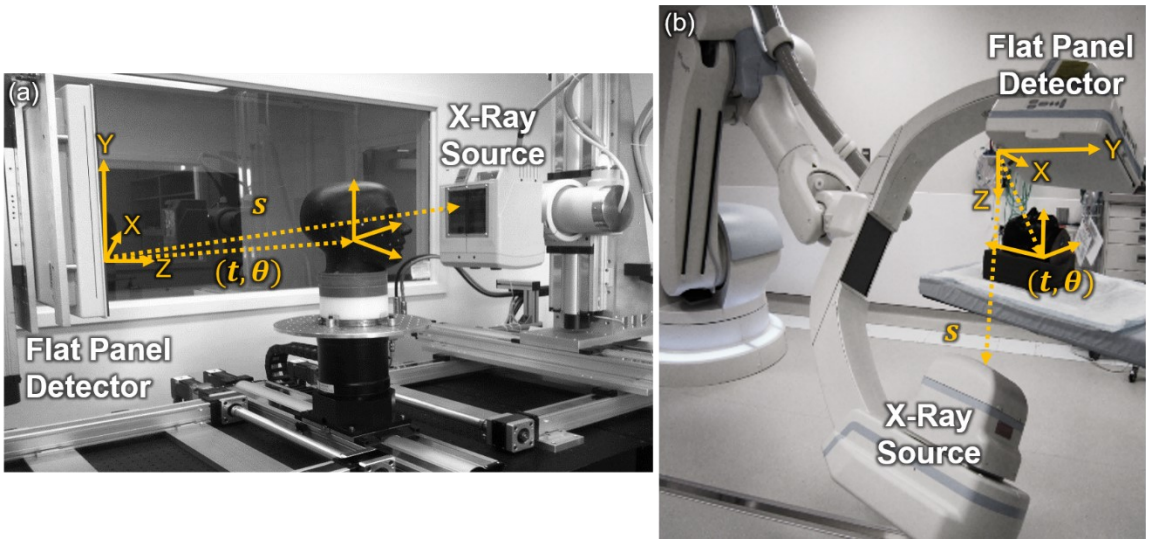

Figure 5.3. Imaging systems. (a) CBCT imaging bench with an anthropomorphic phantom shown on the rotation stage. (b) The robotic C-arm system with phantom and coordinate frames.

CBCT images from the bench and robotic C-arm systems were reconstructed by FBP for cases of a nominally circular orbit (Experiments 1, 2, and 3, below). An MBIR method was used to reconstruct images for the case of a non-circular orbit considered in Experiment 4 (below). The PL objective function was used for this maximization, and the reconstructed image was computed in 50 iterations of 20 subsets with regularization strength $\beta = 1\times10^2$ (Wang et al 2014).

Two imaging phantoms were used to evaluate the performance of the "self-calibration" in comparison to the "reference calibration". The first (Figure 5.4a) used the same cylindrical phantom as used in the calibration of the bench system (above) with the addition of a 0.13 mm diameter tungsten wire suspended along the central axis and a 2 mm diameter lead BB and 3 acrylic spheres (5, 6.5 , and 10 mm diameter) attached to the surface of the cylinder. This configuration provided data in which the geometric calibration data (derived from the steel BBs) and the data for imaging performance assessment

(derived from the tungsten wire, lead BB, and acrylic spheres) were identical, eliminating the question of orbit reproducibility. A second phantom (Figure 5.4b) involved a natural human skull in tissue-equivalent plastic with the addition of a 0.13 mm diameter tungsten wire inserted in the oropharynx and a 2 mm diameter lead BB attached to the surface.

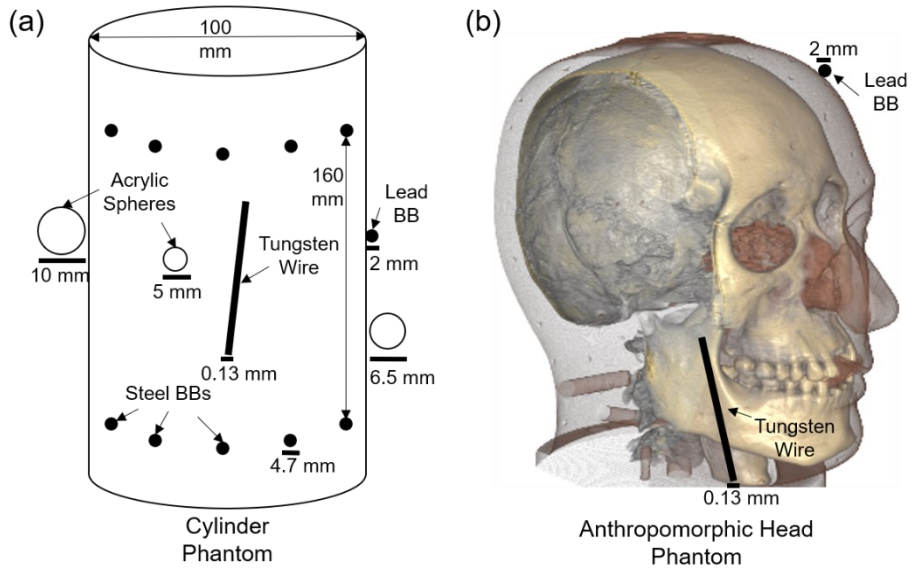

Figure 5.4. Imaging phantoms. (a) Cylindrical phantom that combines the reference calibration phantom for the bench system (two circular patterns of steel BBs) with a tungsten wire, lead BB, and acrylic spheres to test geometric accuracy of the CBCT reconstruction. (b) Anthropomorphic head phantom with a tungsten wire and lead BB.

5.3.2. Experimental Plan

Four experiments were conducted to test the performance of the self-calibration method, progressing systematically from simple geometries and objects (e.g., the bench and cylinder phantom) to more complicated scenarios (e.g., the robotic C-arm and head phantom). In each case, the reference calibration was acquired using the double circle or spiral BB phantom as described in Section 5.3.1. The 3D image input ($\boldsymbol{\mu}_{\mathbf{prior}}$) to the self-calibration method was a distinct scan in each case (i.e., not the same as the projection data acquired in the current CBCT scan) — formed either from a previous CBCT scan or a

previous MDCT scan on a diagnostic scanner. In each case, the calculated system geometry and CBCT images reconstructed using the self-calibration method (for both 6 and 9 DoF characterization of the system geometry) were compared to those from the reference calibration.

5.3.2.1. Exp 1: Cylinder Phantom on an Imaging Bench

Experiment 1 involved the cylinder phantom imaged on the CBCT bench to test the feasibility of the self-calibration method and obtain quantitative analysis of basic performance. A circular orbit was used, with the nominal scan technique described in Section 5.3.1. A previous CBCT scan of the phantom formed the 3D image input to the self-calibration method, with the previous scan acquired with an angular offset in projection views so that the projections used in 3D reconstruction were not identical to those in 3D–2D registration.

5.3.2.2. Exp 2: Anthropomorphic Head Phantom on an Imaging Bench

Experiment 2 involved the anthropomorphic head phantom imaged on the CBCT bench to test the robustness of 3D–2D registration under more clinically / anatomically realistic conditions of x-ray scatter, image noise, and complexity of the subject. A previous scan of the head phantom on a diagnostic MDCT scanner (Somatom Definition, Siemens Healthineers, Forchheim Germany, 120 kV, 227 mAs, $0.46 \times 0.46 \times 0.40$ mm^3 voxels) formed the 3D image input to the self-calibration method.

5.3.2.3. Exp 3: Anthropomorphic Head Phantom on a Robotic C-Arm

Experiment 3 involved the anthropomorphic head phantom imaged on the robotic C-arm to test the method in a clinically realistic system geometry and orbit. A previous CBCT scan of the head phantom acquired using the robotic C-arm formed the 3D image input to the self-calibration method. To challenge the method further, a realistic, pronounced change in image content was introduced between the previous 3D image and the projection images acquired in the current CBCT scan — viz., a 2 mm diameter steel biopsy needle placed in the nasal sinuses and positioning the head with a strong (~30°) canthomeatal tilt to mimic a typical clinical setup. The reference calibration (using the spiral BB phantom mentioned above) was performed by the system service engineer as part of regular preventative maintenance within 6 months of the current scan in accordance with standard clinical practice.

5.3.2.4. Exp 4: Non-Circular Orbit

Experiment 4 tested the self-calibration algorithm on a non-circular orbit — specifically, a saddle-shaped orbit that could be used to extend the longitudinal FOV, reduce cone-beam artifacts, or improve image quality in the manner of task-driven imaging — all cases for which a conventional geometric calibration acquired prior to the scan may be irreproducible or infeasible. The scan was conducted on the CBCT bench using the anthropomorphic head phantom with the same nominal scan protocol as above, except that the source and detector were moved along the y and z axes of the detector (as defined in Figure 5.1 and shown in Figure 5.3) during the scan to produce the saddle trajectory illustrated in Figure 5.5. The total deviation in both t_y and s_y was ±25 mm to maintain

approximately the same FOV as previous experiments within the constraints of the test bench system. As in Experiment 2, a previous diagnostic MDCT scan of the head provided the 3D image input to the self-calibration method. A CBCT image was reconstructed using the MBIR method described above and the self-calibration result for system geometry. Since the reference calibration method (Cho et al 2005) strictly holds only for circular orbits, an image of the head phantom scanned in a circular orbit was used as a reference and basis of image quality comparison (using the same MBIR method for reconstruction).

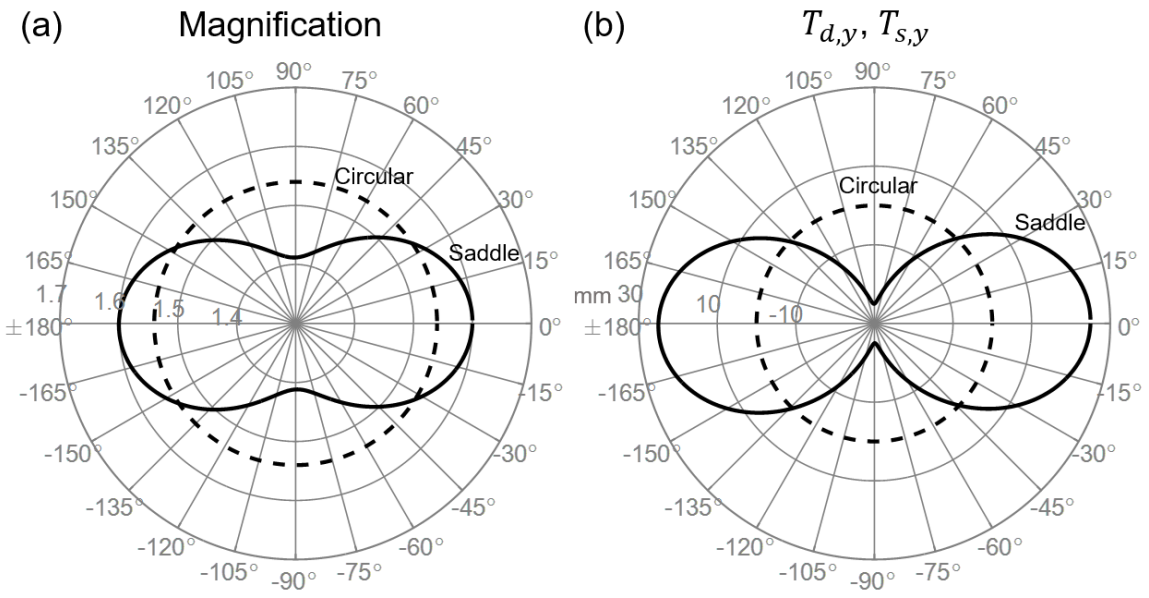

Figure 5.5. Illustration of the saddle orbit for Experiment 4. (a) Polar plot showing magnification for the saddle and circular orbits. (b) t_y and s_y for the saddle and circular orbits.

5.3.3. Performance Evaluation

Performance was evaluated in terms of three measures of image quality / geometric accuracy of the self-calibration method in comparison to conventional reference calibration. The first was the FWHM of a PSF measured from the tungsten wire in each phantom. From CBCT images reconstructed with 0.05 mm isotropic voxels, line profiles

through the center of the wire in 10 axial images were sampled radially over 360°. A Gaussian distribution was fit to each line profile, and the FWHM was averaged over all line profiles and slices.

The second performance measure was the reprojection error (RPE) associated with the position of (the centroid of) the lead BB placed on the surface of both phantoms. The BB centroid was localized in each 2D projection of the scan data using a Gaussian fit about the BB position. The centroid position was then transformed into 3D space using the $\mathbf{PM}_{\mathbf{cal}}^{\boldsymbol{k}}$ corresponding to each projection, and its location on the detector was connected to the calibrated 3D source location by a line segment. This process was repeated for all projections, and the closest point of intersection for line segments spaced 90° apart was computed, yielding a point cloud. The width of the point cloud was evaluated using principal component analysis (PCA) and averaging the lengths of the principal components:

$$\text{RPE} = \frac{1}{C}\sum_{c=1}^{C} |\boldsymbol{V_c}| \tag{5.9}$$

where $\boldsymbol{V_c}$ is a principal component of the 3D data and $C \leq 3$. Analysis in terms of PCA is analogous to simply evaluating the width of the point cloud (e.g., by Gaussian fit) but better accommodates possible bias in the orientation of the point cloud.

Finally, the performance of geometric calibration was assessed with respect to the quality of 3D image reconstructions themselves. Each was qualitatively evaluated in terms of blur, noise, and artifacts associated with geometric calibration errors — e.g., streak artifacts and distortion of high contrast details such as the temporal bone trabeculae.

5.4. Results

5.4.1. Outlier Detection

In all experiments reported below, there were no outliers detected in the self-calibration data, indicating a suitable degree of robustness of the 3D–2D registration process, including the various forms of initialization for the $k = 1$ and $k = 2$ projections, the prediction method for initializing the $k > 2$ projections, the similarity objective (NGI) even in the presence of image content mismatch (e.g., the biopsy needle in Experiment 3), and the CMA-ES optimization method. To stress test the outlier detection and recovery method, a study was conducted as described in Section 5.2.5 in which the geometry estimates were purposely perturbed. Example results are shown in Figure 5.6, in which the magnification is plotted as a function of projection view angle before outlier detection (dashed black line) and after detection and recovery (solid black line). Following perturbation, 12 outliers were detected among the 360 projections, and all were recovered by the re-start method described in Section 5.2.5 (re-starting and / or using the previous view for initialization).

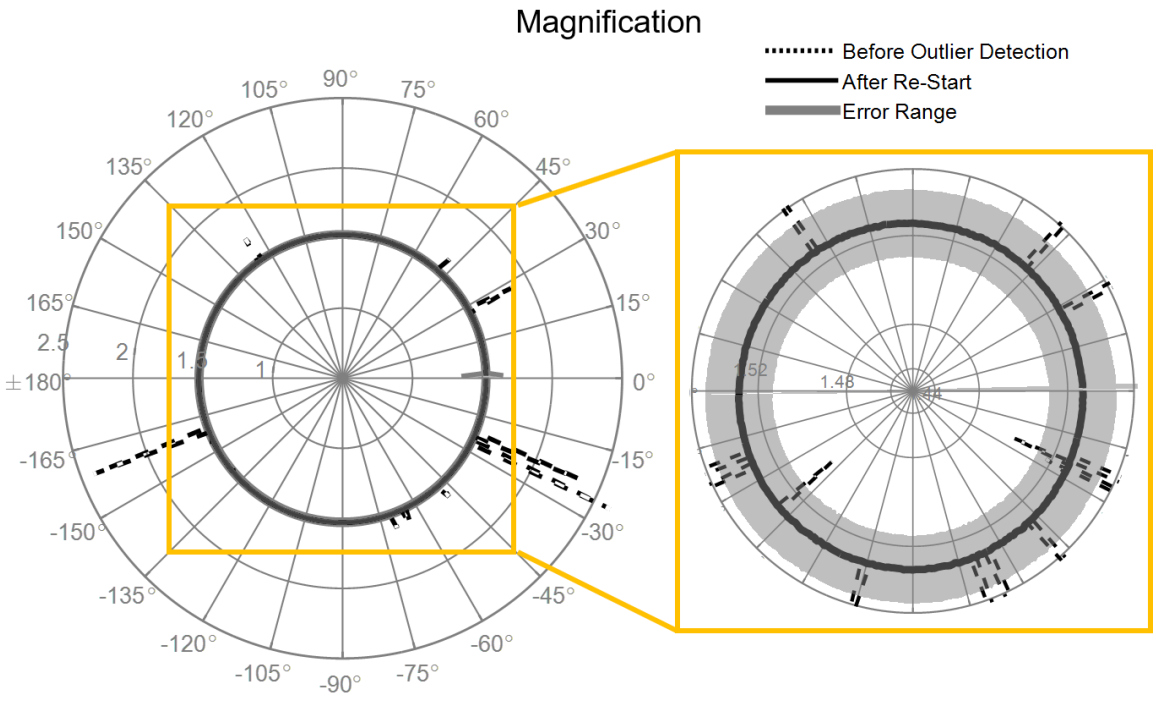

Figure 5.6. Outlier detection. The dashed black line shows the magnification of the registration before outlier detection using a perturbed initialization (σ = 20 mm, 20°). The solid black line shows the magnification after outlier detection and re-starting the registration using the previous view for initialization. The grey region represents the window for allowable magnification (10% for the $k = 1$ view, 1% for subsequent views).

5.4.2. FWHM of the PSF

The PSF about the tungsten wire in Experiments 1–4 is shown in Figure 5.7 for the reference calibration (top row) and the self-calibration using both 6 DoF (middle row) and 9 DoF (bottom row) representation of system geometry. Overall improvement is noted for self-calibration compared to reference calibration — both quantitatively (FWHM for each case) and qualitatively (apparent distortion and intensity of the PSF). For Experiment 1 (cylinder phantom on the imaging bench; Figures 5.7a, 5.7e, 5.7i), the PSFs are comparable, indicating that self-calibration performs as well as (simultaneous) reference calibration for a simple object on a near-perfect system (stable, high-precision imaging bench).

Experiment 2 (head phantom on the imaging bench; Figures 5.7b, 5.7f, 5.7j) shows improvement in FWHM (0.66 mm for self-calibration, 0.86 mm for reference calibration, $p < 0.001$) as well as the general shape and intensity of the PSF. Note that the wire in the head phantom was located ~9 cm inferior to the central axial slice (whereas the wire in the cylinder phantom of Experiment 1 was analysed at the central axial slice). The improvement compared to the reference calibration likely indicates that while the reference calibration is suitable near the central slice (Figure 5.7a) it may include errors in detector angulation that become apparent farther from isocenter (Figure 5.7b). An alternative explanation is that the scan geometry was slightly irreproducible between the reference calibration and the current scan (whereas Experiment 1 involved simultaneous imaging and calibration in the same phantom). However, this is less likely since the imaging bench is rated to a fairly high degree of reproducibility (~0.001 mm) in positioning of the motion control system. Also, previous work showed that detector angulation is among the more difficult parameters to estimate in reference calibration (Bronnikov 1999, Noo et al 2000) and can have a large impact on the geometric accuracy of CBCT reconstructions (Daly et al 2008).

Experiment 3 (head phantom on the robotic C-arm; Figures 5.7c, 5.7g, 5.7k) shows measurable improvement of the PSF using self-calibration compared to the standard clinical reference calibration. The two most likely explanations are similar to those noted above: (1) slight intrinsic errors in the reference calibration; and / or (2) slight differences between the reference calibration and current scan, owing either to irreproducibility of the C-arm orbit and / or aging of the reference calibration over time.

Finally, Figures 5.7d, 5.7 h, and 5.7l show the results of Experiment 4 involving the head phantom on the imaging bench with a non-circular orbit. Note that the reference for comparison (Figure 5.7d) is for a circular orbit (calibrated with the phantom containing the double circular pattern of BBs), and all images were reconstructed with MBIR using the same regularization and optimization parameters. The results demonstrate the feasibility of self-calibration for non-circular orbits, suggesting the same level of geometric accuracy in pose estimation as for circular orbits (Experiments 1 and 2) and compatibility of the resulting geometry estimates with MBIR.

Comparing the self-calibration results for 6 DoF (Figure 5.7e–h) and 9 DoF (Figure 5.7i–l) characterization of system geometry, no appreciable (or statistically significant) differences were seen in the PSF or FWHM, implying relative insensitivity to the additional 3 DoF associated with variations in source position relative to the detector for the systems considered in this work. This is not a surprising result for the imaging bench (for which the source is rigidly fixed with respect to the detector) and suggests that possible variations in source position on the robotic C-arm (e.g., due to C-arm flex under gravity) are minor with respect to the PSF of image reconstructions.

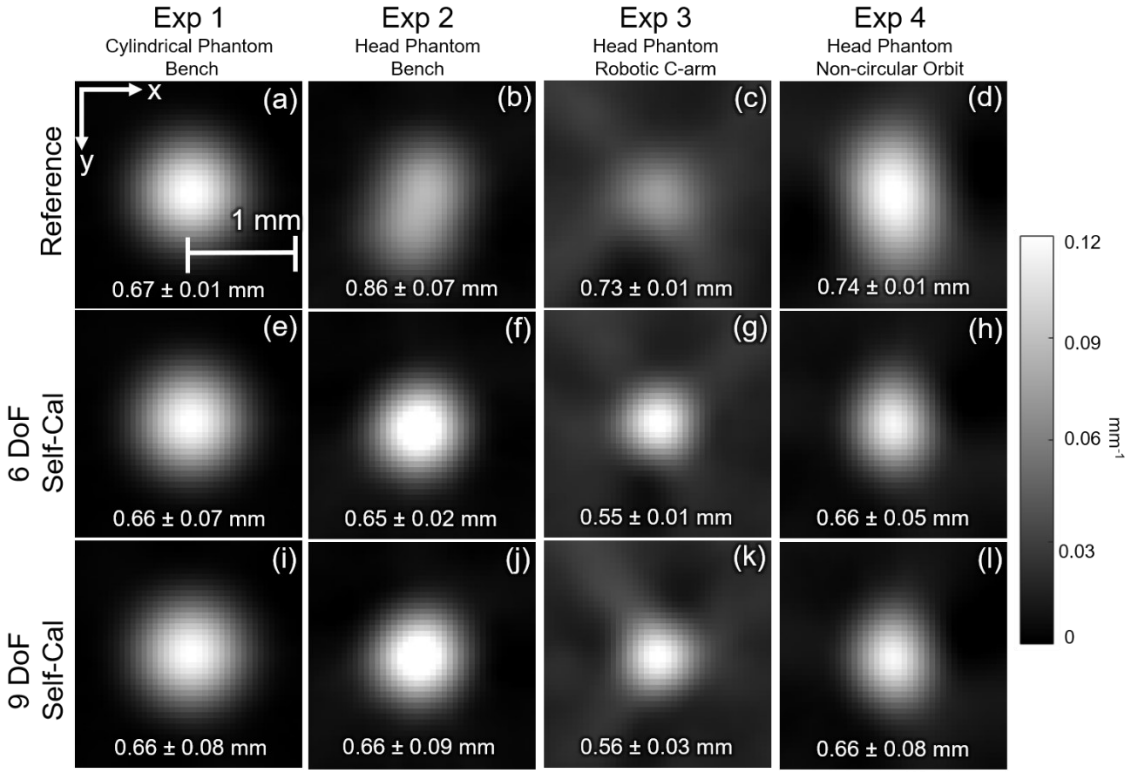

Figure 5.7. Effect of geometric calibration on spatial resolution (FWHM of the PSF). Images show an axial slice through the tungsten wire in the cylinder or head phantom. (Top row, a–d) Images reconstructed using the reference calibration. (Middle row, e–h) Images reconstructed using self-calibration and 6 DoF characterization of system geometry. (Bottom row, i–l) Images reconstructed using self-calibration and 9 DoF characterization of system geometry. Each column represents one of the four experiments detailed in Section 5.3.

5.4.3. Reprojection Error

Figure 5.8 summarizes the results for the four experiments in terms of the RPE, echoing the results of Figure 5.7. Figure 5.8a shows an example point cloud from which the RPE was determined as detailed in Section 5.3.3, and Figure 5.8b shows the improvement in RPE obtained by self-calibration in comparison to reference calibration. For Experiment 1, a statistically significant improvement is seen in RPE (~0.69 mm for self-calibration) compared to reference calibration (0.83 mm) under ideal conditions

($p < 0.001$), which also shows RPE to be a more sensitive test of geometric calibration than PSF width (Figures 5.7a, 5.7e, 5.7i).

Experiment 2 demonstrates an additional characteristic of self-calibration: the 6 DoF self-calibration was significantly improved compared to reference calibration (RPE = 0.61 mm versus 0.84 mm, $p < 0.001$); in addition, the 6 DoF self-calibration was superior to the 9 DoF self-calibration (RPE = 0.61 mm versus 0.82 mm, $p < 0.001$). This result may seem counterintuitive and points to an interesting characteristic of self-calibration: the 9 DoF method allows potentially unrealistic variations in source position with respect to the detector — e.g., excursions in s_z; while FBP reconstruction image quality (Figures 5.7f and 5.7j) may be relatively insensitive to such excursions since backprojected rays are still along the correct lines (recognizing a fairly small effect associated with distance weighting), the difference is evident in the RPE among orthogonal rays. The 6 DoF self-calibration holds the position of the source fixed with respect to the detector, which appears to incur less error in geometry estimation, at least for the rigid geometry of the imaging bench.

For Experiment 3, the mean and median RPE are lower for the self-calibration methods than the reference calibration method, but the difference was not statistically significant ($p = 0.08$). The overall performance appears better (consistent with Figures 5.7c, 5.7g, and 5.7k), but errors in finding the BB centroid in the projection images may have contributed to a reduction in reliability of the RPE estimates. Another factor is that the C-arm undergoes significant deviations from a circular orbit, which broadens the point cloud distributions. Experiment 4 is not shown, since RPE as defined by Equation (5.9) assumes a circular orbit.

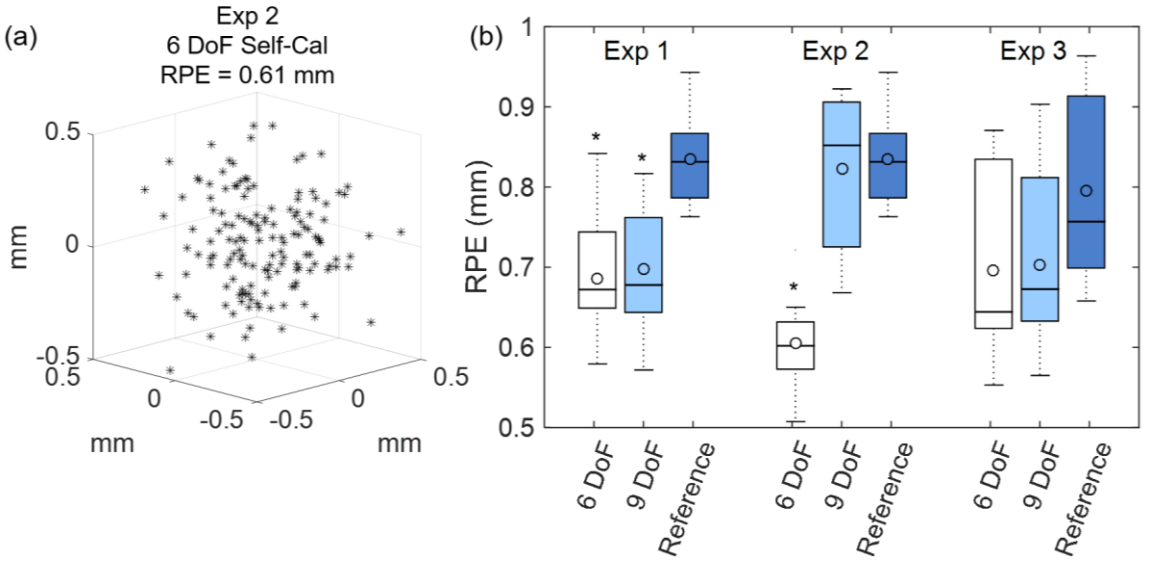

Figure 5.8. Effect of geometric calibration on RPE. (a) Example point cloud distribution used to measure the RPE, generated by backprojecting the centroid of a BB in each projection and finding the closest point of intersection between orthogonal views. (b) The RPE resulting from 6 and 9 DoF self-calibration compared to conventional reference calibration. An asterisk indicates significant difference from the reference, an open circle indicates mean value, a horizontal line indicates median value, a closed box indicates interquartile range, and whiskers indicate full range of the data.

5.4.4. Image Quality

Figure 5.9 illustrates the effects quantified above in terms of qualitative visualization of high-contrast details in the anthropomorphic head phantom, including streaks (from a high-contrast biopsy needle) and distortion (wisps about cortical bone and temporal bone trabeculae). Images from Experiment 1 are not shown because they were essentially identical: both reference calibration and self-calibration yielded qualitatively accurate reconstruction of the cylinder phantom without appreciable geometric artifacts. The same result is seen for Experiment 2 (Figures 5.9a, 5.9d, 5.9g), where both reference and self-calibration yield a qualitatively accurate reconstruction of the skull. Other sources of image quality degradation include x-ray scatter and beam hardening, but not geometric calibration.

Experiment 3 demonstrates noticeable improvement in images reconstructed using self-calibration, evident as a reduction in streak artifact arising from the high-contrast biopsy needle located at the anterior aspect of the axial slice in Figures 5.9b, 5.9e, and 5.9h. The reduction in streaks indicates that the self-calibration method reduced imprecisions in geometric calibration that are accentuated in the reconstruction of a high-contrast, high-frequency objects such as a needle. The self-calibration method yields a more accurate geometric calibration and is more robust against such streak artifacts — analogous to the observation of De Man et al (1998) that patient motion causes substantially increased streak artifacts when metal is present in the image.

Experiment 4 shows MBIR images formed using reference and self-calibration methods, the former for a circular orbit and the latter for a saddle orbit. The results are qualitatively identical, with both methods yielding calibration suitable for MBIR. Minor differences in cone-beam artifacts may be appreciated in Figures 5.9f and 5.9i compared to Figure 5.9c, but that is due to the non-circular orbit, not the fidelity of geometric calibration. Overall, even in cases for which the difference between reference calibration and self-calibration is negligible, the results are positive findings: they demonstrate not only the feasibility to compute a geometric calibration using the proposed method, but also that the resulting calibration is comparable to well-established methods for reference calibration; moreover, the self-calibration method is extensible to non-circular orbits and imaging systems for which reference calibration is irreproducible or infeasible.

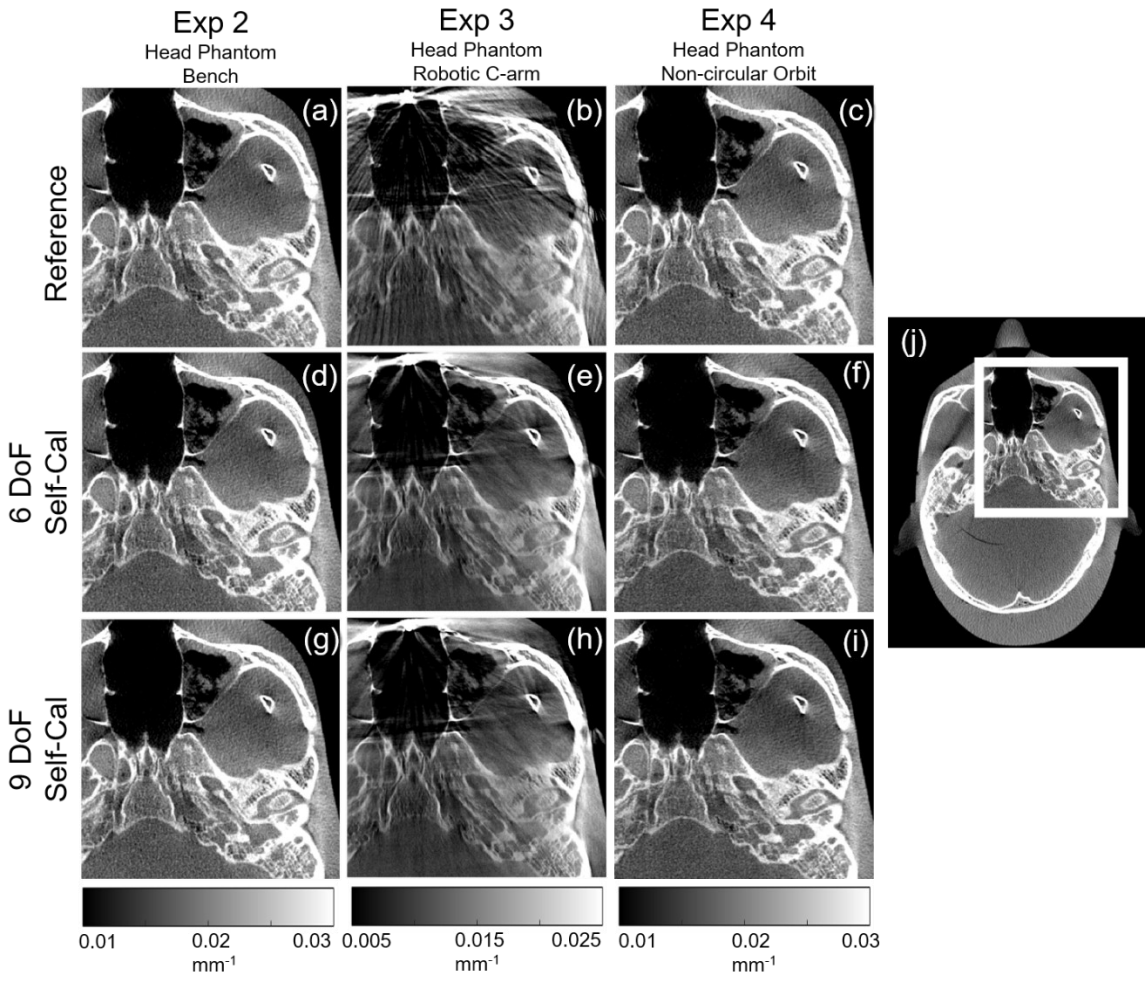

Figure 5.9. Effect of geometric calibration on image quality. (a–c) Detailed region of an axial slice of the head phantom in Experiments 2–4 reconstructed using reference calibration. (d–f) The same, reconstructed using the 6 DoF self-calibration and (g–i) the 9 DoF self-calibration. Image (j) shows the full axial FOV and detailed region.

5.5. Discussion and Conclusions

The self-calibration method presents a promising means to obtain accurate geometric calibration not only for standard circular orbits and presumably well-calibrated systems, but also for more complicated non-circular orbits and / or systems for which system geometry is unknown / irreproducible. The studies detailed above demonstrate that the self-calibration method yields system geometry sufficient to reconstruct images with

comparable or improved image quality compared to reference calibration methods and is extensible to cases where conventional reference calibration may not be possible—e.g., non-circular orbits. It is interesting to note that while both 6 and 9 DoF self-calibration performed better overall than the reference calibrations, the 6 DoF self-calibration method slightly outperformed the 9 DoF self-calibration, specifically in Experiment 2. This result may indicate that although the 9 DoF method yields a more complete system description, it may be subject to local minima in the larger search space. With the 6 DoF method, the 3 DoF describing the source position are held fixed and reduce the search space in a manner that appears to reduce susceptibility to such local minima and is consistent with the mechanical rigidity of the robotic C-arm used in this work. It is also possible that the 9 DoF optimization is more susceptible to image noise. The optimization was not strongly affected by propagation of error from previous views to the next, even though the algorithm is sequential in nature and uses previous views to initialize the next. In addition to trapping outliers as described in Section 5.2.5, the registration for each view is computed de novo (i.e., with a new CMA-ES population and a search for the current pose that is largely independent of the previous pose) and demonstrates capture range that is more than sufficient to recover from small errors in $\mathbf{PM}_{\mathbf{init}}$ resulting from previous views.

The primary objective of the current study was to assess the feasibility and geometric accuracy of the self-calibration method; accordingly, the run-time of the algorithm was not fully optimized. The algorithm was implemented in Matlab (The MathWorks, Inc, Natick MA) and yielded a run-time of approximately 3 s per registration for the 6 DoF method (or 5 s per registration for the 9 DoF method), excluding the projections for which multiple initializations are used and scale the registration time

accordingly. A variety of ways to reduce the run-time for a complete scan could be developed in future work, such as parallelizing registrations by binning the projections into sub-groups and registering these groups in parallel (as opposed to registering all projections sequentially), or simultaneously registering more than one projection during the same optimization as in Uneri et al (2013).

One limitation of the algorithm is that the accuracy of registration is dependent on the quality of the 3D volume and the 2D images forming the basis of registration. However, as shown in Experiment 3 where a CBCT image acquired from the robotic C-arm system was used as the 3D volume for registration, the registration algorithm is fairly robust to artifacts present in the 3D images (e.g., cone-beam artifacts, scatter, truncation). A second limitation is its dependence on the initialization of the geometric parameters in the first view, and poor initialization could result in registration failure. Initialization is most important for the first projection, which requires knowledge of the nominal system parameters, since if the first projection fails to register correctly, the algorithm may be unable to proceed. Another limitation is that the registration between the 3D volume and 2D projections is limited to affine transformations that presume rigid patient anatomy. Although limited to affine transformations, the registration is still fairly robust against anatomical deformation, as described in previous work (Otake et al 2013), since the similarity objective incorporated in the registration process uses strong edges consistent in both images, which in CBCT most likely represent rigid, bony structures. Registration therefore aligns consistent bony structures in the images while tending to ignore soft-tissue deformations. Such robustness to deformation was previously investigated in the context of spine surgery (Otake et al 2013), where it was found that the 3D–2D registration

framework was able to register images with a median projection distance error of 0.025 mm even under conditions of strong deformation (e.g., preoperative CT with the patient oriented supine and the spine straight (or lordotic) registered to an intraoperative projection image in which the patient is oriented prone with the spine in kyphosis).

In summary, the self-calibration method performed as well as a reliable (up to date) reference calibration on a highly stable CBCT imaging bench and performed better than the reference calibration (subject to periodic quality assurance updates) on a clinical robotic C-arm. This indicates that self-calibration could improve 3D image reconstruction even for presumably well-calibrated systems and could offer a sentinel alert against "aging" of the reference calibration. The algorithm demonstrated robustness to changes in the image between the 3D volume and the 2D projection data, such as changes in object positioning and / or the presence of strong extraneous gradients in the 2D projections (e.g., the presence of a metal biopsy needle). Furthermore, the self-calibration method provides feasibility for task-driven imaging on real imaging systems, demonstrated in Chapter 6.

Chapter 6: Application of Task-Driven Source–Detector Trajectories to Neuro-Interventional Radiology

6.1. Introduction

CBCT is used in a growing number of scenarios in interventional imaging including verification of patient positioning, 3D image guidance, and visualization of instrumentation or embolic agents delivered to the patient (Berris et al 2013, Carrino et al 2014). As introduced in Chapter 4, robotic CBCT C-arms greatly expand the possibilities for scanning geometries beyond those of conventional circular source–detector orbits. In clinical practice, such motion capabilities have been used to provide fast, reproducible positioning of the C-arm gantry and to increase the FOV of the reconstructed 3D image. As demonstrated in the work reported below, the additional DoF enabled by such robotic C-arm gantries can be leveraged to improve image quality and / or reduce radiation dose using non-circular orbits computed to maximize imaging performance with respect to a particular imaging task(s).

CBCT-guided interventional procedures often include a considerable amount of prior information regarding patient-specific anatomy, devices to be delivered to the patient during treatment, and the imaging task(s). As shown in Stayman et al (2015), Gang et al (2015), Dang et al (2017), and Ouadah et al (2017), definition of the imaging task and a patient-specific prior image can be used to optimize both the acquisition and reconstruction of CBCT image data. Such prospective design of the CBCT scan technique and / or reconstruction method based on a task-based objective function is referred to as “task-

driven imaging." This chapter focuses on task-driven design of the CBCT source–detector trajectory, taking the mathematical theory and methods detailed in Chapter 4, combining with the geometric calibration methods of Chapter 5, and applying them to scenarios emulating neurosurgical / neuroradiological interventions.

An example clinical scenario in which task-driven imaging could be applied is neurovascular embolization, which may be performed in response to a cerebral aneurysm, AVM, carotid-cavernous fistula, or dural arteriovenous fistula (Miracle and Mukherji 2009). The embolization agent occludes feeder vessels and vascular abnormalities, and during the procedure it is important to avoid embolization of normal / non-target vessels, identify incomplete embolization, and locate possible hemorrhage resulting from perforated vessels (Alabdulghani et al 2018). CBCT is frequently used as a tool to localize the target and instrumentation as well as to check against possible complications arising from the intervention. However, image quality is often degraded by the presence of materials that are highly attenuating to x-rays, including coils, plugs, balloons, particulate agents such as polyvinyl alcohol and microspheres, and liquids such as tissue adhesives and injectable liquid embolic agents (e.g., Onyx, Medtronic, Dublin Ireland) (Leyon et al 2014). As a result, CBCT images often exhibit strong artifacts that challenge reliable visualization of the target and surrounding vessels.

Task-driven imaging is applied to two clinical scenarios in this chapter: (1) the assessment of embolization in the case of aneurysm, where perforation of the aneurysm would necessitate detection of ICH adjacent to the region of embolization; and (2) AVM ablation, in which detection of untreated regions of the nidus requires visualization of incomplete embolization. These two scenarios are investigated both in simulation and in

real data using a CBCT test bench and a clinical robotic C-arm. We also extend the task-driven optimization framework to situations for which multiple tasks with unknown location underlie the clinical objective.

A potential clinical workflow is depicted in Figure 6.1 for practical application of task-driven imaging to neurovascular IGI. The process begins with some form of prior 3D image as a model of the patient ($\boldsymbol{\mu}_{\mathbf{prior}}$). The prior image could be an MDCT acquired for diagnostic or planning purposes or an initial CBCT acquired at the beginning of the case for navigation or target localization. Based on the expected surgical outcome of the procedure, high-contrast features are added to the anatomical model (e.g., embolization coils, catheters, contrast agent). The imaging tasks are defined mathematically in $H_{\text{task}}(\boldsymbol{f}, \boldsymbol{\Omega}; v)$, where $\boldsymbol{f}$ denotes the 3D spatial frequency dependence of the imaging task, $\boldsymbol{\Omega}$ parameterizes the CBCT acquisition, and v indicates the location specified within an ROI in $\boldsymbol{\mu}_{\mathbf{prior}}$ ($\boldsymbol{v}_{\mathbf{ROI}}$). Note that the coordinate system of $\boldsymbol{\mu}_{\mathbf{prior}}$ must be registered to the world coordinate system of the intraoperative scene — i.e., to the C-arm gantry. To accomplish this, two or more projections are acquired, and the registration of the prior 3D image and intraoperative scene is solved via 3D–2D registration as in Uneri et al (2013). The resulting 6 DoF transformation $\boldsymbol{T}_{\boldsymbol{\mu}_{\mathbf{prior}}}^{\mathbf{C-arm}}$ (containing three rotations and three translations in x, y, and z) can be applied to the image coordinates ($\boldsymbol{x}$) of $\boldsymbol{\mu}_{\mathbf{prior}}$ to yield transformed coordinates registered to the C-arm gantry.

Maximization of task-based detectability index ($d'(\boldsymbol{\Omega}; v)$) is solved with respect to the source–detector orbit (parametrized by $\boldsymbol{\Omega}$) to yield the optimal source–detector trajectory $\widehat{\boldsymbol{\Omega}}$ — the topic of Chapter 4. An important consideration is the need for geometric calibration to precisely characterize the source and detector pose for each vertex on the

resulting orbit — the topic of Chapter 5. Even conventional circular orbits require such calibration to obtain accurate 3D reconstruction, usually solved by prior (offline) calibration techniques using a phantom of fiducial markers (Noo et al 2000, Cho et al 2005, Mennessier et al 2009). Offline calibration of the full range of possible vertices may or may not be practical; however, a solution can also be obtained using the "self-calibration" method described in Chapter 5 (Ouadah et al 2016), and MBIR techniques can be utilized to reconstruct the acquired task-driven image $\widehat{\boldsymbol{\mu}}$.

The work appearing in this chapter was reported in the following conference proceeding and journal paper: (S. Ouadah et al, *Proc. SPIE Medical Imaging,* 10132, 2017) and (S. Capostagno et al, *J. Med. Imag.,* 6(2), 2019).

6.2. Task-Driven Imaging for Design of Source–Detector Trajectories

Chapter 4 provided an in-depth description of the theoretical methods of trajectory design in task-driven imaging, briefly reviewed here. Task-driven imaging is an imaging framework well suited to IGI, in which a preoperative 3D image is acquired for diagnostic or planning purposes — or alternatively, in which multiple 3D images are acquired over the course of the intervention. The prior 3D image is leveraged to define the imaging task in terms of both the patient-specific anatomy and the clinical objective of an intraoperative CBCT scan. For example, after an interventional embolization of a neurovascular target, the imaging task may be to detect a subtle, low-contrast hemorrhage adjacent to the high-contrast embolization coil.

Table 6.1. Notation for task-driven source–detector trajectories for neuro-IR.

Property	Symbol
Detectability	
Prior patient image	$\boldsymbol{\mu}_{\mathbf{prior}}$
Source–detector trajectory parameters	$\boldsymbol{\Omega}$
Spatial frequencies	$\boldsymbol{f}$
Location of interest	v
Region of interest (ROI)	$\boldsymbol{v}_{\mathbf{ROI}}$
Detectability index	$d'(\boldsymbol{\Omega}; v)$
Task definition	$H_{\text{task}}(\boldsymbol{f}; v)$
Modulation transfer function	$\text{MTF}(\boldsymbol{f}, \boldsymbol{\Omega}; v)$
Noise power spectrum	$\text{NPS}(\boldsymbol{f}, \boldsymbol{\Omega}; v)$
3D–2D Registration	
6 DoF transform mapping prior image coordinates to C-arm coordinates	$\boldsymbol{T}^{\mathbf{C-arm}}_{\boldsymbol{\mu}_{\mathbf{prior}}}$
Prior image coordinates	$\boldsymbol{x}$
Source–detector trajectory	
Rotation angle	θ
Tilt angle	ϕ
3D source location	$S(\theta, \phi)$
Projection views	$k = 1, \ldots, N_{\text{proj}}$
Image reconstruction	
Reconstructed image volume	$\boldsymbol{\mu}$
Attenuation coefficient	μ
Projection measurements	$\boldsymbol{y}$
Log-likelihood	$L(\boldsymbol{\mu}; \boldsymbol{y})$
Roughness penalty	$R(\boldsymbol{\mu})$
Regularization strength parameter	β

The imaging task can be defined mathematically according to the location, contrast, and spatial frequencies associated with the feature of interest. Imaging performance is optimized with respect to the task ($H_{\text{task}}(\boldsymbol{f};v)$) by maximizing the detectability index, $d'(\boldsymbol{\Omega};v)$, which in turn is determined by the noise-power spectrum, $\text{NPS}(\boldsymbol{f},\boldsymbol{\Omega};v)$ and modulation transfer function, $\text{MTF}(\boldsymbol{f},\boldsymbol{\Omega};v)$. The non-prewhitening observer model for detectability is:

$$d'(\boldsymbol{\Omega};v)=\left[\frac{\left[\iiint\left(\text{MTF}(\boldsymbol{f},\boldsymbol{\Omega};v)\cdot H_{\text{task}}(\boldsymbol{f};v)\right)^2 df_x df_y df_z\right]^2}{\iiint \text{NPS}(\boldsymbol{f},\boldsymbol{\Omega};v)\cdot\left(\text{MTF}(\boldsymbol{f},\boldsymbol{\Omega};v)\cdot H_{\text{task}}(\boldsymbol{f};v)\right)^2 df_x df_y df_z}\right]^{\frac{1}{2}} \tag{6.1}$$

where $\boldsymbol{\Omega}$ is a vector containing parameters that generally characterize the CBCT scan — e.g., beam energy (as in Gang et al 2017a), fluence (as in Gang et al 2017b), or reconstruction filters or regularization (as in Dang et al 2015), and f_i indicates spatial frequencies in the 3 cardinal directions of the image coordinate system ($i \in \{x,y,z\}$). The non-prewhitening observer model is advantageous in that it combines $H_{\text{task}}(\boldsymbol{f};v)$ with relevant (and predictable) properties of the image, allowing detection of objects ranging from low-frequency (i.e., diffuse lesion) to high-frequency (i.e., stents and small vessels). Other objectives can be envisioned (e.g., $d'(\boldsymbol{\Omega};v)$ or contrast-to-noise ratio per unit dose), additional constraints could be incorporated (e.g., maximum dose to the patient or a radiosensitive volume therein as in Bartolac et al (2011)), and other forms of the observer model could be formulated to incorporate an imaging task with predictions of image properties. Additionally, incorporating other technical, logistic factors such as scan time, collision constraints, or total number of views could be beneficial for workflow in the clinical setting.

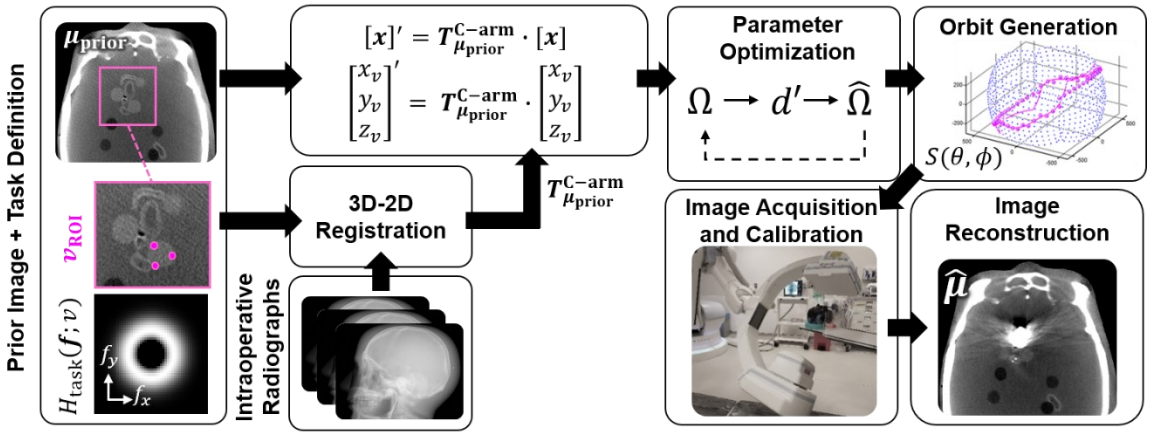

Figure 6.1. Workflow for task-driven imaging. A prior 3D image provides a patient model within which the imaging tasks are defined. The coordinates of the prior image and task locations ($\boldsymbol{x}$ and v, respectively) are mapped to the coordinate system of the imaging system using the 6 DoF transform $\boldsymbol{T}^{\mathbf{C-arm}}_{\boldsymbol{\mu}_{\mathbf{prior}}}$, which is solved by 3D–2D registration of $\boldsymbol{\mu}_{\mathbf{prior}}$ to two or more projection views, yielding the transformed coordinates in $\boldsymbol{x}'$ and v'. Optimization of $\boldsymbol{\Omega}$ with respect to detectability ($d'(\boldsymbol{\Omega}; v)$) yields a task- and patient-specific trajectory $S(\theta, \phi)$ which is carried out on the robotic C-arm and reconstructed using MBIR.

In this work, $\boldsymbol{\Omega}$ comprises parameters that define the source–detector trajectory. This parameterization can take a variety of forms, including periodic basis functions using constant, sine, and cosine functions, and b-spline basis functions using equally spaced knot locations as described in Chapter 4. Calculation of NPS($\boldsymbol{f}, \boldsymbol{\Omega}; v$) and MTF($\boldsymbol{f}, \boldsymbol{\Omega}; v$) uses approximations based on PL reconstruction with a quadratic regularization penalty (Stayman and Fessler 2004, Gang et al 2014), also detailed in Chapter 4.

Through NPS($\boldsymbol{f}, \boldsymbol{\Omega}; v$) and MTF($\boldsymbol{f}, \boldsymbol{\Omega}; v$), the optimization of $\boldsymbol{\Omega}$ yields an orbit that maximizes $d'(\boldsymbol{\Omega}; v)$ with respect to $H_{\text{task}}(\boldsymbol{f}; v)$. As discussed in Chapter 4, it may be useful to optimize with respect to multiple task locations (e.g., when a single location is unknown). For the experiments presented below in which all locations are treated with equal importance, the minimum $d'(\boldsymbol{\Omega}; v)$ is maximized according to the maximum minimum in $d'(\boldsymbol{\Omega}; v)$ over N_{task} tasks:

$$\widehat{\boldsymbol{\Omega}} = \arg\max_{\boldsymbol{\Omega}} \min \left\{ d'^{(\boldsymbol{\Omega}; H_{\text{task}}(\boldsymbol{f}; v_1))}, \ldots, d'^{\left(\boldsymbol{\Omega}; H_{\text{task}}\left(\boldsymbol{f}; v_{N_{\text{task}}}\right)\right)} \right\} \tag{6.2}$$

Using the maxi-min objective better ensures that imaging performance is not sacrificed in some locations in favor of others, recognizing that other objectives may be used, such as maxi-mean or maxi-median (also investigated in Chapter 4), a weighted sum when additional knowledge of the importance of each defined task is available, or another relevant statistical representation of a population.

The optimization was solved using CMA-ES (Hansen 2006) — a stochastic optimization that was previously shown to perform well in the presence of local minima (Otake et al 2013). Once the optimal parameters ($\widehat{\boldsymbol{\Omega}}$) are found, the low-dimensional parametrization of the source–detector trajectory can be converted into a series of source locations ($S_k(\theta, \phi); k = 1, \ldots, N_{\text{proj}}$), using a rotation angle θ and a tilt angle ϕ to indicate the 3D location of the x-ray source for all N_{proj} projection views in the scan. In this work, we assume the position of the detector to be fixed with respect to the x-ray source (fixed SDD) with a single, fixed origin, allowing the source–detector trajectory to move on a sphere of diameter SDD.

For image reconstruction, the PL reconstruction algorithm was used, since such iterative methods naturally accommodate non-circular trajectories generated by task-driven imaging. The PL algorithm maximizes an objective function based on the log-likelihood L of the current image estimate $\boldsymbol{\mu}$ (given the projection data $\boldsymbol{y}$) combined with a regularization term to enforce smoothness in the image with regularization strength, β:

$$\widehat{\boldsymbol{\mu}} = \arg\max_{\boldsymbol{\mu}} L(\boldsymbol{\mu}; \boldsymbol{y}) - \beta R(\boldsymbol{\mu}) \tag{6.3}$$

A quadratic penalty for the regularization term $R(\boldsymbol{\mu})$ was used, matching the theoretical estimators for NPS$(\boldsymbol{f}, \boldsymbol{\Omega}; v)$ and MTF$(\boldsymbol{f}, \boldsymbol{\Omega}; v)$ as discussed in Chapter 4.

6.3. Experimental Methods

6.3.1. Digital Simulation and Physical Experiments

Studies included a combination of simulation and physical experiments. The first experimental system was the CBCT test bench shown in Figure 6.2a, allowing a broad range of trajectories by combining a motorized rotation stage with a manual tilt platform. The second system was a robotic C-arm (Artis Zeego, Siemens Healthineers, Forchheim Germany) shown in Figure 6.2b. Each system permitted task-driven scans in which the x-ray source moved (either in a true world-frame orbit for the robotic C-arm, or relative to the patient for the test bench) to each $S_k(\theta, \phi)$ in $S(\theta, \phi)$ in a step-and-shoot fashion to accumulate $k = 1, \ldots, N_{\text{proj}}$ projections constituting the task-driven image acquisition protocol. To accomplish this, each source location generated by the task-driven orbit was defined using 2 DoF: a rotational angle θ and a tilt angle ϕ for all N_{proj} source locations.

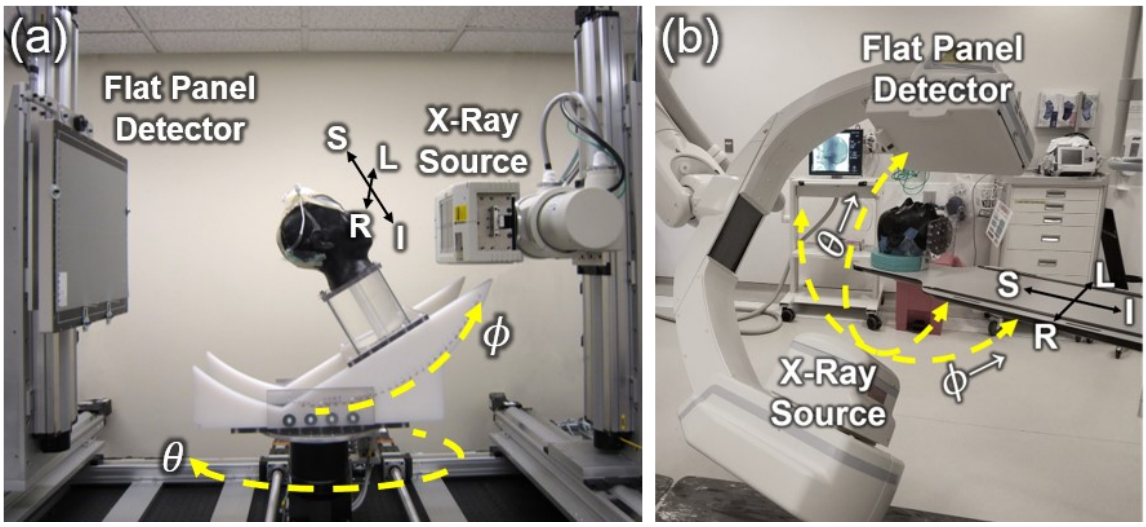

Figure 6.2. Experimental platforms for task-driven imaging: (a) CBCT test bench with rotational platform and manual tilt stage. (b) Robotic C-arm system. In each system, the source–detector trajectory is defined by a series of N_{proj} source locations containing 2 DoF; rotation angle θ and tilt angle ϕ. The patient's right (R), left (L), superior (S), and inferior (I) directions are indicated in the rotating coordinate frame of the patient on the test bench and in the world reference frame for the C-arm.

For the test bench system, scans were performed at 100 kV (with 2.0 mm Al + 0.2 mm Cu added filtration) and 0.63 mAs per projection. System geometry was set to SDD = 120 cm and SAD = 60 cm, and the detector was read at 768 × 768 pixel format with 0.556 mm square pixels. A fairly complete sampling of vertices was obtained by a combination of rotations (1° to 360° in 1° increments of the rotation stage, equivalent to source-detector rotation) and tilts (–30° to +30° in 2.5° increments of a tilt platform, equivalent to source–detector tilt). Since the tilt platform was placed on top of the rotary stage (as in Figure 6.2a), this yields an incomplete sampling pattern, particularly in the direction orthogonal to the tilt platform; therefore, the tilt platform was also physically rotated by 90° on the rotation axis for additional coverage of the sphere. From each circular scan, 182 samples were used, giving 10,556 vertices in total (182 views × 2 tilt platform orientations × 29 tilt angles). Geometric calibration of each 360° orbit was performed using

a BB phantom and the method described in Cho et al (2005). Task-driven orbits were formed by selecting 364 vertices from this set of projection data as nearest match to the solution of Equation (6.2). The scan dose was evaluated by measurement of air kerma using a 0.6 cc air ionization chamber placed within a 16 cm diameter computed tomography dose index (CTDI) phantom at isocenter (Fahrig et al 2006, Daly et al 2006) and computing the weighted sum (denoted D_w, given by the 1/3 and 2/3 weighted sum of the central and average peripheral dose, respectively).

For the robotic C-arm platform, system geometry was set to SDD = 120 cm and SAD = 80 cm, and the detector was read at 960 × 1240 pixel format with 0.308×0.308 mm^2 pixels. Rotation and tilt parameters for the C-arm gantry were uploaded to the Artis control system as an XML file, and individual projections were acquired at 102 kV and 0.18 mAs per projection to avoid saturation of the detector with AEC disabled and no added filtration, resulting in 63 mAs total for the scan. Raw projection data were collected using an engineering workstation, and the self-calibration method was used for geometric calibration (described in Chapter 5, Ouadah et al 2016), since only vertices belonging to non-circular orbits were collected (cf., full sampling of vertices on the test bench).

The following sections outline experiments that translate the task-driven imaging method to the context of neuro-IR. First, the embolization of an intracranial aneurysm was simulated in a digital anthropomorphic head phantom to demonstrate the use of a multi-task objective function, progressing from non-anthropomorphic phantoms in Chapter 4. The CBCT test bench described above was then used to test the embolization scenario in real data. Next, AVM embolization was digitally simulated to show the effect of

surrounding anatomy on optimal orbits by moving the location of stimuli within the (digital) cranium and repeating the task-driven optimization. Finally, the task-driven imaging framework was implemented on the robotic C-arm system described above to demonstrate task-driven source-detector trajectories computed and exercised on a real clinical system.

6.3.2. Multi-Task Optimization

The first experiment emulated the assessment of an intracranial aneurysm coil embolization. Postoperative MDCT or CBCT is commonly used to check for complications about the coil, including perforation of the aneurysm and associated hemorrhage. A digital anthropomorphic head phantom was created with a centrally located, coiled aneurysm (Figure 6.3a). The embolization coil was modeled as a rough ellipsoid with principal axes of $20 \times 12 \times 13$ mm^3 and attenuation coefficient $\mu = 0.8$ mm^{-1} (corresponding to ~8% filling by volume of platinum wire using a 90 kV x-ray beam). Six 11 mm diameter spheres were placed around the coil representing ICH with contrast 0.002 mm^{-1} relative to background (similar to fresh blood in brain). Simulations used a monoenergetic forward model with Poisson noise added to approximate realistic levels of x-ray quantum noise. System geometry was the same as the test bench geometry described in Section 6.3.1 with uniform sampling in θ from 1° to 360° and uniform sampling in ϕ from $-50°$ to 50° (in 1° increments). Bare-beam fluence was modeled with 1×10^5 photons per detector element, approximating an exposure of 85 mAs with a beam energy of 90 kV.

The task function corresponding to the 11 mm spherical hemorrhage is shown in Figure 6.3e. A low-frequency task function was chosen for detecting the low-contrast, diffuse hemorrhage and a maxi-min, multi-location objective was solved with 30 locations

surrounding the embolization coil using the on-the-fly computation approach described in Chapter 4. The locations were uniformly distributed over an ellipsoid about the coil with principal axes of 36 × 24 × 24 mm^3. The source–detector orbit was parameterized using nine periodic basis functions with ϕ constrained to ±50°. The CMA-ES algorithm was applied using λ_{CMAES} = 40 and five initializations corresponding to circular orbits with $\phi = \{-50°, -25°, 0°, 25°, 50°\}$. The solution with highest maxi-min detectability was chosen and compared with a standard circular orbit using the same number of projections and bare-beam fluence (exposure). Image reconstruction for both the task-driven orbit and reference circular orbit solved the PL objective using dynamically relaxed ordered subsets with the number of subsets decreasing every five iterations in the sequence {54, 24, 12, 6, 4, 2, 1} for a total of 50 iterations to accelerate convergence. Quadratic regularization strength with $\beta = 1\times10^5$ was manually selected to balance the tradeoff between noise and resolution, and the 3D image was reconstructed with 480 × 480 × 500 voxels with 0.5 mm cubic voxels.

6.3.3. Task-Driven Imaging in Real Data (CBCT Test Bench)

An initial physical experiment used the CBCT test bench to further investigate the embolization scenario described in Section 6.3.2. In this case, a custom anthropomorphic phantom (The Phantom Laboratory, Greenwich, NY) with a human skull surrounded by tissue-equivalent plastic and a cranial vault filled with brain-equivalent gelatin (μ = 0.0188 mm^{-1}) was used. A silicone vessel (Vascular Simulations, Stony Brook, NY) representing an intracranial aneurysm in the internal carotid artery was placed in the interior of the cranium. Four 12.7 mm diameter acrylic spheres (μ = 0.0195 mm^{-1}) were attached to the external surface of the aneurysm to simulate ICH as illustrated in

Figure 6.3b. An initial CBCT scan was acquired to provide a preoperative image volume. The intracranial aneurysm was then instrumented with a stent and platinum embolization coils by an interventional radiologist under fluoroscopic guidance until the aneurysm was realistically filled. The phantom was then scanned according to the protocols described in Section 6.3.1 to compare the task-driven orbit with a standard circular trajectory.

The optimal trajectory was solved using a multi-location, maxi-min objective for three locations posterior to the embolization coil with the task function shown in Figure 6.3f describing detection of the low-frequency, low-contrast hemorrhage (identical to the task function described in Section 6.3.2 and shown in Figure 6.3e). The optimal trajectory was computed using a parameterized orbit of 29 periodic basis functions to allow a higher degree of flexibility in the orbit and constrained within ±30° tilt to account for physical constraints of the test bench experimental setup. The on-the-fly computation approach and the same CMA-ES optimization parameters as in Section 6.3.2 were used. As described in Section 6.3.1, the 364 nearest vertices from the projection data acquired over the full range in θ and ϕ were selected for the task-driven orbit. Image reconstruction for both the task-driven orbit and reference circular orbit used the quadratic PL algorithm with the same parameters as in Section 6.3.2, except the regularization parameter β was increased slightly to 7×10^5 to account for differences in fluence levels.

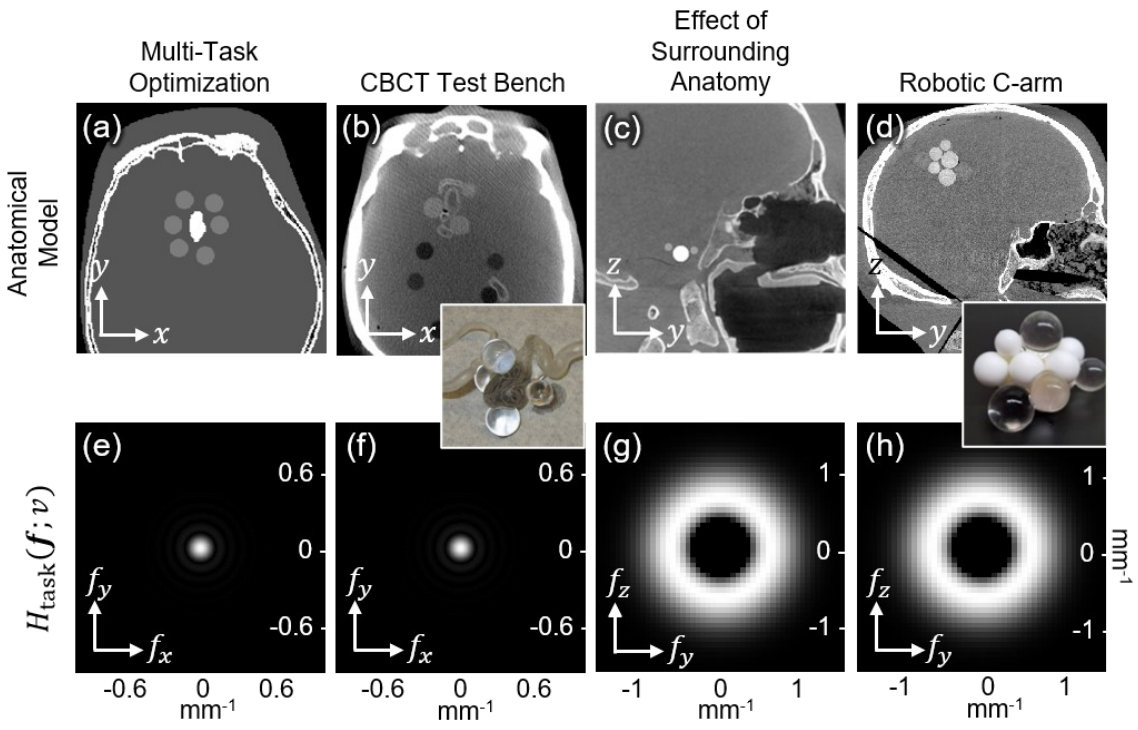

Figure 6.3. Summary of experiments testing task-driven imaging in neuroradiology. (a) Simulation of the postoperative assessment of an embolization coil using multi-location optimization to detect surrounding hemorrhage. (b) Visualization of hemorrhage near an embolization coil using a CBCT test bench. (c) Simulation of an AVM at various locations in the cranium to observe the effect of surrounding anatomy on the optimal orbit. (d) An AVM model created in an anthropomorphic head phantom to demonstrate the full workflow of task-driven imaging on a robotic C-arm. (e–h) The task functions, $H_{\text{task}}(\boldsymbol{f}; v)$, used in experiments (a–d), respectively.

6.3.4. Effect of Surrounding Anatomy

A similar simulation was performed to examine the effect of the location of the stimulus within the cranium on the optimal task-driven trajectory — in this case, embolization of an AVM using a highly-attenuating polymeric glue analogous to Onyx (Medtronic, Dublin Ireland) (Leyon et al 2014). Postoperative assessment of AVM embolization includes localizing untreated regions of the AVM nidus. This experiment used a digital anthropomorphic head phantom as illustrated in Figure 6.3c, locating a simulated AVM in either the skull base, the lateral cranium, or the crown of the skull. The

central core of the AVM after embolization was represented by a sphere of diameter 10 mm with μ = 1.0 mm^{-1} to represent a nidus of vessels filled with high-contrast glue. Six 5 mm diameter low-contrast spheres were placed around the central core with a contrast of 0.005 mm^{-1} compared to the soft-tissue background to represent potential untreated sites. The simulation mimicked the robotic C-arm system geometry with bare-beam fluence set to 1×10^4 photons per detector element to match the exposure of the robotic C-arm system. A monoenergetic forward model with Poisson noise added to approximate a realistic level of x-ray quantum noise was used to generate N_{proj} = 360 projection views over 360°.

Six mid-frequency imaging tasks were defined at the location of each simulated, untreated site for multi-task optimization using the maxi-min objective (Figure 6.3g). In this experiment, mid-frequencies were emphasized to capture the task of distinguishing a small vessel adjacent to the AVM nidus. This experiment used the precomputation approach described in Chapter 4 to utilize the second proposed method. Although more accurate in calculating MTF$(\boldsymbol{f}, \boldsymbol{\Omega}; v)$ and NPS$(\boldsymbol{f}, \boldsymbol{\Omega}; v)$, the precomputation approach is memory intensive, thereby limiting the total number of imaging tasks. To make use of the second proposed parameterization of the source trajectory described in Chapter 4, b-spline basis functions were used with eight equally spaced knots, and the trajectories were constrained to tilt angles in the range $\phi = -30°$ to 30° and rotation angles θ = 1° to 360° to match the extent of the robotic C-arm system. As trajectories from b-spline basis functions have increased flexibility over periodic basis functions, the CMA-ES optimization algorithm was used to estimate $\widehat{\boldsymbol{\Omega}}$ using λ_{CMAES} = 200 with 6 restarts and random uniform initialization.

Quadratic PL reconstructions for the optimal trajectory and a circular trajectory (generated with the same bare-beam fluence and number of projections) were performed using 200 iterations with 10 subsets to stabilize convergence during reconstruction and regularization strength $\beta = 1\times10^5$, again to balance noise with resolution at the task location. Images were reconstructed with 512 × 512 × 512 voxels and 0.5 mm cubic voxel size.

6.3.5. Task-Driven Imaging on a Robotic C-Arm

The full task-driven imaging framework was tested on the robotic C-arm using an AVM model within an anthropomorphic head phantom (The Phantom Laboratory, Greenwich NY) similar to that in Section 6.3.3 and illustrated in Figure 6.3d. The brain-like background was the same as in Section 6.3.3 (μ = 0.0188 mm^{-1}) and the AVM model was created by clustering 10 Teflon spheres (μ = 0.03 mm^{-1}) and six acrylic spheres (μ = 0.0195 mm^{-1}) ranging in diameter from 5–15 mm at the crown of the skull. A prior image was obtained on a CBCT test bench and registered to the robotic C-arm geometry. Six imaging tasks were defined at the edges between the Teflon and acrylic spheres, presenting a mid-frequency task function with contrast 0.0007 mm^{-1} as shown in Figure 6.3h (similar to the task described in Section 6.3.4). Orbit optimization was performed in the same manner as in Section 6.3.4 using the precomputation approach.

The phantom was subsequently imaged on the robotic C-arm operated in step-and-shoot mode to move through the optimal task-driven orbit (N_{proj} = 360 at a fixed technique of 102 kV and 0.18 mAs per projection). Quadratic PL reconstruction was again performed using 200 iterations with 10 subsets and 0.5 mm cubic voxels on a 700 × 700 × 700 voxel

grid, with β lowered to $1\times10^{3.5}$ to increase resolution at the task location. For comparison with a standard circular orbit, a low-dose research scan protocol was used (N_{proj} = 496 over a 200° circular orbit with the same technique as above). Of the 496 acquired projections, 360 approximately equally spaced projections were used for reconstruction for fair comparison to the task-driven orbit. The same PL parameters were applied for image reconstruction for both the task-driven and circular orbit.

6.4. Results

6.4.1. Multi-Task Optimization

Results from the embolization coil imaging experiment are summarized in Figure 6.4. The optimization sought the maxi-min solution for detectability of hemorrhage over an ensemble of locations (Figure 6.4a) surrounding an embolization coil. Compared to a conventional circular orbit, the resulting task-driven orbit exhibits a tilt and low-frequency excursions from a plane as shown in Figure 6.4b. The orbit is clipped at two positions due to the ±50° collision constraint. Figure 6.4c shows maps of fluence through six of the 30 stimulus locations for all possible source rotations / tilts. These maps illustrate the importance of data fidelity in selecting a particular orbit. Both the task-driven orbit (pink) and conventional circular orbit (green horizontal line) are shown superimposed on the fluence maps, showing that the fluence through each stimulus depends on location with respect to surrounding anatomy and the embolization coil. The task-driven orbit tends to vertices that avoid the strong attenuation of the embolization coil (evident as a “black hole” in the fluence maps through which few x-rays are transmitted) and appears to exercise an orbit involving fewer redundant view angles over the 360° orbit — i.e., if rays pass through

the coil on one side of the trajectory, a tilt is sought for the opposing view to avoid the coil. While it is not possible to completely avoid rays passing through the coil for all stimulus locations, redundancy in the orbit allows collection of asymmetric views to compensate low-fidelity data in the opposing view.

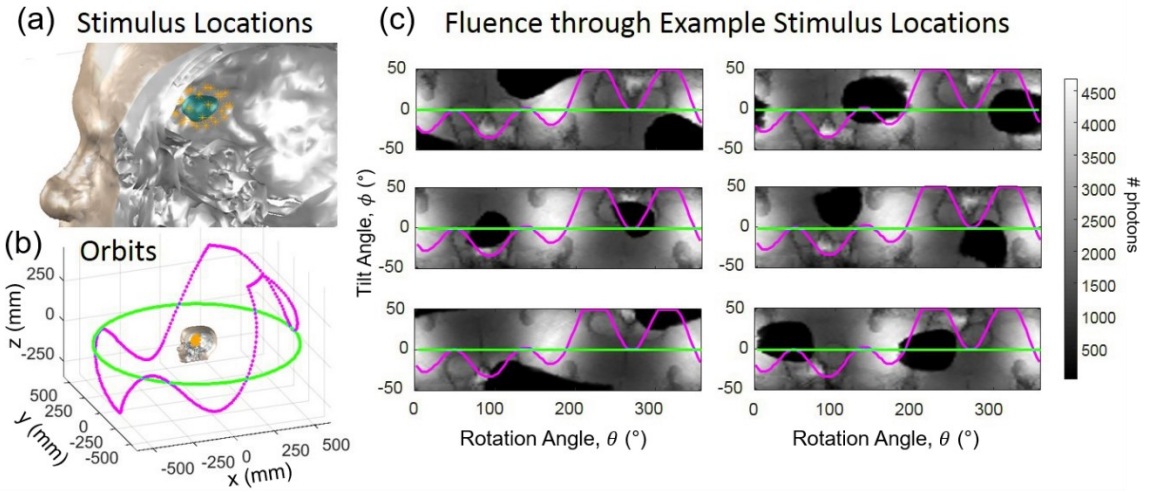

Figure 6.4. Task-driven orbit design for imaging about an embolization coil. (a) Thirty locations (orange markers) in proximity to the embolization coil mark the locations at which detectability of hemorrhage was computed in iterative optimization. (b) The task-driven (pink) and standard circular (green) orbits. (c) Orbits (θ, ϕ) superimposed on maps showing the fluence passing through six of the 30 stimulus locations.

CBCT images reconstructed from the circular and task-driven orbits are shown in Figure 6.5. Images for the circular orbit are degraded severely in proximity to the embolization coil due to decreased data fidelity (high attenuation) for measurements passing through the coil. Note that this degradation is entirely due to measurement statistics (noise) since the simulation in this study did not include polyenergetic effects. Strongly correlated noise (streaks) around the coil obscure many of the stimuli. By contrast, the task-driven orbit improved visualization of the simulated hemorrhages, and while high-frequency noise was elevated at other locations in the head (attributed to view sampling effects), the streaks and shading at the specified locations of interest were markedly

reduced. The multi-task design objective facilitates improved image quality at all locations around the embolization coil, effectively pushing image quality degradations away from the task locations.

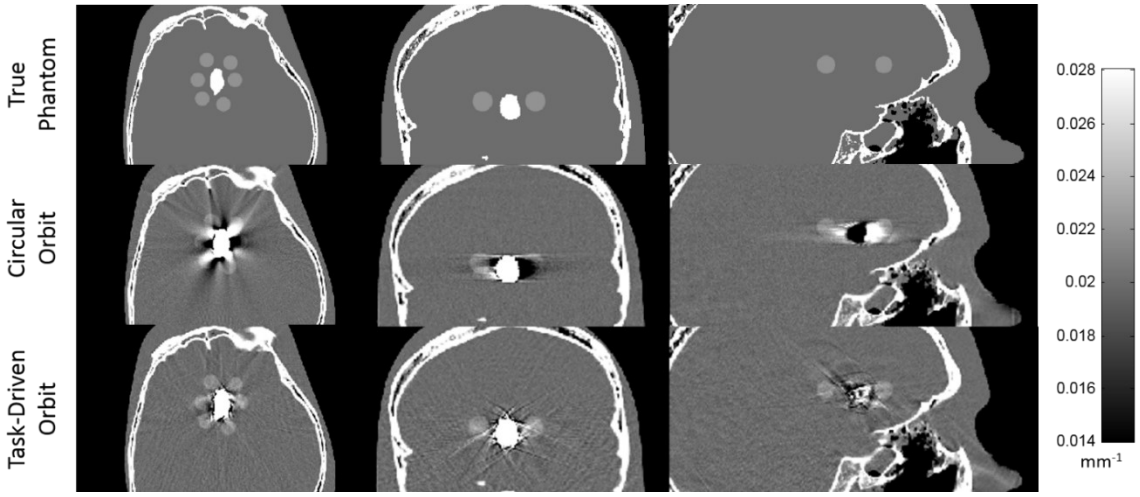

Figure 6.5. Task-driven imaging of simulated hemorrhage about an embolization coil. The circular orbit resulted in strong photon starvation artifacts / noise in proximity to the coil. The task-driven orbit mitigated such effects and improved conspicuity of simulated lesions about the coil.

6.4.2. Task-Driven Imaging in Real Data (CBCT Test Bench)

Figure 6.6 summarizes the test bench experiments involving an embolization coil in an anthropomorphic phantom. The top row of images (acquired before delivery of the coil) shows the locations of the simulated spherical hemorrhage. For this experiment, the task-driven orbit design focused on maximizing detectability at three locations posterior to the aneurysm. The shape of the designed orbit exhibits interesting features including an overall tilt to the orbit — selecting projections that avoid alignment of the highly attenuating skull base with the target ROI. Additionally, the task-driven orbit appears to seek non-redundant views with a slight wobble in the orbit.

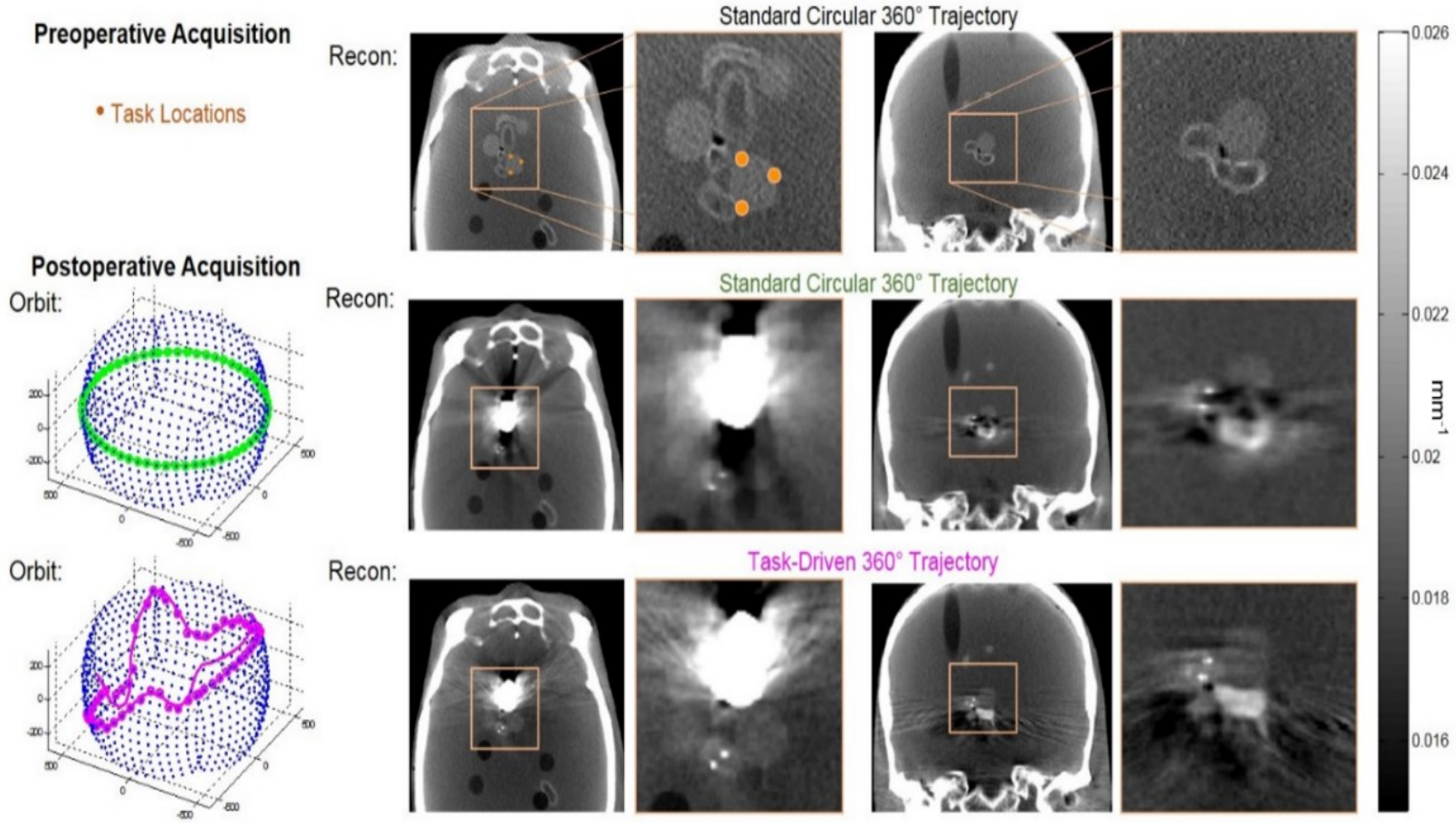

Figure 6.6. Task-driven orbit applied on the CBCT test bench for visualization of hemorrhage posterior to a coiled aneurysm. The preoperative scan shows details of the vessel and simulated spherical bleeds adjacent to an aneurysm. Three stimulus locations were selected posterior to the aneurysm. Following placement of the coil, a standard circular orbit exhibits severe shading and streaks that confound visualization about the embolization coil. The task-driven orbit yields improved visualization of both the posterior bleed and stent as well as residual contrast agent in the vasculature.

For a scan comprising N_{proj} = 364 projections over 360°, the air kerma was D_w ~ 21.1 mGy, recognizing that the dose for a task-driven orbit (with oblique views up to 30° off the central axial plane) likely departs somewhat from the dose for a circular scan. To the extent that the projection views are equally distributed above and below the central axial plane, the difference in dose is believed to be small.

Images from a standard circular orbit exhibit poor visualization in the ROI, and both the posterior hemorrhage and the legs of the stent used to hold the embolization coil in place are obscured by streaking and blooming effects due to low-fidelity measurements through the coil. By contrast, the task-driven trajectory shows good visualization of the posterior bleed as well as the legs of the stent. Residual contrast agent in the simulated vasculature is also evident (whereas the preoperative scan shows only the lumen of the simulated vessel). Since the task-driven optimization specified the posterior hemorrhage as the imaging task, it did not improve image quality anterior to the coil. Additionally, although the performance prediction and system model ignored polyenergetic effects, the models were sufficiently accurate to identify an orbit yielding measurable improvement in image quality.

6.4.3. Effect of Surrounding Anatomy

Figure 6.7 shows the fluence maps, task-driven trajectories, and reconstructed images of a simulated AVM — with the goal of optimizing detectability for six locations around the high-contrast embolization of an AVM nidus — in the skull base, the lateral cranial vault, or the interior crown of the skull. The task-driven approach solved the maxi-min objective for each ROI shown in Figure 6.7a–c. Fluence maps are shown for stimuli that exhibited the greatest increase in detectability. Analogous to the embolization coil in

Section 6.4.1, the embolized AVM strongly influences the fluence maps in each ROI, but the fluence maps differ for each location due to the differences in surrounding anatomy — influencing the overall attenuation so as to drive the solution to a distinct optimal orbit for different locations in the head and demonstrating that knowledge of both the surrounding anatomy and the location of interest for the imaging task(s) are necessary for trajectory optimization.

CBCT reconstructions at the stimulus exhibiting the greatest increase in d' are shown in Figure 6.7d–f, comparing results for a circular orbit to task-driven orbits. The spherical stimulus is more conspicuous in the task-driven images due to a reduction and / or reorientation of streaking and blooming effects arising from the high-contrast AVM embolization. Detectability for tasks at the skull base improved on average by 20.2%, at the lateral cranium on average by 28.6%, and at the crown on average by 7.0%. The smaller increase in d' at the crown is due to the fact that there is little room for improvement in a ROI for which rays traversing the stimulus is already low.

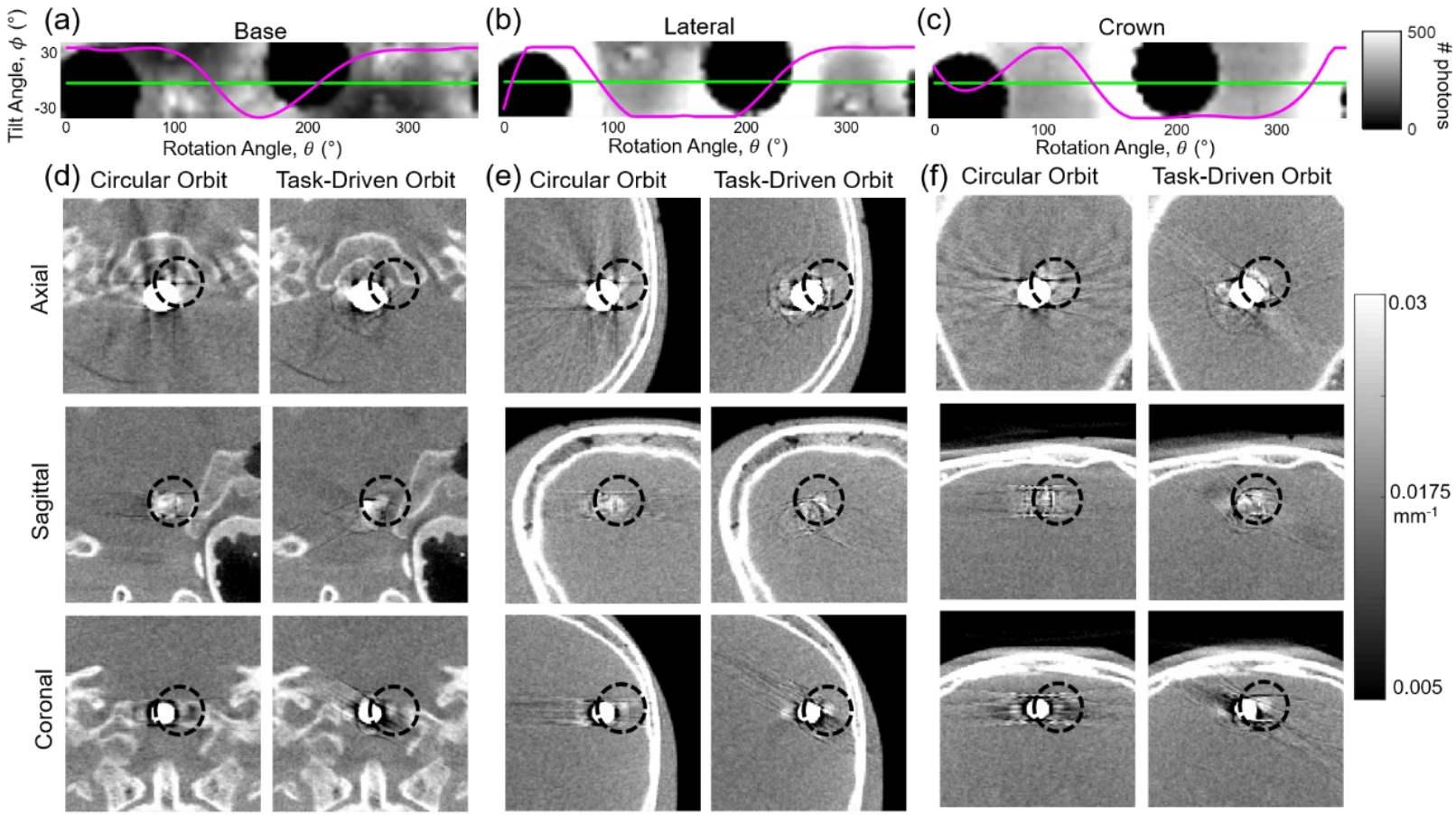

Figure 6.7. Task-driven imaging of a simulated AVM at the skull base, lateral cranium, and crown using six imaging tasks surrounding the AVM. Fluence maps in (a–c) show that the task-driven orbit seeks a path yielding highest fluence through the location of interest. Reconstructed images in (d–f) show slices through the spherical stimulus exhibiting the greatest increase in d'.

6.4.4. Task-Driven Imaging on a Robotic C-Arm

The AVM model imaged on the robotic C-arm is shown in Figure 6.8. The task-driven trajectory used a maxi-min objective over six task locations, as shown in Figure 6.8a, giving an increase in d' at all locations compared to a circular orbit. The lowest increase in d' was 7.0%, and the greatest increase was 13.0%, with an average increase of 10.3%. As illustrated in Figure 6.8a, the task-driven orbit favors large, positive tilt angles, with an excursion at $\theta = 170°$ that provides higher fidelity (lower attenuation) lateral views. Continuity of the scan orbit is ensured by the underlying b-spline model, but there was no constraint that the C-arm pose should match at the start ($\theta = 0°$) and stop ($\theta = 360°$) locations, which explains the observed discontinuity at the endpoints of the orbit. As shown in Chapter 4, this increased flexibility can, in certain cases, be advantageous in orbit design. The images in Figure 6.8b show a slight improvement in visibility of the acrylic spheres for the task-driven images in the axial, sagittal, and coronal images.

The air kerma was measured as described in Section 6.3.1 for a low-dose research protocol with a circular orbit and $N_{\text{proj}} = 360$ projections over 200°, giving a value of $D_w \sim 9.0$ mGy, recognizing that the dose for a task-driven scan may differ from that of a circular scan due to oblique views and differences in attenuation by the table.

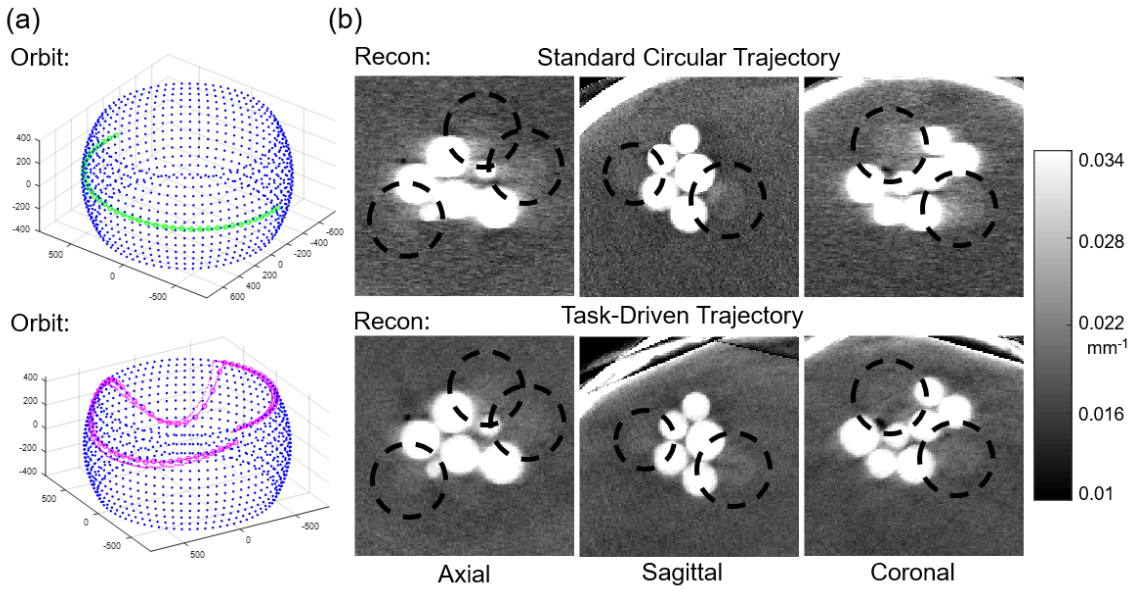

Figure 6.8. A simulated AVM imaged on the robotic C-arm using circular and task-driven trajectories. (a) Illustration of circular and task-driven orbits (green and pink, respectively). (b) CBCT reconstructions for each orbit, showing improved visualization of low-contrast spheres (highlighted by black dashed circles). The task-driven orbit exhibits reduced blurring of sphere edges, most noticeably in the axial and coronal planes.

6.5. Discussion and Conclusions

The work reported in this chapter builds on the theoretical framework detailed in Chapter 4 and the practical method for geometric calibration of non-circular orbits in Chapter 5 to investigate particular imaging scenarios in interventional neuroradiology — e.g., detection of hemorrhage in proximity to a coiled aneurysm and detection of untreated regions within an AVM nidus. The results demonstrate improvements in detectability index for task-driven orbits, with visible improvements in both simulated and real CBCT images.

The optimized orbits generally sought the highest fidelity (lowest attenuation) views and tended toward asymmetric vertices to reduce data redundancy in a 360° orbit. In the task-driven orbit, vertices separated by 180° were oblique relative to one another so that a lower fidelity view in the first half of the orbit may be compensated in the second

half of the orbit. The task-driven orbits resulted in improved visualization of ICH due to reduced noise and improved sampling in the ROI and by distributing streak artifacts to interfere less with detection of the stimuli. The work also investigated the effect of stimulus location and surrounding anatomy on trajectory design for different sites within the cranium. As demonstrated in Section 6.4.3., the cranial anatomy local to the ROI can change the optimal orbit for the same task, showing the sensitivity of the optimization to both the anatomy and instrumentation or implants.

Additionally, this work demonstrated operation of a clinical robotic C-arm for task-driven imaging by moving it through an optimal, non-circular orbit designed to improve performance of imaging tasks. A complex, task-driven orbit was demonstrated in a realistic clinical scenario, encompassing calculation of the task-driven orbit from a prior CBCT image, transfer of the trajectory to the robotic C-arm, acquisition of a non-circular orbit, geometric calibration of the non-circular orbit using a self-calibration technique, and reconstructing the 3D image using MBIR.

For this scenario, the effect of regularization in MBIR was apparent in the final images. Because the circular orbit involved lower fidelity projection data, the regularization was increased accordingly and resulted in increased blur of the sphere edges. The task-driven orbit, on the other hand, gathered higher-fidelity projection data and was less reliant on regularization to mitigate noise, yielding clearer delineation of the sphere edges. These results demonstrate the first successful implementation of task-driven imaging on a real clinical system for a semi-realistic anatomical context and imaging task.

The experiments involved optimization over a small number of task functions limited to a small ROI in the cranium using the maxi-min objective function, which ensures

that imaging performance is not sacrificed in some locations in favor of others. There may very well be situations for which a different, multi-location objective would be a better choice. It may also be of interest to perform the optimization over larger ROIs by including task locations farther from the attenuating object to give more uniform image quality over a larger ROI. In theory, one could define locations throughout the entire cranial vault as locations of interest to generate an orbit that provides globally increased detectability. In addition, imaging tasks of various frequency content and contrast could be included in the optimization to allow uncertainty in the stimulus.

It has been established that the detectability index can be related to real observer performance by way of area under the receiver operating characteristic curve through an error function (Tward et al 2007). Given the shape of an error function, the observer performance increases with d' almost linearly when d' is close to zero. As d' increases, the corresponding increase in observer performance loses its linear dependence and the slope of the function decreases toward zero. The non-linear relationship between d' and observer performance indicates that it is not always guaranteed that an increase in d' will result in a visibly improved image. The relationship between d' and observer performance is an important point to consider when evaluating task-driven images, and an adjusted task-driven optimization function that takes this relationship into account may be of value for future work.

Another important point of future work is the expansion of parameters contained within the optimization to further improve the orbit and overall imaging chain — for example, scan technique factors (kV and mAs) and reconstruction parameters (regularization constant β). Such a task-driven CBCT scanning process presents an

ambitious new paradigm for prospective optimization of image quality and / or reducing patient dose. For flexible imaging platforms such as a robotic C-arm, additional DoF could be incorporated in defining the source-detector trajectory beyond the two (θ, ϕ) investigated in the results reported above — for example, translation of the source and / or detector for non-isocentric orbits with large FOV.

In this work, constraints were imposed on the tilt angle to conservative collision limits and required a 360° total orbit in all cases. Changing or removing these constraints may be of interest to optimal short-scan trajectories and extension of task-driven imaging to tomosynthesis in which the optimal set of limited projection data is solved for difficult imaging scenarios. B-spline knot locations were also constrained to be equally spaced along the trajectory, but a fixed sampling interval may not necessarily be optimal. The sampling of b-spline knots represents another parameter that could be optimized, for example, by allowing a higher sampling density of knots for views carrying spatial frequency content consistent with the imaging task.

In the experiments presented, the anatomical model was an exact representation of the object (i.e., the patient) and did not consider potential uncertainty in the anatomical model. In realistic clinical scenarios, there may be extraneous regions of high attenuation within the patient stemming from surgical tools, contrast agent, and / or embolization sites that were not accounted for in the planning or anatomical model of the patient. This limitation could be explored further by representing the patient model and parameters that define the imaging tasks by probability distributions, rather than fixed quantities. A robust estimate of the ensemble optimum could be chosen from the resulting distribution of orbits.

Recent work (Gang et al 2020) aims to eliminate uncertainty in the anatomical model by performing the optimization over all possible metal location.

Another limitation of relying on an anatomical model is the image quality of $\boldsymbol{\mu}_{\mathbf{prior}}$. It can be envisioned that — depending on clinical workflow — the source of $\boldsymbol{\mu}_{\mathbf{prior}}$ could be a diagnostic quality MDCT acquired prior to a procedure or a CBCT acquired at the beginning of the procedure. The latter raises potential limitations in instances of strong truncation, which introduces error in the forward model in the optimization. T1- or T2-weighted MRI is typically not a useful input model, but numerous methods for synthesizing a CT-like image (i.e., an image with intensities proportional to electron density) from MRI have emerged in the last decade (Chartsias et al 2017, Lee et al 2017, Roy et al 2017).

The current work compared the image quality in task-driven and conventional circular orbits under conditions of matched bare-beam exposure. Dosimetry (e.g., D_w measurements) for task-driven orbits introduces some complexity associated with oblique projections and is difficult to prescribe for cases in which the orbit is not known a priori. Such considerations raise interesting future work in dosimetry for non-circular orbits, including measurement and Monte Carlo methods.

Further testing of task-driven imaging methods would benefit from a more streamlined interface for executing non-circular orbits on the robotic C-arm. In the current work, non-circular orbits were realized using a step-and-shoot method by directing the robot to each vertex via an external workstation. Images were acquired using a 2D radiographic imaging protocol at each vertex, collected individually, and processed offline. This time-consuming workflow (approximately 1.5 hours for a single scan in the work presented above) is not suitable to clinical studies and would be greatly improved by an

interface allowing 3D imaging protocols with orbit and vertex definition consistent with smooth, continuous motion of the robot.

Overall, task-driven orbits appeared to be of most benefit in difficult imaging scenarios in which highly attenuating objects in the FOV cause strong streaks and other metal artifacts that confound visualization of nearby, low-contrast objects. Such difficult imaging scenarios are common in IGI, in which CBCT images acquired during the procedure often include metal instrumentation, and ROIs tend to be in proximity to such instrumentation. Application of task-driven imaging in scenarios beyond neuroradiology may be of similar benefit — for example, orthopedic imaging, dental imaging, and musculoskeletal imaging, where metal implants are a common source of image artifacts and reduced image quality.

Chapter 7: Summary and Conclusions

7.1. Key Findings of the Thesis

7.1.1. 3D–2D Registration as a Basis for Rigid Motion Compensation and Geometric Calibration

In Chapter 2 a fiducial-free method to mitigate motion artifacts was presented using 3D–2D image registration that simultaneously compensates for residual errors in the intrinsic and extrinsic parameters of geometric calibration. The 3D–2D registration process registered each projection to a prior 3D image by maximizing the GO similarity objective using the CMA-ES optimizer. The resulting rigid transforms were applied to the system PMs, and a 3D image was reconstructed via MBIR. Phantom experiments were conducted using a robotic C-arm to image a head phantom undergoing 5–15 cm translations and 5–15º rotations during image acquisition. To further test the algorithm, clinical images were acquired with a CBCT head scanner in which long scan times were susceptible to significant patient motion. For phantom studies, SSIM between motion-free and motion-compensated images was > 0.995, with significant improvement ($p < 0.001$) compared to the SSIM of uncompensated images. Additionally, motion-compensated images exhibited a PSF with FWHM comparable to that of the motion-free reference image. Qualitative comparison of the uncompensated and motion-compensated clinical images demonstrated substantial visible improvement in image quality after motion compensation. These studies indicate that the method could provide a useful approach to motion artifact compensation under assumptions of local rigidity, as in the head and pelvis.

A similar 3D–2D registration method was used in Chapter 5 for geometric calibration of non-circular source–detector orbits. The method used the NGI similarity objective for speed and the CMA-ES optimizer for robustness against local minima and changes in image content. The resulting transformation provided a "self-calibration" of system geometry. The algorithm was tested in phantom studies using both a CBCT test-bench and a robotic C-arm for circular and non-circular orbits. Self-calibration performance was evaluated in terms of the FWHM of the PSF in CBCT reconstructions, RPE of BBs placed on each phantom, and overall image quality and presence of artifacts in CBCT images. Similar to results in Chapter 2 for 3D–2D registration, self-calibration improved the FWHM for all cases — e.g., on the CBCT bench, FWHM = 0.86 mm for conventional calibration compared to 0.65 mm for self-calibration ($p < 0.001$). Similar improvements were measured in RPE — e.g., on the robotic C-arm, RPE = 0.73 mm for conventional calibration compared to 0.55 mm for self-calibration ($p < 0.001$). Visible improvement was evident in CBCT reconstructions using self-calibration, particularly about high-contrast, high-frequency objects (e.g., temporal bone air cells and a biopsy needle). The results indicated that self-calibration can improve even upon systems with presumably accurate geometric calibration and is applicable to situations where conventional calibration is not feasible, such as complex non-circular CBCT orbits and systems with irreproducible source–detector trajectory. The 3D–2D registration methods of Chapter 2 and Chapter 5 are highly parallelizable, and the combined compensation of patient motion and residual geometric calibration errors provides added benefit that could be valuable in routine clinical use.

7.1.2. Deformable Motion Compensation Using a 3D Autofocus Method

In Chapter 3, an image-based motion compensation method was developed to address challenges related to *deformable* patient motion and thereby improve CBCT guidance in soft-tissue interventions (e.g., liver chemoembolization). Motion compensation was achieved by selecting a set of small ROIs in the uncompensated image to minimize a cost function consisting of an autofocus objective and spatiotemporal regularization penalties. Motion trajectories were estimated using CMA-ES and used to interpolate a 4D spatiotemporal MVF. The motion-compensated image was reconstructed using a modified FBP approach. Being purely image-based, the method does not require additional input besides the raw projection imaging data.

Experimental studies investigated: (1) various autofocus objective functions, analyzed using a digital phantom with a range of motion magnitude; (2) spatiotemporal regularization, studied using a CT dataset from TCIA with deformable motion of variable magnitude; and (3) performance in complex anatomy, evaluated in cadavers undergoing simple and complex motion imaged on a CBCT-capable mobile C-arm system. Gradient entropy was found to be the best autofocus objective for soft-tissue CBCT, increasing SSIM by 42% to 92% over the range of motion magnitudes investigated. The optimal temporal regularization strength was found to vary widely (0.5–5 mm^{-2}) over the range of motion magnitudes investigated, whereas optimal spatial regularization strength was relatively constant (0.1). In cadaver studies, deformable motion compensation was shown to improve local SSIM by ~17% for simple motion and ~21% for complex motion and provided strong visual improvement of motion artifacts (reduction of blurring and streaks and improved visibility of soft-tissue edges). The studies demonstrate the robustness of

deformable motion compensation to a range of motion magnitudes, frequencies, and other factors (e.g., truncation and scatter). The results also include initial application of the deformable motion compensation method to an ongoing clinical study, demonstrating its potential utility under conditions of realistic, complex, deformable motion. Remaining challenges to clinical translation are discussed below, including the need for robust initialization and faster computation time.

7.1.3. Task-Driven Source–Detector Trajectories

In Chapter 4, a mathematical framework was reported for the design of orbital trajectories that are optimal to a particular imaging task(s) in CBCT systems that have the capability for general source–detector positioning. The framework allows various parameterizations of the orbit as well as constraints based on imaging system capabilities. An MBIR method was applied to accommodate non-standard system geometries. We used analytical models of local noise and spatial resolution that include dependencies of the reconstruction algorithm on patient anatomy, x-ray technique, and system geometry. These image quality predictors served as inputs to task-based imaging performance in terms of the detectability index, d', which was optimized with respect to the parameters of source–detector orbit in CBCT data acquisition. We investigated the framework for task-driven source–detector trajectory design in several examples to examine the dependence of optimal trajectories on the imaging task(s), including location and spatial-frequency dependence. A variety of multi-task objectives were also investigated, and the advantages to imaging performance were quantified in simulation studies.

In Chapter 6, the methodology as detailed in Chapter 4 was applied to scenarios emulating imaging tasks in neuro-IR. The approach was applied to simulated cases of

endovascular embolization of an aneurysm and AVM, tested with real data using a CBCT test bench, and implemented for the first time on a clinical interventional robotic C-arm. Task-driven trajectories were found to generally favor higher fidelity (i.e., less noisy) views, with an average increase in d' ranging from 7.0% to 28.0%. Visually, increases in d' resulted in improved conspicuity of stimuli by reducing noise and altering noise correlation to a form distinct from the spatial frequencies associated with the imaging task. The improvements in detectability and the demonstration of the task-driven workflow using a real interventional imaging system show the potential of the task-driven imaging framework to improve imaging performance on motorized, multi-axis C-arms.

7.2. Optimization Frameworks

Throughout the thesis, the methods invoked principles of optimization to find the parameters that maximize or minimize an objective function. Optimization problems can effectively be broken down into three components: (1) the objective function, whose value is maximized or minimized over the course of the optimization; (2) a mathematical model of the input values (e.g., geometric transformation model, detector signal and noise model, etc.) included in the objective function; and (3) the optimization algorithm that finds the optimal parameters. Each component plays a role in finding the optimal solution and avoiding local minima in a complex search space.

Table 7.1 summarizes these components of the optimization methods presented in Chapters 2–6. The optimizations for rigid motion compensation and self-calibration are quite similar, differing only in the choice of objective function (GO for rigid motion compensation vs. NGI for self-calibration). We found GO to be the more robust objective

under conditions of content mismatch between the 3D and 2D image data, while NGI was faster by avoiding a median operation. The method for deformable motion compensation involved the most complex objective function, with two regularization functions (temporal R_t and spatial $R_{\mathbf{x}}$) added to the autofocus objective to encourage smooth motion in both time and space. Similarly (but in a context quite distinct from motion estimation), PL image reconstruction uses spatial regularization (R) to encourage smoothness in the reconstructed image. The regularization terms in each of these objectives works to ensure that the resulting solution is physically realistic, to enforce some property believed to be true for the result, and to reduce the complexity of the search space.

The mathematical model for 2D projection image formation in rigid motion compensation and self-calibration is simply the forward projection of a 3D object to generate a 2D projection using Beer's Law. For task-driven imaging and PL reconstruction, the model is extended to include a Poisson distribution of individual photons reaching the detector. By contrast, the 3D image domain model underlying the deformable motion compensation method does not rely on the generation of DRRs, and the motion model was local 6 DoF rigid motion (a separate 6 DoF transform at each ROI in the image), with the FBP reconstruction modified to include "warped" backprojection.

Table 7.1. A summary view of optimization methods underlying the registration and reconstruction approaches presented in the thesis.

Method	Objective	Model	Optimizer
Rigid Motion Compensation	$\widehat{\boldsymbol{T}} = \arg\max_{\boldsymbol{T}} \mathrm{GO}(\boldsymbol{y}, \boldsymbol{y}_{\mathbf{prior}})$	$\boldsymbol{y}_{\mathbf{prior}} = b_0 e^{-\mathbf{A}(\boldsymbol{T})\boldsymbol{\mu}_{\mathbf{prior}}}$	CMA-ES
Deformable Motion Compensation	$\hat{T} = \arg\min_{\boldsymbol{T}} \sum_{m=1}^{M} S(\boldsymbol{\mu}_{\boldsymbol{m}}) + \beta_t R_t(\boldsymbol{T}_{\boldsymbol{m}}) + \beta_{\mathrm{x}} R_{\mathrm{x}}(\boldsymbol{T}_{\boldsymbol{m}})$	$\boldsymbol{T}_{\boldsymbol{m}}(k,j) = \sum_{n=0}^{N} c_{nj} B(k - k_n)$	CMA-ES
Task-Driven Trajectories	$\widehat{\boldsymbol{\Omega}} = \arg\max_{\boldsymbol{\Omega}\in\boldsymbol{\Omega}_{\mathbf{feasible}}} d'(\boldsymbol{\Omega}; v)$	$\bar{y}_i = b_0 e^{-[\mathbf{A}(\boldsymbol{\Omega})\boldsymbol{\mu}]_i}$	CMA-ES
Self-Calibration	$\widehat{\boldsymbol{T}} = \arg\max_{\boldsymbol{T}} \mathrm{NGI}(\boldsymbol{y}, \boldsymbol{y}_{\mathbf{prior}})$	$\boldsymbol{y}_{\mathbf{prior}} = b_0 e^{-\mathbf{A}(\boldsymbol{T})\boldsymbol{\mu}_{\mathbf{prior}}}$	CMA-ES
Penalized-Likelihood Reconstruction	$\widehat{\boldsymbol{\mu}} = \arg\max_{\boldsymbol{\mu}} L(\boldsymbol{y}; \boldsymbol{\mu}) - \beta R(\boldsymbol{\mu})$	$\boldsymbol{y} = b_0 e^{-\mathbf{A}(\boldsymbol{\Omega})\boldsymbol{\mu}}$	Gradient Descent OS-SQS

As seen in Table 7.1, much of this work invoked the CMA-ES optimizer. As discussed in previous chapters, CMA-ES is attractive because it is derivative-free and is robust to local minima in the search space. The search space for non-convex optimization problems (such as those presented in this thesis) can be highly complex and becomes increasingly complex with an increasing number of parameters. The ability to avoid local minima is paramount, and the performance of CMA-ES can be improved by judicious selection of the parameters λ_{CMAES} and σ_{CMAES}. Increasing λ_{CMAES} increases the number of function evaluations at each iteration, thereby increasing the robustness of the algorithm to local minima (at the cost of runtime / computer burden). Increasing σ_{CMAES} expands the extent of the search space, which can also help the algorithm avoid local minima. In contrast, PL estimation used an optimization algorithm based on gradient descent, in which the gradient of the function is evaluated at each iteration of the optimization and used to direct the 3D image estimate in the "direction" (i.e., the voxel value) that maximizes the objective. There is a vast spectrum of optimization methods in the scientific literature, both deterministic (e.g., gradient-based) and stochastic (e.g., CMA-ES), that may be applicable to the methods described in this thesis, typically involving trade-offs of speed and robustness. Further investigation of alternative optimization algorithms may be of interest for future work.

7.3. Future Work and Integration with Clinical Workflow

Preservation (or improvement) of workflow is essential to the success of technology integration in clinical use, and IGI is no exception. Innovation within such complex scenarios must thoughtfully consider routine workflow (and variations in workflow), the diversity and heterogeneity of systems already in use, and the perspectives of all stakeholders — including not only the interventionalist, but the entire care team and even the hospital / healthcare system surrounding the delivery of care (e.g., healthcare information technology integration, cost constraints, and reimbursement models). At a minimum, technology translation must consider how its introduction in clinical workflow will affect the time, cost, and safety associated with its clinical use.

The rigid motion compensation and self-calibration methods of Chapters 2 and 5 both use 3D–2D registration, taking advantage of a high-quality prior image that is often available in the context of IGI. In some clinical scenarios, the availability of a reliable, patient-specific prior image may be unrealistic (e.g., emergent intervention or diagnostic imaging), but in many IGI scenarios, such an image is available from preoperative planning and / or intraoperative imaging performed at the beginning of the case. The results showed that 3D–2D registration was robust in capturing both large-scale (> 10 mm) and small-scale (< 1 mm) motion stemming from both the patient and the C-arm gantry. In particular, the results of Section 5.4 demonstrated that the self-calibration method was even able to improve upon a system's geometric pre-calibration, indicating potential benefit to apply

the method to *all* intraoperative CBCT acquisitions (assuming that a high-quality prior image is available).

Such a bold change to routine workflow requires that the computation time for 3D–2D registration be considered, noting that conventional FBP with a geometric pre-calibration operates in just a few seconds. With NGI as the objective function in self-calibration, 3D–2D registration for a single projection was ~3 s for 6 DoF registration and ~5 s for 9 DoF registrations. Using the GO objective increased runtime by a factor of ~3 (due to the median operator in the current GO implementation). Since these registrations could in principle be fully parallelized (i.e., all projection data registered in parallel), 3D–2D registration within a few seconds could be amenable to clinical translation.

Given a high degree of parallelization, these runtimes may be consistent with clinical workflow requirements, but future work to support such translation is warranted. In the work presented in Chapters 2 and 5, each 3D–2D registration was performed sequentially to utilize the results of previous registrations to initialize subsequent registrations (which breaks parallelizability). An alternative approach could incorporate the conventional geometric pre-calibration (typically performed by a service engineer) to initialize each PM. Furthermore, post-processing of a fully parallelized self-calibration is certainly possible (e.g., smoothing or regularization); however, such processing should preserve real, high frequency jitter / vibration from the C-arm system and / or tremor from the patient while maintaining the ability to trap outliers (e.g., in the work reported above, detecting unrealistic change in magnification between views). Further parallelization techniques, namely, the sampling of candidate solutions during CMAE-ES iterations, could decrease the registration time further. All of these solutions likely carry increased cost

associated with computing hardware — e.g., the incorporation of multi-GPU capability in the image reconstruction workstation.

Compared to 3D–2D registration for simultaneous compensation of motion and geometric error (which may be applicable to all CBCT images for which a suitable prior image exists), the *deformable* motion compensation method is more likely to be invoked on a case-by-case basis for CBCT images that exhibit highly deformable motion of the patient. To identify CBCT images that require deformable motion compensation, the radiologist could flag images manually, or a method to automatically detect residual artifacts can be envisioned. Deep learning techniques are well suited to such tasks in image classification using. For example, Sisniega et al (2020) developed a CNN capable of quantifying the spatially varying patient motion amplitude in a reconstructed CBCT image. Such a network could be used not only to identify images that need deformable motion compensation, but also to initialize parameters of the deformable motion compensation algorithm, as discussed in Section 3.5.

If no prior image is available, the deformable motion compensation method could in principle be used in place of the 3D–2D registration (to correct rigid motion and geometrical calibration error). By virtue of the autofocus objective, the method relies only on the raw projection data from the intraoperative CBCT scan. If a single ROI is used (cf., multiple small ROIs placed throughout the volume) without spatial interpolation, the method simplifies to the rigid motion compensation problem. The reduction in optimization parameters for this simple case greatly reduces the dimensionality of the search space (and subsequently the runtime), making the method more amenable to clinical workflow. However, it should be noted that the loss of spatial regularization within the

optimization may make the optimizer more susceptible to local minima, producing solutions that exaggerate image artifacts with sharp gradients (e.g., the streaks from highly attenuating objects).

Recently, hybrid rooms featuring both an MDCT scanner and a fixed-room C-arm system present the opportunity to exploit each modality to its strengths in image quality and workflow — e.g., diagnostic-quality MDCT before and / or after the case and CBCT and fluoroscopy throughout. An obvious disadvantage is the cost associated with such an installation. The ability to acquire MDCT images within the interventional suite permits a high level of diagnostic quality and imaging modes not commonly available in CBCT — e.g., dual-energy MDCT; however, the workflow associated with patient transfer between the interventional setup and the bore of the MDCT scanner must be carefully considered relative to the time of the procedure and safety of the patient.

The integration of task-driven imaging into clinical workflow presents its own distinct considerations. The method invokes several key elements of prior information that need to be defined prior to acquiring a "task-driven" image. For example, the imaging task must be defined. Furthermore, the patient model (either a patient-specific prior image or a suitable 3D model) must be identified and augmented — if appropriate — to contain interventional devices (namely, highly attenuating metal objects) that tend to play a strong role in the orbit optimization. The patient model (image or atlas) must be registered to the patient — for example, by 3D–2D registration using two projection views. The C-arm orbit must be constrained so as not to collide with the patient, operating table, or other systems in the interventional setup, which may require additional levels of measurement, monitoring, and system integration than currently in use. Successful translation of task-

driven imaging to routine workflow requires such measures to be incorporated in a practical manner such that the benefits to image quality, assurance of treatment delivery, reduction in comorbidity, and improvements in patient outcome are justified.

To reduce the burden on the interventional radiologist in task-driven imaging workflow, certain aspects of the workflow fall naturally to the physician assistant and / or radiology technologist. Tasks that may be increasingly routine and suitable to such support staff include specification of prior images (or models), registration to the patient, and ensuring safety from collision. Even specification of the imaging task, which in this work was derived from spatial-frequency-dependent, hypothesis-testing task-functions, could be reduced to relatively simple formulation of: (1) location; (2) contrast (e.g., soft-tissue or metal); and (3) scale (e.g., a large diffuse bleed or fine discrimination between structures).

The methods established in this thesis help to address some of the most pressing challenges in CBCT imaging — namely, reducing artifacts associated with complex patient motion and improving the detectability of fine and / or low-contrast structures. The work has answered the overall thesis statement — ***image quality in CBCT for IGI can be improved through patient motion compensation and task-based design of CBCT imaging protocols*** — and points to the ambitious endeavor still ahead to incorporate such advanced imaging methods into the clinical workflow and to demonstrate the benefits to the performance of IGI as well as the safety and clinical outcome of patients.

Abbreviations

AEC	Automatic exposure control
AP	Anterior-posterior
AVM	Arteriovenous malformation
BB	Ball bearing
CBCT	Cone-beam computed tomography
CMA-ES	Covariance matrix adaptation-evolution strategy
CT	Computed tomography
CTDI	Computed tomography dose index
DICOM	Digital Imaging and Communications in Medicine
DoF	Degrees of freedom
DRR	Digitally reconstructed radiograph
FBP	Filtered backprojection
FDK	Feldkamp-Davis-Kress
FOV	Field of view
FPD	Flat-panel detector
FWHM	Full-width at half-maximum
GC	Gradient correlation
(N)GI	(Normalized) Gradient information
GO	Gradient orientation
GPU	Graphics processing unit
ICH	Intracranial hemorrhage
IGI	Image-guided interventions
IGRT	Image-guided radiation therapy
IR	Interventional radiology
IRB	Institutional Review Board
LLAT	Left lateral
MBIR	Model-based iterative reconstruction
MDCT	Multi-detector computed tomography
MR	Magnetic resonance
MVF	Motion vector field
PA	Posterior-anterior
PCA	Principle component analysis
PICCS	Prior image constrained compressed sensing
PL	Penalized-likelihood
PM	Projection matrix
PSF	Point spread function
PWLS	Penalized weighted least-squares
RLAT	Right lateral
RMSE	Root-mean-square error
ROI	Region of interest
RPE	Reprojection error
SAD	Source-to-axis distance
SDD	Source-to-detector distance
SI	Superior-inferior
SSIM	Structural similarity
TACE	Transarterial chemoembolization
TCIA	The Cancer Imaging Archive

Bibliography

Alabdulghani, F., O'Brien, A., and Brophy, D. (2018). Application of cone-beam computed tomography angiography in a uterine fibroid embolization procedure: a case report. *Radiology Case Reports*, 13(1), 130–134.

Bartolac, S., Graham, S., Siewerdsen, J., and Jaffray, D. (2011). Fluence field optimization for noise and dose objectives in CT. *Medical Physics*, 38(S1), S2–S17.

Berger, M., Müller, K., Aichert, A., Unberath, M., Thies, J., Choi, J.-H., Fahrig, R., and Maier, A. (2016). Marker-free motion correction in weight-bearing cone-beam CT of the knee joint. *Medical Physics*, 43(3), 1235–1248.

Berris, T., Gupta, R., and Rehani, M. M. (2013). Radiation dose from cone-beam CT in neuroradiology applications. *American Journal of Roentgenology*, 200(4), 755–761.

Binder, N., Matthäus, L., Burgkart, R., and Schweikard, A. (2005). A robotic C-arm fluoroscope. *The International Journal of Medical Robotics and Computer Assisted Surgery*, 1(3), 108–116.

Boone, J. M., Nelson, T. R., Lindfors, K. K., and Seibert, J. A. (2001). Dedicated breast CT: radiation dose and image quality evaluation. *Radiology*, 221(3), 657–667.

Brehm, M., Paysan, P., Oelhafen, M., and Kachelrieß, M. (2013). Artifact-resistant motion estimation with a patient-specific artifact model for motion-compensated cone-beam CT. *Medical Physics*, 40(10), 101913.

Brilstra, E. H., Rinkel, G. J. E., van der Graaf, Y., van Rooij, W. J. J., and Algra, A. (1999). Treatment of intracranial aneurysms by embolization with coils: a systematic review. *Stroke*, 30(2), 470–476.

Bronnikov, A. V. (1999). Virtual alignment of x-ray cone-beam tomography system using two calibration aperture measurements. *Optical Engineering*, 38(02), 381–386.

Bueno-Ibarra, M. A., Álvarez-Borrego, J., Acho, L., and Chávez-Sánchez, M. C. (2005). Fast autofocus algorithm for automated microscopes. *Optical Engineering*, 44(6), 063601.

Cao, Q., Sisniega, A., Brehler, M., Stayman, J. W., Yorkston, J., Siewerdsen, J. H., and Zbijewski, W. (2018). Modeling and evaluation of a high-resolution CMOS detector for cone-beam CT of the extremities. *Medical Physics*, 45(1), 114–130.

Capostagno, S., Stayman, J. W., Jacobson, M. W., Ehtiati, T., Weiss, C. R., and Siewerdsen, J. H. (2019). Task-driven source–detector trajectories in cone-beam computed tomography: II. application to neuroradiology. *Journal of Medical Imaging*, 6(2), 025004.

Capostagno, S., Sisniega, A., Stayman, J. W., Ehtiati, T., Weiss, C. R., and Siewerdsen, J. H. (2020). Image-based deformable motion compensation in cone-beam CT: translation to clinical studies in interventional body radiology. *Medical Imaging 2020: Image-Guided Procedures, Robotic Interventions, and Modeling,* 11315, 113150B.

Carrino, J. A., Al Muhit, A., Zbijewski, W., Thawait, G. K., Stayman, J. W., Packard, N., Senn, R., Yang, D., Foos, D. H., Yorkston, J., and Siewerdsen, J. H. (2014).

Dedicated cone-beam CT system for extremity imaging. *Radiology*, 270(3), 816–824.

Chartsias, A., Joyce, T., Dharmakumar, R., and Tsaftaris, S. A. (2017). Adversarial image synthesis for unpaired multi-modal cardiac data. *Simulation and Synthesis in Medical Imaging,* 10557, 3–13.

Chen, G. H., Tang, J., and Leng, S. (2008). Prior image constrained compressed sensing (PICCS): a method to accurately reconstruct dynamic CT images from highly undersampled projection data sets. *Medical Physics*, 35(2), 660–663.

Chetley Ford, J., Zheng, D., and Williamson, J. F. (2011). Estimation of CT cone-beam geometry using a novel method insensitive to phantom fabrication inaccuracy: implications for isocenter localization accuracy. *Medical Physics*, 38(6Part1), 2829–2840.

Cho, Y., Moseley, D. J., Siewerdsen, J. H., and Jaffray, D. A. (2005). Accurate technique for complete geometric calibration of cone-beam computed tomography systems. *Medical Physics*, 32(4), 968–983.

Choi, J. H., Fahrig, R., Keil, A., Besier, T. F., Pal, S., McWalter, E. J., Beaupré, G. S., and Maier, A. (2013). Fiducial marker-based correction for involuntary motion in weight-bearing C-arm CT scanning of knees. Part I. Numerical model-based optimization. *Medical Physics*, 40(9), 091905.

Cleary, K. and Peters, T. M. (2010). Image-guided interventions: technology review and clinical applications. *Annual Review of Biomedical Engineering*, 12, 119–142.

Daly, M. J., Siewerdsen, J. H., Moseley, D. J., Jaffray, D. A., and Irish, J. C. (2006). Intraoperative cone-beam CT for guidance of head and neck surgery: assessment of dose and image quality using a C-arm prototype. *Medical Physics*, 33(10), 3767–3780.

Daly, M. J., Siewerdsen, J. H., Cho, Y. B., Jaffray, D. A., and Irish, J. C. (2008). Geometric calibration of a mobile C-arm for intraoperative cone-beam CT. *Medical Physics*, 35(5), 2124–2136.

Dang, H., Wang, A. S., Sussman, M. S., Siewerdsen, J. H., and Stayman, J. W. (2014). dPIRPLE: a joint estimation framework for deformable registration and penalized-likelihood CT image reconstruction using prior images. *Physics in Medicine & Biology*, 59(17), 4799–4826.

Dang, H., Siewerdsen, J. H., and Stayman, J. W. (2015). Prospective regularization design in prior-image-based reconstruction. *Physics in Medicine & Biology*, 60(24), 9515–9536.

Dang, H., Stayman, J. W., Xu, J., Zbijewski, W., Sisniega, A., Mow, M., Wang, X., Foos, D. H., Aygun, N., Koliatsos, V. E., and Siewerdsen, J. H. (2017). Task-based statistical image reconstruction for high-quality cone-beam CT. *Physics in Medicine & Biology*, 62(22), 8693–8719.

De Man, B., Nuyts, J., Dupont, P., Marchal, G., and Suetens, P. (1998). Metal streak artifacts in X-ray computed tomography: a simulation study. *1998 IEEE Nuclear Science Symposium Conference Record,* 3, 1860–1865.

De Silva, T., Uneri, A., Ketcha, M. D., Reaungamornrat, S., Kleinszig, G., Vogt, S., Aygun, N., Lo, S.-F., Wolinsky, J.-P., and Siewerdsen, J. H. (2016). 3D–2D image registration for target localization in spine surgery: investigation of similarity

metrics providing robustness to content mismatch. *Physics in Medicine & Biology*, 61(8), 3009–3025.

Dennerlein, F. and Jerebko, A. (2012). Geometric jitter compensation in cone-beam CT through registration of directly and indirectly filtered projections. *2012 IEEE Nuclear Science Symposium and Medical Imaging Conference Record (NSS/MIC)*, 2892–2895.

Dinelle, K., Blinder, S., Cheng, J.-C., Lidstone, S., Buckley, K., Ruth, T. J., and Sossi, V. (2006). Investigation of subject motion encountered during a typical positron emission tomography scan. *2006 IEEE Nuclear Science Symposium Conference Record,* 6, 3283–3287.

Erdogan, H. and Fessler, J. A. (1999). Ordered subsets algorithms for transmission tomography. *Physics in Medicine & Biology*, 44(11), 2835–2851.

Fahrig, R., Dixon, R., Payne, T., Morin, R. L., Ganguly, A., and Strobel, N. (2006). Dose and image quality for a cone-beam C-arm CT system. *Medical Physics*, 33(12), 4541–4550.

Feldkamp, L. A., Davis, L. C., and Kress, J. W. (1984). Practical cone-beam algorithm. *Journal of the Optical Society of America A*, 1(6), 612–619.

Fessler, J. A. (1996). Mean and variance of implicitly defined biased estimators (such as penalized maximum likelihood): applications to tomography. *IEEE Transactions on Image Processing*, 5(3), 493–506.

Fessler, J. A. and Rogers, W. L. (1996). Spatial resolution properties of penalized-likelihood image reconstruction: space-invariant tomographs. *IEEE Transactions on Image Processing*, 5(9), 1346–1358.

Fieselmann, A., Steinbrener, J., Jerebko, A. K., Voigt, J. M., Scholz, R., Ritschl, L., and Mertelmeier, T. (2016). Twin robotic x-ray system for 2D radiographic and 3D cone-beam CT imaging. *Medical Imaging 2016: Physics of Medical Imaging*, 9783, 97830G.

Gang, G. J., Lee, J., Stayman, J. W., Tward, D. J., Zbijewski, W., Prince, J. L., and Siewerdsen, J. H. (2011). Analysis of Fourier-domain task-based detectability index in tomosynthesis and cone-beam CT in relation to human observer performance. *Medical Physics*, 38(4), 1754–1768.

Gang, G. J., Stayman, J. W., Zbijewski, W., and Siewerdsen, J. H. (2014). Task-based detectability in CT image reconstruction by filtered backprojection and penalized likelihood estimation. *Medical Physics*, 41(8Part1), 081902.

Gang, G. J., Stayman, J. W., Ehtiati, T., and Siewerdsen, J. H. (2015). Task-driven image acquisition and reconstruction in cone-beam CT. *Physics in Medicine & Biology*, 60(8), 3129–3150.

Gang, G. J., Siewerdsen, J. H., and Stayman, J. W. (2017a). Task-driven optimization of CT tube current modulation and regularization in model-based iterative reconstruction. *Physics in Medicine & Biology*, 62(12), 4777–4797.

Gang, G. J., Siewerdsen, J. H., and Stayman, J. W. (2017b). Task-driven optimization of fluence field and regularization for model-based iterative reconstruction in computed tomography. *IEEE Transactions on Medical Imaging*, 36(12), 2424–2435.

Gang, G. J., Guo, X., and Stayman IV, J. W. (2019). Performance analysis for nonlinear tomographic data processing. *The 15th International Meeting on Fully Three-*

Dimensional Image Reconstruction in Radiology and Nuclear Medicine, 11072, 110720W.

Gang, G. J., Siewerdsen, J. H., and Stayman, J. W. (2020). Non-circular CT orbit design for elimination of metal artifacts. *Medical Imaging 2020: Physics of Medical Imaging*, 11312, 1131227.

Goodwin, S. C., Vedantham, S., McLucas, B., Forno, A. E., and Perrella, R. (1997). Preliminary experience with uterine artery embolization for uterine fibroids. *Journal of Vascular and Interventional Radiology*, 8(4), 517–526.

Gupta, S., Johnson, M. M., Murthy, R., Ahrar, K., Wallace, M. J., Madoff, D. C., McRae, S. E., Hicks, M. E., Rao, S., Vauthey, J.-N., Ajani, J. A., and Yao, J. C. (2005). Hepatic arterial embolization and chemoembolization for the treatment of patients with metastatic neuroendocrine tumors: variables affecting response rates and survival. *Cancer*, 104(8), 1590–1602.

Hall, W. H., McGahan, J. P., Link, D. P., and deVere White, R. W. (2000). Combined embolization and percutaneous radiofrequency ablation of a solid renal tumor. *American Journal of Roentgenology*, 174(6), 1592–1594.

embolization and percutaneous radiofrequency ablation of a solid renal tumor. *American Journal of Roentgenology*, 174(6), 1592–1594.

Hansen, N. (2006). The CMA evolution strategy: a comparing review. *Towards a new evolutionary computation*, 192, 75–102.

Herbst, M., Schebesch, F., Berger, M., Choi, J.-H., Fahrig, R., Hornegger, J., and Maier, A. (2015). Dynamic detector offsets for field of view extension in C-arm computed tomography with application to weight-bearing imaging. *Medical Physics*, 42(5), 2718–2729.

Hirota, S., Nakao, N., Yamamoto, S., Kobayashi, K., Maeda, H., Ishikura, R., Miura, K., Sakamoto, K., Ueda, K., and Baba, R. (2006). Cone-beam CT with flat-panel-detector digital angiography system: early experience in abdominal interventional procedures. *Cardiovascular and Interventional Radiology*, 29(6), 1034–1038.

Hohenforst-Schmidt, W., Zarogoulidis, P., Vogl, T., Turner, J. F., Browning, R., Linsmeier, B., Huang, H., Li, Q., Darwiche, K., Freitag, L., Simoff, M., Kioumis, I., Zarogoulidis, K., and Brachmann, J. (2014). Cone beam computertomography (CBCT) in interventional chest medicine - high feasibility for endobronchial realtime navigation. *Journal of Cancer*, 5(3), 231–241.

Hsieh, J. (2003). *Computed Tomography: Principles, Design, Artifacts, and Recent Advances*, 114.

Hu, Z., Gui, J., Zou, J., Rong, J., Zhang, Q., Zheng, H., and Xia, D. (2011). Geometric calibration of a micro-CT system and performance for insect imaging. *IEEE Transactions on Information Technology in Biomedicine*, 15(4), 655–660.

Hussain, S. (1996). Gantry angulation in CT-guided percutaneous adrenal biopsy. *American Journal of Roentgenology*, 166(3), 537–539.

Isola, A. A., Grass, M., and Niessen, W. J. (2010). Fully automatic nonrigid registration-based local motion estimation for motion-corrected iterative cardiac CT reconstruction. *Medical Physics*, 37(3), 1093–1109.

Jacobson, M. W., and Stayman, J. W. (2008). Compensating for head motion in slowly-rotating cone beam CT systems with optimization transfer based motion estimation. *2008 IEEE Nuclear Science Symposium Conference Record*, 5240–5245.

Jaffray, D. A., Siewerdsen, J. H., Wong, J. W., and Martinez, A. A. (2002). Flat-panel cone-beam computed tomography for image-guided radiation therapy. *International Journal of Radiation Oncology · Biology · Physics*, 53(5), 1337–1349.

Kakeda, S., Korogi, Y., Ohnari, N., Moriya, J., Oda, N., Nishino, K., and Miyamoto, W. (2007). Usefulness of cone-beam volume CT with flat panel detectors in conjunction with catheter angiography for transcatheter arterial embolization. *Journal of Vascular and Interventional Radiology*, 18(12), 1508–1516.

Kingston, A., Sakellariou, A., Varslot, T., Myers, G., and Sheppard, A. (2011). Reliable automatic alignment of tomographic projection data by passive auto-focus. *Medical Physics*, 38(9), 4934–4945.

Kyriakou, Y., Lapp, R. M., Hillebrand, L., Ertel, D., and Kalender, W. A. (2008). Simultaneous misalignment correction for approximate circular cone-beam computed tomography. *Physics in Medicine & Biology*, 53(22), 6267–6289.

Lee, I. J., Chung, J. W., Yin, Y. H., Kim, H.-C., Kim, Y. I., Jae, H. J., and Park, J. H. (2014). Cone-beam CT hepatic arteriography in chemoembolization for hepatocellular carcinoma: angiographic image quality and its determining factors. *Journal of Vascular and Interventional Radiology*, 25(9), 1369–1379.

Lee, J., Carass, A., Jog, A., Zhao, C., and Prince, J. L. (2017). Multi-atlas-based CT synthesis from conventional MRI with patch-based refinement for MRI-based radiotherapy planning. *Medical Imaging 2017: Image Processing*, 10133, 101331I.

Lewis, M., Toms, A. P., Reid, K., and Bugg, W. (2010). CT metal artefact reduction of total knee prostheses using angled gantry multiplanar reformation. *The Knee*, 17(4), 279–282.

Leyon, J. J., Littlehales, T., Rangarajan, B., Hoey, E. T., and Ganeshan, A. (2014). Endovascular embolization: review of currently available embolization agents. *Current Problems in Diagnostic Radiology*, 43(1), 35–53.

Li, J., Jaszczak, R. J., Wang, H., Gullberg, G. T., Greer, K. L., and Coleman, R. E. (1994). A cone beam SPECT reconstruction algorithm with a displaced center of rotation. *Medical Physics*, 21(1), 145–152.

Li, L., Chen, Z., Jin, X., Yu, H., and Wang, G. (2010). Experimental measurement of human head motion for high-resolution computed tomography system design. *Optical Engineering*, 49(6), 063201.

Li, X., Zhang, D., and Liu, B. (2010). A generic geometric calibration method for tomographic imaging systems with flat-panel detectors—a detailed implementation guide. *Medical Physics*, 37(7Part1), 3844–3854.

Li, X., Zhang, D., and Liu, B. (2011). Sensitivity analysis of a geometric calibration method using projection matrices for digital tomosynthesis systems. *Medical Physics*, 38(1), 202–209.

Marchant, T. E., Price, G. J., Matuszewski, B. J., and Moore, C. J. (2011). Reduction of motion artefacts in on-board cone beam CT by warping of projection images. *The British Journal of Radiology*, 84(999), 251–264.

McGee, K. P., Manduca, A., Felmlee, J. P., Riederer, S. J., and Ehman, R. L. (2000). Image metric-based correction (autocorrection) of motion effects: analysis of image metrics. *Journal of Magnetic Resonance Imaging*, 11(2), 174–181.

McWilliams, J. P., Kuo, M. D., Rose, S. C., Bagla, S., Caplin, D. M., Cohen, E. I., Faintuch, S., Spies, J. B., Saad, W. E., and Nikolic, B. (2014). Society of Interventional

Radiology position statement: prostate artery embolization for treatment of benign disease of the prostate. *Journal of Vascular Interventional Radiology*, 25(9), 1349–1351.

Meng, Y., Gong, H., and Yang, X. (2013). Online geometric calibration of cone-beam computed tomography for arbitrary imaging objects. *IEEE Transactions on Medical Imaging*, 32(2), 278–288.

Mennessier, C., Clackdoyle, R., and Noo, F. (2009). Direct determination of geometric alignment parameters for cone-beam scanners. *Physics in Medicine & Biology*, 54(6), 1633–1660.

Menzel, H. G. S. H., Schibilla, H., and Teunen, D. (2000). European guidelines on quality criteria for computed tomography. *Luxembourg: European Commission*, 16262.

Miracle, A. C., and Mukherji, S. K. (2009). Conebeam CT of the head and neck, part 2: clinical applications. *American Journal of Neuroradiology*, 30(7), 1285–1292.

Müller, K., Maier, A. K., Schwemmer, C., Lauritsch, G., De Buck, S., Wielandts, J.-Y., Hornegger, J., and Fahrig, R. (2014). Image artefact propagation in motion estimation and reconstruction in interventional cardiac C-arm CT. *Physics in Medicine & Biology*, 59(12), 3121–3138.

Navab, N., Bani-Hashemi, A., Nadar, M. S., Wiesent, K., Durlak, P., Brunner, T., Barth, K., and Graumann, R. (1998). 3D reconstruction from projection matrices in a C-arm based 3D-angiography system. *Medical Image Computing and Computer-Assisted Intervention – MICCAI'98*, 1496, 119–129.

Nazarparvar, B., Shamsaei, M., and Rajabi, H. (2012). Correction of head movements in positron emission tomography using point source tracking system: a simulation study. *Annals of Nuclear Medicine*, 26(1), 7–15.

Nikupaavo, U., Kaasalainen, T., Reijonen, V., Ahonen, S. M., and Kortesniemi, M. (2015). Lens dose in routine head CT: comparison of different optimization methods with anthropomorphic phantoms. *American Journal of Roentgenology*, 204(1), 117–123.

Noo, F., Clack, R., White, T. A., and Roney, T. J. (1998). The dual-ellipse cross vertex path for exact reconstruction of long objects in cone-beam tomography. *Physics in Medicine & Biology*, 43(4), 797–810.

Noo, F., Clackdoyle, R., Mennessier, C., White, T. A., and Roney, T. J. (2000). Analytic method based on identification of ellipse parameters for scanner calibration in cone-beam tomography. *Physics in Medicine & Biology*, 45(11), 3489–3508.

Orth, R. C., Wallace, M. J., Kuo, M. D., and Technology Assessment Committee of the Society of Interventional Radiology. (2008). C-arm cone-beam CT: general principles and technical considerations for use in interventional radiology. *Journal of Vascular and Interventional Radiology*, 19(6), 814–820.

Otake, Y., Schafer, S., Stayman, J. W., Zbijewski, W., Kleinszig, G., Graumann, R., Khanna, A. J., and Siewerdsen, J. H. (2012). Automatic localization of vertebral levels in x-ray fluoroscopy using 3D-2D registration: a tool to reduce wrong-site surgery. *Physics in Medicine & Biology*, 57(17), 5485–5508.

Otake, Y., Wang, A. S., Stayman, J. W., Uneri, A., Kleinszig, G., Vogt, S., Khanna, A. J., Gokaslan, Z. L., and Siewerdsen, J. H. (2013). Robust 3D–2D image registration: application to spine interventions and vertebral labeling in the presence of anatomical deformation. *Physics in Medicine & Biology*, 58(23), 8535–8553.

Otake, Y., Wang, A. S., Uneri, A., Kleinszig, G., Vogt, S., Aygun, N., Lo, S. L., Wolinsky, J.-P., Gokaslan, Z. L., and Siewerdsen, J. H. (2015). 3D–2D registration in mobile radiographs: algorithm development and preliminary clinical evaluation. *Physics in Medicine & Biology*, 60(5), 2075–2090.

Ouadah, S., Stayman, J. W., Gang, G. J., Ehtiati, T., and Siewerdsen, J. H. (2016). Self-calibration of cone-beam CT geometry using 3D–2D image registration. *Physics in Medicine & Biology*, 61(7), 2613–2632.

Ouadah, S., Jacobson, M., Stayman, J. W., Ehtiati, T., Weiss, C., and Siewerdsen, J. H. (2017). Task-driven orbit design and implementation on a robotic C-arm system for cone-beam CT. *Medical Imaging 2017: Physics of Medical Imaging*, 10132, 101320H.

Pack, J. D., Noo, F., and Kudo, H. (2004). Investigation of saddle trajectories for cardiac CT imaging in cone-beam geometry. *Physics in Medicine & Biology*, 49(11), 2317–2336.

Panetta, D., Belcari, N., Del Guerra, A., and Moehrs, S. (2008). An optimization-based method for geometrical calibration in cone-beam CT without dedicated phantoms. *Physics in Medicine & Biology*, 53(14), 3841–3861.

Park, S., Jennings, R., Liu, H., Badano, A., and Myers, K. (2010). A statistical, task-based evaluation method for three-dimensional x-ray breast imaging systems using variable-background phantoms. *Medical Physics*, 37(12), 6253–6270.

Patel, V., Chityala, R. N., Hoffmann, K. R., Ionita, C. N., Bednarek, D. R., and Rudin, S. (2009). Self-calibration of a cone-beam micro-CT system. *Medical Physics*, 36(1), 48–58.

Pearson, E. A., Cho, S., Pelizzari, C. A., and Pan, X. (2010). Non-circular cone beam CT trajectories: a preliminary investigation on a clinical scanner. *IEEE Nuclear Science Symposium & Medical Imaging Conference*, 3172–3175.

Penney, G. P., Weese, J., Little, J. A., Desmedt, P., Hill, D. L. G., and Hawkes, D. J. (1998). A comparison of similarity measures for use in 2-D-3-D medical image registration. *IEEE Transactions on Medical Imaging*, 17(4), 586–595.

Pluim, J. P., Maintz, J. A., and Viergever, M. A. (2000). Image registration by maximization of combined mutual information and gradient information. *Medical Image Computing and Computer-Assisted Intervention – MICCAI 2000,* 1935, 452–461.

Prakash, P., Zbijewski, W., Gang, G. J., Ding, Y., Stayman, J. W., Yorkston, J., Carrino, J. A., and Siewerdsen, J. H. (2011). Task-based modeling and optimization of a cone-beam CT scanner for musculoskeletal imaging. *Medical Physics*, 38(10), 5612–5629.

Qi, J. and Leahy, R. M. (1999). Fast computation of the covariance of MAP reconstructions of PET images. *Medical Imaging 1999: Image Processing*, 3661, 344–355.

Reiser, I. and Nishikawa, R. M. (2010). Task-based assessment of breast tomosynthesis: effect of acquisition parameters and quantum noise. *Medical Physics*, 37(4), 1591–1600.

Richard, S. and Siewerdsen, J. H. (2008). Cascaded systems analysis of noise reduction algorithms in dual-energy imaging. *Medical Physics*, 35(2), 586–601.

Rit, S., Sarrut, D., and Desbat, L. (2009). Comparison of analytic and algebraic methods for motion-compensated cone-beam CT reconstruction of the thorax. *IEEE Transactions on Medical Imaging*, 28(10), 1513–1525.

Rohkohl, C., Bruder, H., Stierstorfer, K., and Flohr, T. (2013). Improving best-phase image quality in cardiac CT by motion correction with MAM optimization. *Medical Physics*, 40(3), 031901.

Rougée, A., Picard, C., Ponchut, C., and Trousset, Y. (1993). Geometrical calibration of x-ray imaging chains for three-dimensional reconstruction. *Computerized Medical Imaging and Graphics*, 17(4–5), 295–300.

Roy, S., Butman, J. A., and Pham, D. L. (2017). Synthesizing CT from ultrashort echo-time MR images via convolutional neural networks. *Simulation and Synthesis in Medical Imaging,* 10557, 24–32.

Schmitt, S. M. and Fessler, J. A. (2015). Fast variance prediction for iteratively reconstructed CT with arbitrary geometries. *The 13th International Meeting on Fully Three-Dimensional Image Reconstruction in Radiology and Nuclear Medicine,* 228–231.

Schmitt, S. M., Goodsitt, M. M., and Fessler, J. A. (2017). Fast variance prediction for iteratively reconstructed CT images with locally quadratic regularization. *IEEE Transactions on Medical Imaging*, 36(1), 17–26.

Shah, J. P., Mann, S. D., McKinley, R. L., and Tornai, M. P. (2018). Characterization of CT Hounsfield units for 3D acquisition trajectories on a dedicated breast CT system. *Journal of X-Ray Science and Technology*, 26(4), 535–551.

Sharp, P., Barber, D. C., Brown, D. G., Burgess, A. E., Metz, C. E., Myers, K. J., Taylor, C. J., Wagner, R. F., Brooks, R., Hill, C. R., Kuhl, D. E., Smith, M. A., Wells, P., and Worthington, B. (1996). Report 54. *Journal of the International Commission on Radiation Units and Measurements*, 28(1).

Siddon, R. L. (1985). Fast calculation of the exact radiological path for a three-dimensional CT array. *Medical Physics*, 12(2), 252–255.

Siewerdsen, J. H. and Antonuk, L. E. (1998). DQE and system optimization for indirect-detection flat-panel imagers in diagnostic radiology. *Medical Imaging 1998: Physics of Medical Imaging*, 3336, 546–555.

Siewerdsen, J. H. and Jaffray, D. A. (2000). Optimization of x-ray imaging geometry (with specific application to flat-panel cone-beam computed tomography). *Medical Physics*, 27(8), 1903–1914.

Siewerdsen, J. H., Moseley, D. J., Burch, S., Bisland, S. K., Bogaards, A., Wilson, B. C., and Jaffray, D. A. (2005). Volume CT with a flat-panel detector on a mobile, isocentric C-arm: pre-clinical investigation in guidance of minimally invasive surgery. *Medical Physics*, 32(1), 241–254.

Sisniega, A., Stayman, J. W., Yorkston, J., Siewerdsen, J. H., and Zbijewski, W. (2017). Motion compensation in extremity cone-beam CT using a penalized image sharpness criterion. *Physics in Medicine & Biology*, 62(9), 3712–3734.

Sisniega, A., Zbijewski, W., Wu, P., Stayman, J. W., Aygun, N., Stevens, R., Wang, X., Foos, D. H., and Siewerdsen, J. H. (2018). Multi-motion compensation for high-quality cone-beam CT of the head. *The 5th International Conference on Image Formation in X-Ray Computed Tomography*, 73–77.

Sisniega, A., Capostagno, S., Zbijewski, W., Weiss, C. R., Ehtiati, T., and Siewerdsen, J. H. (2019). Image-based deformable motion compensation for interventional cone-beam CT. *Medical Imaging 2019: Physics of Medical Imaging*, 10948, 109481O.

Sisniega, A., Thawait, G. K., Shakoor, D., Siewerdsen, J. H., Demehri, S., and Zbijewski, W. (2019). Motion compensation in extremity cone-beam computed tomography. *Skeletal Radiology,* 48(1), 1999–2007.

Sisniega, A., Capostagno, S., Zbijewski, W., Stayman, J. W., Weiss, C. R., Ehtiati, T., and Siewerdsen, J. H. (2020). Estimation of local deformable motion in image-based motion compensation for interventional cone-beam CT. *Medical Imaging 2020: Physics of Medical Imaging*, 11312, 113121M.

Stayman, J. W. and Fessler, J. A. (2000). Regularization for uniform spatial resolution properties in penalized-likelihood image reconstruction. *IEEE Transactions on Medical Imaging*, 19(6), 601–615.

Stayman, J. W. and Fessler, J. A. (2004). Efficient calculation of resolution and covariance for penalized-likelihood reconstruction in fully 3-D SPECT. *IEEE Transactions on Medical Imaging*, 23(12), 1543–1556.

Stayman, J. W. and Siewerdsen, J. H. (2013). Task-based trajectories in iteratively reconstructed interventional cone-beam CT. *The 12th International Meeting on Fully Three-Dimensional Image Reconstruction in Radiology and Nuclear Medicine*, 257–260.

Stayman, J. W., Dang, H., Ding, Y., and Siewerdsen, J. H. (2013). PIRPLE: a penalized-likelihood framework for incorporation of prior images in CT reconstruction. *Physics in Medicine & Biology*, 58(21), 7563–7582.

Stayman, J. W., Gang, G. J., and Siewerdsen, J. H. (2015). Task-based optimization of source-detector orbits in interventional cone-beam CT. *The 13th International Meeting on Fully Three-Dimensional Image Reconstruction in Radiology and Nuclear Medicine*, 55–58

Stayman, J. W., Capostagno, S., Gang, G. J., and Siewerdsen, J. H. (2019). Task-driven source–detector trajectories in cone-beam computed tomography: I. theory and methods. *Journal of Medical Imaging*, 6(2), 025002.

Tacher, V., Radaelli, A., Lin, M., and Geschwind, J. F. (2015). How I do it: cone-beam CT during transarterial chemoembolization for liver cancer. *Radiology*, 274(2), 320–334.

Tang, Q., Cammin, J., Srivastava, S., and Taguchi, K. (2012). A fully four-dimensional, iterative motion estimation and compensation method for cardiac CT. *Medical Physics*, 39(7Part1), 4291–4305.

Tang, X. and Ning, R. (2001). A cone beam filtered backprojection (CB-FBP) reconstruction algorithm for a circle-plus-two-arc orbit. *Medical Physics*, 28(6), 1042–1055.

Tuy, H. K. (1983). An inversion formula for cone-beam reconstruction. *SIAM Journal on Applied Mathematics*, 43(3), 546–552.

Tward, D. J., Siewerdsen, J. H., Daly, M. J., Richard, S., Moseley, D. J., Jaffray, D. A., and Paul, N. S. (2007). Soft-tissue detectability in cone-beam CT: evaluation by 2AFC tests in relation to physical performance metrics. *Medical Physics*, 34(11), 4459–4471.

Uneri, A., Otake, Y., Wang, A. S., Kleinszig, G., Vogt, S., Khanna, A. J., and Siewerdsen, J. H. (2013). 3D–2D registration for surgical guidance: effect of projection view angles on registration accuracy. *Physics in Medicine & Biology*, 59(2), 271–287.

Vidal-Migallon, I., Abella, M., Sisniega, A., Vaquero, J. J., and Desco, M. (2008). Simulation of mechanical misalignments in a cone-beam micro-CT system. *2008 IEEE Nuclear Science Symposium Conference Record*, 5007–5009.

Von Smekal, L., Kachelrieß, M., Stepina, E., and Kalender, W. A. (2004). Geometric misalignment and calibration in cone-beam tomography: geometric misalignment and calibration in cone-beam tomography. *Medical Physics*, 31(12), 3242–3266.

Wagner, A., Schicho, K., Kainberger, F., Birkfellner, W., Grampp, S., and Ewers, R. (2003). Quantification and clinical relevance of head motion during computed tomography. *Investigative Radiology*, 38(11), 733–741.

Wang, A. S., Stayman, J. W., Otake, Y., Kleinszig, G., Vogt, S., Gallia, G. L., Khanna, A. J., and Siewerdsen, J. H. (2014). Soft-tissue imaging with C-arm cone-beam CT using statistical reconstruction. *Physics in Medicine & Biology*, 59(4), 1005–1026.

Wang, W., Gang, G. J., and Stayman, J. W. (2017). Spatial resolution properties in penalized-likelihood reconstruction of blurred tomographic data. *The 14th International Meeting on Fully Three-Dimensional Image Reconstruction in Radiology and Nuclear Medicine*, 702–707.

Wang, Z., Bovik, A. C., Sheikh, H. R., and Simoncelli, E. P. (2004). Image quality assessment: from error visibility to structural similarity. *IEEE Transactions on Image Processing*, 13(4), 600–612.

Wicklein, J., Kunze, H., Kalender, W. A., and Kyriakou, Y. (2012). Image features for misalignment correction in medical flat-detector CT. *Medical Physics*, 39(8), 4918–4931.

Wicklein, J., Kyriakou, Y., Kalender, W. A., and Kunze, H. (2013). An online motion- and misalignment-correction method for medical flat-detector CT. *Medical Imaging 2013: Physics of Medical Imaging*, 8668, 86681S.

Wu, P., Sisniega, A., Stayman, J. W., Zbijewski, W., Foos, D., Wang, X., Khanna, N., Aygun, N., Stevens, R. D., and Siewerdsen, J. H. (2020). Cone-beam CT for imaging of the head/brain: development and assessment of scanner prototype and reconstruction algorithms. *Medical Physics,* Early view.

Xu, J., Sisniega, A., Zbijewski, W., Dang, H., Stayman, J. W., Wang, X., Foos, D. H., Aygun, N., Koliatsos, V. E., and Siewerdsen, J. H. (2016). Modeling and design of a cone-beam CT head scanner using task-based imaging performance optimization. *Physics in Medicine & Biology*, 61(8), 3180–3207.

Yamagami, T., Kato, T., Iida, S., Hirota, T., and Nishimura, T. (2004). Percutaneous needle biopsy for small lung nodules beneath the rib under CT scan fluoroscopic guidance with gantry tilt. *Chest*, 126(3), 744–747.

Yang, K., Kwan, A. L., Miller, D. F., and Boone, J. M. (2006). A geometric calibration method for cone beam CT systems. *Medical Physics*, 33(6Part1), 1695–1706.

Yu, H. and Wang, G. (2007). Data consistency based rigid motion artifact reduction in fan-beam CT. *IEEE Transactions on Medical Imaging*, 26(2), 249–260.

Yu, Z., Lauritsch, G., Dennerlein, F., Mao, Y., Hornegger, J., and Noo, F. (2016). Extended ellipse-line-ellipse trajectory for long-object cone-beam imaging with a mounted C-arm system. *Physics in Medicine & Biology*, 61(4), 1829–1851.

Zeng, G. L., and Gullberg, G. T. (1992). A cone-beam tomography algorithm for orthogonal circle-and-line orbit. *Physics in Medicine & Biology*, 37(3), 563–577.

Zhang, J., Weir, V., Fajardo, L., Lin, J., Hsiung, H., and Ritenour, E. R. (2009). Dosimetric characterization of a cone-beam O-arm™ imaging system. *Journal of X-Ray Science and Technology*, 17(4), 305–317.

Zhang, H., Gang, G. J., Dang, H., and Stayman, J. W. (2018). Regularization analysis and design for prior-image-based x-ray CT reconstruction. *IEEE Transactions on Medical Imaging*, 37(12), 2675–2686.

Zhao, Z., Gang, G. J., and Siewerdsen, J. H. (2014). Noise, sampling, and the number of projections in cone-beam CT with a flat-panel detector. *Medical Physics*, 41(6Part1), 061909.

Zhao, C., Herbst, M., Vogt, S., Ritschl, L., Kappler, S., Siewerdsen, J. H., and Zbijewski, W. (2019). A robotic x-ray cone-beam CT system: trajectory optimization for 3D imaging of the weight-bearing spine. *Medical Imaging 2019: Physics of Medical Imaging*, 10948, 109481L.

Curriculum Vitae

The Johns Hopkins University School of Medicine

Name: Sarah J. Capostagno (née Ouadah) Date of this Version: 04/30/2020

Educational History

MD *Medical Innovators Development Program* 2024 (Expected)
Vanderbilt University

PhD *Biomedical Engineering* 2020 (Expected)
Johns Hopkins University
Mentor: Jeffrey H. Siewerdsen, PhD

BS *Bioengineering* 2013
University of California, Los Angeles

Experience

Johns Hopkins University Baltimore, MD
Graduate Research Assistant, lab of Dr. Jeffrey H. Siewerdsen 2014–present

University of California, Los Angeles Los Angeles, CA
Undergraduate Research Assistant, lab of Dr. Daniel B. Ennis 2011–2013

eBioscience, Inc. San Diego, CA
Quality Control Intern 2011

Sanford Burnham Prebys Medical Discovery Institute San Diego, CA
Research Intern, lab of Dr. John C. Reed 2010

Scholarships and Fellowships

- Recipient of the Medical Innovators Development Program Scholarship (2020)
- Recipient of the Translational Research in Imaging Training Grant (2013)
- Recipient of the James N. Harger Scholarship in Engineering (2013)

Academic Awards and Honors

- Invited Participant at Rising Stars in Biomedical: Women (2019)
- Early Career Scholar at the Winter Institute for Medical Physics (2019)
- Dean's Honor List (2010–2013)

Peer-Reviewed Publications

[1] **Capostagno, S.**, Sisniega, A., Stayman, J. W., Ehtiati, T., Weiss, C. R., and Siewerdsen, J. H. Image-based deformable motion compensation for interventional cone-beam CT. *Physics in Medicine & Biology*, under review.

[2] Ouadah, Y., Rojas, E. R., Riordan, D. P., **Capostagno, S.**, Kuo, C. S., and Krasnow, M. A. (2019). Rare pulmonary neuroendocrine cells are stem cells regulated by rb, p53, and notch. *Cell*, 179(2), 403–416.

[3] **Capostagno, S.**, Stayman, J. W., Jacobson, M. W., Ehtiati, T., Weiss, C. R., and Siewerdsen, J. H. (2019). Task-driven source–detector trajectories in cone-beam computed tomography: II. application to neuroradiology. *Journal of Medical Imaging*, 6(2), 025004.

[4] Stayman, J. W., **Capostagno, S.**, Gang, G. J., and Siewerdsen, J. H. (2019). Task-driven source–detector trajectories in cone-beam computed tomography: I. theory and methods. *Journal of Medical Imaging*, 6(2), 025002.

[5] Jacobson, M. W., Ketcha, M. D., **Capostagno, S.**, Martin, A., Uneri, A., Goerres, J., De Silva, T., Reaungamornrat, S., Han, R., Manbachi, A., Stayman, J. W., Vogt, S., Kleinszig, G., and Siewerdsen, J. H. (2018). A line fiducial method for geometric calibration of cone-beam CT systems with diverse scan trajectories. *Physics in Medicine & Biology*, 63(2), 025030.

[6] **Ouadah, S.**, Jacobson, M., Stayman, J. W., Ehtiati, T., Weiss, C., and Siewerdsen, J. H. (2017). Correction of patient motion in cone-beam CT using 3D–2D registration. *Physics in Medicine & Biology*, 62(23), 8813–8831.

[7] Tung, R., Kim, S., Yagishita, D., Vaseghi, M., Ennis, D. B., **Ouadah, S.**, Ajijola, O. A., Bradfield, J. S., Mahapatra, S., Finn, P., and Shivkumar, K. (2016). Scar voltage threshold determination using ex vivo magnetic resonance imaging integration in a porcine infarct model: influence of interelectrode distances and three-dimensional spatial effects of scar. *Heart Rhythm*, 13(10), 1993–2002.

[8] **Ouadah, S.**, Stayman, J. W., Gang, G. J., Ehtiati, T., and Siewerdsen, J. H. (2016). Self-calibration of cone-beam CT geometry using 3D–2D image registration. *Physics in Medicine & Biology*, 61(7), 2613–2632.

Conference Proceedings

[1] **Capostagno, S.**, Sisniega, A., Stayman, J. W., Ehtiati, T., Weiss, C. R., and Siewerdsen, J. H. (2020). Image-based deformable motion compensation in cone-beam CT: translation to clinical studies in interventional body radiology. *Medical Imaging 2020: Image-Guided Procedures, Robotic Interventions, and Modeling*, 11315, 113150B.

[2] Sisniega, A., **Capostagno, S.**, Zbijewski, W., Stayman, J. W., Weiss, C. R., Ehtiati, T., and Siewerdsen, J. H. (2020). Estimation of local deformable motion in image-based motion compensation for interventional cone-beam CT. *Medical Imaging 2020: Physics of Medical Imaging*, 11312, 113121M.

[3] Sisniega, A., Stayman, J. W., **Capostagno, S.**, Weiss, C. R., Ehtiati, T., and Siewerdsen, J. H. (2019). Accelerated model-based iterative 3D image

reconstruction using a multi-level morphological pyramid. *Medical Physics,* 46(6), E222–E223.

[4] Sisniega, A., Stayman, J. W., **Capostagno, S.**, Weiss, C. R., Ehtiati, T., and Siewerdsen, J. H. (2019). Convergence criterion for MBIR based on the local noise-power spectrum: theory and implementation in a framework for accelerated 3D image reconstruction with a morphological pyramid. *The 15th International Meeting on Fully Three-Dimensional Image Reconstruction in Radiology and Nuclear Medicine*, 11072, 1107209.

[5] **Capostagno, S.**, Sisniega, A., Ehtiati, T., Stayman, J., Weiss, C., and Siewerdsen, J. (2019). Deformable motion correction for interventional cone-beam CT. *Bulletin of the American Physical Society*, 64(2), L30.00003.

[6] **Capostagno, S.**, Sisniega, A., Ehtiati, T., Stayman, J., Weiss, C., and Siewerdsen, J. (2019). Correction of organ motion in cone-beam CT-guided transarterial chemoembolization. *Journal of Vascular and Interventional Radiology*, 30(3), S215.

[7] Sisniega, A., **Capostagno, S.**, Zbijewski, W., Weiss, C. R., Ehtiati, T., and Siewerdsen, J. H. (2019). Image-based deformable motion compensation for interventional cone-beam CT. *Medical Imaging 2019: Physics of Medical Imaging*, 10948, 109481O.

[8] **Ouadah, S.**, Jacobson, M., Stayman, J. W., Ehtiati, T., Weiss, C., and Siewerdsen, J. H. (2017). Task-driven orbit design and implementation on a robotic C-arm system for cone-beam CT. *Medical Imaging 2017: Physics of Medical Imaging*, 10132, 101320H.

[9] **Ouadah, S.**, Jacobson, M., Stayman, J. W., Ehtiati, T., and Siewerdsen, J. H. (2016). Correction of patient motion in C-arm cone-beam CT using 3D–2D registration. *Medical Physics*, 43(6Part38), 3792–3793.

[10] Gang, G., Stayman, J., **Ouadah, S.**, Ehtiati, T., and Siewerdsen, J. (2015). Task-driven imaging for cone-beam CT in interventional guidance. *Medical Physics*, 42(6Part39), 3680–3681.

[11] **Ouadah, S.**, Stayman, J. W., Gang, G., Uneri, A., Ehtiati, T., and Siewerdsen, J. H. (2015). Self-calibration of cone-beam CT geometry using 3D–2D image registration: development and application to task-based imaging with a robotic C-arm. *Medical Imaging 2015: Image-Guided Procedures, Robotic Interventions, and Modeling,* 9415, 94151D.

[12] Gang, G. J., Stayman, J. W., **Ouadah, S.**, Ehtiati, T., and Siewerdsen, J. H. (2015). Task-driven imaging in cone-beam computed tomography. *Medical Imaging 2015: Physics of Medical Imaging*, 9412, 941220.

[13] Kung, G. L., **Ouadah, S.**, Hsieh, Y. C., Garfinkel, A., Chen, P. S., and Ennis, D. (2013). Transmural heterogeneity of microstructural remodeling in pacing induced heart failure measured by diffusion tensor MRI. *Journal of Cardiovascular Magnetic Resonance*, 15(S1), P119.

Presentations

Invited Presentations

[1] Sisniega, A., **Capostagno, S.**, Zbijewski, W., Stayman, J. W., Weiss, C. R., Ehtiati, T., and Siewerdsen, J. H. (2020). Motion compensation for interventional cone-beam CT. *Siemens Healthineers, AT Division*, Baltimore, MD, April 23, 2020, Oral presentation.

[2] **Capostagno, S.**, Sisniega, A., Zbijewski, W., Stayman, J. W., Ehtiati, T., Weiss, C. R., and Siewerdsen, J. H. (2020). Image-based deformable motion compensation for interventional cone-beam CT. *Johns Hopkins University Biomedical Engineering PhD Admissions 2020*, Baltimore, MD, February 13, 2020, Poster presentation.

[3] **Capostagno, S.**, Sisniega, A., Stayman, J. W., Weiss, C. R., Ehtiati, T., and Siewerdsen, J. H. (2020). Image-based deformable motion compensation for interventional cone-beam CT. *Siemens Healthineers, AT Division*, Baltimore, MD, January 15, 2020, Oral presentation.

[4] **Capostagno, S.**, Sisniega, A., Zbijewski, W., Stayman, J. W., Ehtiati, T., Weiss, C. R., and Siewerdsen, J. H. (2019). Image-based deformable motion compensation for interventional cone-beam CT. *Winter Institute of Medical Physics Early Career Program 2019*, Breckenridge, CO, February 24, 2019, Poster presentation.

[5] **Capostagno, S.**, Sisniega, A., Jacobson, M., Stayman, J. W., Ehtiati, T., and Siewerdsen, J. H. (2018). Compensation of patient motion in C-arm cone-beam CT. *Siemens Healthineers, AT Division,* Baltimore, MD, January 17, 2018, Oral presentation.

[6] **Ouadah, S.**, Jacobson, M., Stayman, J. W., Gang, G. J., Ehtiati, T., Weiss, C., Wolinsky, J-P., and Siewerdsen, J. H. (2016). Advanced 3D imaging on a robotic C-arm: design and implementation of task-driven imaging. *Johns Hopkins University Biomedical Engineering Student Talk*, Baltimore, MD, December 5, 2016, Oral presentation.

Scientific Conferences (Presenting Author)

[1] **Capostagno, S.**, Sisniega, A., Stayman, J. W., Ehtiati, T., Weiss, C. R., and Siewerdsen, J. H. (2020). Image-based deformable motion compensation in cone-beam CT: translation to clinical studies in interventional body radiology. *SPIE Medical Imaging 2020*, Houston, TX, February 15–20, 2020, Oral presentation.

[2] **Capostagno, S.**, Sisniega, A., Ehtiati, T., Stayman, J. W., Weiss, C. R., and Siewerdsen, J. H. (2019). Correction of organ motion in cone-beam CT-guided transarterial chemoembolization. *SIR 2019 Annual Scientific Meeting*, Austin, TX, March 23–28, 2019, ePoster presentation.

[3] **Capostagno, S.**, Sisniega, A., Ehtiati, T., Stayman, J. W., Weiss, C. R., and Siewerdsen, J. H. (2019). Deformable motion correction for interventional cone-beam CT. *APS March Meeting 2019*, Boston, MA, March 4–8, 2019, Oral presentation.

[4] **Ouadah, S.**, Jacobson, M., Stayman, J. W., Ehtiati, T., Weiss, C., and Siewerdsen, J. H. (2017). Task-driven orbit design and implementation on a robotic C-arm system for cone-beam CT. *SPIE Medical Imaging 2017*, Orlando, FL, February 11–16, 2017, Oral presentation.

[5] **Ouadah, S.**, Jacobson, M., Stayman, J. W., Ehtiati, T., and Siewerdsen, J. H. (2016). Correction of patient motion in C-arm cone-beam CT using 3D–2D registration. *AAPM 58th Annual Meeting & Exhibition*, Washington, D.C., July 31–August 4, 2016, Oral presentation.

[6] **Ouadah, S.**, Stayman, J. W., Gang, G., Jacobson, M., Ehtiati, T., and Siewerdsen, J. H. (2015). Self-calibration of cone-beam CT geometry using 3D–2D image registration. *5th Annual Hopkins Imaging Conference*, Baltimore, MD, October 26, 2015, Poster presentation.

[7] **Ouadah, S.**, Stayman, J. W., Gang, G., Uneri, A., Ehtiati, T., and Siewerdsen, J. H. (2015). Self-calibration of cone-beam CT geometry using 3D–2D image registration: development and application to task-based imaging with a robotic C-arm. *SPIE Medical Imaging 2015*, Orlando, FL, February 21–26, 2015, Oral presentation.

Scientific Conferences (Contributing Author)

[1] Sisniega, A., **Capostagno, S.**, Zbijewski, W., Stayman, J. W., Weiss, C. R., Ehtiati, T., and Siewerdsen, J. H. (2020). Local motion estimation for improved cone-beam CT deformable motion compensation. *CT Meeting 2020 Medical Imaging*, Regensburg, Germany, August 3–7, 2020, Oral presentation.

[2] Sisniega, A., **Capostagno, S.**, Zbijewski, W., Stayman, J. W., Weiss, C. R., Ehtiati, T., and Siewerdsen, J. H. (2020). Estimation of local deformable motion in image-based motion compensation for interventional cone-beam CT. *SPIE Medical Imaging 2020*, Houston, TX, February 15–20, 2020, Oral presentation.

[3] Sisniega, A., Stayman, J. W., **Capostagno, S.**, Weiss, C. R., Ehtiati, T., and Siewerdsen, J. H. (2019). Accelerated model-based iterative 3D image reconstruction using a multi-level morphological pyramid. *AAPM 61st Annual Meeting & Exhibition*, San Antonio, TX, July 14–18, 2019, Oral presentation.

[4] Sisniega, A., Stayman, J. W., **Capostagno, S.**, Weiss, C. R., Ehtiati, T., and Siewerdsen, J. H. (2019). Convergence criterion for MBIR based on the local noise-power spectrum: theory and implementation in a framework for accelerated 3D image reconstruction with a morphological pyramid. *The 15th International Meeting on Fully Three-Dimensional Image Reconstruction in Radiology and Nuclear Medicine*, Philadelphia, PA, June 2–6, 2019, Oral presentation.

[5] Sisniega, A., **Capostagno, S.**, Zbijewski, W., Weiss, C. R., and Siewerdsen, J. H. (2019). Image-based deformable motion compensation for interventional cone-beam CT. *SPIE Medical Imaging 2019*, San Diego, CA, February 16–21, 2019, Oral presentation.

[6] Solomon, A., Moreland, A. J., Sisniega, A., **Capostagno, S.**, Siewerdsen, J. H., and Hong, K. (2018). The utility and challenges of cone-beam CT guidance during transarterial chemoembolization of hepatocellular carcinoma. *SIR 2018 Annual Scientific Meeting*, Los Angeles, CA, March 17–22, 2018, Poster presentation.

[7] Gang, G., Stayman, J. W., **Ouadah, S.**, Ehtiati, T., and Siewerdsen, J. H. (2015). Task-driven imaging for cone-beam CT in interventional guidance. *AAPM 57th Annual Meeting & Exhibition*, Anaheim, CA, July 12–16, 2015, Oral presentation.

[8] Gang, G. J., Stayman, J. W., **Ouadah, S.**, Ehtiati, T., and Siewerdsen, J. H. (2015). Task-driven imaging in cone-beam computed tomography. *SPIE Medical Imaging 2015*, Orlando, FL, February 21–26, 2015, Oral presentation.

[9] Kung, G. L., **Ouadah, S.**, Hsieh, Y. C., Garfinkel, A., Chen, P. S., and Ennis, D. (2013). Transmural heterogeneity of microstructural remodeling in pacing induced heart failure measured by diffusion tensor MRI. *16th Annual SCMR Scientific Sessions*, San Francisco, CA, January 31–February 3, 2013, Poster presentation.

Conference Abstracts

[1] Sisniega, A., **Capostagno, S.**, Stayman, J. W., Weiss, C. R., Ehtiati, T., and Siewerdsen, J. H. (2020). High-quality cone-beam CT for interventional radiology with deformable motion compensation and accelerated model-based iterative reconstruction. *RSNA Annual Meeting*, Chicago, IL, 2020 (abstract ID 20016155).

[2] Sisniega, A., Stayman, J. W., **Capostagno, S.**, Weiss, C. R., Ehtiati, T., and Siewerdsen, J. H. (2020). Stochastic backprojection for accelerated model-based iterative 3D image reconstruction. *Joint AAPM/CMP Meeting 2020*, Vancouver, CA, 2020 (abstract ID 53460).

[2] Sisniega, A., **Capostagno, S.**, Zbijewski, W., Stayman, J. W., Weiss, C. R., Ehtiati, T., and Siewerdsen, J. H. (2020). Local motion estimation for improved cone-beam CT deformable motion compensation. *CT Meeting 2020 Medical Imaging*, Regensburg, Germany, 2020 (abstract ID CT2020-133).

[3] **Capostagno, S.**, Sisniega, A., Stayman, J. W., Ehtiati, T., Weiss, C. R., and Siewerdsen, J. H. (2020). Image-based deformable motion compensation in cone-beam CT: translation to clinical studies in interventional body radiology. *SPIE Medical Imaging 2020*, Houston, TX, 2020 (paper no. MI104-97).

[4] Sisniega, A., **Capostagno, S.**, Zbijewski, W., Stayman, J. W., Weiss, C. R., Ehtiati, T., and Siewerdsen, J. H. (2020). Estimation of local deformable motion in image-based motion compensation for interventional cone-beam CT. *SPIE Medical Imaging 2020*, Houston, TX, 2020 (paper no. MI104-97).

[5] Sisniega, A., Stayman, J. W., **Capostagno, S.**, Weiss, C. R., Ehtiati, T., and Siewerdsen, J. H. (2019). Accelerated model-based iterative 3D image reconstruction using a multi-level morphological pyramid. *AAPM 61st Annual Meeting & Exhibition*, San Antonio, TX, 2019 (abstract ID:45252).

[6] Sisniega, A., Stayman, J. W., **Capostagno, S.**, Weiss, C. R., Ehtiati, T., and Siewerdsen, J. H. (2019). Convergence criterion for MBIR based on the local noise-power spectrum: theory and implementation in a framework for accelerated 3D image reconstruction with a morphological pyramid. *The 15th International Meeting on Fully Three-Dimensional Image Reconstruction in Radiology and Nuclear Medicine*, Philadelphia, PA, 2019 (abstract ID: 132).

[7] **Capostagno, S.**, Sisniega, A., Ehtiati, T., Stayman, J. W., Weiss, C. R., a nd Siewerdsen, J. H. (2019). Correction of organ motion in cone-beam CT-guided

transarterial chemoembolization. *SIR 2019 Annual Scientific Meeting*, Austin, TX, 2019 (paper no. 0230).

[8] **Capostagno, S.**, Sisniega, A., Ehtiati, T., Stayman, J. W., Weiss, C. R., and Siewerdsen, J. H. (2019). Deformable motion correction for interventional cone-beam CT. *APS March Meeting 2019*, Boston, MA, 2019 (abstract no. 3094192).

[9] Sisniega, A., **Capostagno, S.**, Zbijewski, W., Weiss, C. R., and Siewerdsen, J. H. (2019). Image-based deformable motion compensation for interventional cone-beam CT. *SPIE Medical Imaging 2019*, San Diego, CA, 2019 (paper no. MI101-232).

[10] Solomon, A., Moreland, A. J., Sisniega, A., **Capostagno, S.**, Siewerdsen, J. H., and Hong, K. (2018). The utility and challenges of cone-beam CT guidance during transarterial chemoembolization of hepatocellular carcinoma. *SIR 2018 Annual Scientific Meeting*, Los Angeles, CA, 2018.

[11] **Ouadah, S.**, Jacobson, M., Stayman, J. W., Ehtiati, T., Weiss, C., and Siewerdsen, J. H. (2017). Task-driven orbit design and implementation on a robotic C-arm system for cone-beam CT. *SPIE Medical Imaging 2017*, Orlando, FL, 2017.

[12] **Ouadah, S.**, Jacobson, M., Stayman, J. W., Ehtiati, T., and Siewerdsen, J. H. (2016). Correction of patient motion in C-arm cone-beam CT using 3D–2D registration. *AAPM 58th Annual Meeting & Exhibition*, Washington, D.C., 2016.

[13] **Ouadah, S.**, Stayman, J. W., Gang, G., Jacobson, M., Ehtiati, T., amd Siewerdsen, J. H. (2015). Self-calibration of cone-beam CT geometry using 3D–2D image registration. *5th Annual Hopkins Imaging Conference*, Baltimore, MD, 2015.

[14] Gang, G., Stayman, J. W., **Ouadah, S.**, Ehtiati, T., and Siewerdsen, J. H. (2015). Task-driven imaging for cone-beam CT in interventional guidance. *AAPM 57th Annual Meeting & Exhibition*, Anaheim, CA, 2015.

[15] **Ouadah, S.**, Stayman, J. W., Gang, G., Uneri, A., Ehtiati, T., and Siewerdsen, J. H. (2015). Self-calibration of cone-beam CT geometry using 3D–2D image registration: development and application to task-based imaging with a robotic C-arm. *SPIE Medical Imaging 2015*, Orlando, FL, 2015.

[16] Gang, G. J., Stayman, J. W., **Ouadah, S.**, Ehtiati, T., and Siewerdsen, J. H. (2015). Task-driven imaging in cone-beam computed tomography. *SPIE Medical Imaging 2015*, Orlando, FL, 2015.

[17] Kung, G. L., **Ouadah, S.**, Hsieh, Y. C., Garfinkel, A., Chen, P. S., and Ennis, D. (2013). Transmural heterogeneity of microstructural remodeling in pacing induced heart failure measured by diffusion tensor MRI. *16th Annual SCMR Scientific Sessions*, San Francisco, CA, 2013.

Patents

[1] Siewerdsen, J. H., Otake, Y., Stayman, J. W., Uneri, A., Wang, A. S. and **Ouadah, S.**, inventors; Johns Hopkins University, assignee. Self-calibrating projection geometry for volumetric image reconstruction. *U.S. Patent 10,478,148.* 19 Nov 2019.

Service and Leadership

- Volunteer at Healthcare for the Homeless as a help desk specialist and surveyor (2019–2020)
- Teaching Assistant for junior and senior-level laboratory course (BME 580.424—Systems Bioengineering Laboratory) covering control systems, speech perception, movement control, and biointerfacing (2017–2018)
- Team Captain of the Hopkins Marathon Team (2015–2017)
- Vice President of General Affairs for the Graduate Student Association (2014–2015)
- President of the Hopkins Imaging Initiative (2014–2015)
- Conference Director for the Hopkins Imaging Initiative Annual Conference (2014)